THE UNIVERSITY *of* EDINBURGH

Modelling elastic dynamics and fracture with coupled mixed correction Eulerian Total Lagrangian SPH

James Young
Doctor of Philosophy
The University of Edinburgh
May 25, 2018

James Young

Modelling elastic dynamics and fracture with coupled mixed correction Eulerian Total Lagrangian SPH

May 25, 2018

Reviewers: Dr Nathan Quinlan and Dr Kevin Hanley

Supervisors: Dr Filipe Teixeira-Dias and Dr Frank Mill

The University of Edinburgh

Institute for Materials and Processes

School of Engineering

Robert Stevenson Road

Edinburgh

EH9 3FB

Abstract

In this thesis, the Smoothed Particle Hydrodynamics (SPH) method is applied to elastic dynamics and fracture. More specifically, two coupling methods are presented which make use of both the Eulerian and Total Lagrangian formulations. These coupling methods are intended for problems whereby SPH particles, which constitute the domain, are required to convert from a Total Lagrangian kernel to an Eulerian kernel once a damage criterion is activated.

The conservation equations are derived for the Eulerian and Total Lagrangian formulations, in a consistent manner which naturally presents the conditions required for the conservation of momentum and energy. These derivations are written such that they make no use of the symmetrical nature of the kernel function or the anti-symmetrical nature of the kernel function gradient. The conservation of momentum and energy is then enforced, along with improving the consistency of the formulations, by implementing the mixed kernel-and-gradient correction. This mixed correction can be applied to both the Eulerian and Total Lagrangian formulations without detracting from the energy and momentum preserving properties provided that the kernel gradient anti-symmetry property is not exploited. The symmetry terms, which are often found in SPH, are included in the derivation of the conservation equations. This is done both to reduce the number of calculations required and to simplify the first coupling procedure.

Both coupled formulations are further expanded by highlighting how artificial viscosity can be introduced. A disadvantage of the first coupling method, this being the incompatibility with artificial stress, is also detailed. The equations of state and the plasticity and damage models used in this work are outlined. Additionally, a number of practical details concerning numerical implementation are given. These include the coupled implementations of ghost particle boundary conditions, memory storage, OpenMP implementation, and the Predict, Evaluate, Correct (PEC) form of leapfrog time integration used.

Lastly, the proposed formulations and models are verified and validated. This is done by modelling progressively more complex simulations that verify individual aspects of the formulations. Either analytical or experimental results are used for validation where possible. The final simulations highlight how high velocity impacts can be modelled using the proposed coupled mixed correction Eulerian Total Lagrangian SPH method.

Acknowledgements

I'd like to dedicate this thesis to my grandfather Roger Sorenson. Only he could convince a six year old that a career as an engineer might be more exciting than that of a train driver. It is safe to say that I would not have ended up where I am without the support of my parents. Thank you both for your investment in my education, love, and support.

On the academic side of things, I firstly need to mention my supervisor Filipe Teixeira-Dias. Filipe has been my friend for nearly half a decade, despite not being able to pronounce his name. Unfortunately for him, for four out of those five years he has also been my PhD supervisor. I am indebted to him for treating me like a colleague and entertaining all my rants with equal measures of humour and thoughtful response. I am also grateful to Filipe for putting up with my foul moods when at the bottom of the PhD sine curve and always making time for me despite possibly being the busiest academic in Edinburgh. Thanks to Frank Mill for his open door policy and always being happy to talk about running, cycling and sausage skins. A big thank you to Jane Blackford for always having time to chat and for teaching me most of what I know about academic writing. Adam Robinson deserves a thank you for regularly listening to me vent my problems over coffee and for pressuring me to get up early in the morning to go running. It was great to have had a friend who could offer meaningful advice, having been where I was. I also appreciated the unconventional post-viva hot chocolate.

Not everyone is quite so lucky to have such great colleagues. Thanks to Rohan, Stephen, Nick, Davide, Patrick, Sofia, Adam, Arunn, Hikaru, Alessio, Dimitrios, and everyone else in 116 for making the PhD experience so enjoyable. Thank you to Stephen Blowers for listening to all my SPH quandaries and offering useful advice. Throughout the duration of our PhD's I think you helped me more than I helped you. Thank you Nick Roberts for always advocating fun over work and dragging me out of the office to go for a much-needed cycle every now and then. A sincere thank you to the many people who made the effort to stay friends throughout the PhD mania, especially Alex, Ashleigh, Callum, Connor and Fraser. I would also like to express my gratitude to my sister Nicky for her confidence in me.

Thank you to both Dr Nathan Quinlan and Dr Kevin Hanley for being my viva examiners. I very much appreciate that you took the time to read my thesis and helped me to understand how I could improve it. The viva was the first time that my work had been scrutinized as a whole. Thank you both for your insightful comments and for helpful suggestions. Thank you to G. R. Liu and M. B. Liu for providing Filipe with the Fortran code from their book "Smoothed Particle Hydrodynamics A Meshfree Particle Method". The Engineering and Physical Sciences Research Council funded this PhD through Grant EP/M506515/1. Without their support, this PhD and many others would not be possible. Thank you to the users on the StackExchange sites Stack Overflow, Physics, and Tex for answering my questions whether I was stumped by some horrific mathematics, an obscure Fortran bug or a LaTeX conundrum. If you would like to see my questions search for the username and misnomer "1QuickQuestion" on any of those sites.

Finally, I need to express my gratitude to the wonderful Dr Charalambous for putting up with me. I don't know what happens next, but I hope that it will be with you. Προφανώς.

James Young
Edinburgh, May 2018

Declaration

I, James Young, declare that this thesis titled, 'Modelling elastic dynamics and fracture with coupled mixed correction Eulerian Total Lagrangian SPH' and the work presented in it are my own. I confirm that:

- This work was done wholly while in candidature for a research degree at this University.
- Where any part of this thesis has previously been submitted for a degree or any other qualification at this University or any other institution, this has been clearly stated.
- Where I have consulted the published work of others, this is always clearly attributed.
- Where I have quoted from the work of others, the source is always given. With the exception of such quotations, this thesis is entirely my own work.
- I have acknowledged all main sources of assistance.
- Where the thesis is based on work done by myself jointly with others, I have made clear exactly what was done by others and what I have contributed myself.

James Young
Edinburgh, May 25, 2018

Contents

Nomenclature

Indices

a	Particle in question.
b	Neighbour of the particle in question.
i	Einstein convention, first index.
j	Einstein convention, second index.
k	Einstein convention, third index.

Greek Symbols

α	First artificial viscosity constant.
α_d	Smoothing function parameter defined in one, two or three-dimensional space.
$\alpha(\boldsymbol{x})$	Parameter in kernel correction for first order consistency.
β	Second artificial viscosity constant.
$\boldsymbol{\beta}(\boldsymbol{x})$	Vector of parameters in kernel correction for first order consistency.
Γ	Gruneisen parameter used in linear Hugoniot form.
γ_0	Gruneisen coefficient used in cubic Hugoniot form.
δ	Denotes virtual field variable in virtual work derivations.
δ^{ij}	Kronecker delta function.
δx	Particle spacing.
$\boldsymbol{\varepsilon}$	An arbitrary anti-symmetric third order tensor.
$\boldsymbol{\epsilon}$	Strain tensor.
$\boldsymbol{\epsilon}'$	Deviatoric component of strain.
$\boldsymbol{\epsilon}_{\mathrm{e}}$	Elastic strain.
$\boldsymbol{\epsilon}_{\mathrm{p}}$	Plastic strain.
ϵ_{as}	Artificial stress parameter.
ϵ_{D_0}	Lemaitre equivalent strain constant.
$\bar{\epsilon}$	Equivalent strain.
$\bar{\epsilon}_{\mathrm{p}}$	Equivalent plastic strain.
ϵ_{f}	Johnson-Cook damage strain at fracture.
$\dot{\epsilon}_0$	Johnson-Cook equivalent plastic strain-rate constant.
η	Mie-Gruneisen compression term.
κ	Smoothing length multiplier.
λ	Lamé's first parameter.
μ	Lamé's second parameter or shear modulus.
μ_{ab}	Term in the artificial viscosity equation.
ν	Poisson's ratio.
Π	Artificial viscosity value.

ρ	Density.
$\boldsymbol{\sigma}$	Cauchy stress tensor.
$\boldsymbol{\sigma}'$	Deviatoric component of the Cauchy stress tensor.
σ_{tr}	Trial Stress.
σ_{vm}	Equivalent or von Mises stress.
σ_{y}	Yield Stress.
θ_a	Principal stress angle.
$\boldsymbol{\Omega}$	Spin tensor.
Ω	Integral or particle domain.

Higher order tensors

$\mathbf{a}$	Acceleration.
$\mathbf{b}$	External body forces.
$\mathbf{C}$	Fourth order elasticity tensor.
$\mathbf{D}$	Rate of deformation tensor.
$\mathbf{D}'$	Deviatoric component of the rate of deformation tensor.
$\mathbf{E}$	Green-Lagrange strain.
$\hat{\mathbf{e}}^1$	Unit vector in x-direction.
$\hat{\mathbf{e}}^2$	Unit vector in y-direction.
$\hat{\mathbf{e}}^3$	Unit vector in z-direction.
$\mathbf{F}$	Deformation gradient.
$\dot{\mathbf{F}}$	Material velocity gradient.
$\mathbf{I}$	Identity matrix.
$\mathbf{K}$	Gradient correction matrix.
$\mathbf{L}$	Spatial velocity gradient.
$\mathbf{N}$	Nominal stress.
$\mathbf{n}$	Outward pointing surface normal.
$\mathbf{P}$	First Piola-Kirchhoff stress tensor.
$\mathbf{P}'$	Deviatoric component of the first Piola-Kirchhoff stress tensor.
$\mathbf{Q}$	Matrix which rotates to the principal axes.
$\mathbf{R}$	The modified principal stress tensor.
$\mathbf{R}_{\text{g}}$	Ghost particle rotation matrix.
$\mathbf{r}_{\text{g}}$	Ghost particle rotation vector.
$\mathbf{S}$	Second Piola-Kirchhoff stress tensor.
$\mathbf{t}$	Internal force.
$\mathbf{t}_{\text{g}}$	Ghost particle translation vector.
$\mathbf{u}$	Displacement from initial position.
$\mathbf{v}$	Velocity.
$\mathbf{v}_{\text{g}}$	Ghost particle velocity.
$\mathbf{X}$	Initial, undeformed or material position.
$\mathbf{x}$	Current, deformed or spatial position.
$\mathbf{x}_g$	Current, deformed or spatial position of ghost particle.

Scalars

A_{JC}	Johnson-Cook yield constant.
A_{L}	Lematitre damage model constant.

a_0	Mie-Gruneisen equation of state constant.
a_{mg}	Mie-Gruneisen volume correction coefficient.
B_{JC}	Johnson-Cook equivalent plastic strain constant.
B_{L}	Lematitre damage model constant.
b_0	Mie-Gruneisen equation of state constant.
C_{JC}	Johnson-Cook plastic strain rate constant.
C_{v}	Specific heat capacity.
C_{f}	Mixed correction factor.
c	Speed of sound.
c_{l}	Longitudinal or pressure wave speed.
c_{r}	Rayleigh wave speed.
c_{s}	Shear wave speed.
c_{t}	Transverse wave speed.
D	Particle scalar damage value between 0 and 1.
D_{1-5}	Five Johnson-Cook damage constants.
E	Young's modulus.
E_{p}	Plastic modulus.
E_{t}	Tangent modulus.
e	Internal energy.
f_{ab}	Ratio of pair kernel value to average spacing kernel value.
G	Shear modulus.
h	Smoothing length.
J	Jacobian (determinant of the deformation gradient).
K	Bulk modulus.
K_{ca}	Contact algorithm first constant.
M_{JC}	Johnson-Cook thermal constant.
m	Mass.
N	Number of particles within support domain.
N_{JC}	Johnson-Cook plastic strain constant.
n_{as}	Artificial stress factor.
n_{ca}	Contact algorithm second constant.
p	Hydrostatic pressure component of the stress tensor.
Δp	Average particle spacing.
q	Normalised particle spacing.
r_{ab}	Scalar distance between particle pairs.
S	Closed surface volume boundary.
s_{1-3}	Mie-Gruneisen coefficients of shock velocity-particle velocity curve.
T	Temperature.
T_{m}	Melting temperature.
T_{r}	Ambient temperature.
t	Time.
t'_{g}	Ghost particle translation index.
u_{p}	Mie-Gruneisen particle velocity.
u_{s}	Mie-Gruneisen shock wave velocity.
V	Volume.
ΔV	Discretised volume increment.

$\dot{w}_\epsilon$	Internal work done by stresses.

Operators and functions

:	Double dot product.
<>	Kernel approximation.
$\bar{\Delta}$	Taylor impact test average error.
$\circ$	Componentwise multiplication of tensors.
Δ	Denotes incremental value in time unless explicitly stated.
$\otimes$	Outer product.
$\times$	Cross product.
$\boldsymbol{f}(\boldsymbol{x})$	Any vector-valued function dependent on variable $\boldsymbol{x}$.
$f(\boldsymbol{x})$	Any scalar-valued function dependent on variable $\boldsymbol{x}$.
$\delta(\boldsymbol{x} - \boldsymbol{x'})$	Dirac Delta function.
div $\boldsymbol{f}(\boldsymbol{x})$	Divergence of generic vector-valued function.
grad $\boldsymbol{f}(\boldsymbol{x})$	Gradient of generic vector-valued function.
$\phi(\boldsymbol{X}, t)$	Mapping function from material to spatial coordinates.
$W(\boldsymbol{x} - \boldsymbol{x'}, h)$	Smoothing or kernel function.
$\nabla W(\boldsymbol{x} - \boldsymbol{x'}, h)$	Gradient of the smoothing or kernel function.
$\widetilde{W}$	Normalised or corrected kernel.
$\nabla \widetilde{W}$	Gradient of the corrected kernel.
$\widetilde{\nabla} \widetilde{W}$	Corrected gradient of the corrected kernel.

1 Introduction

1.1 Motivation and objectives

Both the Eulerian and Total Lagrangian formulations have alternative advantages and disadvantages in the Smoothed Particle Hydrodynamics (SPH) method. The Total Lagrangian formulation is suitable for solid mechanics but cannot manage large distortions. The Eulerian formulation easily handles large distortions but can exhibit the tensile instability in the presence of tensile stresses. The motivation and aim of this research is to couple these formulations to model elastic dynamics and fracture. A number of objectives had to be completed in order to fulfil this aim of a coupled formulation. These were:

1. To derive the solid mechanics conservation equations for both the Eulerian formulation and Total Lagrangian formulation in a consistent manner and to demonstrate the conditions required for the conservation of linear and angular momentum and energy.
2. To apply mixed correction to both formulations in a consistent manner in order to achieve a desired degree of consistency.
3. To propose a coupled formulation which does not detract from the previously mentioned properties and is compatible with artificial stress and artificial viscosity.
4. To ensure that the proposed formulation is compatible with conventional techniques for enforcing boundary conditions.
5. To verify and validate each aspect of the proposed mixed correction coupled formulation and to demonstrate its ability to model elastic dynamics and fracture.

1.2 A brief overview of the development of SPH

SPH has developed rapidly over the last forty years. There are a number of dedicated textbooks [1, 2], a specialised research interest community "SPHERIC", and many online codes. In addition to these resources, a number of excellent review papers have been published [3–7]. Consequently, a broad overview of SPH and its development is not provided here. Instead, the components and applications of this method, which were found to be relevant to this thesis, are discussed. These included numerical methods, meshless methods, the instabilities found in SPH, corrections which have been applied to SPH, applications to fracture, and coupled Eulerian Total Lagrangian methodologies.

1.2.1 Numerical methods

It can be argued that science generally and engineering in particular have become dependent on computer simulations. These simulations can accurately predict the behaviour of complicated

systems where an experiment may be prohibitively expensive, difficult to construct or dangerous to conduct [8]. Furthermore, they can aid in the understanding of novel experimental results in addition to predicting their own [9]. These numerical simulations usually solve sets of ordinary differential equations or partial differential equations that define the underlying physics of the problem. Conventional grid or mesh-based methods do so by splitting the continuum domain into a finite number of sub-domains. This procedure is referred to as discretisation, or it is referred to as meshing in the context of a mesh-based method. The Finite Difference Method (FDM) [10–12], Finite Element Method (FEM) [13] and the Finite Volume Method (FVM) [14, 15] are perhaps the most widely used of the mesh-based methods. In the FEM, the finite elements themselves are bounded by nodes which can be shared between elements. Values at these nodes can be used, along with shape functions, to interpolate values within the elements themselves. The differential equations that define the problem can be replaced, at each element, with a local approximation to these equations. These local approximations can be grouped to provide a global approximation.

Although these mesh-based methods have proven to be a highly effective modelling tool, they are not without fault. The accuracy of the solutions provided by these methods is intricately linked to the quality of the mesh. Liu and Liu [5] stated that it can prove difficult to simulate large deformations, crack propagation, deformable boundaries, free surfaces and moving interfaces, with these methods due to this mesh or grid dependence. Liu and Liu also pointed out that generating a mesh for a complicated geometry can be both time-consuming and complicated. It is possible to remesh the domain but this can similarly prove time-consuming and difficult in three dimensions [16]. Moës et al. [17] and Belytschko et al. [18, 19] developed the Extended Finite Element Method (XFEM) in order to model discontinuities, such as cracks, accurately. In their method, the discontinuity was independent of the mesh and therefore did not require remeshing. Nguyen [16] stated that whilst the XFEM manages to combine the advantages of the FEM and meshless methods, it does not produce smooth derivatives nor easily manage distorted meshes.

1.2.2 Meshless methods

In comparison to mesh-based methods, meshless methods, in which there is no fixed connectivity between nodes or particles, are a recent development. Smoothed Particle Hydrodynamics (SPH) was first formulated for astrophysical problems by Gingold and Monaghan [20] in 1977 and by Lucy [21] later that same year. The SPH method is a meshless particle method whereby the governing differential equations are written using approximations that are resolved for each particle. Each particle has a kernel or smoothing function that weights the contributions from other particles by their respective distances. Liu and Liu [1] stated that there are essentially three types of meshless methods: those based on strong form formulations, like the Generalised Finite Difference Method (GFDM), the Finite Point method (FPM) and HP-cloud method; those based on weak form formulations, like the Element Free Galerkin (EFG) method, the Meshless Local Petrov-Galerkin (MLPG) method and the Particle Interpolation Method (PIM); and particle methods like SPH. Liu and Liu explained that the difference between the SPH method and weak form methods is that the weak form operation is introduced when approximating a function using the SPH method, as opposed to when converting the governing equations into a discrete system of equations.

1.2.3 SPH and its instabilities

As detailed by Liu and Liu [5] and Shadloo et al. [22], SPH has been extended to encompass a broad range of applications in both fluid and solid mechanics. These vary from coastal hydrodynamics to magneto-hydrodynamics to explosive detonations [5]. SPH was not applied to solid mechanics until 1991 when Libersky and Petschek [23] modelled a plane-strain Taylor impact test. They achieved this by adding a deviatoric component, which is zero for pure hydrodynamic flow, to the viscous stress tensor, and by adding a perfectly plastic constitutive model. These authors noted a discrepancy when comparing their results to those of the Lagrangian finite element code EPIC-2. Subsequently, a numerical instability in the method, referred to as the "tensile instability", was investigated by Swegle et al. [24] where particles were observed to clump together. Swegle et al. attributed the tensile instability to a combination of the sign of the kernel's second derivative and tensile stresses in their one-dimensional von Neumann stability analysis. As tensile stresses play a role in activating the tensile instability, Swegle et al. stated that it is more likely to manifest in applications of the SPH method to solid mechanics. A later three-dimensional study by Bonet and Kulasegaram [25] highlighted that the elastic continuum equations, which are frequently approximated using the SPH method, are unstable under tensile pressures. This instability was found to manifest as negative eigenvalues in the stiffness matrix. This analysis was for an isotropic stress tensor where the pressure component was a function of density.

Following the analysis carried out by Swegle et al., a number of attempts were made to address the tensile instability. Dyka and Ingel [26] and Dyka et al. [27] introduced the concept of stress points to SPH whereby kinematic information was carried by one set of "velocity particles" and another set of "stress particles" carried stress information. Although this method was found to be effective at removing the tensile instability, it was also found to be computationally expensive considering that an equal number of stress and velocity particles were effectively required [28]. Monaghan [29], shortly followed by Gray et al. [30], introduced artificial stress, which added an additional stress term to the conservation of momentum equation. In the development by Gray et al., the repulsive stress term was only added to particles that had a positive principal stress and acted to oppose the tensile instability, which caused the particles to clump together. The tensile instability was completely circumvented by Belytschko et al. [31] who noted that it was a product of using an Eulerian kernel. When using an Eulerian kernel, the weighting function is calculated using the current configuration of particles or the spatial coordinates. Belytschko et al. [31] showed that the tensile instability did not manifest when the kernel was a function of the material coordinates. This is known as a Total Lagrangian [32] formulation. They further showed that another instability caused by rank deficiency and known as "zero-energy" modes can occur in either an Eulerian or a Total Lagrangian kernel form. Bonet and Kulasegaram [25] noted that the mode that caused the spurious terms in the tangent stiffness of the system in the Eulerian configuration was converted into a spurious mechanism in the Total Lagrangian configuration. These authors also stated that this mechanism could be managed with artificial viscosity [25, 33].

As the initial configuration of particles is used as the reference condition, the Total Lagrangian formulation may become unstable in the presence of large distortions. Bonet and Kulasegaram and Bonet et al. [33, 34] suggested that, in this case, the reference configuration could be updated. Subsequently, Vidal et al. [35] explained how updating the reference configuration might activate zero energy modes in the Total Lagrangian configuration, but these authors stressed that this formulation does not manifest the tensile instability. These authors also highlighted how, in an Eulerian configuration, the tensile instability can be controlled by implementing artificial stress or by introducing

stress points, as previously discussed. Vidal et al. further stated that when updates are performed infrequently, the error that causes the zero energy modes might not be detected. Liu and Liu [1] demonstrated how zero energy modes might be activated by a finite difference method and drew comparisons with how it could be activated by the SPH method with Eulerian kernels. Vidal et al. [35] outlined a "Hessian's Difference Stabilization" technique where the approximation of the gradient of a function included an additional higher order derivative term. This term contained the difference of two Hessians, these being symmetric square matrices of second order partial derivatives. Although this technique was found to prevent zero energy modes, Ganzenmüller [36] and Ganzenmüller et al. [37] stated that the computation of the third-order tensor, required for the Hessian, "*dramatically affects the numerical efficacy*". As Vidal et al. [35] found that they needed to update the reference configuration for a simulation that did not undergo plastic flow, Ganzenmüller [36] and Ganzenmüller et al. [37] stated that "*the stabilizing effect is not very clear for large deformations*". Ganzenmüller et al. [37] recommend their stiffness-based hourglass control and viscous hourglass control schemes for suppressing zero energy modes. The aim of the stiffness-based hourglass control was to minimise the discrepancy between the distance between particle pairs as calculated using the deformation gradient of each particle and the actual distance between particle pairs. The viscous hourglass control scheme was similar to the stiffness-based scheme but it considered velocities rather than positions and was written in a similar form to the artificial viscosity, as devised by Monaghan [38, 39].

1.2.4 Kernel and kernel gradient consistency correction

Both Vidal et al. [35] and Ganzenmüller et al. [37] detailed their formulations with gradient correction. They did this because the SPH method cannot guarantee 0^{th} order consistency or 1^{st} order accuracy without some modification. It would appear that the origins of this correction began with Johnson and Beissel [40] who presented a Normalised Smoothing Function (NSF) algorithm. These authors modified the derivative of the kernel function such that linear velocity distributions resulted in exact principal strain rates. This normalisation technique inspired Randles and Libersky [41] to use a normalised kernel sum to predict the value of density at boundaries more accurately and to extend the algorithm presented by Johnson and Beissel [40] to tensors. In doing so, they derived the correction matrix, which ensured the correct calculation of the divergence of a linear field and 0^{th} order consistency. Bonet and Lok [42] later presented the same correction matrix and referred to this as "gradient correction". They proved that Eulerian SPH, with an isotropic stress tensor, conserves linear momentum but does not unconditionally conserve angular momentum. They further showed how this gradient correction ensures the conservation of angular momentum. Bonet and Lok [42] continued to propose a "mixed correction scheme" which combined both gradient correction and "kernel correction". This kernel correction was a process where the kernel was modified so that a polynomial up to a specified order could be exactly reproduced, which Bonet and Lok attributed to Li et al. [43] and Liu et al. [43]. Bonet and Lok [42] enforced a degree of one, which resulted in a weighted average of Shepard's interpolation of functions. Chen and Beraun [44] and Chen et al. [45] further developed the theory by taking the SPH integral approximation of the gradient of a function and expanded this using a Taylor series. Having done so, they gave a generalised approach to reproduce any order of derivative exactly, in one or two dimensions, by rearranging the Taylor series and neglecting unwanted derivatives. Chen et al. named their method the Corrective Smoothed Particle Method (CSPM). Ganzenmüller [36] stated that in the work done by Randles and Libersky [41], Bonet and Lok [42] and Vignjevic et al. [46], the local conservation of linear

momentum was destroyed as, due to the correction, the particle internal forces were not equal and opposite.

1.2.5 Fracture

Liu and Liu [5] attributed the foundation of SPH for high strain hydrodynamics problems to Libersky and Petschek [23], Libersky et al. [47] and Randles and Libersky [41]. As previously mentioned, the first of these papers was the original application of SPH for solid mechanics. Following this work, Libersky et al. [47] applied SPH to a hypervelocity impact problem. Subsequently, Randles and Libersky [41] modelled both damage and fracture using the Johnson-Cook damage model and a novel tensor form of damage. This tensor form of damage was then used to modify a "damage interaction factor" between particle pairs. This may have been the inspiration for the much later work by Chakraborty and Shaw [48–50]. These authors modelled fracture by considering that the connection between neighbouring particles could be modelled as a pseudo-spring with an "interaction factor", which defined the damage in the spring. Benz and Asphaug [51] began investigating simulations of brittle solids using SPH at a similar time to Libersky et al. These authors modelled fracture by enforcing an initial distribution of flaws with activation thresholds, which were distributed using the Weibull distribution [52]. Once the strain at a particle was found to exceed this threshold, damage was allowed to accumulate. Das and Cleary [53] and De Vuyst and Vignjevic [54] later employed a similar methodology.

Rabczuk and co-authors provided a number of methods for modelling fracture using meshless methods. Rabczuk and Belytschko [55] proposed a two-dimensional "cracking particles" method using an EFG-P formulation which these authors stated was a particle method that belonged within the EFG framework. In this method, discrete cracks passed through particles and were modelled as discontinuous enrichments. Rabczuk and Belytschko [55] further stated that the cracking particle method could be applied to SPH. Rabczuk and Belytschko [56] later expanded their EFG-P cracking particle model so that particles which used Total Lagrangian kernels switched to using Eulerian kernels once they cracked. At the same time, Rabczuk and Zi [57] proposed a fracture model based on the local partition of unity using a method that these authors named the Extended Element Free Galerkin (XEFG) method. The premise of this fracture model was that once the material lost stability, a jump in displacement was given by enrichment. Rabczuk et al. [58] later expanded their cracking particles method to three dimensions. They changed their procedure so that particles split once cracked. A visibility method was then used along the crack front. This meant that the discontinuity in the displacement field was modelled by neglecting the contributions from particles on alternate sides of the cracked particle.

Rajagopal and Gumpta [59] compiled a comparative study of fracture modelling techniques for meshless methods. These authors made use of the EFG method and compared the "natural fracture method", the "smeared crack method" [60], the "discrete crack method" and the "discrete crack segment method". In the natural fracture method, fracture was modelled by particles that translated so that they were no longer included in the support domain of particles on either side of the fracture path. In the smeared crack method [60], energy dissipation caused by fracture was captured by varying the stress-strain curve. In the discrete crack method fracture was explicitly modelled and the visibility method was applied across the fracture path. Lastly, in the discrete crack segment method the crack path was modelled discretely as for the cracking particle method [55]. These authors generally found the natural fracture method to produce the worst results whilst the discrete crack method was able to model complicated fracture paths accurately. It should be noted that these authors

made use of Total Lagrangian kernels only and therefore their natural fracture method required that they apply some distance fracture criterion to degrade the connection between particles on either side of the fracture path.

1.2.6 Coupled Eulerian Total Lagrangian SPH

As indicated in Section 1.2.3, the Total Lagrangian and the Eulerian SPH kernel types both have distinct advantages and disadvantages. The Total Lagrangian approach does not manifest the tensile instability but cannot manage large distortions. The Eulerian kernel type easily handles large distortions but exhibits the tensile instability in the presence of tensile stresses. To overcome these problems it would appear sensible to couple both kernel types and allow an adaptive, irreversible, conversion from the Total Lagrangian kernel type to the Eulerian kernel type. This could allow the simulation of fracture and impact beyond the point when the Total Lagrangian formulation would fail. This was done by Rabczuk and Belytschko [56] for the EFG-P method, as previously mentioned. There would appear to be little literature concerning the coupling of the Eulerian and the Total Lagrangian formulations for solid mechanics. In 2009, Lacome et al. [61] presented a conference paper titled "SPH Formulation with Lagrangian Eulerian adaptive kernel". These authors developed a model in which particles with Eulerian kernels treated all other particles as having Eulerian kernels. Eulerian particles that were neighbours with Total Lagrangian particles behaved like Total Lagrangian particles and were required to have Total Lagrangian particle properties. However, these authors subsequently discontinued this line of research[1].

It is noted that the conversion from an Eulerian kernel type to a Total Lagrangian kernel type is not investigated in this work, nor in the supporting literature. This is because there is a lack of physically interesting situations, in elasticity and fracture, where a continuum would be subjected to severe distortions and then settles to a more placid state, which could be taken advantage of by a conversion from an Eulerian kernel type to a Total Lagrangian kernel type.

It would appear that the convention for describing the kernel type varies between the solid mechanics and the fluid mechanics SPH communities. Lind and Stansby [62] and Fourtakas et al. [63] referred to the formulation where calculations were carried out with respect to the current particle positions as a Lagrangian formulation and the form where calculations were carried out with respect to a reference state as the Eulerian formulation. In their work, the Lagrangian formulation considered moving particles and the Eulerian formulation considered fixed particles. Conventionally, in the application of SPH to solid mechanics the Total Lagrangian formulation considers fixed support domains and the Eulerian formulation considers moving support domains. There has been recent interest in the development of an Eulerian-Lagrangian formulation using incompressible SPH (ISPH) to model fluid flows. This began with Lind and Stansby [62], who were followed by Fourtakas et al. [63] with their recent 2018 publication. In order to transition from a Lagrangian (moving particles) to an Eulerian (fixed particles) formulation, Fourtakas et al. [63] explicitly added an advection term switch to the Navier-Stokes equation.

[1] Private email communication with co-author Professor Christine Espinosa.

1.3 Definition of conventions, differential operators and notation

The chapters which follow rely on mathematics involving higher order tensors, divergences and gradients. Consequently, these operators and the shorthand notation used to describe them are briefly described in order to avoid ambiguity and confusion. Coordinates are defined in one, two, and three-dimensional space using a Cartesian coordinate system [64] with directions denoted by x, y and z. Spatial coordinates are denoted by the vector $\mathbf{x}$ in this system. Vectors may be written in terms of unit vectors $\hat{\mathbf{e}}^1$, $\hat{\mathbf{e}}^2$ and $\hat{\mathbf{e}}^3$, which are described by

$$\hat{\mathbf{e}}^1 = \begin{bmatrix} 1 \\ 0 \\ 0 \end{bmatrix}, \qquad \hat{\mathbf{e}}^2 = \begin{bmatrix} 0 \\ 1 \\ 0 \end{bmatrix}, \qquad \hat{\mathbf{e}}^3 = \begin{bmatrix} 0 \\ 0 \\ 1 \end{bmatrix}. \tag{1.1}$$

The unit vectors are denoted by $\hat{\mathbf{e}}^1$, $\hat{\mathbf{e}}^2$, $\hat{\mathbf{e}}^3$ rather than the conventional i, j and k so as to avoid confusion with the indices which are commonly used in Einstein summation [65] and to denote tensor components. Einstein summation convention can be used in order to reduce sums into a more compact form. In this convention, summation takes place over repeated indices. For example, the dot product of two three-dimensional vectors $\mathbf{a}$ and $\mathbf{b}$ is given by

$$\mathbf{a} \cdot \mathbf{b} = \sum_{i=1}^{3} a^i b^i \, . \tag{1.2}$$

In the Einstein summation notation the summation symbol is implicit and the above reduces to

$$\mathbf{a} \cdot \mathbf{b} = a^i b^i \, . \tag{1.3}$$

Combining the Einstein summation notation with the unit vectors defined above allows for a compact representation of higher order tensor operations, such as the divergence of a second order tensor and the gradient of a first order tensor. This is necessary as the definition of these operations can vary between texts and therefore warrants an explanation. Both definitions are applicable if used consistently. In this work, the gradient of a first order tensor field, or a vector field, is given by [66, 67]

$$\text{grad}\, \mathbf{a} = \frac{\partial \mathbf{a}}{\partial x^j} \otimes \hat{\mathbf{e}}^j = \frac{\partial a^i}{\partial x^j} \hat{\mathbf{e}}^i \otimes \hat{\mathbf{e}}^j \, . \tag{1.4}$$

Note that references given may not use the same notation on the left-hand side of Equation 1.4, but the definition on the right-hand side is the same. This form of the gradient of a vector field is not interchangeable with the alternative definition, that being $\nabla \otimes \mathbf{a}$, as this equals [68]

$$\nabla \otimes \mathbf{a} = \hat{\mathbf{e}}^i \frac{\partial}{\partial x^i} \otimes a^j \hat{\mathbf{e}}^j = \frac{\partial a^j}{\partial x^i} \hat{\mathbf{e}}^i \otimes \hat{\mathbf{e}}^j \, . \tag{1.5}$$

The above definitions have also been abbreviated to $\text{grad}\, \mathbf{a} = \mathbf{a}\nabla$ and $\nabla \otimes \mathbf{a} = \nabla \mathbf{a}$ [69]. These two definitions produce the same vector for the gradient of a scalar field. Yet for the gradient of vector fields the resulting second order tensors are the transpose of each other such that $\text{grad}\, \mathbf{a} = (\nabla \otimes \mathbf{a})^{\mathsf{T}}$.

In the equations that follow, the divergence of any order tensor field is defined as the trace of its gradient. For a second order tensor this leads to the definition that [70]

$$\text{div}\mathbf{A} = \text{grad}\,\mathbf{A} : \mathbf{I} = \frac{\partial A^{ij}}{\partial x^j}\hat{\mathbf{e}}^i \,, \tag{1.6}$$

where the tensor double dot product is defined as $\mathbf{A} : \mathbf{B} = A_{ij}B_{ij}$. Note that this definition of divergence of a second order tensor differs from the alternative form [68]:

$$\nabla \cdot \mathbf{A} = \hat{\mathbf{e}}^i \frac{\partial}{\partial x^i} \cdot (A^{jk}\hat{\mathbf{e}}^j \otimes \hat{\mathbf{e}}^k) = \frac{\partial A^{ji}}{\partial x^j}\hat{\mathbf{e}}^i \,. \tag{1.7}$$

The importance of clarifying the above becomes apparent when investigating the momentum equation as given in the Total Lagrangian configuration. Authors use different stress tensors depending on the chosen definition of the gradient and divergence. Both methods are interchangeable but if the definitions are not stated this can cause confusion.

The typesetting convention used is as follows: in general, scalar values are denoted by lower case, italic and non-bold; vectors are generally denoted by lower case, non-italic and bold; lastly, higher order tensors are denoted by upper case, non-italic and bold. There are some exceptions to these rules including some variables denoted by Greek letters and model-specific parameters. When a variable is associated with a particle, the variable is written with the subscript a, for example $\mathbf{x}_a$. When a variable is associated with a particle's neighbour, the variable is written with the subscript b. If a component of a tensor is explicitly referenced, this is done using the subscripts x, y and z such as P_{xy}. If both particle and tensor component are simultaneously referenced the particle subscript notation takes preference and the tensor component is moved to a superscript, for example K_a^{xx}.

Bonet et al. [25], Belytschko et al. [32] and Rabczuk et al. [55] are referred to for the descriptions of the formulations used. According to Belytschko et al. [32], "*formulations in terms of the Lagrangian measures of stress and strain in which derivatives and integrals are taken with respect to the Lagrangian (material) coordinates X* [are] *called total Lagrangian formulations*". These authors continue to state that "*formulations expressed in terms of Eulerian measures of stress and strain in which derivatives and integrals are taken with respect to the Eulerian (spatial) coordinates x* [are] *often called updated Lagrangian formulations*". The common convention to refer to the second of these formulations as an Eulerian formulation is followed [25, 33]. Consequently, in this work any reference to Total Lagrangian or Eulerian kernels refers to kernels that are calculated in the material and spatial coordinates, respectively [55]. Additionally, Total Lagrangian and Eulerian particles are particles which make use of a kernel in either the material or spatial coordinates, respectively.

The term "mixed correction" is often used in the following chapter. This is written as a shortened version of the first-order mixed kernel-and-gradient consistency correction developed by Bonet and Lok [42]. The hyphenation in the full terminology is borrowed from Basa et al. [71] as it makes it transparent that "mixed kernel-and-gradient" correction refers to a specific type of correction.

With the conventions, differential operations and notation defined, it is now possible to expand upon the theory of the SPH approximations, formulations, corrections and coupling.

1.4 Structure

This thesis has been organised into five chapters, which contain the following:

Chapter 1 begins by stating the motivation and aim for this work, this being to couple the Eulerian and Total Lagrangian SPH formulations to model elastic dynamics and fracture. The objectives that had to be fulfilled to meet this aim are then listed. Next, an overview of the SPH method is given. Emphasis is placed on the elements and applications of the method which are relevant to the subject matter in this thesis. This included a brief description of numerical methods and meshless methods, a review of the instabilities found in SPH, an overview of the methods commonly used to restore consistency to the kernel and the kernel gradient, an account of the various methods used to model fracture in the SPH method and, a literature review of coupled kernel-type formulations. The definition of conventions, differential operators, and notation is then given. Finally, the structure of this thesis is detailed.

Chapter 2 introduces the fundamental SPH approximations along with the additional symmetry terms used in these approximations. These are then applied to the conservation equations for both an Eulerian and a Total Lagrangian formulation. The SPH conservation of momentum equation is derived using the principles of virtual work in both material and spatial coordinates. The conditions required for the conservation of momentum and energy are given. Next, the mixed kernel-and-gradient correction is detailed along with its application to both formulations. A description of the two methods proposed to couple the Eulerian and Total Lagrangian formulations are then given. The first coupling method is limited to applications where the kernel support domain does not significantly change shape and size between the material and spatial coordinates at the interface between formulations. This limitation largely decreases the computational cost in comparison to the second coupling method. In the second coupling method particles of differing kernel types treat each other as using the same kernel type, which requires more neighbour searches and the translation of field variables from material to spatial coordinates and vice versa.

Chapter 3 extends the Eulerian and Total Lagrangian formulations so that they are capable of modelling plasticity and fracture. This involves expanding artificial viscosity to be compatible with the mixed correction Eulerian, Total Lagrangian, and coupled formulations. A similar methodology is given for artificial stress. Equations of state, plasticity and damage models are described. The application of symmetry planes is explained, along with the rules applied to a mixed correction scheme. Next, essential boundary conditions are discussed in addition to the contact algorithm used to transfer momentum between different bodies which use a Total Lagrangian formulation. Lastly, a Predict, Evaluate, Correct time integration scheme is described and details regarding the numerical implementation are given, including the benefits of OpenMP parallel programming.

Chapter 4 evaluates eleven verification and validation examples. These serve to ensure that both the application of the theory given in Chapters 2 and 3 is correct and that the proposed formulations can recreate experimental results. It is first proven that the mixed correction gives identical results regardless of whether symmetry terms are included or not. The one dimensional Total Lagrangian formulation is then validated using a one-dimensional wave problem. Next, the tensile instability is highlighted for the Eulerian formulation and the advantages of the mixed correction are demonstrated. Following this, energy and momentum conservation are demonstrated. After this, artificial stress is applied to both coupled formulations and is compared. Then, both the Eulerian and Total Lagrangian formulations are verified by highlighting how they give the same results for small displacements. In addition, the proposed artificial viscosity is verified. Plasticity is then validated using the Taylor

impact test before exploring crack branching. The modelling of impact and fracture is validated using the Kalthoff-Winkler problem. Lastly, the advantages and disadvantages of the proposed coupling methodologies are highlighted using a high-velocity impact problem and a three-dimensional debris impact test.

Chapter 5 outlines the significance and implications of this work. Additionally, the limitations of the proposed formulation are given along with recommendations for future work.

2 SPH approximations, formulations, corrections and coupling

2.1 Overview

If seeking to couple the Eulerian and Total Lagrangian formulations of the SPH method it would appear logical to derive them in a robust and consistent manner. A strong argument for so doing is that the elimination of unnecessary incompatibilities will prevent false negatives arising when verifying and validating the coupling methods. More specifically, if it has been ensured that both formulations conserve mass, momentum and energy, then it can be reasonably argued that the coupling methods should do likewise.

Both formulations are dependent on the selection of fundamental SPH approximations. Therefore, it would seem sensible to explain these selections, their background and any underpinning assumptions. With this in mind, the fundamental approximations using the SPH method are first derived. These include the kernel approximation of a function, the gradient of a function and the divergence of a function. Having done this, the particle approximations can then be applied to these expressions. These particle approximations form the tools required to apply the SPH method to continuum mechanics. Using these tools the SPH approximations are first used to derive the Total Lagrangian formulation of the SPH method for solid mechanics. This includes the Total Lagrangian form of the conservation of mass, momentum and energy, where the conservation of momentum is derived using the principles of virtual work. Having done so, the derived equations are then proven to conserve mass, linear momentum and energy unconditionally and to conserve angular momentum conditionally. These derivations and proofs are given such that they make no use of any rules that break down once they are modified to include additional correction terms. The benefit of this approach is that the correction can be directly applied to the end result of the derivations which in no way impacts the validity of the aforementioned proofs. Similarly, the Eulerian formulation for the SPH method as applied to solid mechanics is given. With the exception of the conservation of mass, for which no particle approximation is required for the Total Lagrangian formulation, the Eulerian derivations are given following the same methodology as for the Total Lagrangian approach. It is shown that the given Eulerian formulation also unconditionally conserves mass, linear momentum and energy and conditionally conserves angular momentum.

Some drawbacks common to both approaches are given, namely their order of consistency, having derived both formulations in a consistent manner. These drawbacks are addressed using both kernel and kernel gradient modification. Both the derivation and the effects of these modifications are explained in an Eulerian and Total Lagrangian context. Lastly, two coupling procedures are proposed along with their advantages and drawbacks.

2.2 Fundamental approximations using the SPH method

The derivation of the SPH method must be given before applying the SPH method to the conservation equations. This begins with the integral representation of a function, which is then approximated using a kernel or smoothing function, known as the kernel approximation. After giving the properties of this smoothing function, the kernel approximations of the divergence and gradient are given. Having done this, the particle approximations are given for a function and its divergence and gradient. The particle approximations are the conversion of the kernel approximations, which involve integrals, into summations that are computationally useful. Lastly, an alternative symmetrical formulation for the divergence and gradient of a function is given.

2.2.1 Integral representation and kernel, divergence and gradient approximations

The derivation of the SPH method starts with the integral representation of a function [1]:

$$f(\mathbf{x}) = \int_{\Omega} f(\mathbf{x}')\delta(\mathbf{x}-\mathbf{x}')\mathrm{d}\mathbf{x}' \ , \tag{2.1}$$

where f is a generic function which is dependent on the spatial coordinate $\mathbf{x}$, Ω is the domain of the integral which contains the point $\mathbf{x}$, $\mathbf{x}'$ is a variable spatial coordinate within the domain, and $\delta(\mathbf{x}-\mathbf{x}')$ is the Dirac delta [72] function which is defined by

$$\delta(\mathbf{x}-\mathbf{x}') = \begin{cases} \infty & \text{if } \mathbf{x} = \mathbf{x}' \\ 0 & \text{if } \mathbf{x} \neq \mathbf{x}' \end{cases} \ . \tag{2.2}$$

By replacing the Dirac delta function with some smoothing function, Equation 2.1 can be re-written as

$$f(\mathbf{x}) \approx \int_{\Omega} f(\mathbf{x}')W(\mathbf{x}-\mathbf{x}',h)\mathrm{d}\mathbf{x}' \ . \tag{2.3}$$

In this equation $W(\mathbf{x}-\mathbf{x}',h)$ is the smoothing function that is dependent on both the vector distance between the spatial coordinates and some smoothing length h. This smoothing length defines the range of influence of the smoothing function $W(\mathbf{x}-\mathbf{x}',h)$. The smoothing function must approximate the Dirac delta function in order for the above equation to be valid and, consequently,

$$\lim_{h\to 0} W(\mathbf{x}-\mathbf{x}',h) = \delta(\mathbf{x}-\mathbf{x}') \ . \tag{2.4}$$

In addition to approximating the Dirac delta function, the smoothing function must also satisfy the unity condition:

$$\int_{\Omega} W(\mathbf{x}-\mathbf{x}',h)\mathrm{d}\mathbf{x}' = 1 \ , \tag{2.5}$$

and commonly satisfies the compact support condition:

$$W(\mathbf{x}-\mathbf{x}',h) = 0 \text{ when } |\mathbf{x}-\mathbf{x}'| > \kappa h \ , \tag{2.6}$$

where κ is a multiplier that is determined by the selection of smoothing function. The compact support condition ensures that the smoothing function has no effect once the distance between points exceeds that of the domain of influence.

The smoothing function approximates the Dirac delta function. Therefore, the integral representation (Equation 2.1) loses its exact replication of $f(\mathbf{x})$ once the smoothing function has been substituted. This substitution is known as a kernel approximation and is denoted using angled brackets such that

$$< f(\mathbf{x}) >= \int_{\Omega} f(\mathbf{x}')W(\mathbf{x}-\mathbf{x}',h)\mathrm{d}\mathbf{x}' \ . \tag{2.7}$$

The kernel approximation of the divergence of a vector function is derived by replacing the generic function $f(\mathbf{x})$ with the divergence of a vector-valued function div $\boldsymbol{f}(\mathbf{x})$, resulting in

$$< \text{div } \boldsymbol{f}(\mathbf{x}) >= \int_{\Omega} [\text{div } \boldsymbol{f}(\mathbf{x}')]\, W(\mathbf{x}-\mathbf{x}',h)\mathrm{d}\mathbf{x}' \ . \tag{2.8}$$

Recalling that the divergence of the product of a vector field and a scalar field can be written using the following identity:

$$\text{div } (\mathbf{v}u) = u \text{ div } \mathbf{v} + \mathbf{v} \cdot \text{grad } u \ , \tag{2.9}$$

then the integrand in the right-hand side of Equation 2.8 can be written, using a rearrangement of Equation 2.9, as

$$[\text{div } \boldsymbol{f}(\mathbf{x}')]\, W(\mathbf{x}-\mathbf{x}',h) = \text{div } [\boldsymbol{f}(\mathbf{x}')W(\mathbf{x}-\mathbf{x}',h)] - \boldsymbol{f}(\mathbf{x}') \cdot \text{grad } W(\mathbf{x}-\mathbf{x}',h) \ . \tag{2.10}$$

As the kernel is a scalar-valued function there is no possibility of confusing the definition of its gradient. Therefore grad $W(\mathbf{x}-\mathbf{x}',h)$ is now written as $\nabla W(\mathbf{x}-\mathbf{x}',h)$ so as to conform with common practice. Substituting Equation 2.10 into Equation 2.8 yields

$$< \text{div } \boldsymbol{f}(\mathbf{x}) >= \int_{\Omega} \text{div } [\boldsymbol{f}(\mathbf{x}')W(\mathbf{x}-\mathbf{x}',h)]\, \mathrm{d}\mathbf{x}' - \int_{\Omega} \boldsymbol{f}(\mathbf{x}') \cdot \nabla W(\mathbf{x}-\mathbf{x}',h)\mathrm{d}\mathbf{x}' \ . \tag{2.11}$$

The first term on the right-hand side in the equation above can be re-written using Gauss' theorem[1] [73], which produces

$$< \text{div } \boldsymbol{f}(\mathbf{x}) >= \int_{S} \boldsymbol{f}(\mathbf{x}')W(\mathbf{x}-\mathbf{x}',h) \cdot \mathbf{n}\mathrm{d}S - \int_{\Omega} \boldsymbol{f}(\mathbf{x}') \cdot \nabla W(\mathbf{x}-\mathbf{x}',h)\mathrm{d}\mathbf{x}' \ . \tag{2.12}$$

If the support domain of the coordinate $\mathbf{x}$ is within the volume itself, then the surface integral can be neglected due to the compact support condition as stated in Equation 2.6. Using this assumption the divergence of a vector-valued function can be written as

$$< \text{div } \boldsymbol{f}(\mathbf{x}) >= -\int_{\Omega} \boldsymbol{f}(\mathbf{x}') \cdot \nabla W(\mathbf{x}-\mathbf{x}',h)\mathrm{d}\mathbf{x}' \ . \tag{2.13}$$

If the support domain does not truncate the boundary, the above equation highlights how the differential operator can move through the kernel approximation to act on the smoothing function

[1] Gauss' theorem is given by $\int_V \text{div } \boldsymbol{f}(\mathbf{x})\, \mathrm{d}V = \oint_S \boldsymbol{f}(\mathbf{x}) \cdot \mathbf{n}\, \mathrm{d}S$ and states that the integral of the divergence of a vector $\boldsymbol{f}(\mathbf{x})$ over a volume V is equal to the integral of that vector over an enclosing surface S, which bounds that volume. In this equation, $\mathbf{n}$ is the surface normal that points outwards from the boundary.

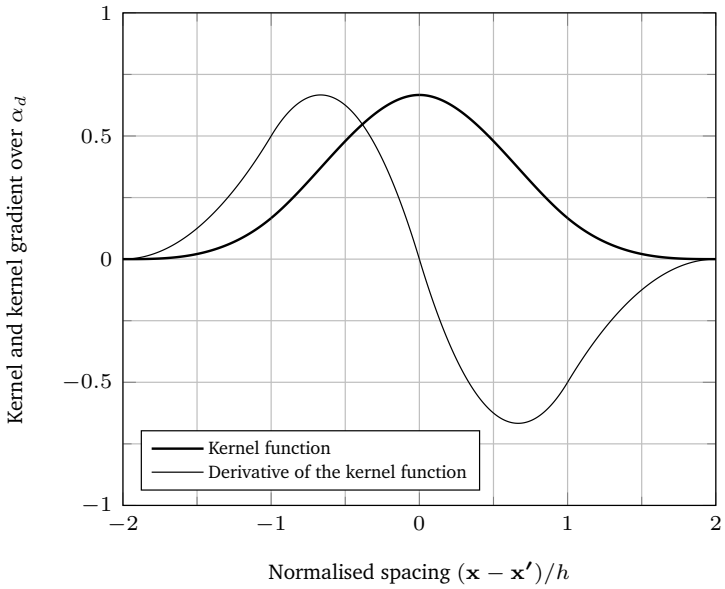

Figure 2.1: One-dimensional plot of the cubic kernel function and its derivative against distance. The spacing has been normalised by the smoothing length h, and the kernel function and kernel gradient by α_d.

itself. This is a useful property as it means that in order to calculate the divergence of a function only the gradient of the smoothing function is required rather than the gradient of the function itself. Following precisely the same procedure in replacing the generic function with the gradient of a vector-valued function, applying the appropriate gradient identity and neglecting the surface term, the SPH approximation of the gradient of a vector-valued function can be written as

$$< \text{grad } \boldsymbol{f}(\mathbf{x}) >= -\int_{\Omega} \boldsymbol{f}(\mathbf{x}') \otimes \nabla W(\mathbf{x} - \mathbf{x}', h) \mathrm{d}\mathbf{x}' \ . \tag{2.14}$$

It can be seen from these equations that the accuracy of the divergence and gradient approximations is dependent on the kernel gradient and consequently the selection of the smoothing function. This selection of smoothing function is briefly discussed before continuing to describe the particle approximation.

2.2.2 The cubic spline smoothing function

The SPH representation of a function, its divergence and gradient, are dependent on the smoothing function itself. There is a large range of smoothing functions available and some of the earliest include the original [20] and improved [74] Gaussian kernel, the bell-shaped kernel [21], the cubic spline kernel [75] and higher order spline kernels including the quartic and quintic spline kernels [76, 77]. These kernels fall into the category of bell-shaped or gaussian-shaped kernels. Fulk and Quinn [78] showed that these bell-shaped kernels tend to outperform alternatives such as parabolic-shaped, hyperbolic-shaped and double hump-shaped kernels. Although it would appear that the Gaussian kernel would be the optimal choice, it has the disadvantage of an infinite support domain resulting in all particles in the domain being neighbours with each other. Therefore, a kernel function with compact support is preferable. The numerical examples presented in Chapter 4 made use of the cubic kernel, as displayed in Figure 2.1. This kernel is used in order to be consistent with the

literature [26, 30, 33, 79], from which a number of the numerical examples were taken and compared. The cubic spline function is defined over the normalised spacing $[-2, 2]$ and is given by

$$W(\mathbf{x}-\mathbf{x}', h) = \alpha_d \begin{cases} \frac{2}{3} - q^2 + \frac{1}{2}q^3 & 0 \le q < 1 \\ \frac{(2-q)^3}{6} & 1 \le q < 2 \\ 0 & q \ge 2 \end{cases}, \tag{2.15}$$

where q is the normalised spacing given by $\|\mathbf{x}-\mathbf{x}'\|/h$ and α_d is a parameter valued as $1/h$, $15/(7\pi h^2)$ and $3/(2\pi h^3)$ dependent on whether the domain is defined in one, two or three-dimensional space. Using $\mathrm{d}q/\mathrm{d}\mathbf{x} = (\mathbf{x}-\mathbf{x}')/qh^2$, the first derivative of the cubic spline function is given by

$$\nabla W(\mathbf{x}-\mathbf{x}', h) = (\mathbf{x}-\mathbf{x}')\alpha_d \begin{cases} -\frac{2}{h^2} + \frac{3}{2h^2}q & 0 \le q < 1 \\ -\frac{(2-q)^2}{2qh^2} & 1 \le q < 2 \\ 0 & q \ge 2 \end{cases}. \tag{2.16}$$

According to Liu and Liu [1], a disadvantage of this kernel is that its second derivative is a piecewise linear function resulting in reduced stability properties in comparison to smoother functions such as the quartic, quintic or gaussian kernels. As stated by Price [80], the use of these higher order splines improves the smoothness of the SPH representations, as the compact support radius is larger than kernels such as the cubic. Price continues to explain that simply stretching the kernel function, through either the modification of h or the particle spacing, is entirely different from using a kernel with a larger compact support radius. Quinlan et al. [81] demonstrated that, in one-dimensional SPH with uniformly spaced particles, the accuracy becomes limited by second-order error in smoothing length as the ratio of the discrete particle volume to smoothing length decreases. Quinlan et al. [81] similarly demonstrated that, under the same conditions, if the smoothing length is decreased with a constant ratio of discrete particle volume to smoothing length, then the error becomes dominated by a residual term that is dependent on this ratio.

2.2.3 Particle approximation

The kernel, divergence and gradient approximations given in Equations 2.7, 2.13 and 2.14 must be converted from integrals into summations to be of use for computation. This is achieved by populating the domain with spatial points as highlighted in Figure 2.2 and is known as a particle approximation. In this case, a particle a now contains many neighbouring particles b within its support domain. The particle approximation involves replacing the infinitesimal volume $\mathrm{d}\mathbf{x}'$ associated with particle b with a finite volume ΔV_b. The integral in Equation 2.7 is approximated by a summation from 1 to N, where N is the number of particles within the support domain. Therefore, the particle approximation of the kernel approximation of the function $f(\mathbf{x})$ is given by

$$< f(\mathbf{x}) >= \int_{\Omega} f(\mathbf{x}')W(\mathbf{x}-\mathbf{x}', h)\mathrm{d}\mathbf{x}' \simeq \sum_{b=1}^{N} f(\mathbf{x}_b)W(\mathbf{x}-\mathbf{x}_b, h)\Delta V_b \,. \tag{2.17}$$

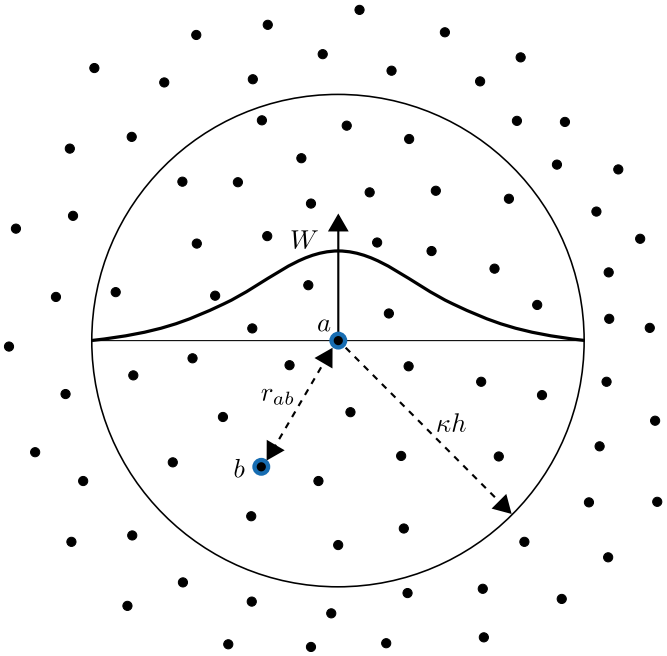

Figure 2.2: Support domain of particle a defined by smoothing function W and populated with particles b. The magnitude of the distance between particles a and b is given by r_{ab}. The radius of the support domain is given by κh.

As the finite volume of the particle ΔV_b located at b can be written as

$$\Delta V_b = \frac{m_b}{\rho_b} , \tag{2.18}$$

where m_b is the mass of particle b and ρ_b is its density, therefore

$$< f(\mathbf{x}) >= \sum_{b=1}^{N} \frac{m_b}{\rho_b} f(\mathbf{x}_b) W(\mathbf{x} - \mathbf{x}_b, h) . \tag{2.19}$$

The particle approximation of a function at particle a can now be written as

$$< f(\mathbf{x}_a) >= \sum_{b=1}^{N} V_b f(\mathbf{x}_b) W_{ab} , \tag{2.20}$$

where

$$W_{ab} = W(\mathbf{x}_a - \mathbf{x}_b, h) . \tag{2.21}$$

Similarly, a particle approximation can be applied to the divergence of a vector-valued function, as given in Equation 2.13, resulting in

$$< \text{div } \boldsymbol{f}(\mathbf{x}_a) >= - \sum_{b=1}^{N} V_b \boldsymbol{f}(\mathbf{x}_b) \cdot \nabla_b W(\mathbf{x}_a - \mathbf{x}_b, h) . \tag{2.22}$$

In the above equation the gradient of the kernel is taken with respect to particle b, which is the negative of the kernel if taken with respect to particle a assuming a radially symmetric smoothing

function. Consequently, the equation above can be re-written in terms of the divergence of a vector-valued function at particle a as

$$< \text{div } \boldsymbol{f}(\mathbf{x}_a) >= \sum_{b=1}^{N} V_b \boldsymbol{f}(\mathbf{x}_b) \cdot \nabla_a W_{ab} \ , \tag{2.23}$$

where

$$\nabla_a W_{ab} = \frac{\mathbf{x}_a - \mathbf{x}_b}{r_{ab}} \frac{\mathrm{d}W_{ab}}{\mathrm{d}r_{ab}} = \frac{\mathbf{x}_{ab}}{r_{ab}} \frac{\mathrm{d}W_{ab}}{\mathrm{d}r_{ab}} = -\nabla_b W_{ab} \ , \tag{2.24}$$

and

$$r_{ab} = \|\mathbf{x}_a - \mathbf{x}_b\| \ . \tag{2.25}$$

The particle approximation of the gradient of a vector-valued function (Equation 2.14) can be written using the same methodology as

$$< \text{grad } \boldsymbol{f}(\mathbf{x}_a) >= -\sum_{b=1}^{N} V_b \boldsymbol{f}(\mathbf{x}_b) \otimes \nabla_b W_{ab} = \sum_{b=1}^{N} V_b \boldsymbol{f}(\mathbf{x}_b) \otimes \nabla_a W_{ab} \ . \tag{2.26}$$

2.2.4 Symmetrical formulation for gradients and divergences

In SPH, the divergence and gradient of a function are commonly rewritten to include the value of the function at both $\mathbf{x}_b$ and $\mathbf{x}_a$. The addition of this symmetry term, $f(\mathbf{x}_a)$, has been shown to produce results that are more accurate. For example, this symmetry term is commonly added to the SPH approximation of a velocity divergence to ensure that it goes to zero in the presence of a uniform velocity field [42]. Furthermore, it ensures that Newton's third law and Galilean invariance is respected [82]. Rearranging the divergence identity given in Equation 2.9, and considering a vector-valued field function $\boldsymbol{f}(\mathbf{x})$ and a scalar-valued field function $g(\mathbf{x})$, it can be shown that

$$\text{div } \boldsymbol{f}(\mathbf{x}) = \frac{1}{g(\mathbf{x})} \left[\text{div } (\boldsymbol{f}(\mathbf{x}) g(\mathbf{x})) - \boldsymbol{f}(\mathbf{x}) \cdot \text{grad } g(\mathbf{x}) \right] \ . \tag{2.27}$$

Applying the SPH particle approximation of a divergence and gradient to the right-hand side yields

$$< \text{div } \boldsymbol{f}(\mathbf{x}_a) >= \frac{1}{g(\mathbf{x}_a)} \left[\left(\sum_{b=1}^{N} V_b \boldsymbol{f}(\mathbf{x}_b) g(\mathbf{x}_b) \cdot \nabla_a W_{ab} \right) - \left(\boldsymbol{f}(\mathbf{x}_a) \cdot \sum_{b=1}^{N} V_b g(\mathbf{x}_b) \nabla_a W_{ab} \right) \right] \ , \tag{2.28}$$

which can be simplified to

$$< \text{div } \boldsymbol{f}(\mathbf{x}_a) >= \frac{1}{g(\mathbf{x}_a)} \sum_{b=1}^{N} V_b g(\mathbf{x}_b) \left[\boldsymbol{f}(\mathbf{x}_b) - \boldsymbol{f}(\mathbf{x}_a) \right] \cdot \nabla_a W_{ab} \ . \tag{2.29}$$

If setting the scalar field function $g(\mathbf{x}) = 1$ then the particle approximation of the divergence of a function becomes

$$< \text{div } \boldsymbol{f}(\mathbf{x}_a) >= \sum_{b=1}^{N} V_b \left[\boldsymbol{f}(\mathbf{x}_b) - \boldsymbol{f}(\mathbf{x}_a) \right] \cdot \nabla_a W_{ab} \ . \tag{2.30}$$

The gradient of a function can be written to include a symmetry term using a similar methodology, but involving a gradient identity, as

$$< \text{grad } \boldsymbol{f}(\mathbf{x}_a) >= \sum_{b=1}^{N} V_b \left[\boldsymbol{f}(\mathbf{x}_b) - \boldsymbol{f}(\mathbf{x}_a)\right] \otimes \nabla_a W_{ab} \ . \tag{2.31}$$

As mixed kernel-and-gradient correction is implemented, these symmetry terms are not strictly necessary, as discussed in Section 2.5.3. They are used in the following calculations of gradients and divergences as they result in both a conceptually simpler and a more computationally efficient model. If considering mixed correction, the same results are obtained whether these symmetry terms are implemented or not, as proven theoretically in Section 2.5.3 and highlighted by the numerical example presented in Section 4.2. It is also noted that the use of these symmetry terms in gradients and divergences lead to the derivation of internal forces which are equal and opposite for particle pairs. This will be clarified in the following section.

From this point onwards the representation of the kernel approximation using the angled brackets <> is dropped for clarity. It is therefore implied that the kernel and subsequent particle representations are approximations even though the equals sign is used.

2.3 Total Lagrangian SPH for solid mechanics

In this section the derivations of the conservation of mass, momentum and energy are given for a Total Lagrangian formulation. The main property of the Total Lagrangian formulation is that it applies a material description. This means that it describes deformation with reference to the undeformed state. This is both a benefit and a hindrance as the Total Lagrangian SPH formulation does not suffer from tensile instability as all uses of the kernel gradient are with reference to the undeformed state. Yet the formulation may become unstable in the presence of large distortions. An obvious solution might be to update the reference condition, but as discussed by Vidal et al. [35], this may activate zero-energy modes and require additional stabilization terms.

It is also shown that the derived conservation equations conserve momentum and energy. In the derivations given, the property of the kernel that $\nabla_a W_{ab} = -\nabla_b W_{ba}$ is not used as this is no longer true once the kernel is corrected. The benefit to this approach is that once mixed kernel-and-gradient correction is introduced, these derivations and consequent proofs are still valid. Consequently, the references cited in this section highlight the methodology and starting points of the derivations and proofs, but do not follow the same steps. Some of the referenced authors [41, 42] use a different kernel gradient convention. These are interchangeable as

$$\nabla_a W_{ab} = -\nabla_b W_{ab} \qquad \text{and} \qquad \nabla_b W_{ba} = -\nabla_a W_{ba} \ . \tag{2.32}$$

Though, as stated above, once the kernel has been modified

$$\nabla_a \widetilde{W}_{ab} \neq -\nabla_b \widetilde{W}_{ba} \ , \tag{2.33}$$

as is discussed in Section 2.5.

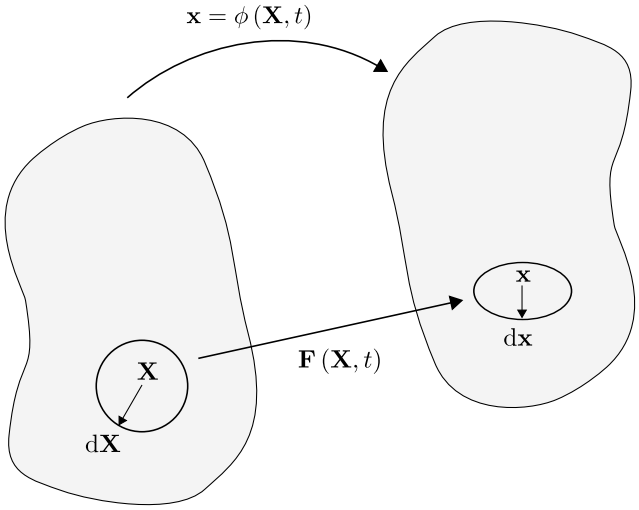

Figure 2.3: Initial and deformed reference state of a deformable body with mapping function and deformation gradient. Figure adapted from [35].

2.3.1 Mapping functions and conservation of mass

If a continuum has a prescribed motion from an initial or undeformed state $\mathbf{X}$ to a current or deformed state $\mathbf{x}$, as displayed in Figure 2.3, then the current state can be written as a function of both the initial state and time by [32]

$$\mathbf{x} = \phi(\mathbf{X}, t) \ . \tag{2.34}$$

The displacement at any point in time can be described by $\mathbf{u} = \mathbf{x} - \mathbf{X}$. The deformation and rotation of the continuum can be described using the deformation gradient $\mathbf{F}$, which is given by

$$\mathbf{F} = \frac{\partial \mathbf{x}}{\partial \mathbf{X}} = \mathbf{I} + \frac{\partial \mathbf{u}}{\partial \mathbf{X}} \ , \tag{2.35}$$

where $\mathbf{I}$ is the identity matrix. The SPH approximation of the deformation gradient is the addition of the identity matrix and the gradient of displacement with respect to the undeformed state. Applying the symmetrical form of the SPH approximation of the gradient of a function (Equation 2.31) results in

$$\mathbf{F}_a = \left[\sum_{b=1}^{N} V_{b,0} (\mathbf{u}_b - \mathbf{u}_a) \otimes \nabla_{a,0} W_{ab,0} \right] + \mathbf{I} \ , \tag{2.36}$$

where the nought subscript indicates the reference state. The volume distortion from the reference state to the current state can be calculated through the Jacobian, J, this being the determinant of the deformation gradient [32]:

$$J = \det \mathbf{F} = \frac{\mathrm{d}V}{\mathrm{d}V_0} \ . \tag{2.37}$$

As the masses of the SPH particles do not evolve with time, using the above, it can be shown that

$$\rho_a = J_a^{-1} \rho_{a,0} \ , \tag{2.38}$$

which describes the conservation of mass in material coordinates.

2.3.2 Conservation of momentum approximation

The conservation of momentum in a Total Lagrangian framework is given, including body forces $\mathbf{b}$, by [32]

$$\frac{\partial \mathbf{v}(\mathbf{X},t)}{\partial t} = \frac{1}{\rho_0}\nabla_{\mathbf{X}} \cdot \mathbf{P} + \mathbf{b} \ . \tag{2.39}$$

The first Piola-Kirchhoff stress $\mathbf{P}$ is used rather than its transpose, the nominal stress $\mathbf{N}$. This is because, in this work, the definition that the divergence of a second order tensor contracts with the second index of the tensor is adopted [68]. This has been discussed in more detail in Section 1.3. Rather than applying the SPH approximations of a gradient to this directly, Bonet and Kulasegaram [33] are followed in order to derive the internal forces. These authors use the principle of virtual work to draw out the internal forces as

$$\delta \dot{w}_\epsilon = \int_{V_0} \mathbf{P} : \delta\dot{\mathbf{F}} \mathrm{d}V_0 = \sum_{a=1}^{N} \mathbf{t}_a \cdot \delta \mathbf{v}_a \ , \tag{2.40}$$

where $\dot{w}_\epsilon$ is the material form of the internal virtual work, $\delta\dot{\mathbf{F}}$ is the virtual material velocity gradient, $\mathbf{t}_a$ is the particle internal forces and $\delta\mathbf{v}_a$ is the virtual velocity. The material velocity gradient $\dot{\mathbf{F}} = \partial\mathbf{v}/\partial\mathbf{X}$ is calculated following the same method as for the deformation gradient in Equation 2.36. The equilibrium equation is then written on a particle basis as

$$m_a \frac{\partial \mathbf{v}(\mathbf{X},t)}{\partial t} = m_a \mathbf{b}_a - \mathbf{t}_a \ . \tag{2.41}$$

In order to derive the internal forces the expression for virtual work is first expressed in summation form as

$$\delta \dot{w}_\epsilon = \sum_{a=1}^{N} V_{a,0} \mathbf{P}_a : \delta\dot{\mathbf{F}}_a \ . \tag{2.42}$$

It is then noted that the virtual material velocity gradient can be written, using a material equivalent of Equation 2.31, as

$$\delta\dot{\mathbf{F}}_a = \sum_{b=1}^{N} V_{b,0}(\delta\mathbf{v}_b - \delta\mathbf{v}_a) \otimes \nabla_{a,0} W_{ab,0} \ . \tag{2.43}$$

Substituting this back into the internal virtual work gives

$$\delta \dot{w}_\epsilon = \sum_{a=1}^{N} V_{a,0} \mathbf{P}_a : \sum_{b=1}^{N} V_{b,0}(\delta\mathbf{v}_b - \delta\mathbf{v}_a) \otimes \nabla_{a,0} W_{ab,0} \ , \tag{2.44}$$

which can be simplified to

$$\delta \dot{w}_\epsilon = \sum_{a=1}^{N} \sum_{b=1}^{N} V_{a,0} V_{b,0} \mathbf{P}_a : (\delta\mathbf{v}_b - \delta\mathbf{v}_a) \otimes \nabla_{a,0} W_{ab,0} \ . \tag{2.45}$$

The identity provided by Bonet and Wood [66], which states that $\mathbf{S} : (\mathbf{u} \otimes \mathbf{v}) = \mathbf{u} \cdot \mathbf{S}\mathbf{v}$, where $\mathbf{S}$ is any second order tensor and $\mathbf{u}$ and $\mathbf{v}$ are any first order tensors, can now be called upon along with the commutative property of the dot product, such that

$$\delta \dot{w}_\epsilon = \sum_{a=1}^{N} \sum_{b=1}^{N} V_{a,0} V_{b,0} \mathbf{P}_a \nabla_{a,0} W_{ab,0} \cdot (\delta\mathbf{v}_b - \delta\mathbf{v}_a) \ . \tag{2.46}$$

Multiplying out the virtual velocities, separating the summations, swapping the indices for the summations involving the $\delta\mathbf{v}_b$ term, and then combining leads to

$$\delta\dot{w}_\epsilon = \sum_{a=1}^{N}\left[\sum_{b=1}^{N} V_{a,0}V_{b,0}(\mathbf{P}_b\nabla_{b,0}W_{ba,0} - \mathbf{P}_a\nabla_{a,0}W_{ab,0})\right]\cdot\delta\mathbf{v}_a \ . \tag{2.47}$$

From this expression it is clear that the internal forces for a particle a are given by

$$\mathbf{t}_a = \sum_{b=1}^{N} V_{a,0}V_{b,0}(\mathbf{P}_b\nabla_{b,0}W_{ba,0} - \mathbf{P}_a\nabla_{a,0}W_{ab,0}) \ , \tag{2.48}$$

and, if neglecting body forces, the acceleration of a particle in a Total Lagrangian configuration is given by

$$\frac{\partial\mathbf{v}_a}{\partial t} = -\frac{1}{m_a}\sum_{b=1}^{N} V_{a,0}V_{b,0}\left(\mathbf{P}_b\nabla_{b,0}W_{ba} - \mathbf{P}_a\nabla_{a,0}W_{ab}\right) \ . \tag{2.49}$$

It can be seen that this original derivation of the momentum equation for a Total Lagrangian formulation has produced an expression that is equal and opposite for particle pairs.

It should be noted that the expression for the internal forces given in Equation 2.48 is not unique. This is because Equation 2.42 could be approximated in a number of different ways, leading to different internal forces which satisfy the comparison between Equations 2.40 and 2.47. For example, should the symmetry term $-\mathbf{u}_a$ have not been used in the definition of the deformation gradient (Equation 2.36), then the above acceleration equation would not include the symmetry term $-\mathbf{P}_a\nabla_{a,0}W_{ab}$. These symmetry terms were intentionally used so as to ensure that a consistent derivation of the internal forces produced an expression which was equal and opposite with respect to particle pairs.

In their work, Bonet and Kulasegaram [33] first ensured that a uniform deformation gradient was exactly reproduced using a correction matrix $\mathbf{M}$. They then derived their internal forces using the principles of virtual work. Re-writing the internal forces that these authors derived, using the conventions in this work, produces

$$\mathbf{t}_a = \sum_{b=1}^{N} m_a m_b\left(\frac{\mathbf{P}_b\mathbf{M}_b^{-1}}{\rho_{b,0}} + \frac{\mathbf{P}_a\mathbf{M}_a^{-1}}{\rho_{a,0}}\right)\nabla_{b,0}W_{ba} \ , \tag{2.50}$$

which bears some resemblance to Equation 2.48 in that it produces equal and opposite pairwise particle forces.

The relationship between the first Piola-Kirchhoff stress and the Cauchy stress is given by [32]

$$\mathbf{P} = J\boldsymbol{\sigma}\cdot\mathbf{F}^{-\mathsf{T}} \ , \tag{2.51}$$

where the Cauchy stress tensor $\boldsymbol{\sigma}$ can be split into its hydrostatic and deviatoric components such that $\boldsymbol{\sigma} = \boldsymbol{\sigma}' - p\mathbf{I}$, where primed symbols denote a deviatoric matrix and p is the pressure. The pressure is calculated through an equation of state, for example

$$p_a = c_a^2(\rho_a - \rho_{a,0}) \ , \tag{2.52}$$

where c is the speed of sound in the material. The deviatoric stress is evolved incrementally in time. The Cauchy stress rate is not objective and therefore a corotational derivative is needed to evolve the

Cauchy stress tensor [32]. This is achieved using the Jaumann rate of the Cauchy stress and evolving the deviatoric stress as [23]

$$\frac{\mathrm{d}\boldsymbol{\sigma}'}{\mathrm{d}t} = 2G\mathbf{D}' + \boldsymbol{\Omega}\boldsymbol{\sigma}' - \boldsymbol{\sigma}'\boldsymbol{\Omega} \,. \tag{2.53}$$

In the above, $\mathbf{D}'$ is the deviatoric component of the rate of deformation tensor, $\boldsymbol{\Omega}$ is the spin tensor and G is the shear modulus. The rate of deformation tensor is given by the symmetric component of the spatial velocity gradient, $\mathbf{L}$, that is [23]

$$\mathbf{D} = \frac{1}{2}(\mathbf{L} + \mathbf{L}^{\mathsf{T}}) = \frac{1}{2}\left[\text{grad}\,\mathbf{v} + (\text{grad}\,\mathbf{v})^{\mathsf{T}}\right] \,. \tag{2.54}$$

The deviatoric component can be found by subtracting the isotropic strain rate from the tensor given above. The spin tensor is given by the anti-symmetric component of the velocity gradient as [23]

$$\boldsymbol{\Omega} = \frac{1}{2}(\mathbf{L} - \mathbf{L}^{\mathsf{T}}) = \frac{1}{2}\left[\text{grad}\,\mathbf{v} - (\text{grad}\,\mathbf{v})^{\mathsf{T}}\right] \,. \tag{2.55}$$

The rate of deformation and spin tensors are dependent on the spatial velocity gradient, which, in a Total Lagrangian context, is given by

$$\mathbf{L} = \frac{\partial \mathbf{v}}{\partial \mathbf{x}} = \frac{\partial \mathbf{v}}{\partial \mathbf{X}}\frac{\partial \mathbf{X}}{\partial \mathbf{x}} = \dot{\mathbf{F}}\mathbf{F}^{-1} \,. \tag{2.56}$$

The method for updating the Cauchy stress follows the same procedure as given for the Eulerian SPH, where an equation of state is used for the isotropic component and the deviatoric component is incrementally updated in time. Once calculated, the Cauchy stress is converted into the first Piola-Kirchhoff stress and used in the Total Lagrangian momentum equation.

2.3.3 Conservation of internal energy approximation

The conservation of internal energy in the Total Lagrangian reference condition is given by [32]

$$\frac{\partial e(\mathbf{X}, t)}{\partial t} = V_0 \mathbf{P} : \dot{\mathbf{F}} \,. \tag{2.57}$$

Note that this has been adapted to be in terms of energy rather than in terms of specific internal energy, i.e. per unit mass. The material velocity gradient is calculated in a similar manner as the virtual material velocity gradient, as shown in Equation 2.43, leading to

$$\dot{e}_a = V_{a,0}\mathbf{P}_a : \sum_{b=1}^{N} V_{b,0}(\mathbf{v}_b - \mathbf{v}_a) \otimes \nabla_{a,0} W_{ab,0} \,. \tag{2.58}$$

Again using the identity [66] that $\mathbf{S} : (\mathbf{u} \otimes \mathbf{v}) = \mathbf{u} \cdot \mathbf{S}\mathbf{v}$ results in

$$\dot{e}_a = \sum_{b=1}^{N} V_{a,0} V_{b,0}(\mathbf{v}_b - \mathbf{v}_a) \cdot \mathbf{P}_a \nabla_{a,0} W_{ab,0} \,. \tag{2.59}$$

2.3.4 Conservation of linear and angular momentum

In order to highlight the conservation properties of the momentum equation the same methodology given by Bonet and Lok [42] and Bonet and Kulasegaram [25, 33] is applied, noting that most

formulations conserve linear momentum. The conservation of linear momentum is guaranteed when, given any arbitrary stress state, the internal forces balance. The overall internal force experienced by a particle can be written as the sum of the pairwise internal forces acting on it:

$$\mathbf{t}_a = \sum_{b=1}^{N} \mathbf{t}_{ab} \ . \tag{2.60}$$

Comparing this against Equation 2.48 it can be shown that the pair-based internal force is given by

$$\mathbf{t}_{ab} = V_{a,0} V_{b,0} (\mathbf{P}_b \nabla_{b,0} W_{ba,0} - \mathbf{P}_a \nabla_{a,0} W_{ab,0}) \ . \tag{2.61}$$

From the above it is clear that $\mathbf{t}_{ab} = -\mathbf{t}_{ba}$ and as a result $\sum_{a=1}^{N} \mathbf{t}_a = 0$, guaranteeing the conservation of linear momentum.

Angular momentum is similarly conserved if the sum of the moments caused by the internal forces at any point in space balance. Alternatively, it is conserved if the rate of change of angular momentum is zero. This can be written as

$$\sum_{a=1}^{N} \mathbf{x}_a \times \mathbf{t}_a = 0 \ . \tag{2.62}$$

Bonet and Wood [66] are again referred to for the identity that $\mathbf{u} \times \mathbf{v} = \boldsymbol{\varepsilon} : (\mathbf{u} \otimes \mathbf{v})$, where $\boldsymbol{\varepsilon}$ is an anti-symmetric third order tensor. This allows the above to be expressed as

$$\sum_{a=1}^{N} \mathbf{x}_a \times \mathbf{t}_a = -\boldsymbol{\varepsilon} : \sum_{a=1}^{N} (\mathbf{t}_a \otimes \mathbf{x}_a) \ . \tag{2.63}$$

Substituting in Equation 2.48 results in

$$\sum_{a=1}^{N} \mathbf{x}_a \times \mathbf{t}_a = -\boldsymbol{\varepsilon} : \sum_{a=1}^{N} \left(\sum_{b=1}^{N} V_{a,0} V_{b,0} (\mathbf{P}_b \nabla_{b,0} W_{ba,0} - \mathbf{P}_a \nabla_{a,0} W_{ab,0}) \otimes \mathbf{x}_a \right) , \tag{2.64}$$

where a rearrangement of the above yields

$$\sum_{a=1}^{N} \mathbf{x}_a \times \mathbf{t}_a = \boldsymbol{\varepsilon} : \left(\sum_{a=1}^{N} \sum_{b=1}^{N} V_{a,0} V_{b,0} \mathbf{P}_a \nabla_{a,0} W_{ab,0} \otimes \mathbf{x}_a - \sum_{a=1}^{N} \sum_{b=1}^{N} V_{a,0} V_{b,0} \mathbf{P}_b \nabla_{b,0} W_{ba,0} \otimes \mathbf{x}_a \right) . \tag{2.65}$$

The above can be reduced by swapping indices on the second term and combining the summations, leading to

$$\sum_{a=1}^{N} \mathbf{x}_a \times \mathbf{t}_a = -\boldsymbol{\varepsilon} : \sum_{a=1}^{N} \sum_{b=1}^{N} V_{a,0} V_{b,0} \mathbf{P}_a \nabla_{a,0} W_{ab,0} \otimes (\mathbf{x}_b - \mathbf{x}_a) \ . \tag{2.66}$$

Noting that the deformation gradient can be written as

$$\mathbf{F}_a = \frac{\partial \mathbf{x}_a}{\partial \mathbf{X}_a} = \sum_{b=1}^{N} V_{b,0} (\mathbf{x}_b - \mathbf{x}_a) \otimes \nabla_{a,0} W_{ab,0} \ , \tag{2.67}$$

and substituting this into Equation 2.66 gives

$$\sum_{a=1}^{N} \mathbf{x}_a \times \mathbf{t}_a = -\boldsymbol{\varepsilon} : \sum_{a=1}^{N} V_{a,0} \mathbf{P}_a \mathbf{F}_a^{\mathsf{T}} \ . \tag{2.68}$$

Recalling the definition of the Jacobian (Equation 2.37) and the relation between the first Piola-Kirchhoff stress and the Cauchy stress (Equation 2.51) it can be shown that $V\boldsymbol{\sigma} = V_0\mathbf{P}\mathbf{F}^{\mathsf{T}}$. Applying this leads to

$$\sum_{a=1}^{N} \mathbf{x}_a \times \mathbf{t}_a = -\boldsymbol{\varepsilon} : \sum_{a=1}^{N} V_a \boldsymbol{\sigma}_a = 0 \,. \tag{2.69}$$

As the Cauchy stress tensor is symmetric and $\boldsymbol{\varepsilon}$ is anti-symmetric, the double dot product of the two must reduce to zero [83].

This is an interesting discovery as it states that the Total Lagrangian approach conserves both linear momentum, without requiring any correction, and angular momentum, if the deformation gradient is approximated exactly. Bonet and Kulasegaram [25, 33] write their formulation in terms of a gradient function $\mathbf{G}$, which contains the corrected kernel gradient. These authors start at Equation 2.63 and use a different form of internal forces to prove the conservation of angular momentum. Having done so, these authors state that angular momentum is conserved in a Total Lagrangian formulation for any choice of the gradient vectors within the function $\mathbf{G}$. In the formulation presented here, the conservation of angular momentum depends on the exact approximation of the deformation gradient. This is explored further when correction is introduced in Section 2.5. The Eulerian approach requires further explicit conditions, as is demonstrated in Section 2.4.4.

2.3.5 Conservation of energy

The first step to demonstrating the conservation of energy is given by Violeau [2] who, considering an isolated system, takes the partial derivative of the Lagrangian to show that

$$\frac{\mathrm{d}E}{\mathrm{d}t} = 0 \,, \tag{2.70}$$

where E is the total energy of the system made up of kinetic and potential energy. Following Violeau again the rate of change of total energy can be written as

$$\frac{\mathrm{d}E}{\mathrm{d}t} = \sum_{a=1}^{N} m_a \mathbf{v}_a \cdot \frac{\mathrm{d}\mathbf{v}_a}{\mathrm{d}t} + \frac{\mathrm{d}e_a}{\mathrm{d}t} \,, \tag{2.71}$$

where, in this case, the potential is solely comprised of the internal energy. Substituting in for the Total Lagrangian form of particle acceleration (Equation 2.49) and the Total Lagrangian rate of internal energy (Equation 2.59), it transpires that

$$\frac{\mathrm{d}E}{\mathrm{d}t} = \sum_{a=1}^{N} -m_a \mathbf{v}_a \cdot \frac{1}{m_a} \left(\sum_{b=1}^{N} V_{a,0} V_{b,0} \left(\mathbf{P}_b \nabla_{b,0} W_{ba} - \mathbf{P}_a \nabla_{a,0} W_{ab} \right) \right) + \left(\sum_{b=1}^{N} V_{a,0} V_{b,0} (\mathbf{v}_b - \mathbf{v}_a) \cdot \mathbf{P}_a \nabla_{a,0} W_{ab,0} \right) , \tag{2.72}$$

which can be rearranged to show that

$$\frac{\mathrm{d}E}{\mathrm{d}t} = \sum_{a=1}^{N} \sum_{b=1}^{N} V_{a,0} V_{b,0} (\mathbf{v}_b - \mathbf{v}_a) \cdot \mathbf{P}_a \nabla_{a,0} W_{ab,0} - \sum_{a=1}^{N} \sum_{b=1}^{N} \mathbf{v}_a \cdot V_{a,0} V_{b,0} \left(\mathbf{P}_b \nabla_{b,0} W_{ba} - \mathbf{P}_a \nabla_{a,0} W_{ab} \right) \,. \tag{2.73}$$

The first term on the right-hand side can be expanded to show

$$\begin{aligned}\frac{\mathrm{d}E}{\mathrm{d}t} = &\left[\sum_{a=1}^{N}\sum_{b=1}^{N}\mathbf{v}_b\cdot V_{a,0}V_{b,0}\mathbf{P}_a\nabla_{a,0}W_{ab,0} - \sum_{a=1}^{N}\sum_{b=1}^{N}\mathbf{v}_a\cdot V_{a,0}V_{b,0}\mathbf{P}_a\nabla_{a,0}W_{ab,0}\right] \\ &- \sum_{a=1}^{N}\sum_{b=1}^{N}\mathbf{v}_a\cdot V_{a,0}V_{b,0}\left(\mathbf{P}_b\nabla_{b,0}W_{ba} - \mathbf{P}_a\nabla_{a,0}W_{ab}\right)\ ,\end{aligned} \tag{2.74}$$

where swapping the indices in the first double summation above and then combining it with the second double summation results in

$$\frac{\mathrm{d}E}{\mathrm{d}t} = \sum_{a=1}^{N}\sum_{b=1}^{N}\mathbf{v}_a\cdot V_{a,0}V_{b,0}\left(\mathbf{P}_b\nabla_{b,0}W_{ba} - \mathbf{P}_a\nabla_{a,0}W_{ab}\right) - \sum_{a=1}^{N}\sum_{b=1}^{N}\mathbf{v}_a\cdot V_{a,0}V_{b,0}(\mathbf{P}_b\nabla_{b,0}W_{ba,0} - \mathbf{P}_a\nabla_{a,0}W_{ab,0})\ , \tag{2.75}$$

$$\frac{\mathrm{d}E}{\mathrm{d}t} = 0\ . \tag{2.76}$$

Hence, the conservation of internal energy equation given will conserve the total energy of the system.

2.4 Eulerian SPH for solid mechanics

The derivation of the conservation of mass, momentum and energy are given for an Eulerian formulation in this section. The main difference between the Eulerian and Total Lagrangian formulations is that the Eulerian formulation describes deformation with reference to the deformed state. Tensile instability is able to manifest as a direct result of this. Furthermore, the Eulerian approach requires that neighbour lists are updated frequently, which is computationally expensive. The benefit to applying an Eulerian formulation is that large distortions are easily handled due to the spatial description.

It is also shown that the derived conservation equations conserve linear momentum and energy unconditionally. The requirements for the conservation of angular momentum are derived in a similar fashion to what was done for the Total Lagrangian reference. In the derivations shown the property of the kernel that $\nabla_a W_{ab} = \nabla_b W_{ba}$ is not used. The benefit to this approach is that once mixed kernel-and-gradient correction is introduced these derivations and consequent proofs will still be valid.

2.4.1 Continuity

The continuity equation is given by [5]

$$\frac{\mathrm{d}\rho}{\mathrm{d}t} = -\rho\ \mathrm{div}\ \mathbf{v}\ , \tag{2.77}$$

where ρ is the density, $\mathbf{v}$ the velocity and t is time. Following Liu and Liu [1], the application of the SPH particle approximation to the continuity equation is referred to as the continuity density approach.

By writing the symmetrical velocity divergence, using Equation 2.30, the velocity divergence can be approximated and inserted in to the continuity equation as

$$\frac{\mathrm{d}\rho_a}{\mathrm{d}t} = -\rho_a \sum_{b=1}^{N} V_b(\mathbf{v}_b - \mathbf{v}_a) \cdot \nabla_a W_{ab} \ , \tag{2.78}$$

where the symmetrical formulation, which includes the term $-\mathbf{v}_a$, has been used to ensure that in the presence of a uniform velocity field, the divergence goes to zero.

An alternative approach exists for calculating a particle's density. This is referred to as the summation density approach [1] and involves the direct application of the SPH particle approximation of a function, namely density:

$$\rho_a = \sum_{b=1}^{N} m_b W_{ab} \ . \tag{2.79}$$

Both the continuity and summation density approach can effectively update the value of density. The summation density approach exactly calculates the value of density as the mass of the SPH particles does not evolve [5]. The disadvantage of this approach is that it is heavily affected by truncated particle support domains, this being when a particle's support domain does not contain sufficient particles. Using this approach at boundaries will cause the value of density to drop, if assuming no correction [38]. Although the continuity density approach may not exactly calculate the appropriate value of density [38], it is not as sensitive to deficiencies at the boundary [84]. This is especially the case with the symmetrical formulation.

Regardless of the approach selected, it is important to select the corresponding conservation of momentum equation as failure to do so will result in a formulation that is not consistent [42].

2.4.2 Conservation of momentum approximation

As for the Total Lagrangian framework, the Eulerian conservation of momentum equation could be evaluated in a number of ways by applying different SPH approximations to the momentum equation. In an Eulerian reference, this is given by the Cauchy momentum equation [5]:

$$\frac{\mathrm{d}\mathbf{v}}{\mathrm{d}t} = \frac{1}{\rho}\mathrm{div}\ \boldsymbol{\sigma} + \mathbf{b} \ . \tag{2.80}$$

Arbitrarily selecting an SPH approximation will result in a conservation of momentum equation that is not variationally consistent, as pointed out by both Bonet and Lok [42] and Price [85]. These authors give a variationally consistent derivation of the conservation of momentum equation that is dependent on the selection of conservation of mass equation. Price gives a general formulation for the equations representing the conservation of mass, momentum and energy by writing the continuity density equation in terms of a generic scalar variable ϕ. This variable ϕ can be given a fixed value (such as $\rho^{2-\sigma}$ or $\rho/\sqrt{p}$) so that the general formulation simplifies to the conservation equations commonly found in literature. Price only does this for an isotropic stress tensor. Bonet and Lok give a less general derivation of the compatible momentum equation. They too consider an isotropic stress tensor but also give an additional component to the momentum equation that considers internal forces introduced by fluid viscous shear.

The same derivation as for the Total Lagrangian approach is followed here on the basis that the solid mechanics momentum equation has not been derived for Eulerian SPH using a variational

framework. The internal forces are again determined using the principles of virtual work, where the spatial form of internal virtual work done by stresses is given by [66]

$$\delta \dot{w}_\epsilon = \int_V \boldsymbol{\sigma} : \delta \mathbf{D} \mathrm{d}V = \sum_{a=1}^{N} \mathbf{t}_a \cdot \delta \mathbf{v}_a \ , \tag{2.81}$$

where $\delta \mathbf{D}$ is the virtual rate of deformation given by

$$\delta \mathbf{D} = \frac{1}{2} \left[\mathrm{grad}\ \delta \mathbf{v} + (\mathrm{grad}\ \delta \mathbf{v})^\mathsf{T} \right] \ . \tag{2.82}$$

An SPH approximation of the spatial internal virtual work can be written as

$$\delta \dot{w}_\epsilon = \sum_{a=1}^{N} V_a \boldsymbol{\sigma}_a : \delta \mathbf{D}_a \ , \tag{2.83}$$

which, with the spatial virtual velocity gradient substituted, expands to

$$\delta \dot{w}_\epsilon = \sum_{a=1}^{N} V_a \boldsymbol{\sigma}_a : \frac{1}{2} \left[\sum_{b=1}^{N} V_b (\delta \mathbf{v}_b - \delta \mathbf{v}_a) \otimes \nabla_a W_{ab} + \sum_{b=1}^{N} V_b \nabla_a W_{ab} \otimes (\delta \mathbf{v}_b - \delta \mathbf{v}_a) \right] \ . \tag{2.84}$$

This can be rewritten as

$$\delta \dot{w}_\epsilon = \frac{1}{2} \left[\sum_{a=1}^{N} \sum_{b=1}^{N} V_a V_b \boldsymbol{\sigma}_a : (\delta \mathbf{v}_b - \delta \mathbf{v}_a) \otimes \nabla_a W_{ab} + \sum_{a=1}^{N} \sum_{b=1}^{N} V_a V_b \boldsymbol{\sigma}_a : \nabla_a W_{ab} \otimes (\delta \mathbf{v}_b - \delta \mathbf{v}_a) \right] \ . \tag{2.85}$$

Again using the identity that $\mathbf{S} : (\mathbf{u} \otimes \mathbf{v}) = \mathbf{u} \cdot \mathbf{S}\mathbf{v}$ [66] results in

$$\delta \dot{w}_\epsilon = \frac{1}{2} \left[\sum_{a=1}^{N} \sum_{b=1}^{N} V_a V_b (\delta \mathbf{v}_b - \delta \mathbf{v}_a) \cdot \boldsymbol{\sigma}_a \nabla_a W_{ab} + \sum_{a=1}^{N} \sum_{b=1}^{N} V_a V_b \nabla_a W_{ab} \cdot \boldsymbol{\sigma}_a (\delta \mathbf{v}_b - \delta \mathbf{v}_a) \right] \ . \tag{2.86}$$

The identity that $\mathbf{u} \cdot \mathbf{S}\mathbf{v} = \mathbf{v} \cdot \mathbf{S}^\mathsf{T}\mathbf{u}$ [66], combined with the knowledge that the Cauchy stress tensor is symmetrical such that $\boldsymbol{\sigma} = \boldsymbol{\sigma}^\mathsf{T}$, allows the second term in the equation above to be rewritten, resulting in

$$\delta \dot{w}_\epsilon = \sum_{a=1}^{N} \sum_{b=1}^{N} V_a V_b \boldsymbol{\sigma}_a \nabla_a W_{ab} \cdot (\delta \mathbf{v}_b - \delta \mathbf{v}_a) \ . \tag{2.87}$$

The commutative property of the dot product is also applied in the above. As for the Total Lagrangian derivation, multiplying out the virtual velocities, separating the summations, swapping the indices for the summations involving the $\delta \mathbf{v}_b$ term, and then combining leads to

$$\delta \dot{w}_\epsilon = \sum_{a=1}^{N} \left[\sum_{b=1}^{N} V_a V_b (\boldsymbol{\sigma}_b \nabla_b W_{ba} - \boldsymbol{\sigma}_a \nabla_a W_{ab}) \right] \cdot \delta \mathbf{v}_a \ . \tag{2.88}$$

Comparing this against Equation 2.81 it is apparent that

$$\mathbf{t}_a = \sum_{b=1}^{N} V_a V_b (\boldsymbol{\sigma}_b \nabla_b W_{ba} - \boldsymbol{\sigma}_a \nabla_a W_{ab}) \ , \tag{2.89}$$

and, if neglecting body forces, the Eulerian momentum equation is given by

$$\frac{\mathrm{d}\mathbf{v}_a}{\mathrm{d}t} = -\frac{1}{m_a}\sum_{b=1}^{N} V_a V_b(\boldsymbol{\sigma}_b \nabla_b W_{ba} - \boldsymbol{\sigma}_a \nabla_a W_{ab}) \,. \tag{2.90}$$

Again, it can be seen that this original derivation of the momentum equation has produced an expression that is equal and opposite for particle pairs for an Eulerian formulation.

As for the Total Lagrangian derivation, the expression for the internal forces given in Equation 2.89 is not unique. This is because Equation 2.83 could be approximated in a number of different ways, leading to different internal forces which satisfy the comparison between Equations 2.81 and 2.88. For example, the inclusion of the symmetry term $-\mathbf{v}_a$ in the definition of the velocity gradient (as used in Equation 2.84) has led to the symmetry term $-\boldsymbol{\sigma}_a \nabla_a W_{ab}$ in the expression for internal forces, resulting in an acceleration equation which is equal and opposite for particle pairs. That being said, the expression for the internal forces given in Equation 2.89 is consistent with definition of gradients and divergences that make use of symmetry terms, which are used throughout this work.

It is noted that Bonet and Lok [42] derived a similar internal force equation for Newtonian fluids using a variational approach. Their derivation was dependent on the method used to update density and made use of $\nabla_a W_{ab} = \nabla_b W_{ba}$. They found that the internal force

$$\mathbf{t}_a = \sum_{b=1}^{N} V_a V_b(\boldsymbol{\sigma}_b + \boldsymbol{\sigma}_a)\nabla_b W_{ba} \tag{2.91}$$

was variationally consistent with the continuity density approach. Considering that Equations 2.89 and 2.91 are the same, it would appear sensible to make use of the continuity density approach in this work.

The time evolution of the Cauchy stress tensor follows the same methodology as given for the Total Lagrangian approach. That is, the isotropic pressure component is obtained from an equation of state and the deviatoric component is evolved using the Jaumann rate of the Cauchy stress (Equations 2.53). The notable difference between the two is the calculation of the spatial velocity gradient used in the rate of deformation and spin tensors. The Eulerian formulation calculates this directly as a simple velocity gradient whilst the Total Lagrangian material velocity gradient must be mapped to the spatial velocity gradient using the inverse of the deformation gradient, i.e. $\mathbf{L} = \dot{\mathbf{F}}\mathbf{F}^{-1}$.

2.4.3 Conservation of internal energy approximation

The conservation of internal energy e is given by [32]

$$\frac{\mathrm{d}e}{\mathrm{d}t} = V\boldsymbol{\sigma} : \mathbf{D} \,. \tag{2.92}$$

The above is calculated directly on a particle basis. Note that this has again been adapted to be in terms of energy rather than in terms of specific internal energy, i.e. per unit mass. The rate of deformation tensor is calculated in a similar manner to the virtual rate of deformation, which leads to

$$\dot{e}_a = V_a\boldsymbol{\sigma}_a : \sum_{b=1}^{N} V_b(\mathbf{v}_b - \mathbf{v}_a) \otimes \nabla_a W_{ab} \,. \tag{2.93}$$

Using the identity that $\mathbf{S} : (\mathbf{u} \otimes \mathbf{v}) = \mathbf{u} \cdot \mathbf{S}\mathbf{v}$ [66] results in

$$\dot{e}_a = \sum_{b=1}^{N} V_a V_b (\mathbf{v}_b - \mathbf{v}_a) \cdot \boldsymbol{\sigma}_a \nabla_a W_{ab} \, . \tag{2.94}$$

As highlighted by Hernquist and Katz [86], using inconsistent equations of motion and energy introduces errors of $O(h^2)$ into the conservation of energy.

2.4.4 Conservation of linear and angular momentum

As for the Total Lagrangian formulation, linear momentum is conserved if $\sum_{a=1}^{N} \mathbf{t}_a = 0$ where

$$\mathbf{t}_a = \sum_{b=1}^{N} \mathbf{t}_{ab} \, . \tag{2.60 revisited}$$

Comparing this against Equation 2.89 it is apparent that the pair-based internal force is given by

$$\mathbf{t}_{ab} = V_a V_b (\boldsymbol{\sigma}_b \nabla_b W_{ba} - \boldsymbol{\sigma}_a \nabla_a W_{ab}) \, . \tag{2.95}$$

From the above it is clear that $\mathbf{t}_{ab} = -\mathbf{t}_{ba}$ and as a result $\sum_{a=1}^{N} \mathbf{t}_a = 0$, guaranteeing the conservation of linear momentum.

As for the Total Lagrangian approach, angular momentum is conserved if

$$\sum_{a=1}^{N} \mathbf{x}_a \times \mathbf{t}_a = -\boldsymbol{\varepsilon} : \sum_{a=1}^{N} (\mathbf{t}_a \otimes \mathbf{x}_a) = 0 \, . \tag{2.63 revisited}$$

Substituting in Equation 2.89 results in

$$\sum_{a=1}^{N} \mathbf{x}_a \times \mathbf{t}_a = -\boldsymbol{\varepsilon} : \sum_{a=1}^{N} \left(\sum_{b=1}^{N} V_a V_b (\boldsymbol{\sigma}_b \nabla_b W_{ba} - \boldsymbol{\sigma}_a \nabla_a W_{ab}) \otimes \mathbf{x}_a \right) , \tag{2.96}$$

which leads to

$$\sum_{a=1}^{N} \mathbf{x}_a \times \mathbf{t}_a = -\boldsymbol{\varepsilon} : \sum_{a=1}^{N} V_a \boldsymbol{\sigma}_a \sum_{b=1}^{N} V_b \nabla_a W_{ab} \otimes (\mathbf{x}_b - \mathbf{x}_a) \, . \tag{2.97}$$

As the Cauchy stress tensor is symmetric and $\boldsymbol{\varepsilon}$ is anti-symmetric, the double dot product of the two must reduce to zero [83]. Therefore, in order for angular momentum to be conserved, it can be stated that

$$\sum_{b=1}^{N} V_b \nabla_a W_{ab} \otimes (\mathbf{x}_b - \mathbf{x}_a) = \mathbf{I} \, . \tag{2.98}$$

This is an interesting discovery for a number of reasons. Firstly, it contrasts with the Total Lagrangian formulation, which was dependent on the exact approximation of the deformation gradient. Secondly, the same condition was proven by Bonet and Lok [42] who inspected the problem from a rotational invariance perspective. As Eulerian SPH does not unconditionally meet this condition, correction techniques are required, as is explored in Section 2.5.

Monaghan [3] states that various forms for SPH conserve angular momentum without requiring modification if the internal forces are equal and opposite. This only applies when the stress tensor is purely hydrostatic. When discussing viscous stress in the context of fluid dynamics, Monaghan states,

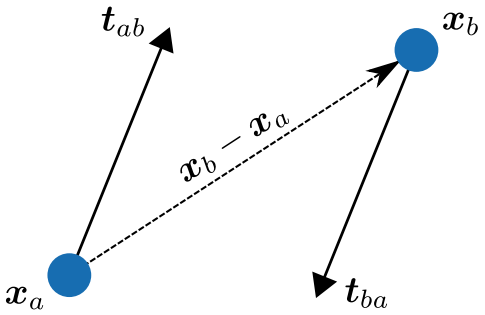

Figure 2.4: Equal and opposite pair-based internal forces between two particles. Figure adapted from Bonet and Lok [42].

"*these forms of the viscous stress tensor conserve linear momentum but not angular momentum*". When discussing elasticity and fracture he states, "*One skeleton in the SPH closet is that the normal SPH elastic equations do not conserve angular momentum*". This can be demonstrated by borrowing an analysis from Bonet and Lok [42]. If considering two particles, as displayed in Figure 2.4, then the moment about the origin of the pair-based internal forces can be described as

$$(\mathbf{x}_a \times \mathbf{t}_{ab}) + (\mathbf{x}_b \times \mathbf{t}_{ba}) = -(\mathbf{x}_b - \mathbf{x}_a) \times \mathbf{t}_{ab} \ , \tag{2.99}$$

if assuming equal and opposite internal forces. In order for the above cross product to equal zero, the vectors $(\mathbf{x}_b - \mathbf{x}_a)$ and $\mathbf{t}_{ab}$ must be co-linear. If assuming a pair-based internal force in the form of

$$\mathbf{t}_{ab} = V_a V_b(\boldsymbol{\sigma}_b \nabla_b W_{ba} - \boldsymbol{\sigma}_a \nabla_a W_{ab}) \ , \tag{2.95 revisited}$$

and recalling that both $\nabla_b W_{ba}$ and $\nabla_a W_{ab}$ are proportional to $(\mathbf{x}_b - \mathbf{x}_a)$, it is clear that the above co-linearity is only guaranteed if the stress tensors are isotropic (i.e. $\boldsymbol{\sigma} = -p\boldsymbol{I}$). As this work considers elasticity, plasticity and fracture, deviatoric stresses must be considered and consequently angular momentum is only conserved in the Eulerian formulation if Equation 2.98 is fulfilled.

2.4.5 Conservation of energy

As for the Total Lagrangian proof of conservation of energy, in order for the total energy of the system to be conserved, it can be stated that

$$\sum_{a=1}^{N} m_a \mathbf{v}_a \cdot \frac{\mathrm{d}v_a}{\mathrm{d}t} + \frac{\mathrm{d}e_a}{\mathrm{d}t} = 0 \ . \tag{2.70 revisited}$$

After substituting in for the Eulerian form of particle acceleration (Equation 2.90) and the Eulerian rate of internal energy (Equation 2.94) this proof follows the same steps as in Section 2.3.5. The only differences are that the Eulerian derivation is with respect to the deformed state (i.e the nought subscript is dropped) and the first Piola-Kirchhoff stress is exchanged with the Cauchy stress. Hence, the Eulerian conservation of internal energy equation given will conserve the total energy of the system.

2.5 Mixed kernel-and-gradient correction

Having derived the conservation of mass, momentum and energy in both an Eulerian and Total Lagrangian framework a number of comments can be made about both methods' conservation properties. Both methods conserve mass, as this is inherent to the SPH fundamental approximations. Similarly, both methods conserve linear momentum if the internal forces sum to zero. The Total Lagrangian approach conserves angular momentum if the deformation gradient is correctly calculated and the Eulerian approach requires that

$$\sum_{b=1}^{N} V_b \nabla_a W_{ab} \otimes (\mathbf{x}_b - \mathbf{x}_a) = \mathbf{I} \,, \tag{2.98 revisited}$$

which is not always the case. Lastly, both methods unconditionally conserve total energy.

Deficiencies in the order of consistency achieved by the kernel and particle approximations are common to both formulations. The order of consistency m defines both the polynomial order a numerical method is able to recreate exactly and its order of accuracy, given by $(m + 1)$ [87].

The SPH kernel approximation guarantees the correct reproduction of a constant field, or 0^{th} order consistency, due to the unity condition as stated in Section 2.2.1, Equation 2.5:

$$\int_{\Omega} W(\mathbf{x} - \mathbf{x}', h) \mathrm{d}\mathbf{x}' = 1 \,. \tag{2.5 revisited}$$

Applying an SPH particle approximation to this equation, results in

$$\sum_{b=1}^{N} V_b W_{ab} = 1 \,, \tag{2.100}$$

which must be met by each particle in order to correctly ensure 0^{th} order consistency. Even though the kernel approximation gives 0^{th} order consistency, the particle approximation fails to do so in cases of non-uniform particle distributions or when a particle's support domain is truncated by a boundary, as shown in Figure 2.5. The effect of non-uniform distributions is discussed in more detail by Quinlan et al. [81] who gave a truncation error analysis for both uniformly spaced particles and non-uniformly spaced particles. In addition, Young et al. [88] demonstrated how non-uniform distributions can produce noisy results by using different particle distributions to model the lid-driven cavity problem. In Figure 2.5, the uniform distribution comes close to upholding the unity condition when support domains are not truncated by the boundary. When support domains are truncated or underpopulated, the unity approximation will be less than one. It will be greater than one when support domains are over populated. In these cases, it is clear that

$$\sum_{a=1}^{N} \frac{m_a}{\rho_a} \neq \int_{\Omega} \mathrm{d}\mathbf{x}' \,. \tag{2.101}$$

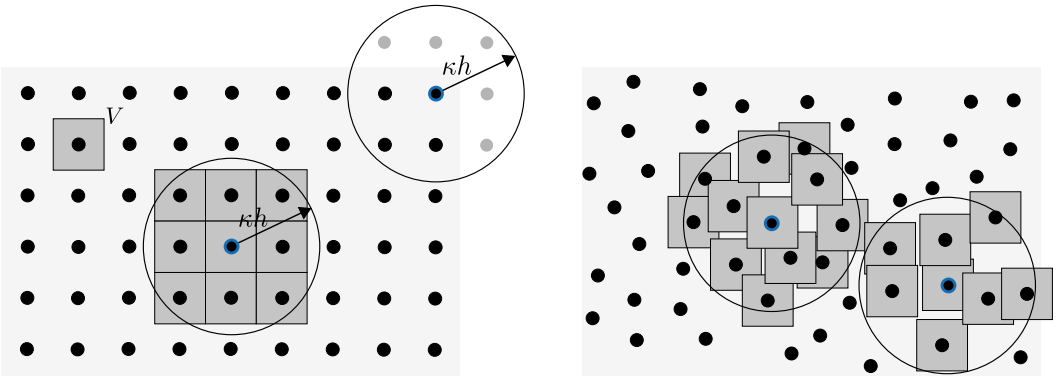

Figure 2.5: Body discretised into particles with volume V and support domain radius κh. The left image is for a uniform distribution and the right-hand side one is for a random distribution. The figure illustrates the effect of boundaries and particle distribution on the particle approximations.

Similarly, the kernel approximation gives 1st order consistency as the unity condition can be manipulated to show that [89]

$$\int_{\Omega} (\mathbf{x} - \mathbf{x}')W(\mathbf{x} - \mathbf{x}', h)\mathrm{d}\mathbf{x}' = \mathbf{0} \,. \tag{2.102}$$

Again, the particle approximation does not guarantee the same order of consistency. Liu and Liu [89] state that the SPH kernel approximation is of 1st order consistency (or 2nd order accuracy), if assuming a non-negative, even, smoothing function. Consequently, if attempting to recreate a constant, linear and polynomial function, only the first two will be correctly approximated assuming a uniform distribution away from the boundaries, as highlighted in Figure 2.6. Liu and Liu [89] state that not even 0th order consistency is achieved at the boundaries, which is also visible in this figure. Note that in this case the particles have been given a smoothing length of 10 times the particle spacing to highlight the boundary effects.

Similarly, the kernel approximation of a derivative guarantees 0th order consistency if the kernel is an even function, but the particle approximation does not. A number of approaches have been developed to restore consistency to the SPH method. Mixed kernel-and-gradient correction, as derived by Bonet and Lok [42], was applied in this work.

2.5.1 Kernel correction

Li and Liu [43] and Liu, Li and Belytschko [90] developed a correction technique whereby any order of consistency could be achieved through modification of the kernel. Following Liu et al. [91], Vidal et al. [35] and Bonet and Lok [42], first order consistency can be achieved by modifying the kernel to

$$\widetilde{W}_{ab} = W_{ab}\alpha(\mathbf{x}_a)\left[1 + \boldsymbol{\beta}(\mathbf{x}_a) \cdot (\mathbf{x}_a - \mathbf{x}_b)\right], \tag{2.103}$$

where $\alpha(\mathbf{v})$ and $\boldsymbol{\beta}(\mathbf{v})$ can be fixed so that 1st order consistency is obtained such that a linear function is calculated exactly:

$$\boldsymbol{f}(\mathbf{x}_a) = \mathbf{k} + \mathbf{l} \cdot \mathbf{x} = \sum_{b=1}^{N} V_b(\mathbf{k} + \mathbf{l} \cdot \mathbf{x}_b)\widetilde{W}_{ab} \,. \tag{2.104}$$

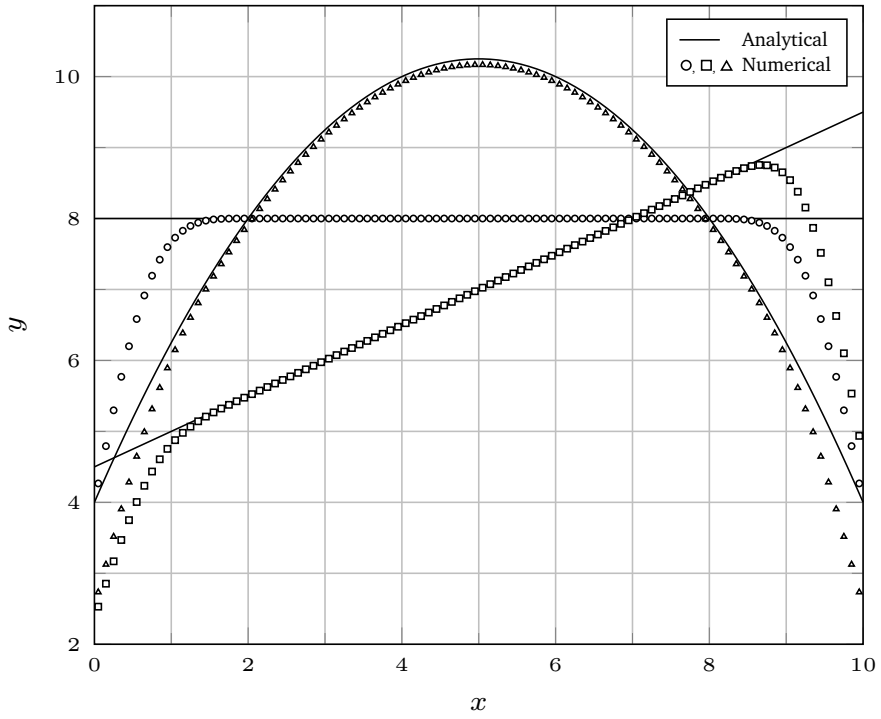

Figure 2.6: Recreation of constant, linear and polynomial functions using a uniform particle distribution and no kernel correction. Only the first two are accurately recreated due to the 1st order consistency of the kernel approximation. The accuracy drastically decreases at the boundaries due to truncated support domains.

Therefore, the previously stated conditions for 0^{th} and 1^{st} order consistency must now be upheld by the corrected kernel, these being

$$\sum_{b=1}^{N} V_b \widetilde{W}_{ab} = 1 \tag{2.105}$$

and

$$\sum_{b=1}^{N} V_b (\mathbf{x}_a - \mathbf{x}_b) \widetilde{W}_{ab} = \mathbf{0} \, . \tag{2.106}$$

Substituting Equation 2.103 into the above leads to

$$\sum_{b=1}^{N} V_b (\mathbf{x}_a - \mathbf{x}_b) W_{ab} \alpha(\mathbf{x}_a) \left[1 + \boldsymbol{\beta}(\mathbf{x}_a) \cdot (\mathbf{x}_a - \mathbf{x}_b) \right] = 0 \, . \tag{2.107}$$

Expanding the summation and rearranging for $\boldsymbol{\beta}(\mathbf{x}_a)$, while noting that $\mathbf{uv}.\mathbf{w} = \mathbf{u} \otimes \mathbf{wv}$ due to the definition of the dot product and outer product, results in

$$\boldsymbol{\beta}(\mathbf{x}_a) = - \left[\sum_{b=1}^{N} V_b (\mathbf{x}_a - \mathbf{x}_b) \otimes (\mathbf{x}_a - \mathbf{x}_b) W_{ab} \right]^{-1} \sum_{b=1}^{N} V_b (\mathbf{x}_a - \mathbf{x}_b) W_{ab} \, . \tag{2.108}$$

After having calculated $\beta(\mathbf{x}_a)$, parameter $\alpha(\mathbf{x}_a)$ can be similarly solved for by substituting Equation 2.103 into the corrected particle approximation of unity (Equation 2.105). This gives

$$\alpha(\mathbf{x}_a) = \left[\sum_{b=1}^{N} V_b W_{ab} \left[1 + \beta(\mathbf{x}_a) \cdot (\mathbf{x}_a - \mathbf{x}_b)\right]\right]^{-1} . \tag{2.109}$$

This type of kernel correction also ensures the conservation of angular momentum as it resolves Equation 2.98. Although this type of kernel correction results in the exact evaluation of linear functions and their gradients, it is both complex and computationally expensive to calculate the corrected kernel gradient $\nabla_a \widetilde{W}_{ab}$ due to the dependence of α and β on $\mathbf{x}$. A computationally cheaper and simpler approach is to compromise to 0^{th} order consistency by setting $\beta(\mathbf{x}) = \mathbf{0}$. This results in a corrected kernel $\widetilde{W}$, which is calculated as a weighted average also known as Shepard's interpolation [42]:

$$\widetilde{W}_{ab} = \frac{W_{ab}}{\sum_{b=1}^{N} V_b W_{ab}} . \tag{2.110}$$

This form of kernel correction is a simplified version of that given by Liu et al. [90] and Li and Liu [43]. Note that this form does not satisfy Equation 2.98 on its own and, as a result, will not ensure the conservation of angular momentum. Figure 2.7 demonstrates the effectiveness of this form of kernel correction. In this figure, a constant, a linear and a polynomial function are recreated using a non-uniform distribution of particles. These functions are then recreated using kernel correction in which case 0^{th} order consistency is achieved along with a reduction in boundary effects.

2.5.2 Kernel gradient correction

Gradient correction is formulated in a similar fashion to kernel correction in that the gradient of the kernel is directly modified such that

$$\widetilde{\nabla}_a W_{ab} = \mathbf{K}_a \nabla_a W_{ab} , \tag{2.111}$$

where $\mathbf{K}$ is the correction matrix[2]. In Subsection 2.4.4 it was shown that in order to conserve angular momentum in an Eulerian formulation for solid mechanics the following must hold true:

$$\sum_{b=1}^{N} V_b \nabla_a W_{ab} \otimes (\mathbf{x}_b - \mathbf{x}_a) = \mathbf{I} . \tag{2.98 revisited}$$

Therefore, both 1^{st} order consistency, as shown by Randles and Libersky [41], and the conservation of angular momentum can be ensured if

$$\sum_{b=1}^{N} V_b \widetilde{\nabla}_a W_{ab} \otimes (\mathbf{x}_b - \mathbf{x}_a) = \mathbf{I} , \tag{2.112}$$

and as a direct result, the correction matrix $\mathbf{K}_a$ becomes

$$\mathbf{K}_a = \left[\sum_{b=1}^{N} V_b \nabla_a W_{ab} \otimes (\mathbf{x}_b - \mathbf{x}_a)\right]^{-1} . \tag{2.113}$$

[2]Note that the letter $\mathbf{K}$ is used as opposed to the conventional $\mathbf{L}$ to distinguish from the spatial velocity gradient.

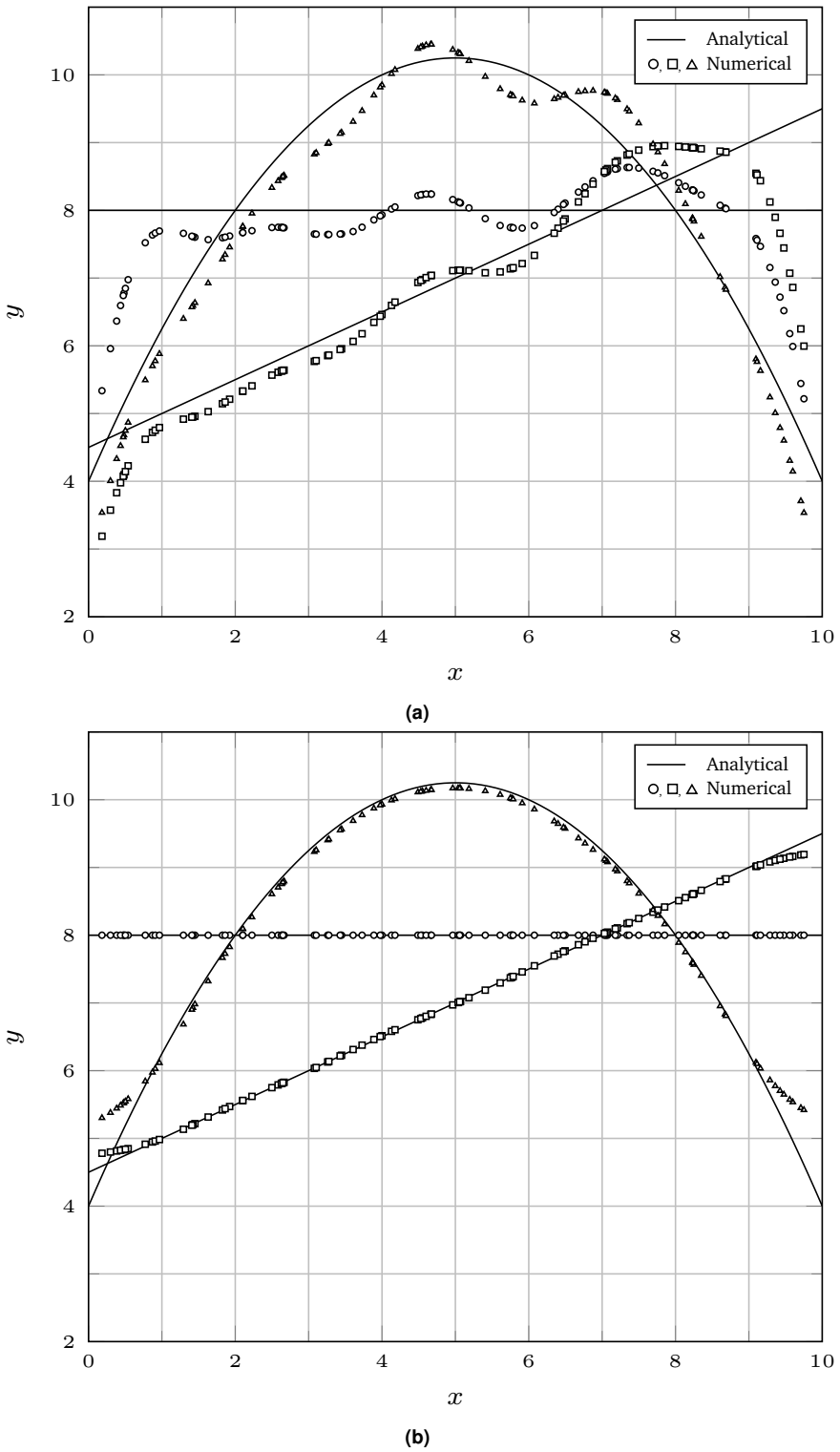

Figure 2.7: Recreation of constant, linear and polynomial functions using a non-uniform particle distribution (a) without and (b) with kernel correction. Kernel correction results in the constant function being exactly recreated. The linear function is similarly restored away from the boundaries. The linear and polynomial functions deviate at the boundary as only 0^{th} order consistency is restored.

Similarly, the conservation of angular momentum in a Total Lagrangian formulation requires that

$$\mathbf{F}_a = \sum_{b=1}^{N} V_{b,0}(\mathbf{x}_b - \mathbf{x}_a) \otimes \nabla_{a,0} W_{ab,0} \, . \qquad \text{(2.67 revisited)}$$

If this is to be upheld by the gradient of the corrected kernel, it can be shown that

$$\mathbf{K}_a = \mathbf{F}_a^{\mathsf{T}} \left[\sum_{b=1}^{N} V_{b,0} \nabla_{a,0} W_{ab} \otimes (\mathbf{x}_b - \mathbf{x}_a) \right]^{-1} = \left[\sum_{b=1}^{N} V_{b,0} \nabla_{a,0} W_{ab} \otimes (\mathbf{x}_b - \mathbf{x}_a) \right]^{-1} \, . \qquad (2.114)$$

In the Total Lagrangian configuration the kernel and the gradient of the kernel are calculated in the undeformed state, where $\mathbf{F} = \mathbf{I}$. Therefore, the gradient correction, which results in the conservation of angular momentum in the Total Lagrangian formulation, is the analogue of the gradient correction used in the Eulerian formulation. The key difference being that one is with reference to the deformed state whilst the other is with reference to the undeformed state.

2.5.3 Mixed correction

Bonet and Lok [42] propose a mixed kernel-and-gradient correction technique, this being a combination of the kernel correction (Section 2.5.1) and kernel gradient correction (Section 2.5.2). This combines the benefits of both approaches: the 0^{th} order consistency of kernel approximations using the kernel correction and the 1^{st} order consistency of the kernel gradient approximations, along with the conservation of angular momentum, using the kernel gradient correction. Using this technique the kernel is corrected such that

$$\widetilde{W}_{ab} = \frac{W_{ab}}{\sum_{b=1}^{N} V_b W_{ab}} \, , \qquad \text{(2.110 revisited)}$$

and the corrected gradient of the corrected kernel is given by

$$\widetilde{\nabla}_a \widetilde{W}_{ab} = \mathbf{K}_a \nabla_a \widetilde{W}_{ab} \, , \qquad (2.115)$$

where the gradient of the corrected kernel, $\nabla \widetilde{W}$, is calculated by applying the quotient rule to Equation 2.110 as

$$\nabla_a \widetilde{W}_{ab} = \frac{\nabla_a W_{ab} \left(\sum_{b=1}^{N} V_b W_{ab} \right) - \left(\sum_{b=1}^{N} V_b \nabla_a W_{ab} \right) W_{ab}}{\left(\sum_{b=1}^{N} V_b W_{ab} \right)^2} \, . \qquad (2.116)$$

The correction matrix $\mathbf{K}$ is now defined using the gradient of the corrected kernel as

$$\mathbf{K}_a = \left(\sum_{b=1}^{N} V_b \nabla_a \widetilde{W}_{ab} \otimes (\mathbf{x}_b - \mathbf{x}_a) \right)^{-1} \, . \qquad (2.117)$$

Bonet and Lok [42] implement a different form of mixed correction to that given here. They do not make use of symmetry terms used in the particle approximations of divergences and gradients, which is discussed in Section 2.2.4, as they are not strictly required. The reason for this is that the kernel correction results in 0^{th} order consistency and hence velocity gradients and divergences of constant functions are calculated exactly. Symmetry terms are used in the following as they result in a simpler and more computationally efficient model. This is because symmetry terms $-f(\mathbf{x}_a)$ are also included in the SPH approximations of gradients and divergences. As a result, when $b = a$

the corrected gradient of the corrected kernel $\widetilde{\nabla}_a \widetilde{W}_{aa}$ is not required. However, this is not the case when the particle approximations of divergences and gradients that do not use symmetry terms are implemented. In this scenario the correction matrix would be derived as

$$\mathbf{K}_a = \left(\sum_{b=1}^{N} V_b \nabla_a \widetilde{W}_{ab} \otimes \mathbf{x}_b \right)^{-1} , \tag{2.118}$$

and when $b = a$, the term $\widetilde{\nabla}_a \widetilde{W}_{aa}$ will be required in the approximation of gradients and divergences. It should be noted that Equation 2.117 and Equation 2.118 are equal. Although not demonstrated in literature, this can be proven by expanding the summation in Equation 2.117 as

$$\sum_{b=1}^{N} V_b \nabla_a \widetilde{W}_{ab} \otimes (\mathbf{x}_b - \mathbf{x}_a) = \left(\sum_{b=1}^{N} V_b \nabla_a \widetilde{W}_{ab} \otimes \mathbf{x}_b \right) - \left(\sum_{b=1}^{N} V_b \nabla_a \widetilde{W}_{ab} \right) \otimes \mathbf{x}_a , \tag{2.119}$$

and noting that the second bracketed term on the right-hand side is the gradient of the particle approximation of the unity condition (Equation 2.105). As 0^{th} order consistency is enforced by the kernel correction, this term must equal zero. Section 4.2 further proves that these equations are interchangeable using a numerical example.

It is noted that when applying mixed kernel-and-gradient correction $\widetilde{\nabla}_a \widetilde{W}_{ab} = -\widetilde{\nabla}_b \widetilde{W}_{ab}$ and $\widetilde{\nabla}_b \widetilde{W}_{ba} = -\widetilde{\nabla}_a \widetilde{W}_{ba}$. However, once the gradient of the kernel has been modified $\widetilde{\nabla}_a \widetilde{W}_{ab} \neq -\widetilde{\nabla}_b \widetilde{W}_{ba}$. As the derivations and proofs given for the Eulerian (Section 2.4) and Total Lagrangian (Section 2.3) formulations did not make use of $\nabla_a W_{ab} = -\nabla_b W_{ba}$ these can be easily modified for mixed correction by simply replacing W_{ab} with $\widetilde{W}_{ab}$ and $\nabla_a W_{ab}$ with $\widetilde{\nabla}_a \widetilde{W}_{ab}$. Doing so will not influence the conservation properties other than restoring the conservation of angular momentum. With this in mind the conservation equations, for solid mechanics, in an SPH Eulerian framework are given by

$$\begin{cases} \dfrac{\mathrm{d}\rho_a}{\mathrm{d}t} = -\rho_a \displaystyle\sum_{b=1}^{N} V_b (\mathbf{v}_b - \mathbf{v}_a) \cdot \widetilde{\nabla}_a \widetilde{W}_{ab} \\ \dfrac{\mathrm{d}\mathbf{v}_a}{\mathrm{d}t} = -\dfrac{1}{m_a} \displaystyle\sum_{b=1}^{N} V_a V_b (\boldsymbol{\sigma}_b \widetilde{\nabla}_b \widetilde{W}_{ba} - \boldsymbol{\sigma}_a \widetilde{\nabla}_a \widetilde{W}_{ab}) \\ \dfrac{\mathrm{d}e_a}{\mathrm{d}t} = \displaystyle\sum_{b=1}^{N} V_a V_b (\mathbf{v}_b - \mathbf{v}_a) \cdot \boldsymbol{\sigma}_a \widetilde{\nabla}_a \widetilde{W}_{ab} \end{cases} \tag{2.120}$$

and the corresponding equations in a Total Lagrangian framework are given by

$$\begin{cases} \rho_a = \dfrac{\rho_{a,0}}{\det\left[\left(\sum_{b=1}^{N} V_{b,0} (\mathbf{u}_b - \mathbf{u}_a) \otimes \widetilde{\nabla}_{a,0} \widetilde{W}_{ab,0} \right) + \mathbf{I} \right]} \\ \dfrac{\partial \mathbf{v}_a}{\partial t} = -\dfrac{1}{m_a} \displaystyle\sum_{b=1}^{N} V_{a,0} V_{b,0} \left(\mathbf{P}_b \widetilde{\nabla}_{b,0} \widetilde{W}_{ba} - \mathbf{P}_a \widetilde{\nabla}_{a,0} \widetilde{W}_{ab} \right) \\ \dfrac{\partial e_a}{\partial t} = \displaystyle\sum_{b=1}^{N} V_{a,0} V_{b,0} (\mathbf{v}_b - \mathbf{v}_a) \cdot \mathbf{P}_a \widetilde{\nabla}_{a,0} \widetilde{W}_{ab,0} \end{cases} . \tag{2.121}$$

These novel sets of equations retain their conservation properties and ensure 1^{st} order consistency of the kernel gradient approximation. For the Total Lagrangian formulation, the kernel, the kernel

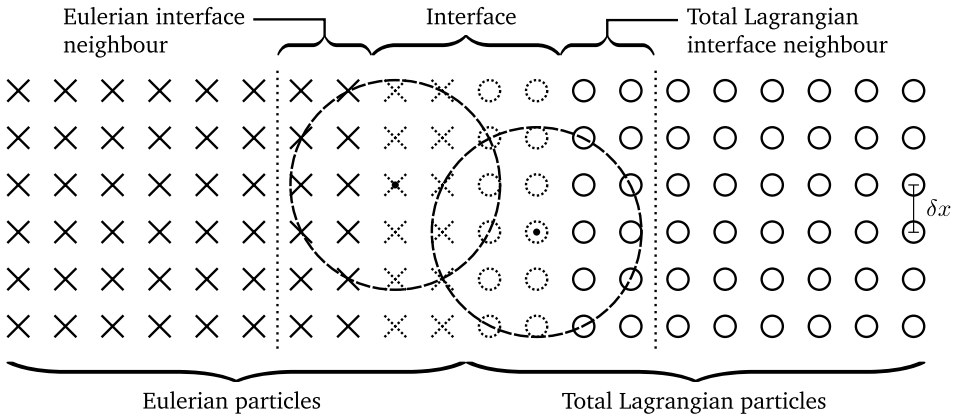

Figure 2.8: Representative continuum discretised into Total Lagrangian and Eulerian particles with noteworthy zones highlighted. The particle influence range is approximately equal to $2\delta x$ for illustrative purposes.

gradient, the corrected kernel and the corrected kernel gradient are calculated once in the undeformed reference state and are then reused in subsequent time steps. The Eulerian formulation requires that these values are updated at each time step. It is now possible to demonstrate the proposed coupling methodologies, having stated the corrected momentum and energy conserving forms of the Eulerian and Total Lagrangian formulations.

2.6 Eulerian Total Lagrangian coupling methods

The Total Lagrangian formulation does not suffer from the tensile instability and is computationally efficient, though large distortions can be challenging to model. The Eulerian formulation easily handles large distortions, though it requires frequent updates of neighbour lists and suffers from the tensile instability. Considering these strengths and weaknesses, it would appear that an ideal formulation would be able to combine both such that in the presence of large distortions particles could convert from Total Lagrangian to Eulerian.

Consider an Eulerian particle in whose influence range there are only other Eulerian particles. In this case, no modification is required to the formulation and the description of Eulerian SPH given in Section 2.4 is followed. The same applies to a Total Lagrangian particle in whose influence range there are only other Total Lagrangian particles. However, modifications are required in the scenario where an Eulerian particle has a Total Lagrangian particle in its support domain and vice versa. In this work, such a region is referred to as the interface zone. Figure 2.8 displays an example of a discretised continuum with this zone highlighted. Terminology and notation is adapted from Randles and Libersky [41] in order to explain the coupling methods. The set of particles within the neighbourhood of a particle a is denoted as $\mathbb{N}_{(a)}$. The set $\mathbb{N}_{(a)}$ is divided into two subsets including $\mathbb{S}_{(a)}$ and $\mathbb{I}_{(a)}$. $\mathbb{S}_{(a)}$ contains neighbouring particles of the same kernel type as a and $\mathbb{I}_{(a)}$ contains neighbouring particles of a different kernel type, which are in the interface zone. The following two methods were used in the interface zone to couple the Eulerian and Total Lagrangian formulations.

2.6.1 Coupling method one

In this new coupling method, Eulerian particles use Total Lagrangian particles in the interface zone in the Eulerian conservation of mass equation (Equation 2.78) as if they were Eulerian particles:

$$\frac{\mathrm{d}\rho_a}{\mathrm{d}t} = -\rho_a \sum_{b\in\mathbb{N}_{(a)}} V_b(\mathbf{v}_b - \mathbf{v}_a)\cdot\widetilde{\nabla}_a\widetilde{W}_{ab}\ . \tag{2.122}$$

This requires the corrected gradient of the corrected kernel ($\widetilde{\nabla}_a\widetilde{W}_{ab}$) to be calculated in spatial coordinates for each Eulerian-Total Lagrangian pair in the interface zone. Similarly, the Total Lagrangian particles use the Eulerian particles in their deformation gradient summations ($\mathbf{F}$ from Equation 2.36), which then affects their Jacobians, J, and consequently their densities:

$$\rho_a = \frac{\rho_{a,0}}{\det\left[\left(\sum_{b\in\mathbb{N}_{(a)}} V_{b,0}(\mathbf{u}_b - \mathbf{u}_a)\otimes\widetilde{\nabla}_{a,0}\widetilde{W}_{ab,0}\right) + \mathbf{I}\right]} \tag{2.123}$$

In this case, the corrected gradient of the corrected kernel, $\widetilde{\nabla}_{a,0}\widetilde{W}_{ab}$, is required in material coordinates for each Eulerian-Total Lagrangian pair. This only needs to be calculated once, which is done at the start of the simulation. In this coupling method, it is required that all Eulerian-Total Lagrangian particle pairs be within each other's support domains in the undeformed state. In the equation of conservation of energy, both formulations contribute to each other's summations as for the conservation of mass as

$$\frac{\mathrm{d}e_a}{\mathrm{d}t} = \sum_{b\in\mathbb{N}_{(a)}} V_a V_b(\mathbf{v}_b - \mathbf{v}_a)\cdot\boldsymbol{\sigma}_a\widetilde{\nabla}_a\widetilde{W}_{ab} \tag{2.124}$$

and

$$\frac{\partial e_a}{\partial t} = \sum_{b\in\mathbb{N}_{(a)}} V_{a,0}V_{b,0}(\mathbf{v}_b - \mathbf{v}_a)\cdot\mathbf{P}_a\widetilde{\nabla}_{a,0}\widetilde{W}_{ab,0}\ . \tag{2.125}$$

Consider a pair of particles in the interface zone. Assume that particle a uses an Eulerian kernel and particle b uses a Total Lagrangian kernel. The force exerted by b on a is given by the Eulerian momentum equation

$$\mathbf{t}_{\mathrm{E},ab} = m_a\frac{\mathrm{d}\mathbf{v}_a}{\mathrm{d}t} = V_a V_b\left(\boldsymbol{\sigma}_b\widetilde{\nabla}_b\widetilde{W}_{ba} - \boldsymbol{\sigma}_a\widetilde{\nabla}_a\widetilde{W}_{ab}\right)\ . \tag{2.126}$$

The force exerted by a on b is given by the Total Lagrangian momentum equation

$$\mathbf{t}_{\mathrm{L},ba} = m_b\frac{\partial\mathbf{v}_b}{\partial t} = V_{b,0}V_{a,0}\left(\mathbf{P}_a\widetilde{\nabla}_{a,0}\widetilde{W}_{ab} - \mathbf{P}_b\widetilde{\nabla}_{b,0}\widetilde{W}_{ba}\right)\ . \tag{2.127}$$

In both of the equations above it is evident that $\mathbf{t}_{\mathrm{E},ab} = -\mathbf{t}_{\mathrm{E},ba}$ and $\mathbf{t}_{\mathrm{L},ab} = -\mathbf{t}_{\mathrm{L},ba}$, as swapping indices merely reverses the summation in the brackets. This coupling method assumes that both the Eulerian and the Total Lagrangian formulations give the same internal forces, or that $\mathbf{t}_{\mathrm{L},ba} = -\mathbf{t}_{\mathrm{E},ab}$. The consequence of this assumption is that the following must hold true:

$$\widetilde{\nabla}_b\widetilde{W}_{ba} = J_b\mathbf{F}_b^{-\mathsf{T}}\widetilde{\nabla}_{b,0}\widetilde{W}_{ba} \tag{2.128}$$

and

$$\widetilde{\nabla}_a\widetilde{W}_{ab} = J_a\mathbf{F}_a^{-\mathsf{T}}\widetilde{\nabla}_{a,0}\widetilde{W}_{ab}\ . \tag{2.129}$$

The above equalities are found by comparing the two equations for internal forces and recalling the relationship between the two stress measures that

$$\mathbf{P} = J\boldsymbol{\sigma} \cdot \mathbf{F}^{-\mathsf{T}} . \qquad \text{(2.51 revisited)}$$

Therefore, the momentum equations are given by

$$\frac{\mathrm{d}\mathbf{v}_a}{\mathrm{d}t} = -\frac{1}{m_a}\left[\sum_{b\in\mathbb{S}_{(a)}} V_a V_b(\boldsymbol{\sigma}_b\widetilde{\nabla}_b\widetilde{W}_{ba} - \boldsymbol{\sigma}_a\widetilde{\nabla}_a\widetilde{W}_{ab}) + \sum_{b\in\mathbb{I}_{(a)}} V_a V_b(\boldsymbol{\sigma}_b\widetilde{\nabla}_b\widetilde{W}_{ba} - \boldsymbol{\sigma}_a\widetilde{\nabla}_a\widetilde{W}_{ab})\right] \qquad (2.130)$$

and

$$\frac{\partial\mathbf{v}_a}{\partial t} = -\frac{1}{m_a}\left[\sum_{b\in\mathbb{S}_{(a)}} V_{a,0}V_{b,0}\left(\mathbf{P}_b\widetilde{\nabla}_{b,0}\widetilde{W}_{ba} - \mathbf{P}_a\widetilde{\nabla}_{a,0}\widetilde{W}_{ab}\right) - \sum_{b\in\mathbb{I}_{(a)}} V_a V_b(\boldsymbol{\sigma}_b\widetilde{\nabla}_b\widetilde{W}_{ba} - \boldsymbol{\sigma}_a\widetilde{\nabla}_a\widetilde{W}_{ab})\right]. \qquad (2.131)$$

It is noted that Bonet and Kulasegaram [25], who implement similar conservation of momentum equations to those given here (Equations 2.120 and 2.121) but without the symmetry terms, state that in general Equations 2.128 and 2.129 are not satisfied. These authors state that this is due to differences in discretisation. These equations are only valid when the support domain of the Eulerian particle a is the same size and shape in both the spatial and material coordinates. This is because, in the material coordinates, the support domain stretches depending on the displacement of particles. In the spatial coordinates the support domain retains its size and shape. However, this coupling is efficient as the deformation gradient does not need to be calculated for particles which make use of an Eulerian kernel.

A result of $\mathbf{t}_{\mathrm{L},ba} = -\mathbf{t}_{\mathrm{E},ab}$ (and visible in Equation 2.130) is that particles which make use of Eulerian kernels only use the Eulerian conservation of momentum. As seen in Equation 2.131, particles which use Total Lagrangian kernels do not include any particles with Eulerian kernels in their Total Lagrangian conservation of momentum summations. The advantage of this method is that few additional calculations are required. The Cauchy stress tensor has already been calculated for each Total Lagrangian particle so only the Total Lagrangian particle volumes in the deformed configuration are required. Note that the corrected gradient of the corrected kernel ($\widetilde{\nabla}_a\widetilde{W}_{ab}$) between Eulerian and Total Lagrangian particle pairs, in a spatial coordinates, was already required for the Eulerian conservation of mass equation.

An alternative assumption could make use of $\mathbf{t}_{\mathrm{E},ba} = -\mathbf{t}_{\mathrm{L},ab}$. The disadvantage of this method is that the Eulerian particles in the interface zone must have their Cauchy stresses converted into first Piola-Kirchhoff stresses. This would require the deformation gradient to be calculated for the Eulerian particles in the interface zone. As this further depends on the displacement of particles' neighbours, a record would have to be kept of the Eulerian interface neighbours, as shown in Figure 2.8. That approach is avoided in this method due to the addition of unnecessary complexity and computation.

This coupling is centred on the principle that $\mathbf{t}_{ba} = -\mathbf{t}_{ab}$ as this simplifies the required calculations. Retrospective application of gradient correction to the conventional momentum equation, which is based on one kernel gradient, would not fulfil this condition as $\widetilde{\nabla}_a\widetilde{W}_{ab} \neq -\widetilde{\nabla}_b\widetilde{W}_{ba}$ and therefore $\mathbf{t}_{ba} \neq -\mathbf{t}_{ab}$. Applying the non symmetrical form of gradient correction results in $\mathbf{t}_{ba} \neq -\mathbf{t}_{ab}$, although this form still conserves linear momentum as $\sum_{a=1}^{N}\mathbf{t}_a = 0$.

A disadvantage of this Eulerian Total Lagrangian coupling is that the tensile instability can still manifest in the Eulerian component of the domain. A number of attempts were made to control this

using artificial stress as developed by Gray et al. [30]. These were unsuccessful due to an instability that manifested in the interface zone. Artificial stress was applied using two approaches in the interface zone. Firstly, only Eulerian particles made use of artificial stress and secondly, in addition to the Eulerian particles, the Total Lagrangian particles in the interface zone made use of artificial stress. The second approach would appear to be most appropriate considering that the contribution from the Eulerian particles to the Total Lagrangian particles' momentum equation was calculated using an Eulerian kernel. Neither approach produced satisfactory results. It was recognised that the assumption that $\mathbf{t}_{\mathrm{L},ba} = -\mathbf{t}_{\mathrm{E},ab}$ could lead to tensile instability in Total Lagrangian particles at the interface. Therefore, $\mathbf{t}_{\mathrm{E},ba} = -\mathbf{t}_{\mathrm{L},ab}$ was applied and the two approaches discussed were again tested and an instability developed at the interface in both cases. This coupling method is currently only suitable for problems where tensile instability will not manifest in the Eulerian component as it cannot yet be controlled using artificial stress. This is most likely due to the fact that $\mathbf{t}_{\mathrm{L},ba} = -\mathbf{t}_{\mathrm{E},ab}$ can only be guaranteed when particles which make use of the Eulerian kernel, located in the interface zone, have a support domain with constant shape and size.

Although incompatible with artificial stress, this coupling is compatible with artificial viscosity. If using mixed correction the formulation must be modified in order to implement artificial viscosity in a momentum and energy conserving manner.

2.6.2 Coupling method two

The second approach used to couple the Eulerian and Total Lagrangian formulations is similar to that presented by Lacome et al. [61]. In this case, no assumption of equal and opposite internal forces is presumed between particles in the interface zone (see Figure 2.8). Instead, Eulerian particles treat their Total Lagrangian neighbours as Eulerian particles and vice versa. Consequently, the spatial equations

$$\begin{cases} \dfrac{\mathrm{d}\rho_a}{\mathrm{d}t} = -\rho_a \displaystyle\sum_{b\in\mathbb{N}_{(a)}} V_b(\mathbf{v}_b - \mathbf{v}_a)\cdot\widetilde{\nabla}_a\widetilde{W}_{ab} \\ \dfrac{\mathrm{d}\mathbf{v}_a}{\mathrm{d}t} = -\dfrac{1}{m_a}\displaystyle\sum_{b\in\mathbb{N}_{(a)}} V_aV_b(\boldsymbol{\sigma}_b\widetilde{\nabla}_b\widetilde{W}_{ba} - \boldsymbol{\sigma}_a\widetilde{\nabla}_a\widetilde{W}_{ab}) \\ \dfrac{\mathrm{d}e_a}{\mathrm{d}t} = \displaystyle\sum_{b\in\mathbb{N}_{(a)}} V_aV_b(\mathbf{v}_b - \mathbf{v}_a)\cdot\boldsymbol{\sigma}_a\widetilde{\nabla}_a\widetilde{W}_{ab} \end{cases} \qquad \text{(2.120 revisited)}$$

and the material equations

$$\begin{cases} \rho_a = \dfrac{\rho_{a,0}}{\det\left[\left(\sum_{b\in\mathbb{N}_{(a)}} V_{b,0}(\mathbf{u}_b - \mathbf{u}_a)\otimes\widetilde{\nabla}_{a,0}\widetilde{W}_{ab,0}\right) + \mathbf{I}\right]} \\ \dfrac{\partial\mathbf{v}_a}{\partial t} = -\dfrac{1}{m_a}\displaystyle\sum_{b\in\mathbb{N}_{(a)}} V_{a,0}V_{b,0}\left(\mathbf{P}_b\widetilde{\nabla}_{b,0}\widetilde{W}_{ba} - \mathbf{P}_a\widetilde{\nabla}_{a,0}\widetilde{W}_{ab}\right) \\ \dfrac{\partial e_a}{\partial t} = \displaystyle\sum_{b\in\mathbb{N}_{(a)}} V_{a,0}V_{b,0}(\mathbf{v}_b - \mathbf{v}_a)\cdot\mathbf{P}_a\widetilde{\nabla}_{a,0}\widetilde{W}_{ab,0} \end{cases} , \qquad \text{(2.121 revisited)}$$

can be applied as usual. It is trivial to transform a material stress into its spatial equivalent through

$$\boldsymbol{\sigma} = J^{-1}\mathbf{F}\mathbf{P}^{\mathsf{T}} , \qquad (2.132)$$

which is a rearrangement of Equation 2.51. It is more complex to do the opposite as is needed for the Total Lagrangian conservation of momentum equation. This equation requires that the neighbouring Eulerian particles have a first Piola-Kirchhoff stress tensor. The calculation of this stress tensor requires a deformation gradient. Therefore, the Eulerian particles in the interface zone must calculate their deformation gradient in the reference configuration as

$$\mathbf{F}_a = \left[\sum_{b=1}^{N} V_{b,0}(\mathbf{u}_b - \mathbf{u}_a) \otimes \widetilde{\nabla}_{a,0} \widetilde{W}_{ab,0}\right] + \mathbf{I} \,. \qquad \text{(2.36 revisited)}$$

Lacome et al. [61] calculated the deformation gradient for all particles. Therefore, this second coupling method extends the range of the Total Lagrangian kernel type to the neighbours of the Eulerian interface particles. Consequently, it requires that these Eulerian interface neighbours do not experience any large distortions or else the deformation gradient of the Eulerian interface particles will become unphysical. The benefit to this method is that the internal forces are no longer coupled. Consequently, this coupling is not as sensitive to the scenarios where the Eulerian and Total Lagrangian support domains largely differ at the interface. Furthermore, this coupling method is compatible with artificial stress at the cost of being more complex. Note that in this method, the Eulerian particles must search through the Total Lagrangian particles for neighbours at every time step, while the Total Lagrangian particles only search for Eulerian neighbours in the undeformed configuration. Therefore, the list of interface neighbours can differ in the material and spatial coordinates.

The application of the mixed kernel-and-gradient correction to this coupling method requires further explanation. Namely how the interface particles, which make use of Total Lagrangian kernels, are required to find their nearest neighbours in the spatial coordinates. This can be highlighted by inspecting the gradient of the corrected kernel

$$\nabla_a \widetilde{W}_{ab} = \frac{\nabla_a W_{ab} \left(\sum_{b=1}^{N} V_b W_{ab}\right) - \left(\sum_{b=1}^{N} V_b \nabla_a W_{ab}\right) W_{ab}}{\left(\sum_{b=1}^{N} V_b W_{ab}\right)^2} \qquad \text{(2.116 revisited)}$$

and noticing that the summations $\sum_{b=1}^{N} V_b W_{ab}$ and $\sum_{b=1}^{N} V_b \nabla_a W_{ab}$ must be calculated for particles in the interface zone that use Total Lagrangian kernels. This is required for the corrected gradient of the corrected kernel $\widetilde{\nabla}_b \widetilde{W}_{ba}$ in the spatial conservation of momentum equation. Therefore, the mixed correction extends the range of the Eulerian kernel type to the neighbours of the Total Lagrangian interface particles.

Lastly, it is noted that for small deformations the two proposed coupling methods are identical.

2.7 Concluding remarks

The main objectives of this chapter were (i) to introduce the underpinning principles of the SPH method, (ii) to use these principles to formulate the conservation equations both in an Eulerian and Total Lagrangian reference, (iii) to highlight the angular momentum, linear momentum and total energy conservation properties of both formulations, (iv) to demonstrate the consistency deficiencies common to both formulations as well as to present the correction technique implemented both to

restore consistency and conserve momentum and, (v) to explain the coupling procedures developed along with their advantages and disadvantages.

It should be noted that the kernel property that $\nabla_a W_{ab} = -\nabla_b W_{ba}$ was not made use of when attempting to achieve these objectives, as is commonly done in literature. The reason for this was that once gradient correction is applied $\widetilde{\nabla}_a \widetilde{W}_{ab} = -\widetilde{\nabla}_b \widetilde{W}_{ba}$ does not hold true. Deriving the formulations and demonstrating the conservation properties in this way uncovered a number of interesting properties. Namely, the conditions required for the conservation of angular momentum, in both the Eulerian (Equation 2.98) and the Total Lagrangian (Equation 2.67) formulations, arose naturally from the proof of conservation of angular momentum and were found to be analogous. Having implemented a symmetrical approximation for divergences and gradients, two coupling procedures were proposed, the first of which was dependent on these symmetry terms. As the core components of the coupled formulations have now been discussed, the elements required for a coupled kernel approach to plasticity and fracture can now be presented.

A coupled kernel approach to plasticity and fracture

3

3.1 Overview

Chapter 2 gave an overview of the SPH method along with the Eulerian formulation, the Total Lagrangian formulation and two methods to couple them. By itself this is insufficient for modelling elastic dynamics and fracture using the SPH method. As SPH contains no numerical dissipation, shock fronts cannot be natively resolved without the addition of some dissipative term. Additionally, the Eulerian formulation can manifest the tensile instability if triggered by tensile stresses. This tensile instability hinders the ability of the Eulerian formulation to simulate the behaviour of solids unless it is suppressed by some additional stress term. Therefore, both artificial viscosity and artificial stress are detailed in this chapter, with emphasis on the application to the Eulerian, Total Lagrangian and coupled formulations.

In Chapter 2, a generic equation of state was given in the derivation of both formulations. This should not be used in all cases, as the selection of an equation of state is problem-dependent. In this chapter, three equations of state are discussed including an elastic one and two variations of the Mie-Gruneisen equation of state. These are applicable in a range of problems from elastic response to high velocity impact.

The formulations presented in Chapter 2 assumed linear elasticity. In order to model the response of real engineering materials both plasticity and fracture must also be considered. For this reason, three plasticity models are briefly described including an elastic-perfectly plastic model, an elastic-plastic with isotropic hardening model and the Johnson-Cook plasticity model. The Johnson-Cook plasticity model is the most complex of these models and is an empirical equation which takes stress, stress rate and temperature into account. Additionally, three damage models are discussed including the Rankine damage model, the Lemaitre damage model and the Johnson-Cook damage model. As the Johnson-Cook damage model only determines when a particle is damaged and not the action required once damaged, a method is suggested here which makes use of converting particle kernel types.

Boundary conditions are investigated for both formulations. This investigation was motivated by the reduction in computational cost gained by the usage of symmetry planes, which were modelled using ghost particles. In addition to describing the use of ghost particles in a mixed correction coupled formulation, a contact algorithm is also discussed. This was required for two separate bodies formed of Total Lagrangian particles to transfer momentum between each other.

A Predict, Evaluate, Correct (PEC) form of leapfrog time integration is presented, which evolves both material and spatial field variables in a consistent manner. Additionally, a flow chart is provided which highlights the order of the calculations if implementing either an Eulerian, a Total Lagrangian or a coupled formulation.

The implementation of a mixed correction coupled formulation was challenging as the Eulerian and Total Lagrangian formulations intersect in the interface zone. Furthermore, the Total Lagrangian

neighbours remain fixed whilst the Eulerian neighbours update every time step. The methodology that was used to handle these complexities is outlined along with an application of parallel programming.

3.2 Spatial and material artificial viscosity

Price [92] states that if an SPH formulation is derived from the Lagrangian it is exactly conservative as a consequence. Therefore, if derived from the Lagrangian it contains no intrinsic numerical dissipation. This is an advantage, according to Price, as energy will not dissipate or diffuse unless a term is explicitly added to do so. Price goes on to state that this is similarly a disadvantage in cases such as shock simulation where this term is required. In the Smoothed Particle Hydrodynamics method, it is assumed that field variables vary smoothly across the smallest length scale, this being the smoothing length h, which is conventionally a multiple of the inter-particle spacing δx. This would not be the case when attempting to capture phenomena such as a shock front. The dissipative term, known as artificial viscosity, was first introduced to SPH by Monaghan and Gingold [93] and Lattanzio et al. [94] and has subsequently been widely adopted into the SPH method. The momentum equation including artificial viscosity Π is frequently written for Eulerian SPH and applied to solids as [30, 41, 48, 95]

$$\frac{\mathrm{d}\mathbf{v}_a}{\mathrm{d}t} = -\sum_{b=1}^{N} m_b \left(\frac{\boldsymbol{\sigma}_a}{\rho_a^2} + \frac{\boldsymbol{\sigma}_b}{\rho_b^2} - \Pi_{ab}\mathbf{I} \right) \nabla_b W_{ba} \,. \tag{3.1}$$

Monaghan [38, 39] gives the following commonly used form of artificial viscosity:

$$\Pi_{ab} = \begin{cases} \dfrac{-\alpha \bar{c}_{ab} \mu_{ab} + \beta \mu_{ab}^2}{\bar{\rho}_{ab}} & \text{if } (\mathbf{v}_a - \mathbf{v}_b) \cdot (\mathbf{x}_a - \mathbf{x}_b) < 0 \\ 0 & \text{if } (\mathbf{v}_a - \mathbf{v}_b) \cdot (\mathbf{x}_a - \mathbf{x}_b) \geq 0 \end{cases} \tag{3.2}$$

and

$$\mu_{ab} = \frac{h(\mathbf{v}_a - \mathbf{v}_b) \cdot (\mathbf{x}_a - \mathbf{x}_b)}{|(\mathbf{x}_a - \mathbf{x}_b)|^2 + 0.01h^2} \,. \tag{3.3}$$

The barred notation over c and ρ denotes an average value between particles a and b. The speed of sound is denoted by c. The constant α is dominant for small velocity differences and produces a bulk viscosity [1, 85]. The β term is similar to the von Neumann-Richtmyer artificial viscosity and becomes dominant for large velocity differences. The 0.01 in the denominator is used to prevent singularities. The above form of artificial viscosity is favourable as it is Galilean invariant, conserves momentum and vanishes for rigid body rotation [38]. The dissipative term can be separated from Equation 3.1 and written as

$$\left(\frac{\mathrm{d}\mathbf{v}_a}{\mathrm{d}t} \right)_{\mathrm{diss}} = \sum_{b=1}^{N} m_b \Pi_{ab} \nabla_b W_{ba} \,. \tag{3.4}$$

As $\widetilde{\nabla}_a \widetilde{W}_{ab} \neq -\widetilde{\nabla}_b \widetilde{W}_{ba}$, using Equation 3.1 and retrospectively applying mixed correction would destroy the symmetric nature of the internal forces as these would no longer be equal and opposite for particle pairs. Alternatively, Equation 3.1 is rewritten without artificial viscosity in symmetric form. This is done by first removing the artificial viscosity term, making use of the anti-symmetry

property of the kernel gradient ($\nabla_a W_{ab} = -\nabla_b W_{ba}$) and applying the mixed correction to the kernel gradients, such that

$$\frac{\mathrm{d}\mathbf{v}_a}{\mathrm{d}t} = -\sum_{b=1}^{N} m_b \left(\frac{\boldsymbol{\sigma}_b}{\rho_b^2} \widetilde{\nabla}_b \widetilde{W}_{ba} - \frac{\boldsymbol{\sigma}_a}{\rho_a^2} \widetilde{\nabla}_a \widetilde{W}_{ab} \right) . \tag{3.5}$$

Based on the above, the following adaptation to the artificial viscosity is proposed:

$$\left(\frac{\mathrm{d}\mathbf{v}_a}{\mathrm{d}t} \right)_{\mathrm{diss}} = \sum_{b=1}^{N} \frac{m_b \Pi_{ab}}{2} \left(\widetilde{\nabla}_b \widetilde{W}_{ba} - \widetilde{\nabla}_a \widetilde{W}_{ab} \right) . \tag{3.6}$$

This form of artificial viscosity, based on Equation 3.5, conserves momentum. Furthermore, if the mixed kernel-and-gradient correction is removed, the above equation reduces back to the conventional artificial viscosity.

For both the Total Lagrangian and Eulerian formulations, symmetry terms $-\mathbf{u}_a$ and $-\mathbf{v}_a$ were used in the definition of the deformation gradient and the velocity gradient. These lead to the symmetry terms $-\mathbf{P}_a \nabla_{a,0} W_{ab}$ and $-\boldsymbol{\sigma}_a \nabla_a W_{ab}$ in the derivations of the internal forces (Sections 2.3.2 and 2.4.2). If using mixed correction but not using symmetry terms, it might be presumed that Equation 3.6 would reduce to

$$\left(\frac{\mathrm{d}\mathbf{v}_a}{\mathrm{d}t} \right)_{\mathrm{diss}} = \sum_{b=1}^{N} \frac{m_b \Pi_{ab}}{2} \widetilde{\nabla}_b \widetilde{W}_{ba} . \tag{3.7}$$

However, this equation did not produce results which were consistent with the formulation that included symmetry terms, most likely because Π_{aa} does not exist and therefore $\widetilde{\nabla}_a \widetilde{W}_{aa}$ has no impact. Instead, Equation 3.6 was implemented regardless of whether symmetry terms were included or not as this was found to produce consistent results.

Mapping the dissipative force back to the reference state using Equations 2.128 and 2.129 leads to the Total Lagrangian form of artificial viscosity as

$$\left(\frac{\partial \mathbf{v}_a}{\partial t} \right)_{\mathrm{diss}} = \sum_{b=1}^{N} \frac{m_b \Pi_{ab}}{2} \left(J_b \mathbf{F}_b^{-\mathsf{T}} \widetilde{\nabla}_{b,0} \widetilde{W}_{ba} - J_a \mathbf{F}_a^{-\mathsf{T}} \widetilde{\nabla}_{a,0} \widetilde{W}_{ab} \right) . \tag{3.8}$$

In the case that a Total Lagrangian particle contains an Eulerian particle within its support domain, and vice versa, two approaches are adopted. For the first coupling method, the same methodology is applied as for the momentum equations: the dissipative term is calculated for the pair in the Eulerian reference. An equal and opposite force is then applied to the Total Lagrangian particle. For the second coupling method, the artificial viscosity is calculated for the pair in both the reference configuration and the deformed configuration.

In order to ensure the conservation of energy artificial viscosity must also be added to the evolution of internal energy. Following the same methodology as for the momentum equation, the dissipative component of the energy equation in the Eulerian formulation can be written as[1]

$$\left(\frac{\mathrm{d}e_a}{\mathrm{d}t} \right)_{\mathrm{diss}} = \sum_{b=1}^{N} \frac{m_a m_b \Pi_{ab}}{4} (\mathbf{v}_b - \mathbf{v}_a) \cdot \left(\widetilde{\nabla}_b \widetilde{W}_{ba} - \widetilde{\nabla}_a \widetilde{W}_{ab} \right) . \tag{3.9}$$

[1] See Libersky et al. [47] for the origin of the additional half in the denominator.

In the Total Lagrangian formulation the artificial viscosity term can be written as

$$\left(\frac{\partial e_a}{\partial t}\right)_{\text{diss}} = \sum_{b=1}^{N} \frac{m_a m_b \Pi_{ab}}{4} (\mathbf{v}_b - \mathbf{v}_a) \cdot \left(J_b \mathbf{F}_b^{-\mathsf{T}} \widetilde{\nabla}_{b,0} \widetilde{W}_{ba} - J_a \mathbf{F}_a^{-\mathsf{T}} \widetilde{\nabla}_{a,0} \widetilde{W}_{ab} \right) . \tag{3.10}$$

It is noted that the application of artificial viscosity will result in more artificial dissipation than is necessary. As stated by Price [92], this could be resolved through the usage of an intelligent switch, like that given by Cullen and Dehnen [96]. It is also noted that the use of artificial viscosity could be avoided altogether if the SPH method was reformulated to be compatible with a Riemann solver, as was done by Inutsuka [97]. This work was recently developed further by Sugiura and Inutsuka [98] so as to be applicable to elastic dynamics. However, their method does not yet exactly conserve angular momentum, as they do not modify the gradient of the kernel.

Although the artificial viscosity term is highly effective in problems involving shock, it is not a solution to the tensile instability that arises in problems using an Eulerian kernel. This is commonly addressed through the use of another artificial term, artificial stress.

3.3 Artificial stress

Less than two decades ago, an attempt was first made by Monaghan [29] to control the tensile instability for two-dimensional problems. Monaghan introduced an artificial stress term to the inviscid momentum equation of particles that experienced a tensile stress. This was determined by checking the signs of the particles' pressures. Gray el al. [30], who considered Cauchy stress tensors, improved this method by transforming the stresses to their principal coordinates. This ensured that the artificial repulsive term was only added to the tensile components of stress tensors. The methodology developed by Gray and Monaghan begins with first rotating a particle's stress term to its principal axes. This first requires the particle's principal stress angle θ_a, which in two dimensions is given by

$$\tan(2\theta_a) = \frac{2\sigma_a^{\text{xy}}}{\sigma_a^{\text{xx}} - \sigma_a^{\text{yy}}} . \tag{3.11}$$

Note that the superscripts denote the components of the two-dimensional Cauchy stress tensor. The principal components can be calculated using $\boldsymbol{\sigma}_{a,\text{p}} = \mathbf{Q}_a \boldsymbol{\sigma}_a \mathbf{Q}_a^{\mathsf{T}}$, where $\boldsymbol{\sigma}_{a,\text{p}}$ are the principal stresses and $\mathbf{Q}_a$ is the matrix which rotates a particle's Cauchy stress tensor to its principal axes, and is given by

$$\mathbf{Q}_a = \begin{bmatrix} \cos\theta_a & \sin\theta_a \\ -\sin\theta_a & \cos\theta_a \end{bmatrix} .$$

Alternatively, the principal components could be calculated directly, as done by Gray el al. [30], using

$$\sigma_{a,\text{p}}^{\text{xx}} = \sigma_a^{\text{xx}} \cos^2\theta_a + \sigma_a^{\text{yy}} \sin^2\theta_a + 2\sigma_a^{\text{xy}} \sin\theta_a \cos\theta_a \tag{3.12}$$

and

$$\sigma_{a,\text{p}}^{\text{yy}} = \sigma_a^{\text{xx}} \sin^2\theta_a + \sigma_a^{\text{yy}} \cos^2\theta_a - 2\sigma_a^{\text{xy}} \sin\theta_a \cos\theta_a . \tag{3.13}$$

The off-diagonal components of the principal stresses are, by definition, zero and hence $\sigma_a^{\text{xy}} = \sigma_a^{\text{yx}} = 0$. Gray et al. stated that if either of the principal components of the stress tensor are tensile, which is

denoted by a positive or a negative sign depending on the convention chosen, then that component is modified such that

$$\mathbf{R}_{a,\mathrm{p}} = \begin{cases} R^{\mathrm{xx}}_{a,\mathrm{p}} = -\epsilon_{as}\dfrac{\sigma^{\mathrm{xx}}_{a,p}}{\rho^2} & \text{if } \sigma^{\mathrm{xx}}_{a,\mathrm{p}} \text{ is tensile} \\ R^{\mathrm{yy}}_{a,\mathrm{p}} = -\epsilon_{as}\dfrac{\sigma^{\mathrm{yy}}_{a,p}}{\rho^2} & \text{if } \sigma^{\mathrm{yy}}_{a,\mathrm{p}} \text{ is tensile} \\ R^{\mathrm{xy}}_{a,\mathrm{p}} = 0 \end{cases}, \tag{3.14}$$

otherwise that component is set to zero. The parameter ϵ_{as} in the above is commonly set to ≈ 0.3. The modified principal stress tensor $\mathbf{R}_{a,\mathrm{p}}$ is then rotated back to the original coordinates either using $\mathbf{R}_a = \mathbf{Q}_a^{\mathsf{T}}\mathbf{R}_{a,\mathrm{p}}\mathbf{Q}_a$ or by following Gray et al. as

$$R^{\mathrm{xx}}_a = R^{\mathrm{xx}}_{a,\mathrm{p}}\cos^2\theta_a + R^{\mathrm{yy}}_{a,\mathrm{p}}\sin^2\theta_a\,, \tag{3.15}$$

$$R^{\mathrm{yy}}_a = R^{\mathrm{xx}}_{a,\mathrm{p}}\sin^2\theta_a + R^{\mathrm{yy}}_{a,\mathrm{p}}\cos^2\theta_a \tag{3.16}$$

and

$$R^{\mathrm{xy}}_a = \sin\theta_a\cos\theta_a(R^{\mathrm{xx}}_{a,\mathrm{p}} - R^{\mathrm{yy}}_{a,\mathrm{p}})\,. \tag{3.17}$$

Gray et al. [30] included this artificial stress term in the momentum equation summation as

$$\frac{\mathrm{d}\mathbf{v}_a}{\mathrm{d}t} = -\sum_{b=1}^{N} m_b\left(\frac{\boldsymbol{\sigma}_a}{\rho_a^2} + \frac{\boldsymbol{\sigma}_b}{\rho_b^2} + \mathbf{R}_{ab}f_{ab}^{n_{\mathrm{as}}}\right)\nabla_b W_{ba}\,, \tag{3.18}$$

where

$$\mathbf{R}_{ab} = (\mathbf{R}_a + \mathbf{R}_b) \tag{3.19}$$

and

$$f_{ab} = \frac{W_{ab}}{W(\Delta p)}\,. \tag{3.20}$$

In the equations above Δp is the average particle spacing and n_{as} is a factor which controls the magnitude of the artificial stress [29].

The artificial stress term is modified to account for mixed correction in a similar fashion to the artificial viscosity term as

$$\left(\frac{\mathrm{d}\mathbf{v}_a}{\mathrm{d}t}\right)_{\mathrm{stress}} = -\sum_{b=1}^{N}\frac{m_b f_{ab}^{n_{\mathrm{as}}}}{2}\left(\mathbf{R}_b\widetilde{\nabla}_b\widetilde{W}_{ba} - \mathbf{R}_a\widetilde{\nabla}_a\widetilde{W}_{ab}\right). \tag{3.21}$$

If not considering mixed correction the above reduces back to the conventional artificial stress implementation. Although this was found to be compatible with the Eulerian formulation, it was not successful for the first coupling method. In this coupling method, Eulerian particles included the artificial stress term in their conservation of momentum equations and the Total Lagrangian particles, which were not in the interface, did not. As detailed in Section 2.6, the Total Lagrangian particles in the interface, which have Eulerian and Total Lagrangian particles as neighbours, use both a Total Lagrangian and Eulerian conservation of momentum equation. The former was implemented with their Total Lagrangian neighbours and the latter was implemented with their Eulerian neighbours. As a result, they too required an artificial stress term to be included in the summations that involved Eulerian particles. This term was also required to ensure the conservation of linear momentum. This implementation was not successful as an instability was found to manifest at the interface. Consequently, artificial stress could not be used to suppress the tensile instability if using the first

coupling method. Section 4.6 demonstrates the effectiveness of the mixed correction form of artificial stress when applied to an Eulerian formulation and the instability that arises in the first coupling method. Note that the artificial stress was found to be compatible with the second coupling method. This is discussed in more detail in Section 4.6.

The principal components of the Cauchy stress tensor are used to determine the value of the artificial stress, though the calculation of the Cauchy stress tensor itself has only been partially described. Chapter 2 gave a description of how the rate of change of the deviatoric stress was found. The isotropic pressure component was given by an elastic equation of state, which is not appropriate in all scenarios. The selection of an appropriate equation of state is discussed in the following section.

3.4 Equation of state

Zel'dovich and Raizer [99] state that the pressure in a solid material is comprised of two parts: an elastic component and a thermal component. The thermal component can be further divided into the thermal motion of atoms and the thermal excitation of electrons. The elastic component is solely dependent on density and is independent of temperature. Three equations of state are described in this section. The first is the most common elastic equation of state, which only depends on the sound speed and the change in density. The following two equations of state are variations of the Mie-Gruneisen equation of state. These are appropriate for problems involving shock and take into account both the elastic and thermal component of pressure.

3.4.1 Elastic equation of state

Gray et al. [30], Chakraborty and Shaw [48] and Das and Cleary [79] implemented an equation of state for solid mechanics in the form of

$$p(\rho) = c_0^2(\rho - \rho_0) \, . \tag{3.22}$$

These authors gave the speed of sound as $c = \sqrt{K/\rho}$, where K is the bulk modulus of the material. Woan [100] gave $\sqrt{K/\rho}$ as the speed of sound in a fluid. This author gave the speeds of sound in an infinite isotropic solid as

$$c_\mathrm{t} = \sqrt{\frac{G}{\rho}} \tag{3.23}$$

and

$$c_\mathrm{l} = \sqrt{\frac{E(1-\nu)}{\rho(1+\nu)(1-2\nu)}} \, , \tag{3.24}$$

where ν is the Poisson's ratio of the material, c_t is the transverse or shear wave speed and c_l is the longitudinal or pressure wave speed. The longitudinal wave speed is considered in the linear equation

of state as it is found to be larger than the transverse wave speed. Woan [100] stated the longitudinal wave speed in a thin plate as

$$c_\mathrm{l} = \sqrt{\frac{E}{\rho(1+\nu^2)}} \tag{3.25}$$

and in a thin circular rod as

$$c_\mathrm{l} = \sqrt{\frac{G}{\rho}} \,. \tag{3.26}$$

These correspond to the speeds of sound used in two-dimensional plane stress and one-dimensional simulations, respectively.

3.4.2 Mie-Gruneisen equations of state

Following Bonet and Kulasegaram [33], Libersky et al. [47] and Randles et al. [101], pressure is modelled as a function of both density ρ and specific internal energy e using the Mie-Gruneisen equation of state for solids. This follows the form of

$$p(\rho, e) = \left(1 - \frac{1}{2}\Gamma\eta\right) p_\mathrm{H}(\rho) + \Gamma\rho e \,, \tag{3.27}$$

where $p_\mathrm{H}(\rho)$ refers to the pressure calculated with reference to the Hugoniot curve, η represents compression and is given by $\eta = \rho/\rho_0 - 1$, and Γ is the Gruneisen parameter. The pressure calculated using the Hugoniot curve is given by

$$p_\mathrm{H} = \begin{cases} \dfrac{c^2\eta(1+\eta)}{\left[1-(s_s-1)\eta\right]^2} & \text{if } \eta > 0 \\ \rho_0 c^2 \eta & \text{if } \eta < 0 \end{cases} \,, \tag{3.28}$$

where s_s is the slope of the linear shock velocity u_s and particle velocity u_p equation given by

$$u_\mathrm{s} = c + s_\mathrm{s} u_\mathrm{p} \,. \tag{3.29}$$

An alternative form of the Mie-Gruneisen equation of state presumes a cubic relationship between the shock velocity and the particle velocity [1, 102]. In this case, the pressure is calculated, depending on whether the material is compressed or expanded, as

$$p(\rho, e) = \begin{cases} \dfrac{\rho_0 c^2 \eta \left[1 + \left(1 - \frac{\gamma_0}{2}\right)\eta - \frac{a_\mathrm{mg}}{2}\eta^2\right]}{\left[1 - (s_1 - 1)\eta - s_2 \frac{\eta^2}{\eta+1} - s_3 \frac{\eta^3}{(\eta+1)^2}\right]} + (\gamma_0 + a_\mathrm{mg}\eta)e & \text{if } \eta > 0 \\ \rho_0 c^2 \eta + (\gamma_0 + a_\mathrm{mg}\eta)e & \text{if } \eta < 0 \end{cases} \,. \tag{3.30}$$

In the above s_1, s_2 and s_3 are the coefficients of the cubic shock velocity and particle velocity relationship, γ_0 is the Gruneisen coefficient and a_mg is a volume correction coefficient. Other variables are the same as for the linear Hugoniot form of the Mie-Gruneisen equation.

These three equations of state provide the isotropic pressure component of the Cauchy stress tensor. This Cauchy stress tensor must be inspected and modified in order to incorporate plasticity, as discussed in the following section.

3.5 Plasticity models and implementation

In Chapter 2, linear elasticity was assumed in the derivations of the Eulerian and Total Lagrangian momentum equations. It was stated that the pressure component was calculated through an equation of state and the unobjective deviatoric stress rate was given by $2G\mathbf{D}'$, which assumes linear elasticity. In order to model both plasticity and fracture, additional models are required. In this section, three models [102] are detailed including an elastic-perfectly plastic model, an elastic-plastic isotropic hardening model and the Johnson-Cook model. Each of these models must be calculated on a particle basis.

3.5.1 Elastic-perfectly plastic model

The elastic-perfectly plastic model assumes that the stress cannot exceed the yield surface. The von Mises yield criterion is used, which defines the yield surface as a cylinder with radius $\sqrt{2/3}\sigma_y$, where σ_y is the yield strength of the material. Whether the stress state has exceeded the yield surface is checked using the von Mises stress σ_{vm}. This gives a scalar quantity with which the stress tensor can be evaluated. In terms of general stress components, the von Mises stress is given by

$$\sigma_{\text{vm}} = \sqrt{\frac{1}{2}\left[(\sigma_{\text{xx}} - \sigma_{\text{yy}})^2 + (\sigma_{\text{yy}} - \sigma_{\text{zz}})^2 + (\sigma_{\text{zz}} - \sigma_{\text{xx}})^2 + 6(\sigma_{\text{xy}}^2 + \sigma_{\text{yz}}^2 + \sigma_{\text{zx}}^2)\right]} \,. \tag{3.31}$$

The Cauchy stress tensor is first updated elastically, giving a trial stress $\boldsymbol{\sigma}_{\text{tr}}$. The von Mises stress is then calculated. If it is found to exceed the yield strength then the deviatoric components of the trial stress tensor are scaled back to the yield surface such that

$$\boldsymbol{\sigma}' = \boldsymbol{\sigma}'_{\text{tr}} \frac{\sigma_{\text{y}}}{\sigma_{\text{vm}}} \,, \tag{3.32}$$

followed by an update to the Cauchy stress tensor of $\boldsymbol{\sigma} = \boldsymbol{\sigma}' - p\mathbf{I}$. Next, the increment in equivalent plastic strain can be calculated by

$$\Delta\bar{\epsilon}_{\text{p}} = \frac{\sigma_{\text{vm}} - \sigma_{\text{y}}}{3G} \,. \tag{3.33}$$

Lastly, the total equivalent plastic strain is updated through

$$\bar{\epsilon}_{\text{p}} = \bar{\epsilon}_{\text{p}} + \Delta\bar{\epsilon}_{\text{p}} \,. \tag{3.34}$$

3.5.2 Elastic-plastic isotropic hardening

In this model, the yield surface expands once the von Mises stress exceeds the yield strength. The plastic hardening modulus E_{p} determines the relationship between the stress and strain after yielding. As for the elastic-perfectly plastic model, first the von Mises stress is calculated using Equation 3.31. If this exceeds the yield strength then the increment in equivalent plastic strain is calculated using

$$\Delta\bar{\epsilon}_{\text{p}} = \frac{\sigma_{\text{vm}} - \sigma_{y}}{3G + E_{\text{p}}} \,. \tag{3.35}$$

The total equivalent plastic strain is updated using Equation 3.34. Following this, the yield strength is updated by

$$\sigma_{\text{y}} = \sigma_{\text{y}} + E_{\text{p}}\Delta\bar{\epsilon}_{\text{p}} \tag{3.36}$$

and the deviatoric stresses are scaled back to the new yield surface using Equation 3.32. Lastly, the Cauchy stress tensor is updated using $\boldsymbol{\sigma} = \boldsymbol{\sigma}' - p\mathbf{I}$.

3.5.3 Johnson-Cook plasticity

The Johnson-Cook plasticity model [103] is used to determine the current position of the yield surface. It is given by

$$\sigma_y = [A_{JC} + B_{JC}\bar{\epsilon}_p^{N_{JC}}]\left[1 + C_{JC}\ln\left(\frac{\dot{\bar{\epsilon}}_p}{\dot{\epsilon}_0}\right)\right]\left[1 - \left(\frac{T - T_r}{T_m - T_r}\right)^{M_{JC}}\right], \tag{3.37}$$

where A_{JC}, B_{JC}, C_{JC}, $\dot{\epsilon}_0$, M_{JC} and N_{JC} are material specific constants. T_r is the ambient (room) temperature and T_m is the melting temperature of the material. As this is a nonlinear equation, it can be solved incrementally. Noting that the yield surface can be generalised to

$$\sigma_y(\bar{\epsilon}_p + \Delta\bar{\epsilon}_p, \Delta\bar{\epsilon}_p/\Delta t, T + \Delta T...) = \sigma_{vm} - 3G\Delta\bar{\epsilon}_p\,, \tag{3.38}$$

and combining this with Equation 3.37 leads to

$$\sigma_{vm} - 3G\Delta\bar{\epsilon}_p = \left[A_{JC} + B_{JC}\left(\bar{\epsilon}_p + \Delta\bar{\epsilon}_p\right)^{N_{JC}}\right]\left[1 + C_{JC}\ln\left(\frac{\Delta\bar{\epsilon}_p}{\dot{\epsilon}_0\Delta t}\right)\right]\left[1 - \left(\frac{T + \Delta T - T_r}{T_m - T_r}\right)^{M_{JC}}\right]. \tag{3.39}$$

In the above, T has been replaced with $T + \Delta T$, as the temperature may be a function of stress and strain. Rabczuk [57], who assumed that all plastic deformation was converted into heat, is followed. Therefore, ΔT is approximated by

$$\Delta T = \frac{\sigma_y\Delta\bar{\epsilon}_p}{\rho C_v}\,, \tag{3.40}$$

where C_v is the specific heat capacity of the material. Substituting this into Equation 3.39 gives the following equation which can be solved iteratively for the increment in equivalent plastic strain $\Delta\bar{\epsilon}_p$:

$$\sigma_{vm} - 3G\Delta\bar{\epsilon}_p = \left[A_{JC} + B_{JC}\left(\bar{\epsilon}_p + \Delta\bar{\epsilon}_p\right)^{N_{JC}}\right]\left[1 + C_{JC}\ln\left(\frac{\Delta\bar{\epsilon}_p}{\dot{\epsilon}_0\Delta t}\right)\right]\left[1 - \left(\frac{T + \frac{\sigma_y\Delta\bar{\epsilon}_p}{\rho C_v} - T_r}{T_m - T_r}\right)^{M_{JC}}\right]. \tag{3.41}$$

An algorithm[2] based on that presented by Forsythe et al. [104] is used to solve this equation. Other root-finding algorithms, such as the Newton–Raphson method, could similarly be used.

These plasticity models do not place any limits on the plastic strain. A material simulated using these models will continue to deform plastically after a real material would have failed. Additional damage models are required in order to capture this material failure.

3.6 Damage models and implementation

Three damage models are described including the Rankine model, the Lemaitre model and the Johnson-Cook model. In the Rankine model, once a particle reaches some pre-defined damage

[2]This algorithm is also the basis for the Matlab `fzero` function.

criterion, it loses the ability to support tensile loads. The Lemaitre model continuously degrades the Cauchy stress tensor using a function that is dependent on material specific constants and the equivalent strain. The Johnson-Cook damage model can be used in addition to the Johnson-Cook plasticity model. It is written as a function of temperature, pressure, strain and strain rate. In addition to these damage models, an approach for converting particle kernel types is given. This allows fracture to be modelled using a Total Lagrangian formulation, which adaptively converts to Eulerian kernels where and when required.

3.6.1 Rankine damage model

It is not uncommon to implement the Rankine damage model in SPH due to its simplicity and effectiveness [48, 53, 55, 56, 59, 95]. The basis of this model is that damage initiates once a tensile principal stress component exceeds some multiple of the tensile strength of the material. Following both Das and Cleary [53] and Raymond et al. [95], once a particle has met the Rankine criterion, its principal tensile stress components are set to zero for the remainder of the simulation, reflecting its inability to support tensile loads. Afterwards, the principal stresses are rotated back to the original coordinates.

As shown in Section 3.3, it is trivial to calculate the rotation matrix necessary to find the principal stresses in two dimensions. This becomes less so in three dimensions and requires the calculation of eigenvalues and eigenvectors. This is achieved using the algorithms presented by Kopp [105]. More specifically, his Jacobi algorithm `DSYEVJ3` is used due to its accuracy and speed for real, symmetric matrices. The algorithm `DSYEV2` is used for two-dimensional problems for convenience. Once the principal stresses are found using Kopp's algorithm, they are modified and then rotated back to their original axis using

$$\boldsymbol{\sigma} = \mathbf{V}\boldsymbol{\sigma}_{\mathrm{p}}\mathbf{V}^{\mathsf{T}} \,, \tag{3.42}$$

where $\mathbf{V}$ is the matrix of eigenvectors organised into columns and $\boldsymbol{\sigma}_{\mathrm{p}}$ is the diagonal matrix of eigenvalues or principal stresses. As the Cauchy stress tensor is symmetric, its eigenvectors are orthogonal and, as a result, $\mathbf{V}^{\mathsf{T}} = \mathbf{V}^{-1}$. Although the selection of the inverse or the transpose has no impact on the Rankine model, the transpose was found to be preferable for situations where $\boldsymbol{\sigma} \approx \boldsymbol{\sigma}_{\mathrm{p}}$ due to the small numbers involved.

3.6.2 Lemaitre damage model

The Lemaitre damage model [106] alters the stress-strain relationship such that

$$\boldsymbol{\sigma} = (1 - D)\mathbf{C} : \boldsymbol{\epsilon}, \tag{3.43}$$

where $\mathbf{C}$ is the fourth order elasticity tensor which relates stresses to strains and D represents a particle's current level of damage. This damage is a scalar value that varies between zero and one, unlike the Rankine model where damage is binary. Following Rabczuk et al. [56, 57] the damage can be written in terms of the equivalent strain as

$$D(\bar{\epsilon}) = 1 - (1 - A_{\mathrm{L}})\frac{\epsilon_{\mathrm{D}_0}}{\bar{\epsilon}} - A_{\mathrm{L}} \exp[-B_{\mathrm{L}}(\bar{\epsilon} - \epsilon_{\mathrm{D}_0})] \,, \tag{3.44}$$

where A_L, B_L and ϵ_{D_0} are material specific constants and $\bar{\epsilon}$ is the equivalent strain. The strain is calculated incrementally, in a similar fashion to the total equivalent plastic strain in Equation 3.34, as

$$\boldsymbol{\epsilon} = \boldsymbol{\epsilon} + \mathbf{D}\mathrm{d}t \ , \tag{3.45}$$

where $\mathbf{D}$ is the rate of deformation tensor given by Equation 2.54. The equivalent strain is then given by [102]

$$\bar{\epsilon} = \sqrt{\frac{2}{3}\boldsymbol{\epsilon}' : \boldsymbol{\epsilon}'} \ . \tag{3.46}$$

3.6.3 Johnson-Cook damage model

Johnson et al. [107] developed a damage model to accompany their plasticity model, as described in Section 3.5.3. This damage model defines a strain at fracture as a function of pressure, effective stress, effective plastic strain rate and temperature as

$$\epsilon_f = \left[D_1 + D_2 \exp\left(D_3 \frac{-p}{\sigma_{vm}}\right)\right]\left[1 + D_4 \ln\left(\frac{\dot{\bar{\epsilon}}}{\dot{\epsilon}_0}\right)\right]\left[1 + D_5\left(\frac{T - T_r}{T_m - T_r}\right)\right] \ . \tag{3.47}$$

The term $-p/\sigma_{vm}$ is known as the stress triaxiality and is defined as the division of the hydrostatic stress with the von Mises stress [108]. The terms D_1, D_2, D_3, D_4 and D_5 are material specific constants and the remaining variables are the same as for the Johnson-Cook plasticity model given in Equation 3.37. Damage is defined as the accumulation of the effective plastic strain increments over the corresponding strain at fracture:

$$D = \sum \frac{\Delta\bar{\epsilon}_p}{\epsilon_f} \ . \tag{3.48}$$

Fracture occurs once the damage parameter $D = 1$. If using the Johnson-Cook damage model, fracture can be modelled using a number of approaches. In this work, the following particle kernel type conversion is suggested.

3.6.4 Particle kernel type conversion

The numerical examples presented in Chapter 4 involve problems where particles convert from Total Lagrangian kernel types to Eulerian kernel types. Although the conversion from Eulerian to Total Lagrangian kernel types may be possible, it is speculated that this would involve updating the reference configuration. Vidal et al. [35] showed how updating the reference configuration may excite mechanisms which spoil the solution unless controlled with a stabilization technique. This conversion from Eulerian to Total Lagrangian kernel types was not explored in more detail as it was only seen to be beneficial to scenarios where distorted particles reach a more regular and constant spatial arrangement. The opposite tends of occur in problems involving elastic dynamics and fracture.

The conversion from the Total Lagrangian kernel type to the Eulerian kernel type is theoretically trivial. Once converted to an Eulerian kernel, a particle swaps from the Total Lagrangian conservation equations (Equation 2.121) to the Eulerian conservation equations (Equation 2.120). It is assumed that it is only desirable for a particle to convert kernel type if it has reached some deformation or damage criteria. In the PhD thesis by Reveles [109], once a Total Lagrangian particle reaches a fracture criterion, "*the variable values at the particles are set to zero and they no longer contribute in the* [SPH] *interpolation*". According to de Vuyst and Vignjevic [54], who modelled fracture using the Total Lagrangian method, "*it is not sufficient to simply set the stress of a failed particle to zero and to*

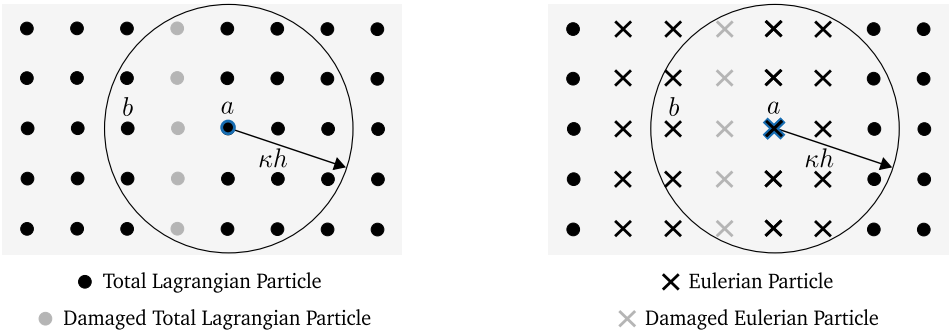

Figure 3.1: The left hand-side image highlights how a particle a can be influenced by another particle b across a fracture path due to the range of the support domain. If using a Total Lagrangian kernel, particles a and b will continue to influence each other unless the reference configuration is updated. The right hand-side image displays damaged particles and their neighbours converting kernel types. Once displaced, the support domains will no longer overlap.

remove it from the neighbour lists". These authors explain that a particle may have a support domain that encompasses both fractured particles and additional particles on the other side of the fracture line. They state that, in this case, the stress state becomes non-physical. An example of this is displayed in the left hand-side image in Figure 3.1. In this image particles a and b are located on either side of damaged particles. Regardless, particle a uses particle b within its summations and will continue to do so as these particles were neighbours in the reference configuration. In order to prevent particles interpolating across fracture lines, or the creation of non-physical deformation gradients, once a particle fractures it converts kernel type along with its neighbours. This is highlighted by the right hand-side image presented in Figure 3.1. Using this approach, the Eulerian particles will separate until the support domains no longer overlap. A further benefit to this approach is that no particles need to be removed from neighbour lists or have their field variables set to zero. The effectiveness of this approach is demonstrated in Section 4.12

The conversion of particles from one kernel type to another not only influences the formulation followed but also impacts upon how boundaries are treated. As the Total Lagrangian formulation depends on the initial configuration whilst the Eulerian formulation depends on the current configuration, a number of modifications are required.

3.7 Boundary conditions

As discussed in Chapter 2, if a particle has an incomplete support domain the SPH integral is truncated, which results in inaccuracies. This can be alleviated either by using correction techniques or by populating the support domain.

The semi-analytical boundary method [110–116] attempts to restore the neglected surface integral term from Equation 2.12. It has been used to model flow accurately next to solid boundaries. Using this method, the SPH gradient approximations are dependent on some wall renormalisation factor. They further include a second summation which takes the surface integral into account and requires an outwards facing normal from the boundary. The wall renormalisation factor can be calculated through an analytical formula in two dimensions [115] and through a dynamic governing

equation in three dimensions [112]. This method further requires vertex or boundary particles that define boundary segments that are used to define the outward facing normal. The gradient of the wall renormalisation factor is also required which tends to be calculated through an analytical formula [112, 114]. Although effective, this method is still in development due to instabilities that have been observed for high Reynolds number three-dimensional flows [116]. Due to the nature of problems explored in this thesis and the additional complexity of the method, the semi-analytical boundary method was not explored.

In this section, the ghost particle methodology is explored along with the special treatment required if using mixed correction or a coupled formulation. These ghost particles not only remove boundary effects but also are capable of enforcing symmetry planes. Having discussed displacement and velocity boundary conditions, a contact algorithm is described. This contact algorithm is required for bodies comprised of Total Lagrangian particles to transfer momentum.

3.7.1 Ghost particles for symmetry planes

Special treatment is required to enforce boundary conditions when standard SPH is applied to conventional fluid dynamics problems. This treatment is required both to rectify the truncated integrals found at boundaries and to prevent particle penetration of the boundary itself. Both problems are commonly solved using ghost SPH particles. Libersky et al. [47] applied ghost particles when modelling the Taylor impact test in order to create three symmetry planes, one for the rigid surface and two for modelling a quarter of the cylindrical impactor. Monaghan [117] first used ghost particles to model a rigid boundary by adding a Lennard-Jones type repulsive force between ghost and real particles. The general principal behind these ghost particles, when used to rectify integrals, is that they are generated once a particle's smoothing length extends beyond the boundary. The ghost particle then derives its properties from the particle that generated it, now referred to as a parent, such that it reproduces the correct boundary condition. For example, in order to reproduce a stationary boundary, the parent particle's mass, density and pressure would be copied to the ghost particle and its position and velocity would be reflected. These ghost particles contribute to the SPH particle summations but they themselves are not updated. These ghost particles derive their properties from their parents. For curved boundaries, ghost particles can be generated by using a local tangent plane to the boundary, as suggested by Colagrossi et al. [118]. In this case, these authors suggest that corrections may be required to ensure that the mass of ghost particles is not too large, as this would presumably result in an overestimation of density at the boundary.

As the mixed correction formulation is applied to solid mechanics problems, truncated integrals and penetration at boundaries are of a lesser concern. Symmetry planes are of interest due to the reduction in simulation time. The algorithm presented in Gourma's PhD thesis [119] was recreated as it was found to be conceptually simple and straightforward to implement. The premise of this algorithm is that a particle may generate a ghost particle at any point on a cubic lattice structure in three dimensions (which corresponds to 26 positions) if considering the generating particle at the centre of this structure as displayed in Figure 3.2. The number of ghost particles generated depends on the number of boundary planes that the generating particle's support domain intersects. The possible intersection combinations are presented in Figure 3.3. If a particle intersects with one boundary plane, it will generate one ghost particle. If it intersects two boundary planes, it will generate three ghost particles comprised of (i) two single plane interaction ghosts and (ii) one double plane intersection ghost. If a particle intersects three boundary planes, it will generate seven ghost particles. This can be visualised by considering the particles located on the corners the sub-cube

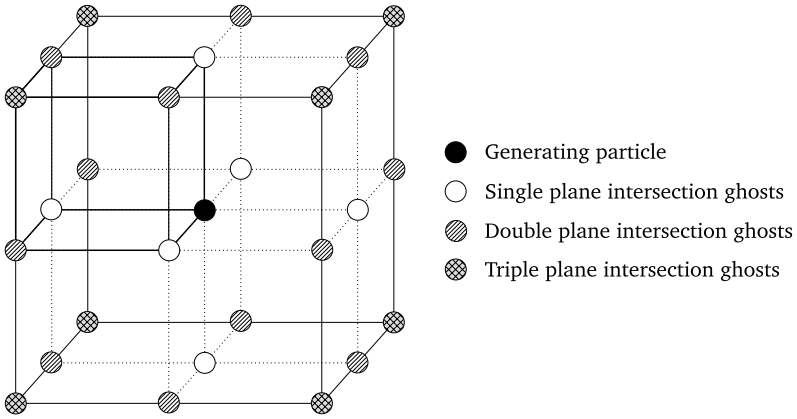

Figure 3.2: The order in which ghost particles are generated as determined by the number of boundary planes that are intersected by the generating particle's smoothing length.

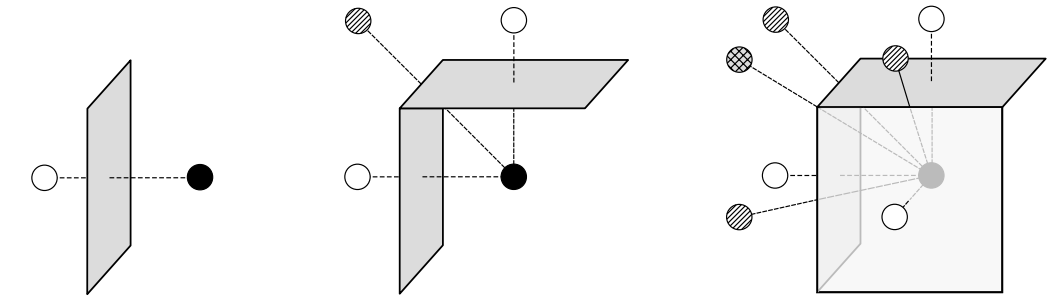

Figure 3.3: The three possible modes of ghost particle generation though particle support domain truncation with either one (left), two (middle) or three (right) boundary planes.

highlighted in Figure 3.2 or the third pane in Figure 3.3. These particles consist of (i) three single plane interaction ghosts and (ii) three double plane intersection ghosts and (iii) one triple plane intersection ghost. Consequently, a particle can generate one, three or seven ghost particles. By using this restriction, the position of a ghost particle can therefore be reduced to an affine transformation built of a rotation and a translation such that

$$\mathbf{x}_\mathrm{g} = \mathbf{r}_\mathrm{g} \circ \mathbf{x}_\mathrm{i} + \mathbf{t}_\mathrm{g} \ , \tag{3.49}$$

where $\mathbf{x}_\mathrm{g}$ is the position of the ghost particle, $\mathbf{x}_\mathrm{i}$ is the position of the parent particle, which is multiplied component-wise with $\mathbf{r}_\mathrm{g} = [r_{\mathrm{g,x}}\ r_{\mathrm{g,y}}\ r_{\mathrm{g,z}}]^\mathsf{T}$ the rotation vector, and $\mathbf{t}_\mathrm{g} = [t_{\mathrm{g,x}}\ t_{\mathrm{g,y}}\ t_{\mathrm{g,z}}]^\mathsf{T}$ is the translation vector corresponding to that ghost particle. Note that the definitions of $\mathbf{r}_\mathrm{g}$ and $\mathbf{t}_\mathrm{g}$ are explained in a later paragraph. This transformation can be seen as a specific case of the generalized affine 4×4 transformation matrix [120] with no shear, unity scaling, rotations of 1 or -1, and a last column of $[0\ 0\ 0\ 1]^\mathsf{T}$ due to the affineness of the transformation.

The velocity of the ghost particle is given by

$$\mathbf{v}_\mathrm{g} = \mathbf{r}_\mathrm{g} \circ \mathbf{v}_\mathrm{i} \ . \tag{3.50}$$

This can be seen as a simplified case of reflecting the velocity through boundaries by inspecting the tangential and normal components, as done by Das and Cleary [79]. In order to determine the number of ghost particles to be generated and the position of these ghost particles, a look-up table is used as given by Gourma [119]. The look-up table is given in Table 3.1 and lists all 26 possible generation combinations, referred to as flags 1 through 26, which are dependent on the number of planes intersected. Each of these flags can result in the generation of 1, 3 or 7 ghost particles, as listed in the look-up table. The boundary planes are given by x^+, x^-, y^+, y^-, z^+, z^-, where the negative denotes a minimum and the positive a maximum. These planes form a cuboid. Note that an amended version of the look-up table is given here rather than referring the reader to the original source as it is believed to contain typos. Although this look-up table gives the number of ghost particles to be generated depending on the planes intersected, it does not give any indication of what the corresponding positions and field variable values should be. Instead a series of secondary look-up tables are used which give the translation indices $t'_{\mathrm{g,x}}$, $t'_{\mathrm{g,y}}$, $t'_{\mathrm{g,z}}$ and rotations $\mathbf{r}_\mathrm{g} = [r_{\mathrm{g,x}}\ r_{\mathrm{g,y}}\ r_{\mathrm{g,z}}]^\mathsf{T}$ for each ghost particle to be generated. Six secondary look-up tables are given by Gourma [119]. A table is required for each dimension, resulting in three translation index look-up tables and three rotation look-up tables. These values are then used in Equations 3.49 and 3.50. The amended look-up tables are repeated here, in Tables 3.2 and 3.3 rather than referring the reader to Gourma. The translation index $t'_{\mathrm{g,x}}$ is converted into the translation $t_{\mathrm{g,x}}$ by

$$t_{g,\mathrm{x}} = \begin{cases} 2x^+ & \text{if } t'_{\mathrm{g,x}} = 1 \\ 2x^- & \text{if } t'_{\mathrm{g,x}} = -1 \\ 0 & \text{if } t'_{\mathrm{g,x}} = 0 \end{cases} \ . \tag{3.51}$$

The $t_{\mathrm{g,y}}$ and $t_{\mathrm{g,z}}$ translations are found by swapping y and z, respectively, with x in Equation 3.51. These are then inserted into the transformation vector $\mathbf{t}_\mathrm{g} = [t_{\mathrm{g,x}}\ t_{\mathrm{g,y}}\ t_{\mathrm{g,z}}]^\mathsf{T}$.

Matrices, such as stress tensors can similarly be reflected using a transformation:

$$\boldsymbol{\sigma}_\mathrm{g} = \mathbf{R}_\mathrm{g} \circ \boldsymbol{\sigma}_\mathrm{i} \ , \tag{3.52}$$

Table 3.1: Ghost particle generation look-up table, flags 1 through 26. This table gives the number of ghosts to be generated depending on the the combination of boundary planes intersected ($x^+, x^-, y^+, y^-, z^+, z^-$). Each of the 26 possible combinations is denoted by a flag index.

Flag:	0	1	2	3	4	5	6	7	8
No. Ghosts:	0	1	1	1	3	3	1	3	3
Plane 1:		x^-	x^+		x^-	x^+		x^-	x^+
Plane 2:				y^-	y^-	y^-	y^+	y^+	y^+

Flag:	9	10	11	12	13	14	15	16	17
No. Ghosts:	1	3	3	3	7	7	3	7	7
Plane 1:		x^-	x^+		x^-	x^+		x^-	x^+
Plane 2:				y^-	y^-	y^-	y^+	y^+	y^+
Plane 3:	z^-	z^-	z^-	z^-	z^-	z^-	z^-	z^-	z^-

Flag:	18	19	20	21	22	23	24	25	26
No. Ghosts:	1	3	3	3	7	7	3	7	7
Plane 1:		x^-	x^+		x^-	x^+		x^-	x^+
Plane 2:				y^-	y^-	y^-	y^+	y^+	y^+
Plane 3:	z^+	z^+	z^+	z^+	z^+	z^+	z^+	z^+	z^+

where in this case $\mathbf{R}_\mathrm{g}$ is a rotation matrix which is multiplied element-wise with the parent stress tensor. Considering the restrictions placed on the locations of ghost particles, it is known that the transformation for matrices should have diagonal components of unity and a value of negative one for the off-diagonal components. The exception to this is for single plane interaction ghosts, in which case the off-diagonal components of the transformation, which do not share an index with the boundary that is intersected, must be a positive one. This transformation can be built using the rotational values given in Table 3.2. This is achieved by noting that if the sum of two rotational values (for the same flag and ghost particle) in any two planes is equal to two, then that ghost particle is a single plane interaction ghost of the third plane. This can be illustrated using an example by considering flag 16, ghost particle 3. When inspecting Table 3.2 it can be seen that $r_{\mathrm{g,x}} = -1$, $r_{\mathrm{g,y}} = 1$ and $r_{\mathrm{g,z}} = 1$, which indicates that this ghost particle is a single plane interaction ghost and will be mirrored through either the maximum or minimum x boundary plane with no change in the y or z coordinate. Using the rules previously discussed

$$\boldsymbol{\sigma}_\mathrm{g} = \mathbf{R}_\mathrm{g} \circ \boldsymbol{\sigma}_\mathrm{i} = \begin{bmatrix} 1 & -1 & -1 \\ -1 & 1 & 1 \\ -1 & 1 & 1 \end{bmatrix} \circ \begin{bmatrix} \sigma_{\mathrm{xx}} & \sigma_{\mathrm{xy}} & \sigma_{\mathrm{xz}} \\ \sigma_{\mathrm{yx}} & \sigma_{\mathrm{yy}} & \sigma_{\mathrm{yz}} \\ \sigma_{\mathrm{zx}} & \sigma_{\mathrm{zy}} & \sigma_{\mathrm{zz}} \end{bmatrix} = \begin{bmatrix} \sigma_{\mathrm{xx}} & -\sigma_{\mathrm{xy}} & -\sigma_{\mathrm{xz}} \\ -\sigma_{\mathrm{yx}} & \sigma_{\mathrm{yy}} & \sigma_{\mathrm{yz}} \\ -\sigma_{\mathrm{zx}} & \sigma_{\mathrm{zy}} & \sigma_{\mathrm{zz}} \end{bmatrix}.$$

This rotation matrix is similarly used for values such as $\mathbf{P}$ and $\mathbf{F}^{-\mathsf{T}}$, which are required in particle summations.

Calculating the mixed kernel-and-gradient correction values with the inclusion of ghost particles can prove confusing (Equations 2.110, 2.113, 2.115 and 2.116). The expressions containing summations include the contribution from the ghost particles in these summations. The ghost particles

Table 3.2: Rotation ($\mathbf{r}_g = [r_{g,x}\ r_{g,y}\ r_{g,z}]^T$) look-up tables for all 26 possible generation modes denoted by the flag number. For all flags either 1, 3 or 7 particles can be generated each with a corresponding rotation value in up to three dimensions. A negative one indicates that a ghost particle will be reflected across that plane whilst a positive one indicates that it will not be reflected about that plane. Not that this is independent of whether the plane is a maximum or a minimum.

x-plane rotations ($r_{g,x}$)

Flag:	1	2	3	4	5	6	7	8	9	10	11	12	13	14	15	16	17	18	19	20	21	22	23	24	25	26
Ghost 1:	−1	−1	1	1	1	1	1	1	1	1	1	1	1	1	1	1	1	1	1	1	1	1	1	1	1	1
Ghost 2:				−1	−1		−1	−1		−1	−1	1	1	1	1	1	1		−1	−1	1	1	1	1	1	1
Ghost 3:				−1	−1		−1	−1		−1	−1	1	−1	−1	1	−1	−1		−1	−1	1	−1	−1	1	−1	−1
Ghost 4:													1	1		1	1					1	1		1	1
Ghost 5:													−1	−1		−1	−1					−1	−1		−1	−1
Ghost 6:													−1	−1		−1	−1					−1	−1		−1	−1
Ghost 7:													−1	−1		−1	−1					−1	−1		−1	−1

y-plane rotations ($r_{g,y}$)

Flag:	1	2	3	4	5	6	7	8	9	10	11	12	13	14	15	16	17	18	19	20	21	22	23	24	25	26
Ghost 1:	1	1	−1	−1	−1	−1	−1	−1	1	1	1	1	1	1	1	1	1	1	1	1	1	1	1	1	1	1
Ghost 2:				1	1		1	1		1	1	−1	−1	−1	−1	−1	−1		1	1	−1	−1	−1	−1	−1	−1
Ghost 3:				−1	−1		−1	−1		1	1	−1	1	1	−1	1	1		1	1	−1	1	1	−1	1	1
Ghost 4:													−1	−1		−1	−1					−1	−1		−1	−1
Ghost 5:													1	1		1	1					1	1		1	1
Ghost 6:													−1	−1		−1	−1					−1	−1		−1	−1
Ghost 7:													−1	−1		−1	−1					−1	−1		−1	−1

z-plane rotations ($r_{g,z}$)

Flag:	1	2	3	4	5	6	7	8	9	10	11	12	13	14	15	16	17	18	19	20	21	22	23	24	25	26
Ghost 1:	1	1	1	1	1	1	1	1	−1	−1	−1	−1	−1	−1	−1	−1	−1	−1	−1	−1	−1	−1	−1	−1	−1	−1
Ghost 2:				1	1		1	1		1	1	1	1	1	1	1	1		1	1	1	1	1	1	1	1
Ghost 3:				1	1		1	1		−1	−1	−1	1	1	−1	1	1		−1	−1	−1	1	1	−1	1	1
Ghost 4:													−1	−1		−1	−1					−1	−1		−1	−1
Ghost 5:													−1	−1		−1	−1					−1	−1		−1	−1
Ghost 6:													1	1		1	1					1	1		1	1
Ghost 7:													−1	−1		−1	−1					−1	−1		−1	−1

Table 3.3: Translation indices $t'_{g,x}$, $t'_{g,y}$, $t'_{g,z}$ look-up tables for all 26 possible generation modes denoted by the flag number. For all flags either 1, 3 or 7 particles can be generated each with a corresponding translation value in up to three dimensions. A negative one indicates a translation value of 2 times the maximum x, y or z plane value and a positive one indicates a value of 2 time the minimum x, y or z plane value. A zero indicates no translation through that axis.

x-plane translations ($t'_{g,x}$)

Flag:	1	2	3	4	5	6	7	8	9	10	11	12	13	14	15	16	17	18	19	20	21	22	23	24	25	26
Ghost 1 :	1	−1	0	0	0	0	0	0	0	0	0	0	0	0	0	0	0	0	0	0	0	0	0	0	0	0
Ghost 2 :				1	−1		1	−1		1	−1	0	0	0	0	0	0		1	−1	0	0	0	0	0	0
Ghost 3 :				1	−1		1	−1		1	−1	0	1	−1	0	1	−1		1	−1	0	1	−1	0	1	−1
Ghost 4 :													0	0		0	0					0	0		0	0
Ghost 5 :													1	−1		1	−1					1	−1		1	−1
Ghost 6 :													1	−1		1	−1					1	−1		1	−1
Ghost 7 :													1	−1		1	−1					1	−1		1	−1

y-plane translations ($t'_{g,y}$)

Flag:	1	2	3	4	5	6	7	8	9	10	11	12	13	14	15	16	17	18	19	20	21	22	23	24	25	26
Ghost 1 :	0	0	1	1	1	−1	−1	−1	0	0	0	0	0	0	0	0	0	0	0	0	0	0	0	0	0	0
Ghost 2 :				0	0		0	0		0	0	1	1	1	−1	−1	−1		0	0	1	1	1	−1	−1	−1
Ghost 3 :				1	1		−1	−1		0	0	1	0	0	−1	0	0		0	0	1	0	0	−1	0	0
Ghost 4 :													1	1		−1	−1					1	1		−1	−1
Ghost 5 :													0	0		0	0					0	0		0	0
Ghost 6 :													1	1		−1	−1					1	1		−1	−1
Ghost 7 :													1	1		−1	−1					1	1		−1	−1

z-plane translations ($t'_{g,z}$)

Flag:	1	2	3	4	5	6	7	8	9	10	11	12	13	14	15	16	17	18	19	20	21	22	23	24	25	26
Ghost 1 :	0	0	0	0	0	0	0	0	1	1	1	1	1	1	1	1	1	−1	−1	−1	−1	−1	−1	−1	−1	−1
Ghost 2 :				0	0		0	0		0	0	0	0	0	0	0	0		0	0	0	0	0	0	0	0
Ghost 3 :				0	0		0	0		1	1	1	0	0	1	0	0		−1	−1	−1	0	0	−1	0	0
Ghost 4 :													1	1		1	1					−1	−1		−1	−1
Ghost 5 :													1	1		1	1					−1	−1		−1	−1
Ghost 6 :													0	0		0	0					0	0		0	0
Ghost 7 :													1	1		1	1					−1	−1		−1	−1

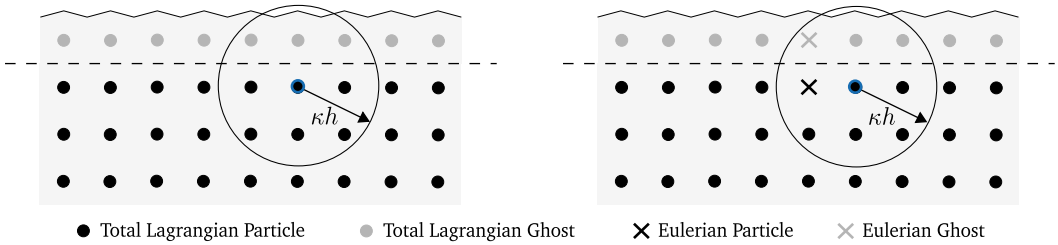

Figure 3.4: Figure that highlights how ghost particles convert kernel type if their generating particle converts type. They must retain their Total Lagrangian properties if they have a Total Lagrangian neighbour as done by the Eulerian interface particles.

then inherit the value of these summations from their parent particle. For example, if considering the normalised kernel gradient

$$\nabla_a \widetilde{W}_{ab} = \frac{\nabla_a W_{ab} \left(\sum_{b=1}^{N} V_b W_{ab} \right) - \left(\sum_{b=1}^{N} V_b \nabla_a W_{ab} \right) W_{ab}}{\left(\sum_{b=1}^{N} V_b W_{ab} \right)^2} = \frac{\nabla_a W_{ab}(A) - (B) W_{ab}}{(A)^2} \,, \quad \text{(2.116 revisited)}$$

then the values of the summations A and B are calculated for each particle and include the contributions from ghost particle neighbours. Having calculated these summations, the ghost particles then inherit values from their parent particle such that $A_\mathrm{g} = A_\mathrm{i}$ and $B_\mathrm{g} = B_\mathrm{i}$. Following this, the normalised kernel gradient can be calculated for all particle pairs. Note that the correction matrix $\mathbf{K}$ is directly inherited, without applying the rotation matrix $\mathbf{R}_\mathrm{g}$, such that $\mathbf{K}_\mathrm{g} = \mathbf{K}_\mathrm{i}$.

In order to use ghost particles with either of the coupling methods, a number of restrictions had to be placed on the interplay between different particle types. Firstly, ghost particles were generated with the same kernel type as their parents. If the parent changed kernel type then the ghost particle did likewise. Eulerian particles were allowed to interact with Total Lagrangian ghost particles and vice versa. The complication to this allowance is that Total Lagrangian particles may only interact with Eulerian ghost particles if they were neighbours in the undeformed reference state, as the Total Lagrangian reference state is not updated in this work. The caveat to this rule is when a Total Lagrangian particle converts type to an Eulerian particle, as displayed in Figure 3.4. In this case, its ghost particles will also convert type. In the scenario that this ghost particle is a neighbour of another Total Lagrangian particle, the Total Lagrangian particle must retain the Eulerian ghost as its neighbour. This can be achieved if the Eulerian ghost retains its previous Total Lagrangian properties. In this case, Eulerian interface ghost particles are treated in the same way as Eulerian interface particles. This being that they contribute to SPH summations in both material and spatial coordinates.

In the first coupling method, the acceleration contributions from Eulerian particles to the Total Lagrangian acceleration summations are carried out in the deformed state. The same is done for the interaction between the Eulerian ghosts and the Total Lagrangian particles, if using this method. This must be the case due to the approach taken in the first coupling method, as described in Section 2.6, whereby the deformation gradient is not calculated for Eulerian particles. As a result, their Cauchy stress tensors cannot be converted into first Piola-Kirchhoff stress tensors for their ghost particles to inherit. This is required to calculate the acceleration in the undeformed state as shown by the Total Lagrangian conservation of momentum equation in Equation 2.121. In the second coupling method the deformation gradient is calculated for Eulerian interface neighbours and consequently, their ghost particles can inherit this value.

In addition to symmetry planes, perfectly rigid boundaries can also be modelled using the ghost particle method [47]. In this work, displacement and velocity boundaries are treated using a simpler method.

3.7.2 Displacement and velocity boundaries

In order to model a fixed boundary, such as a clamp, the Dirchlet boundary condition is applied directly to particles next to the boundary. More specifically, the displacement of particles next to fixed boundaries is set to zero. Vidal et al. [35] state that this is usual practice in SPH as the particles' support domain is small. Although the boundary is actually extended $h/2$ away from particles next to the boundary, this approach was adopted as it was simple to implement and enforces the fixed boundary condition. Lee et al. [121] compared this approach to the exact enforcement of essential boundaries using a Lagrange multiplier method for large strain solid dynamics. They stated that the *"exact enforcement of essential (or Dirichlet) boundary conditions is not strictly essential when employing a SPH discretisation"* and concluded that *"practically identical results can be obtained with and without the exact enforcement of essential boundary conditions"*. A similar approach used to enforce the fixed boundary condition involves extending the domain into the boundary itself and then enforcing zero displacement on these boundary particles. It appears common to use three layers of boundary particles in this approach [36, 122, 123].

Similarly, in this work, the Neumann velocity boundary condition is directly imposed on particles next to the boundary. It is noted that whilst simple to implement and effective, this treatment of displacement and boundary conditions is not exact. Other more complex approaches include the extension to the ghost particle method [41], coupling with mesh-based methods [124], using a semi-analytical approach [110–116] and the Lagrange multiplier method [121].

3.7.3 Contact algorithm

As detailed by Campbell [125], Eulerian SPH generally deals with contact between bodies through the use of the conservation equations. The list of neighbours updates when the bodies come within range of each other, via the comprising particles' support domains. This can result in both mixing and penetration at the contact interface. Further problems include difficulty in separation due to artificial tensile forces, which are generated by the conservation equations and the creation of artificial shear stresses, resulting in friction. Although Monaghan's XPSH [126] does resolve the issue of particle penetration it does not resolve the artificial tensile and shear forces. Using the conservation equations to model contact in the Total Lagrangian formulation is more complex as both bodies must identify each other in the undeformed state or else updates of the reference condition are required. This, in itself, requires careful treatment.

The frictionless contact algorithm developed by Vignjevic et al. [127, 128] is used as it can be implemented with both the Eulerian and Total Lagrangian formulations and does not produce artificial shear or friction. Vignjevic et al. derive a contact force given by

$$\left(\frac{\mathrm{d}\mathbf{v}_a}{\mathrm{d}t}\right)_{\text{cont}} = -\frac{1}{m_a}\sum_{b=1}^{N_{\text{cont}}} V_a V_b K_{\text{ca}} n_{\text{ca}} \frac{W_{ab}^{n_{\text{ca}}-1}}{W(\Delta p)^{n_{\text{ca}}}} \nabla_a W_{ab} \,. \tag{3.53}$$

Summations only take place between particles in separate bodies. In this equation K_{ca} is a contact stiffness penalty parameter, Δp is the average particle spacing and n_{ca} is an exponent of the kernel

values and a multiplier. This contact algorithm also conserves both momentum and energy. It is presumed that this algorithm is termed 'frictionless' as the resulting force acts along the straight line connecting particles. As a result, the shear stresses that are generated if using the conservation equations to simulate contact do not manifest and cause friction. Unlike the artificial viscosity equation, this algorithm has not been modified for a Total Lagrangian or a mixed correction formulation. Therefore, the contact particles will require kernel and kernel gradient values in the deformed state. This does not introduce an inconsistency with the conservation equations which use mixed correction (Equations 2.120 and 2.121) as the contact algorithm is solely used to transfer momentum between two bodies. This could be achieved by using a force defined by the Lennard-Jones potential, which makes no use of the kernel or kernel gradient values. If using kernel values it is simple to define a function that increases as the separation between particles decreases, regardless of the discretisation resolution. Additionally, the kernel values automatically ensure that the force acts along the straight-line connecting particles. Furthermore, applying mixed correction to the contact potential equation would result in a contact potential force which was not equal and opposite between particle pairs and this would damage the conservation properties of the formulation.

In order to ensure the conservation of energy, the contact force must also be added to the evolution of internal energy. The contribution from the contact force to the energy equation can be written as

$$\left(\frac{\mathrm{d}e_a}{\mathrm{d}t}\right)_{\mathrm{cont}} = -\sum_{b=1}^{N_{\mathrm{cont}}} \frac{(\mathbf{v}_b - \mathbf{v}_a)}{2} V_a V_b K_{\mathrm{ca}} n_{\mathrm{ca}} \frac{W_{ab}^{n_{\mathrm{ca}}-1}}{W(\Delta p)^{n_{\mathrm{ca}}}} \nabla_a W_{ab} \ . \tag{3.54}$$

Having described both the conservation equations, coupling methods and the additional elements required to model plasticity and fracture, a time integration scheme is given which combines these algorithms together and describes how to evolve them in time. This influences the run time of the code, the order of the truncation error and the conservation properties as discussed in the following section.

3.8 Time integration

An integration scheme based on the standard leapfrog time integration scheme (also known as the "mid-point rule" or "step-over scheme") was implemented as it is simple, computationally efficient [1], has a truncation error of order $O(\Delta t)^2$ [129] and is symplectic, which results in the conservation of energy. The basis of this scheme is that particle positions and velocities are updated at staggered time intervals such that

$$\mathbf{x}_{t+\Delta t} = \mathbf{x}_t + (\mathbf{v}_{t+\Delta t/2})\Delta t \ , \tag{3.55}$$

$$\mathbf{a}_{t+\Delta t} = f(\mathbf{x}_{t+\Delta t}) \tag{3.56}$$

and

$$\mathbf{v}_{t+3\Delta t/2} = \mathbf{v}_{t+\Delta t/2} + (\mathbf{a}_{t+\Delta t})\Delta t \ , \tag{3.57}$$

where positions and accelerations are calculated at full time steps and velocities are calculated at half time steps. Figure 3.5 displays this pictorially. For the initial step, when $t = 0$, the velocity $\mathbf{v}_{\Delta t/2}$ is

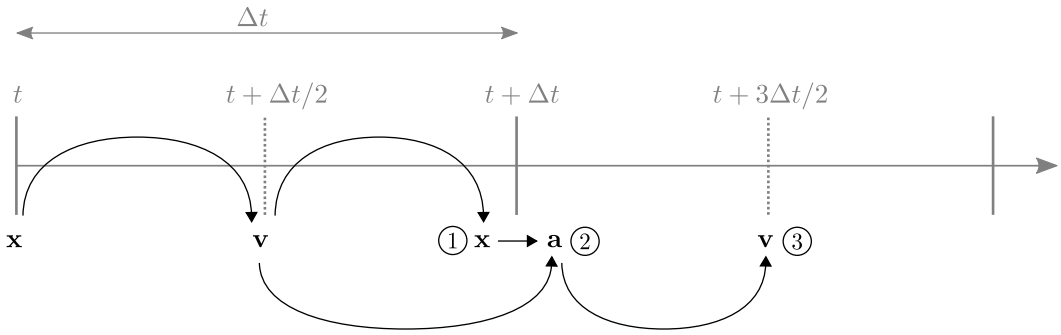

Figure 3.5: Pictorial description of the leapfrog time integration scheme whereby the calculations of position, velocity and acceleration are staggered in time.

calculated using an Euler step:

$$\mathbf{v}_{\Delta t/2} = \mathbf{v}_{t=0} + (\mathbf{a}_{t=0})\Delta t/2 \ . \tag{3.58}$$

Following this initial half step, the scheme continues as normal. This scheme can be modified in a synchronised form such that

$$\mathbf{x}_{t+\Delta t} = \mathbf{x}_t + (\mathbf{v}_t + \frac{\mathbf{a}_t \Delta t}{2})\Delta t \ , \tag{3.59}$$

$$\mathbf{a}_{t+\Delta t} = f(\mathbf{x}_{t+\Delta t}) \tag{3.56 revisited}$$

and

$$\mathbf{v}_{t+\Delta t} = \mathbf{v}_t + (\mathbf{a}_t + \mathbf{a}_{t+\Delta t})\frac{\Delta t}{2} \ , \tag{3.60}$$

where the above is still written in the conventional kick-drift-kick form of leapfrog integration [130]. The benefit to this form is that it does not require values at half time steps. These forms of the leapfrog time integration scheme are similar and are based on the acceleration being dependent solely on position and not velocity. As this is not necessarily the case in this work, a synchronised Predict, Evaluate, Correct (PEC) form of leapfrog integration is used, similar to that presented by Serna et al. [131]. The superscript p is used to denote predicted values. In the PEC method presented by Serna et al. the position is firstly pushed forward and the velocity is predicted:

$$\mathbf{x}_{t+\Delta t} = \mathbf{x}_t + (\mathbf{v}_t + \frac{\mathbf{a}^{\mathrm{p}}_t \Delta t}{2})\Delta t \ , \tag{3.61}$$

$$\mathbf{v}^{\mathrm{p}}_{t+\Delta t} = \mathbf{v}_t + \mathbf{a}^{\mathrm{p}}_t \Delta t \ . \tag{3.62}$$

Using this predicted velocity, the acceleration is then evaluated as $\mathbf{a}^{\mathrm{p}}_{t+\Delta t} = f(\mathbf{x}_{t+\Delta t}, \mathbf{v}^{\mathrm{p}}_{t+\Delta t})$. Lastly, the velocity is corrected as

$$\mathbf{v}_{t+\Delta t} = \mathbf{v}_t + (\mathbf{a}^{\mathrm{p}}_t + \mathbf{a}^{\mathrm{p}}_{t+\Delta t})\frac{\Delta t}{2} = \mathbf{v}^{\mathrm{p}}_{t+\Delta t} + (\mathbf{a}^{\mathrm{p}}_{t+\Delta t} - \mathbf{a}^{\mathrm{p}}_t)\frac{\Delta t}{2} \ . \tag{3.63}$$

This synchronised PEC form of leapfrog time integration is similar to the unsynchronised form suggested by Liu and Liu [1]. It written in similar form to Equations 3.59 - 3.60 although an intermediate velocity is required for the rate of change of density and deviatoric stress, as will be explained.

In the following, all rates of change, except for the deviatoric stress rate and the rate of change of density (for the Eulerian formulation), are calculated at full time steps, as for the acceleration.

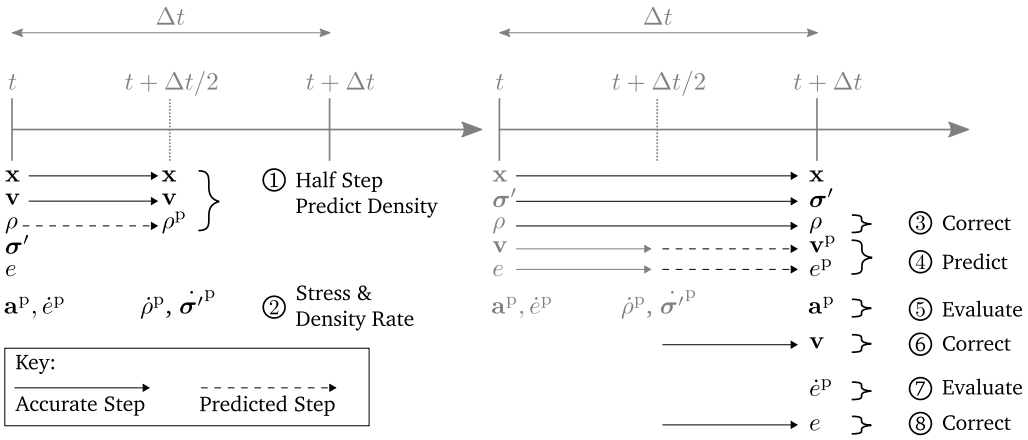

Figure 3.6: Predict, evaluate, correct (PEC) form of the leapfrog time integration scheme for an Eulerian formulation. The dashed arrows highlight the components of the scheme that are predictive and the full arrows denotes the components of the scheme that use the corrected rates of change. The rate of change of density and deviatoric stress are calculated at half time steps due to the equation of state and plasticity calculations at integer time steps.

Therefore, the field variables corresponding to these rates of changes are predicted and corrected, as for the velocity. A simplified version of this is displayed pictorially for an Eulerian formulation in Figure 3.6. Note that in this figure the density is initially predicted forward half a step. This uses the rate of change of density calculated at the previous half time step. If $t = 0$ then the rate of change of density is calculated at this initial time step. This is the only case for which the rate of change of density is calculated at an integer step, i.e. $t = 0$. The reason as to why the rate of change of density is calculated at a half time step is that the pressure p is calculated at integer time steps. This pressure is combined with the deviatoric stress to evaluate the particle accelerations.

The pressure is commonly calculated using an equation of state that is sensitive to density changes. Should the density rate be calculated on an integer step, the equation of state would use a predicted density. The error of so doing was found to accumulate and to lead to discrepancies with the Total Lagrangian formulation. Calculating the rate of change of density at a half time step and consequently using a corrected value of density in the equation of state was found to produce results that were consistent with the Total Lagrangian formulation. Should an equation of state be used which is dependent on internal energy, the leapfrog time integration scheme will not exactly conserve energy. This is because the pressure would be calculated using a predicted value of internal energy. This discrepancy was found to be small, as highlighted by the numerical example presented in Section 4.11 where the total energy was found to change by 0.048 % over the course of the simulation, due to using a predicted value of internal energy in the equation of state.

In Figure 3.6, it can also be seen that the velocity is corrected at the $t + \Delta t$ step, after the acceleration is predicted. Next, the rate of internal energy is evaluated and the internal energy is corrected. These two evaluate-corrected steps were not combined together as, it was found that the rate of change of energy required the corrected velocity in order for both the Total Lagrangian and Eulerian formulations to conserve energy exactly.

The rate of deviatoric stress is calculated at half time steps due to the inclusion of plasticity. Should the stress rate be calculated on integer time steps, then the stress would have to be predicted at integer time steps. Once predicted, the stress state would have to be evaluated to check whether it was within the yield surface. If the predicted stress was not within the yield surface, complications

would arise as some flow stress models, such as the Johnson-Cook plasticity model (Equation 3.37) are nonlinear. The accelerations and consequent corrected velocities would then be dependent on the plasticity, which was assumed when calculating the predicted stress. The corrected stress would then need to be re-evaluated again to determine whether it was within the yield surface. It is nontrivial to determine how to correct the predicted yield stress, plastic strain and temperature. An attempt to merge the values from both yield surface evaluations resulted in a model that over predicted plasticity. Conversely, only using the values from the last yield stress evaluation resulted in a model which under-predicted plasticity. This complication is avoided by calculating the stress rate at half time steps, although the disadvantage of doing so is the extra calculations that are required by the Eulerian formulation. Note that the Total Lagrangian formulation follows the same scheme, but the density is calculated from the deformation gradient and therefore only requires the calculation of the rate of deviatoric stress at half time steps.

This explicit scheme is conditionally stable, where the stability depends on the selection of Δt. The Courant-Friedrichs-Lewy (CFL) condition is taken as the limiting stability condition. Following Das and Cleary [79] the time step is set to

$$\Delta t = \min_{a=1,N} \left(\frac{h_a}{2c_a} \right) . \tag{3.64}$$

The speed of sound is commonly reduced in order to gain computation speed when simulating fluid mechanics using the SPH method. This involves modelling a real incompressible fluid as an artificial fluid with slight compressibility. As the sound speed of the artificial fluid is still larger than the bulk flow of the real fluid, the density variation caused by this manipulation of the speed of sound is small [117]. Following Das and Cleary [79], the real speed of sound is used in this work in order to capture transient stress waves. Other more complex equations are available which allow each particle to have its own time step and take viscous dissipation and external forces into account [1, 86]. Equation 3.64 was found to be sufficient for the problems considered in this work. It is noted that although the CFL condition must be met, it is not the limiting stability condition in all cases, such as when considering a non-adiabatic processes like radiative effects in the thermal energy equation [86].

Figure 3.7 displays a flowchart of the time integration scheme and the algorithms discussed so far. It is applicable to a Total Lagrangian formulation, an Eulerian formulation or a coupled formulation. This flow chart details the order of calculations and highlights the sequence in which field variables must be evolved in time. The interface zone particles contribute to the calculations in both the Eulerian and Total Lagrangain sections. Note that the artificial viscosity, artificial stress and contact algorithm are calculated at the same time as the particle acceleration. The ghost particle algorithm is not included in this flowchart, as it would reduce clarity.

The formulations given in Chapter 2 along with the artificial viscosity in Section 3.2, the artificial stress in Section 3.3, and the contact algorithm are all dependent on the value of the gradient of the kernel. For the Total Lagrangian formulation this remains fixed whilst for the Eulerian formulation this updates at every time step. Consequently, an efficient numerical implementation is required in order to exploit the computational advantages of both coupling methods, as discussed in the following section.

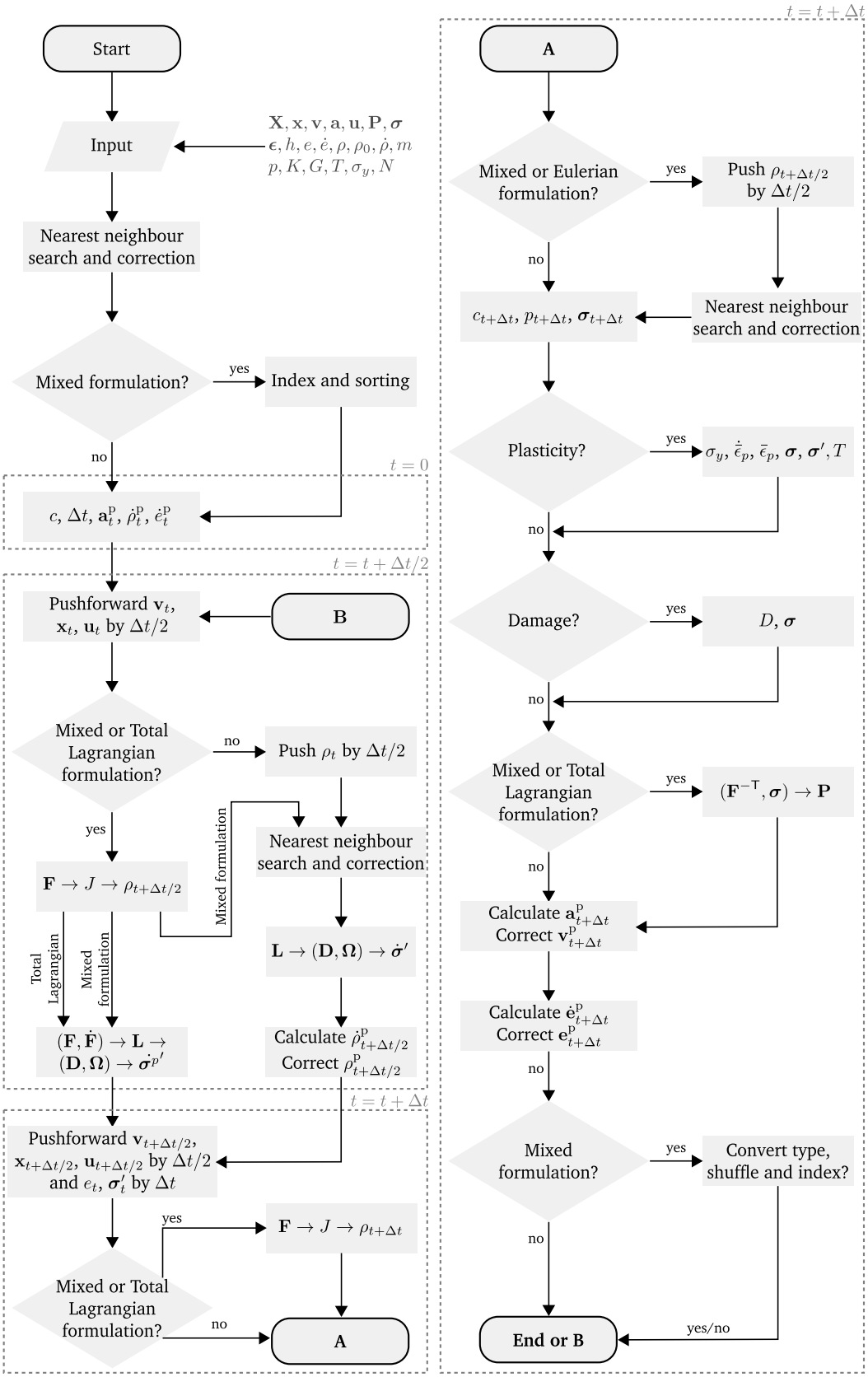

Figure 3.7: Flow chart which details the predict, evaluate and correct leap frog time integration scheme and the order in which variables are updated. The order in which the plasticity and damage algorithms are calculated is also presented.

Table 3.4: Example of how particle data are stored in memory where "E" represents an Eulerian particle value and "L" represents a Total Lagrangian one.

Particle	1	2	3	4	5	6	7	8	9	N=10
Value	E	E	E	L	L	L	E	E	L	L

Table 3.5: Example of how pair data are stored in memory, for the first coupling method, prior to rearrangement by kernel types. "E" represents an Eulerian particle and "L" represents a Total Lagrangian one.

Pair	1	2	3	4	5	6	7	8	9	N_{pairs} =10
Particle 1	L	E	E	L	L	L	E	E	L	E
Particle 2	L	E	L	E	L	L	E	L	L	L

3.9 Numerical implementation

This section addresses the numerical implementation of the coupled formulations with mixed correction. This includes the method used for memory storage along with the benefits of parallel programming. Although these are by no means optimised, they present an outline of how the formulations and additional algorithms presented thus far can be implemented.

3.9.1 Coupling memory storage

Fortran code provided by Liu and Liu [1] was adapted to develop the code written as part of this work. Liu and Liu's original code was written for fluid mechanics in an Eulerian formulation. Although none of the original code remains, with the exception of the kernel functions, some of the methodology was kept including the way in which particle pair-based values were stored in memory. The field variables of individual particles were stored from 1 to N in corresponding vectors, or arrays, where the column index represented the particle and the row index represented the dimension of the field variable. Particle pairs were stored from 1 to N_{pairs} where the column index referred to the pair number and the row index referred to the first and second particle in that pair. Following this, pair-based values were stored where the column index referred to the pair number and the row index represented the dimension of the field variable associated with that pair.

Although this methodology was sufficient for a singularly Eulerian or Total Lagrangian formulation, it was not adequate for a coupled formulation. The reason for this is that contiguous blocks of memory are preferred in order to have efficient computation. A coupled formulation requires indexing of the particle-based values to determine whether they belong in the Eulerian or Total Lagrangian calculations and the pair-based values do likewise. This extra layer of indices was found to slow down the computational speed significantly. The simplest compromise found was to mark particles as either Eulerian or Total Lagrangian and then to index the particle-based values and to rearrange the pair-based values. Considering Table 3.4, which shows particle values marked by either "E" for Eulerian or "L" for Total Lagrangian, the Eulerian particle indices would correspond to $1, 2, 3, 7, 8$ and the Total Lagrangian ones would refer to $4, 5, 6, 9$. Table 3.5 displays how pairs were originally stored in memory for the first coupling method. It can be seen that pairs of different types are scattered and the order of the interface pairs is not consistent. Consequently, the list of pairs is rearranged as shown in Table 3.6. In this case, there are three distinct sections corresponding to the Total Lagrangian pairs, the interface pairs and the Eulerian pairs. This is beneficial to computational

Table 3.6: Example of how pair data are stored in memory, for the first coupling method, after rearrangement by kernel types. "E" represents an Eulerian particle and "L" represents a Total Lagrangian one.

Pair	1	2	3	4	5	6	7	8	9	N_{pairs} =10
Particle 1	L	L	L	L	E	E	E	E	E	E
Particle 2	L	L	L	L	L	L	L	L	E	E

speed as pair-based calculations have definite start and end points, without requiring indices for both formulations. Furthermore, the interface pairs have been adapted such that the Eulerian particle is always the first neighbour. Note that all pair-based values must be organised to match the order of pairs. This organisation methodology is separate from the initial neighbour searching as, in the formulation presented, it is possible for particles to change type. Note that for the second coupling method, the Eulerian and Total Lagrangian formulations have separate pair lists, as the Eulerian interface neighbours can change at every time step. The benefit to this approach to memory storage is highlighted in the following section through the application of parallel programming.

3.9.2 Parallel programming

Although the symmetry boundary conditions, discussed in Section 3.7.1, reduce the computational cost of large simulations, further improvements can be achieved. Both the Total Lagrangian and Eulerian set of conservation equations (Equations 2.121 and 2.120) include summations that are dependent on the number of particle pairs. Consider that a particle with a smoothing length equal to 1.3 times the initial particle spacing could have up to 44 neighbours in three dimensions. Therefore, a simulation with a moderate number of particles requires a large number of calculations. The time taken to complete these calculations can be reduced by implementing parallel programming models such as OpenMP and Message Passing Interface (MPI). A notable difference between these models is that OpenMP is based on shared memory, this being that all the parallel processes can access all the data, whilst MPI operates through message passing. Message passing works on distributed memory meaning that the parallel processes work independently of each other and require explicit instruction to share memory. In the context of this work, OpenMP was found to be the simpler of the two models to implement. Listing 3.1 shows how the deformation gradient and material velocity gradient are calculated in a loop using the OpenMP `Reduction` clause. One of the consequences of Amdahl's law is that, if only a small proportion of the code is made parallel, regardless of the speedup to that proportion of code, it will have little effect on the overall speedup. Furthermore, the overall speedup is limited by the serial fraction of code, if assuming an infinite speedup to the parallel fraction of code. These corollaries indicate that every loop should be made parallel, if possible, in order to reduce the fraction of code that is serial.

All floats are stored in double-precision floating-point format in the Fortran code. As a result, the memory requirements can easily become greater than available in a conventional workstation. This, in combination with the speedup that would be given by additional central processing units (CPU), meant that high performance computing was required. Consequently, the examples presented in Chapter 4, which contained more than 10^6 particle pairs, were carried out on The University of Edinburgh's Eddie Mark 3 compute cluster. An example of this is the Kalthoff-Winker simulation presented in Section 4.10. In this simulation, an investigation into the effect of the number of particles required a simulation with 828,300 particles and 26,057,528 particle pairs. This was achieved using

```
! For all Total Lagrangian - Total Lagrangian particle pairs.
!$OMP PARALLEL DO DEFAULT(SHARED), &
!$OMP& PRIVATE(i,j,k,disp_ij,ii,jj,temp_ten1,temp_ten2,temp_ten3,temp_ten4), &
!$OMP& REDUCTION(+:def_grad, mat_vel_grad),
!$OMP& SCHEDULE(static)
DO k = 1, niac_l
  i = pair_i(k)
  j = pair_j(k)

  ! Difference in pair displacement
  disp_ij(1:dimn) = disp(1:dimn,i) - disp(1:dimn,j)

  ! Difference in displacement and velocity times the mixed correction kernel gradient
  DO jj=1,dimn
    DO ii = 1,dimn
      temp_ten1(ii,jj) = -disp_ij(ii) * dwdx_cor_l(jj,k)
      temp_ten2(ii,jj) = disp_ij(ii) * dwdx_cor_l(dimn+jj,k)
      temp_ten3(ii,jj) = -dvx(ii,k) * dwdx_cor_l(jj,k)
      temp_ten4(ii,jj) = dvx(ii,k) * dwdx_cor_l(dimn+jj,k)
    END DO
  END DO

  ! The deformation gradient reduction (added to identity matrix later)
  def_grad(i,1:dimn,1:dimn) = def_grad(i,1:dimn,1:dimn)+temp_ten1*V_0(j)
  def_grad(j,1:dimn,1:dimn) = def_grad(j,1:dimn,1:dimn)+temp_ten2*V_0(i)

  ! The material velocity gradient reduction
  mat_vel_grad(i,1:dimn,1:dimn) = mat_vel_grad(i,1:dimn,1:dimn)+temp_ten3*V_0(j)
  mat_vel_grad(j,1:dimn,1:dimn) = mat_vel_grad(j,1:dimn,1:dimn)+temp_ten4*V_0(i)
END DO
!$OMP END PARALLEL DO
```

Listing 3.1: Example listing which highlights how OpenMP can be used to reduce the calculation time of a typical pair-based summation.

16 computational cores and 58.88 gigabytes of memory (peak). The simulation wall-clock time was approximately 7 hours.

3.10 Concluding remarks

The purpose of this chapter was to describe the additional algorithms required to implement a mixed correction coupled formulation for problems involving shock, plasticity, fracture and failure. A modified form of artificial viscosity was described in order to add a dissipative term to the scheme. Various applications of the artificial stress term were discussed along with its incompatibility with first coupling method and its compatibility with the second. Three equations of state, plasticity models and damage models were detailed in addition to a proposed method for modelling fracture by making use of particle kernel conversion. The ghost particle boundary condition method was described along with the modifications required in order to use this with both the mixed correction and the coupling methods. The time integration scheme was discussed with emphasis placed on the necessary order of variable evolution in order for both the Eulerian and Total Lagrangian schemes to be compatible. A numerical implementation was discussed including a possible method of memory storage and parallel programming. Having given both the formulations in Chapter 2 and the additional algorithms in this chapter, the proposed methodology can now be verified and validated.

4 Verification and validation numerical examples

4.1 Overview

Chapters 2 and 3 detailed the SPH formulations, the mixed correction, the coupling methods, and the additional algorithms necessary to model plasticity and damage. The objectives of this chapter are to verify that the theory provided in the previous chapters has been implemented correctly, and to validate the suggested methods for both the mixed correction and proposed couplings. In order to do so, increasingly complex problems are explored and numerical results are compared against experimental results or validated simulation results where possible.

To begin, a one-dimensional calculation of a velocity gradient is carried out using mixed correction both with and without symmetry terms. Next, a one-dimensional propagating wave is simulated using the mixed correction Total Lagrangian formulation. A two-dimensional oscillating bar is modelled using the Eulerian formulation and the Total Lagrangian formulation with and without mixed correction. A two-dimensional off-centre rubber ring impact is simulated in order to demonstrate the momentum and energy conserving properties of the proposed Total Lagrangian formulation with the amended form of artificial viscosity. A patch test is intended to show how artificial stress can suppress the tensile instability along with its usage with both coupling methods. A uniaxial compressions test is intended to demonstrate how the Eulerian, the Total Lagrangian and the coupled formulations produce equal results if the tensile instability is not activated. In addition, results are compared with the Finite Element (FE) method. Having demonstrated the ability to model problems involving elasticity, the Taylor impact problem is used to verify and validate the implementation of the Johnson-Cook plasticity model. Following this, two fracture problems are explored including the crack branching problem and the Kalthoff-Winkler problem. The results of both are compared against those found in literature and experiments. Lastly, a two-dimensional high-velocity impact problem and a three-dimensional debris impact problem are explored. In order to be compatible with particle spallation, the former of these required a modification to the mixed correction scheme. The high-velocity impact problem was intended to demonstrate the advantages and disadvantages of the coupling methods. The purpose of the three-dimensional debris impact problem was to demonstrate the effectiveness of both coupling methods at modelling impact and fracture.

4.2 Comparison of correction with and without symmetry terms

In this section, it is shown that the derivation of the corrected gradient of the corrected kernel, $\widetilde{\nabla}_a \widetilde{W}_{ab}$, without the symmetry terms, as originally derived by Bonet and Lok [42], is equivalent to the derivation with symmetry terms. In both cases, the equations used for calculating the corrected kernel

Table 4.1: Comparison of the equations used when deriving the corrected gradient of the corrected kernel for implementation with and without the symmetry terms $\mathbf{v}_a$ and $\mathbf{x}_a$.

Eqn.	With Symmetry Terms	Without Symmetry Terms
$\nabla \cdot \mathbf{v}$	$\sum_{b=1}^{N} V_b(\mathbf{v}_b - \mathbf{v}_a) \cdot \widetilde{\nabla}_a \widetilde{W}_{ab}$	$\sum_{b=1}^{N} V_b \mathbf{v}_b \cdot \widetilde{\nabla}_a \widetilde{W}_{ab}$
$\widetilde{W}_{ab}$	$W_{ab} / \sum_{b=1}^{N} V_b W_{ab}$	
$\nabla_a \widetilde{W}_{ab}$	$\dfrac{\left[\nabla_a W_{ab} \left(\sum_{b=1}^{N} V_b W_{ab}\right) - \left(\sum_{b=1}^{N} V_b \nabla_a W_{ab}\right) W_{ab}\right]}{\left(\sum_{b=1}^{N} V_b W_{ab}\right)^2}$	
$\mathbf{K}_a$	$\left[\sum_{b=1}^{N} V_b \nabla_a \widetilde{W}_{ab} \otimes (\mathbf{x}_b - \mathbf{x}_a)\right]^{-1}$	$\left[\sum_{b=1}^{N} V_b \nabla_a \widetilde{W}_{ab} \otimes \mathbf{x}_b\right]^{-1}$
$\widetilde{\nabla}_a \widetilde{W}_{ab}$	$\mathbf{K}_a \nabla_a \widetilde{W}_{ab}$	

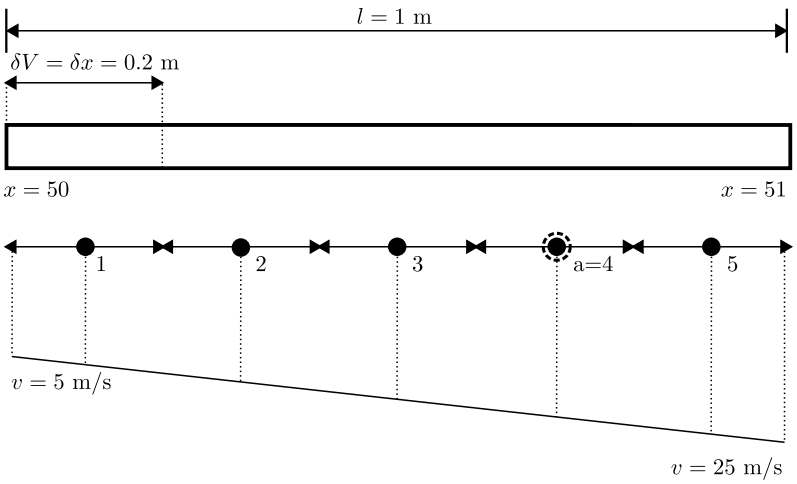

Figure 4.1: Schematic of a one-dimensional bar of length 1 m discretised into five particles starting at 50.1 and ending at 50.9 with a linearly increasing velocity profile varying from 5 to 25 m/s.

$\widetilde{W}_{ab}$ and the gradient of the corrected kernel $\nabla_a \widetilde{W}_{ab}$, give equal values. As proven in Section 2.5.3, the gradient correction matrix, $\mathbf{K}_a$, is equal in both cases even though its form is modified. As a result, the corrected gradient of the corrected kernel is the same whether symmetry terms are used or not. Table 4.1 gives an overview of the equations used in each case. Note that the gradient of the corrected kernel, $\nabla_a \widetilde{W}_{aa}$, is not necessarily zero when calculated for a particle with respect to itself, as is the case for the uncorrected kernel gradient $\nabla_a W_{aa}$. If considering the symmetrical formulation, $\nabla_a \widetilde{W}_{aa}$ is not required as the symmetry terms included in the particle summations render it null, as will be demonstrated.

In this analysis, the selection of an Eulerian or Total Lagrangian formulation was not relevant. In what follows, the velocity divergence of a one-dimensional rod was considered. The rod was discretised into five equally spaced particles with $\delta x = 0.2$ m, starting at coordinate 50.1 and ending at 50.9. The support domain of each particle was based on a smoothing length of $2.8\delta x$. A linear velocity profile was enforced which ranged from 5 to 25 m/s. The corrected gradient of the corrected kernel was applied with and without symmetry terms. Figure 4.1 displays a schematic of the problem. The velocity divergence was calculated for the fourth particle, as highlighted in Figure 4.1. Table 4.2 displays the pair-based terms that make up the summation for the velocity divergence of the fourth

Table 4.2: Breakdown of the pair contribution to the velocity divergence of the fourth particle with and without the symmetry term $\mathbf{v}_a$ for a linear velocity field.

Pairs (a - b)	$V_b(\mathbf{v}_b - \mathbf{v}_a) \cdot \widetilde{\nabla}_a \widetilde{W}_{ab}$	$V_b \mathbf{v}_b \cdot \widetilde{\nabla}_a \widetilde{W}_{ab}$
4 – 2	3.879	−5.333
4 – 3	7.572	−28.395
4 – 4	0.000	4.569
4 – 5	8.549	49.159
$\nabla \cdot \mathbf{v}_{a=4}$	$\sum = 20.000$	$\sum = 20.000$

Table 4.3: Breakdown of the pair contribution to the velocity divergence of the fourth particle with and without the symmetry term $\mathbf{v}_a$ for a quartic velocity field.

Pairs (a - b)	$V_b(\mathbf{v}_b - \mathbf{v}_a) \cdot \widetilde{\nabla}_a \widetilde{W}_{ab}$	$V_b \mathbf{v}_b \cdot \widetilde{\nabla}_a \widetilde{W}_{ab}$
4 – 2	−95159.963	2900053.551
4 – 3	−186899.604	11507941.882
4 – 4	0.000	−1485695.206
4 – 5	−213580.328	−13417940.121
$\nabla \cdot \mathbf{v}_{a=4}$	$\sum = -495639.894$	$\sum = -495639.894$

particle. As is evident from Table 4.2, the formulation that used gradients based on symmetry terms resulted in particles having no contribution to their own summations, or “self-effect". In addition, each pair made less of a contribution to the summation as it was based on velocity differences rather than the magnitude of the neighbouring particles’ velocities. The formulation, which was not based on symmetry terms, retained the self-effect and each term had a larger contribution. This formulation is more demanding due to the extra calculations needed for the self-effect. However, as is highlighted by the example above, both methods produced the same result. To convince sceptical readers that this equality is not merely due to the selection of a linear velocity field, a quartic velocity field of form

$$y = -x^4 + 3x^3 + 15x^2 - x + 15 \tag{4.1}$$

is also evaluated for the same particle distribution. Table 4.3 demonstrates again that the mixed correction with and without symmetry terms produces equal results. From this point onward it can be assumed that the formulation with symmetry terms is used. It should be noted that the first coupling method exclusively makes use of the formulation with symmetry terms, as this results in the particle-pair based internal forces being equal and opposite, as discussed in Section 2.6.

4.3 One-dimensional wave propagation

In order to demonstrate that the Total Lagrangian formulation does not suffer from the tensile instability and to validate the formulation in one dimension, the one-dimensional wave propagation

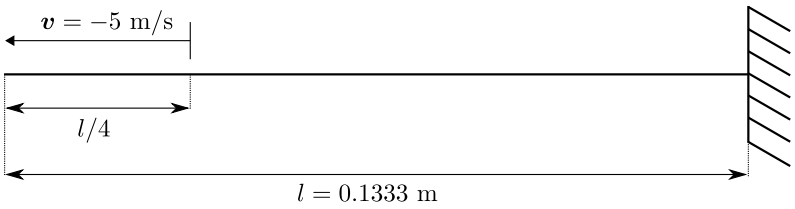

Figure 4.2: One-dimensional bar with an initial velocity imposed along a quarter of its length resulting in a one-dimensional wave propagation.

problem as first presented by Dyka and Ingel [26] was explored. In this problem, a one-dimensional bar was fixed on the right-hand side and an initial velocity was imposed on the first quarter of the left-hand side. This is depicted in Figure 4.2. In this problem, no form of correction or artificial viscosity was used. In the work of Dyka and Ingel, an Eulerian formulation was used where stress was evaluated at stress points, which were located away from the SPH particles. Bonet and Lok [25] successfully approached this problem using their gradient corrected Total Lagrangian approach. Both Dyka and Ingel and Bonet and Lok stated that conventional Eulerian SPH would not succeed in solving this problem due to the instant growth of the tensile instability. Interestingly, the Eulerian SPH formulation presented in Chapter 2 was capable of simulating the problem. Note that the formulation still suffers from the tensile instability, but it did not appear to manifest in this problem.

Dyka and Ingel are followed, who used 40 SPH particles along the length of the rod and gave the Young's modulus as $E = 200 \times 10^9$ Pa, the density as $\rho = 7833$ kg/m^3, the speed of sound as $c = 5033$ m/s and the particle smoothing length of $h = \delta x$. Conventionally, the deviatoric stress rate is calculated and used to update the deviatoric stress, whilst the isotropic pressure component is calculated directly from an equation of state. In order to be consistent with Dyka and Ingel, in this one-dimensional analysis, the rate of Cauchy stress was calculated from the rate of deformation as $\dot{\sigma}_{11} = ED_{11}$.

Figure 4.3 displays the displacement of the free end of the bar against time. The Total Lagrangian results are compared against those given by Dyka and Ingel and a FE analysis. Note that the results presented by Dyka and Ingel have been digitized from the original publication. The results presented by Bonet and Lok are not included for clarity, although these too were in good agreement. Figure 4.4 displays the velocity of the free end of the bar against time. The Total Lagrangian results are compared against those given by a FE analysis. The results from Dyka and Ingel and Bonet and Lok were not included for clarity. As visible from Figure 4.3, the SPH results were in agreement with both the results given by Dyka and Ingel and the FE calculations. Dyka and Ingel attributed the phase discrepancy between the results to the different solver types used in the two analyses as well as the fundamental differences in discretisation. Bonet and Lok attributed the increasing oscillation at the end of the bar to a mechanism that is intrinsic to the one-dimensional Total Lagrangian formulation. They further stated that this could be dampened with artificial viscosity. This oscillation and phase difference are more clearly visible in the tip velocity presented in Figure 4.4. Despite the increasing oscillation, it is clear that the Total Lagrangian formulation presented in this work does not suffer from tensile instability as highlighted by this problem. Additionally, the displacement and velocity profiles were in agreement with the literature and the FE analysis, validating the formulation for elastic, one-dimensional problems.

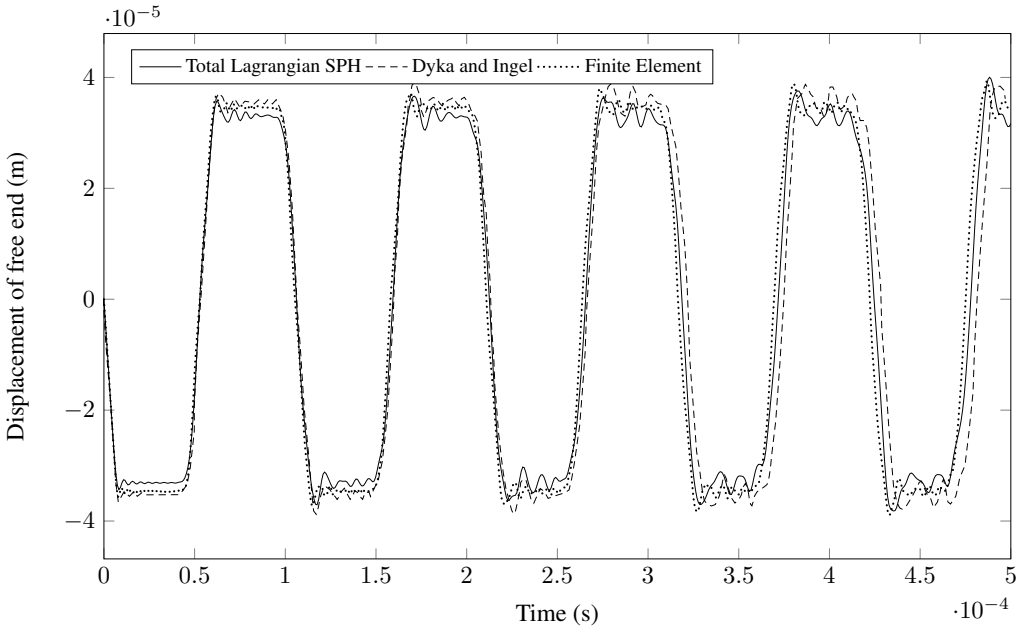

Figure 4.3: Displacement of the rod free end with time due to an initial velocity distribution. Modelled using the Total Lagrangian formulation with no form of correction or artificial viscosity. Results are compared against those given by Dyka and Ingel [26] and a Finite Element analysis.

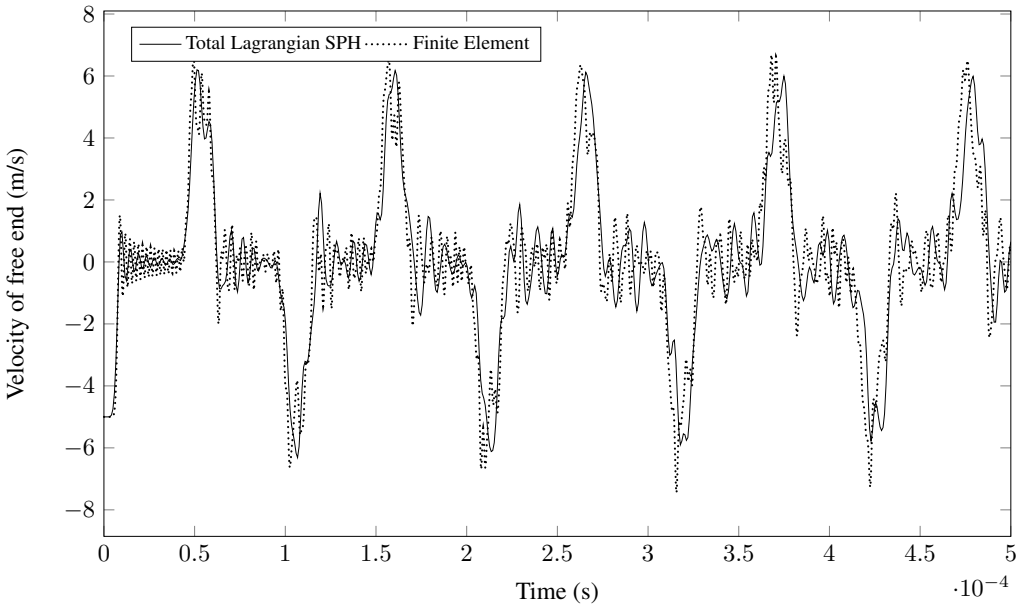

Figure 4.4: Velocity of the rod free end with time due to an initial velocity distribution. Modelled using the Total Lagrangian formulation with no form of correction or artificial viscosity. Results are compared against those given a Finite Element analysis.

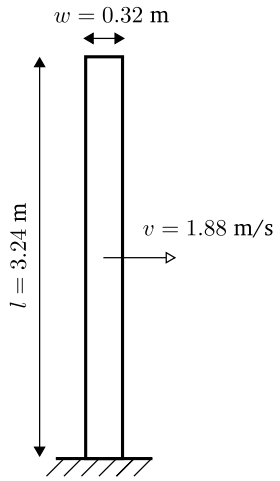

Figure 4.5: Schematic of a compressible neo-Hookean bar, translating with uniform initial velocity which is instantaneously fixed at its base resulting in an oscillatory motion.

4.4 Two-dimensional oscillating bar

The one-dimensional wave propagation validated the Total Lagrangian code in one dimension, but did not highlight the tensile instability that hampers the Eulerian formulation. In order to display both the tensile instability and further demonstrate the effectiveness of the mixed correction formulation, the oscillating column problem presented by Bonet and Kulasegaram [25] and Bonet et al. was revisited [34]. These authors modelled a three-dimensional cylinder, traslating with a constant velocity which was instantaneously clamped at its base. In the example presented here, a two-dimensional bar with unit thickness was modelled. A schematic of the problem is presented in Figure 4.5. Following the two cited papers, a compressible neo-Hookean model was employed. This constitutive model was taken from Bonet and Wood [66]:

$$\boldsymbol{\sigma} = \frac{G}{J}\left(\mathbf{F}\mathbf{F}^{\mathsf{T}} - \mathbf{I}\right) + \frac{\lambda}{J}(\ln J)\mathbf{I}\,, \tag{4.2}$$

where λ is Lamé's first parameter and, as before, G is the shear modulus, J is the Jacobian and the $\mathbf{F}\mathbf{F}^{\mathsf{T}}$ term represents the left Cauchy-Green tensor. The bar had height 3.24 m and width 0.32 m. The bar's shear modulus was given by $G = 357.1$ kPa and the bulk modulus by $K = 1670$ kPa. Note that $\lambda = K - 2G/3$. It had an initial velocity of 1.88 m/s to the right. The density was set to 1050 kg/m, corresponding to rubber [132], as a value was not provided in the references. No artificial viscosity was used in this problem. At the start of the simulation, the bar was clamped at its base resulting in an oscillatory motion. All simulations of this problem used a particle spacing of $\delta x = 0.032$ m and a smoothing length of $h = \delta x$.

This problem was first modelled using a mixed correction Eulerian formulation. This failed shortly after the start of the simulation due to the development of tensile instability. This is displayed in Figure 4.6. Note that this figure has been rotated by 90° for clarity. Following the failed Eulerian simulation, the bar was modelled using the Total Lagrangian formulation without any form of correction. Although the bar did not suffer from the tensile instability, particles were found to clump together. This is highlighted by Figure 4.7, which displays the particles' positions at four instances in time. This clumping of particles is removed if the mixed correction is used, as demonstrated by

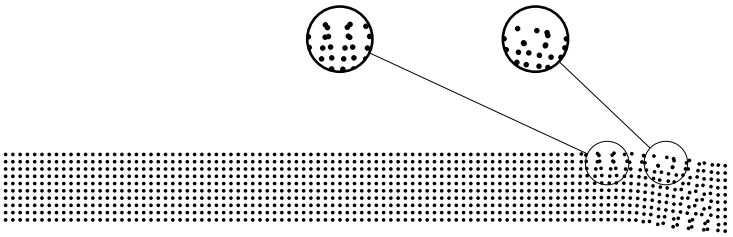

Figure 4.6: Compressible neo-Hookean bar with uniform initial velocity that is fixed at the base. The simulation fails due to the tensile instability that manifests due to the Eulerian formulation. Note that figure has been rotated by 90° for clarity.

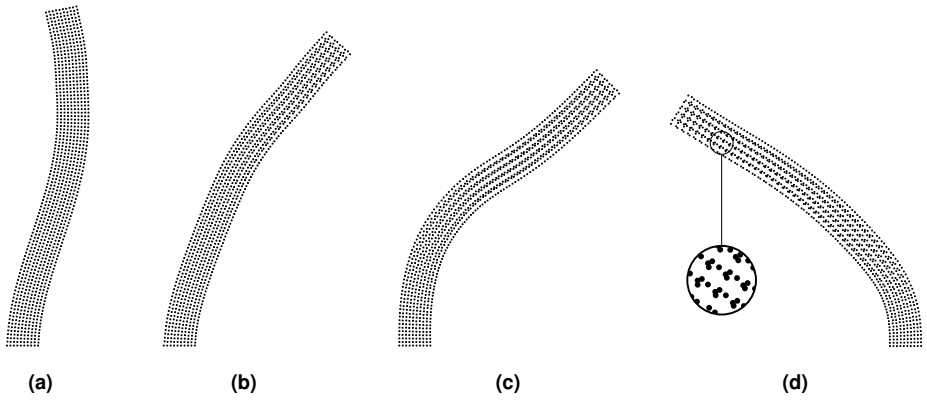

Figure 4.7: Progression of the bar oscillation for the Total Lagrangian formulation, with no form of correction, at (a) 0.224 s (b) 0.537 s (c) 1.791 s and (d) 3.583 s.

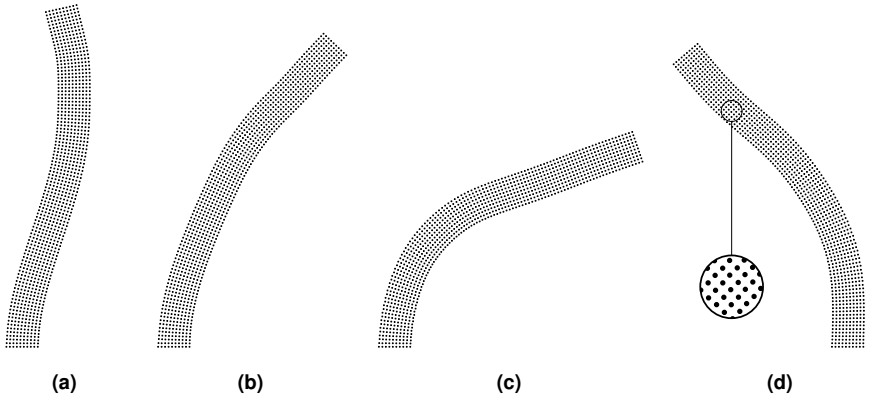

Figure 4.8: Progression of the bar oscillation for the Total Lagrangian formulation, with mixed correction, at (a) 0.224 s (b) 0.537 s (c) 1.791 s and (d) 3.583 s.

Figure 4.8, which displays the particles' positions at the same four instances in time as in Figure 4.7. In addition to the particles retaining their order, the deformed shape was largely different and was presumed to be the more accurate of the two. These results were validated using a FE analysis. This FE model comprised of linear quadrilateral plane strain elements with reduced integration and hourglass control, referred to as CPE4R in Abaqus. The number of elements equalled the number of particles.

Figure 4.9 compares the centrelines of the rods predicted by both the FE analysis and the mixed correction Total Lagrangian calculations. As an even number of SPH particles were used along the width of the bar, the positions were linearly interpolated. The results were in good agreement, which indicated that the formulation with mixed correction will give superior results than the formulation without correction.

4.5 Off-centre rubber ring impact

The purpose of this example was to highlight the momentum and energy conserving properties of the proposed mixed correction formulation. In this example, only the Total Lagrangian formulation was considered. The Eulerian formulation was not used, as the ring impact problem requires the use of artificial stress for Eulerian particles. Artificial stress and its application to the coupled mixed correction formulation are discussed in the next section. Following Gray et al. [30], the rubber rings had an inner radius of 3 cm and an outer radius of 4 cm. Gray originally orientated the particles on a square grid in order to facilitate numerical fracture due to the tensile instability. In this numerical example, the particles were ordered by keeping an approximate arc and radial distance of 0.1 cm between particles, resulting in 2418 particles per ring. The ring's mechanical properties were taken from Falahaty et al. [132] with bulk modulus $K = 3.25 \times 10^6$ Pa and shear modulus $\mu = 7.15 \times 10^5$ Pa. A density of $\rho = 1050$ kg/m^3 and impact velocity of 8 m/s were chosen. The artificial viscosity parameters were set to $\alpha = 0.2$ and $\beta = 0.4$. The left-hand side ring was offset vertically by 2 cm to induce post-impact rotation.

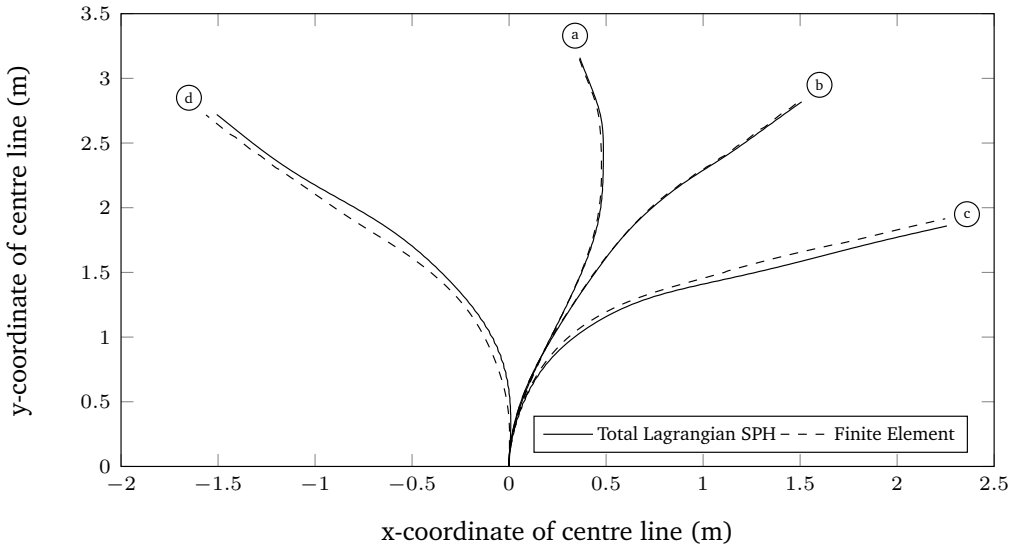

Figure 4.9: Coordinates of the column centre line at four stages in time for both the mixed correction Total Lagrangian formulation and Finite Element analysis. These times are (a) 0.224 s (b) 0.537 s (c) 1.791 s and (d) 3.583 s.

In the Total Lagrangian formulation, the rates of change are calculated with respect to the initial configuration of particles and as a result, a contact algorithm was required for the rings to collide. The contact algorithm developed by Vignjevic et al. [127] was used. This only depends on the distance between particles and user defined penalty parameters, as discussed in Section 3.7.3. These were set to $K_{\text{ca}} = 5 \times 10^9$ and $n_{\text{ca}} = 4$. In keeping with the Courant condition, the time step was set to $\Delta t = 3.56\,\mu\text{s}$. Four tests were run. The first two used no correction and mixed correction without artificial viscosity and the last two were run with artificial viscosity. This was done to demonstrate the preservation properties of both the mixed correction formulation and the proposed form of corrected artificial viscosity.

Figure 4.10 displays the rings' positions before and after impact. In each of the four simulations, the rings impacted off-centre, deformed, began rotating and then travelled in opposite directions. No numerical fracture was observed as the Total Lagrangian formulation was used. Figure 4.11 displays the evolution of total, kinetic and internal energy for the SPH simulations both with and without mixed correction. It would appear that the total energy was conserved, as expected for the SPH method. Figure 4.11 also displays the energy evolution but with the proposed form of mixed correction artificial viscosity. This plot appears to confirm that the mixed correction artificial viscosity conserves energy and has a similar effect to the conventional artificial viscosity used without correction. Figure 4.12 displays a magnified view of the total energy lines displayed in Figure 4.11. On inspecting this plot, it is evident that neither the mixed correction formulation nor the formulation without any correction conserved total energy exactly. It would appear that an error has been introduced by the Predict, Evaluate, Correct time integration scheme. Interestingly, the artificial viscosity appears to reduce this error significantly. In order to confirm that this error was introduced by the time integration scheme, the time step was halved to $\Delta t = 1.78\,\mu\text{s}$. Figure 4.12 displays the total energies over time for the smaller time step. Clearly, halving the time step has reducing the error in the total energy, confirming that the error is a product of the PEC time integration.

(a) 0 ms **(b)** 5.69 ms **(c)** 11.38 ms **(d)** 22.76 ms

Figure 4.10: Off-centre rubber ring positions before and after impact. Modelled using the Total Lagrangian formulation with mixed correction and artificial viscosity ($\alpha = 0.2$ and $\beta = 0.4$). Contact between the rings was handled using the contact algorithm ($K_{\text{ca}} = 5 \times 10^9$ and $n_{\text{ca}} = 4$). The time of the four frames from left to right is 0 ms, 5.69 ms, 11.38 ms and 22.76 ms. The rings collide into each other and compress. The collision causes the rings to start rotating as they translate.

A plot of linear momentum is not given as it remained on the order of 10^{-14} (machine precision) for all cases. This is expected as the velocities of the two rings should have been equal and opposite and all pairwise internal forces were equal and opposite.

Figure 4.13 displays the evolution of the angular momentum. Only the mixed correction formulation appears to have conserved angular momentum. The angular momentum is non-zero as the total angular momentum for a particle system is given by

$$L = \sum_{i=1}^{N} (\mathbf{r}_i \times m_i \mathbf{v}_i) \ , \tag{4.3}$$

where L is the total angular momentum $\mathbf{r}_i$ is the particle distance from the origin and $\mathbf{v}_i$ is the particle velocity relative to the origin. This can be simplified by considering the two rings rather than individual particles. The centre of mass of the left-hand side ring is located at (99.9580, 100.0400) and the centre of mass of the right-hand side ring is located at (100.0420, 100.0000). The rings have an equal and opposite velocity in the horizontal direction, zero velocity in the vertical direction and have equal mass. Therefore, the total angular momentum about the origin is given by

$$L = m_{\text{ring}} v_{\text{ring},x} (r_{2,y} - r_{1,y}) = -0.4062 \ \text{kgm}^2/\text{s} \ , \tag{4.4}$$

where m_{ring} is the mass of one ring, $v_{\text{ring},x}$ is the magnitude of the horizontal velocity of a ring and $r_{1,y}$ and $r_{2,y}$ are the vertical distances between the centres of gravity of both rings and the origin.

Figure 4.14 displays a magnified view of angular momentum for the mixed correction formulation with and without artificial viscosity. The mixed correction Total Lagrangian formulation, without artificial viscosity conserved angular momentum to machine precision. It is evident that the addition of artificial viscosity to the mixed correction Total Lagrangian formulation resulted in an error being introduced into the conservation of angular momentum. In Section 2.4.4 it was demonstrated that angular momentum will only be guaranteed if the pair-based internal forces about the origin caused by neighbouring particles sums to zero. It was consequently shown that this could be guaranteed, without correction, if the stress tensors were isotropic. In Section 3.2 artificial viscosity was modified for a Total Lagrangian formulation. This required the use of the deformation gradient, and consequently converted the artificial viscosity term from a multiple of the identity matrix to some

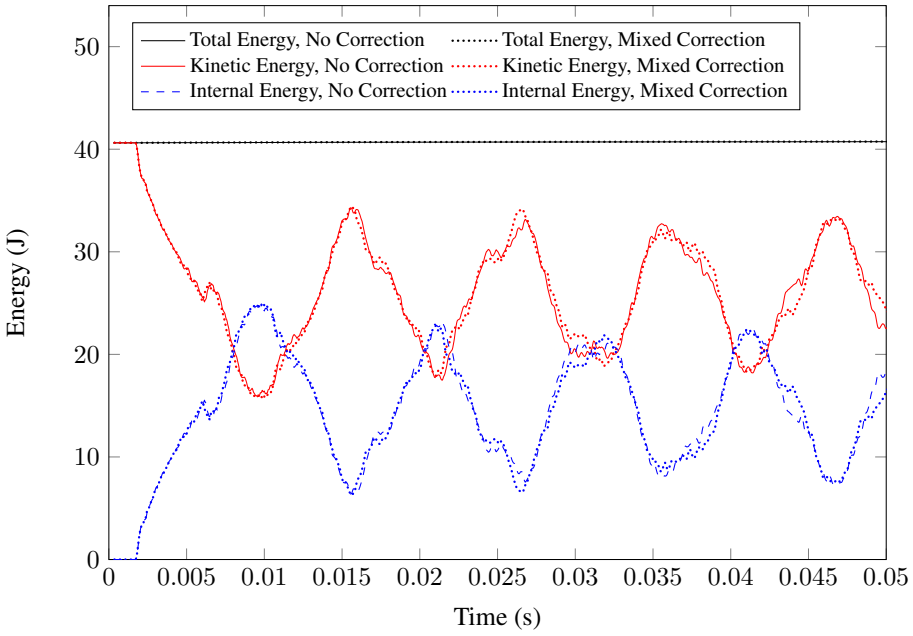

(a)

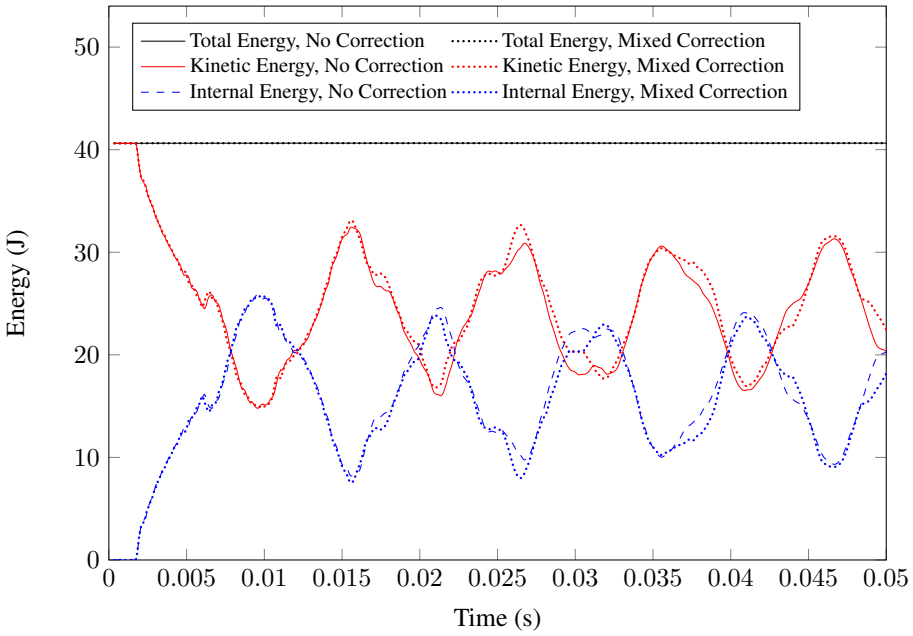

(b)

Figure 4.11: Plots of the total, internal and kinetic energy vs. time for the off-centre rubber ring collision with standard SPH and mixed correction SPH. (a) has no artificial viscosity whilst (b) has artificial viscosity with $\alpha = 0.2$ and $\beta = 0.4$.

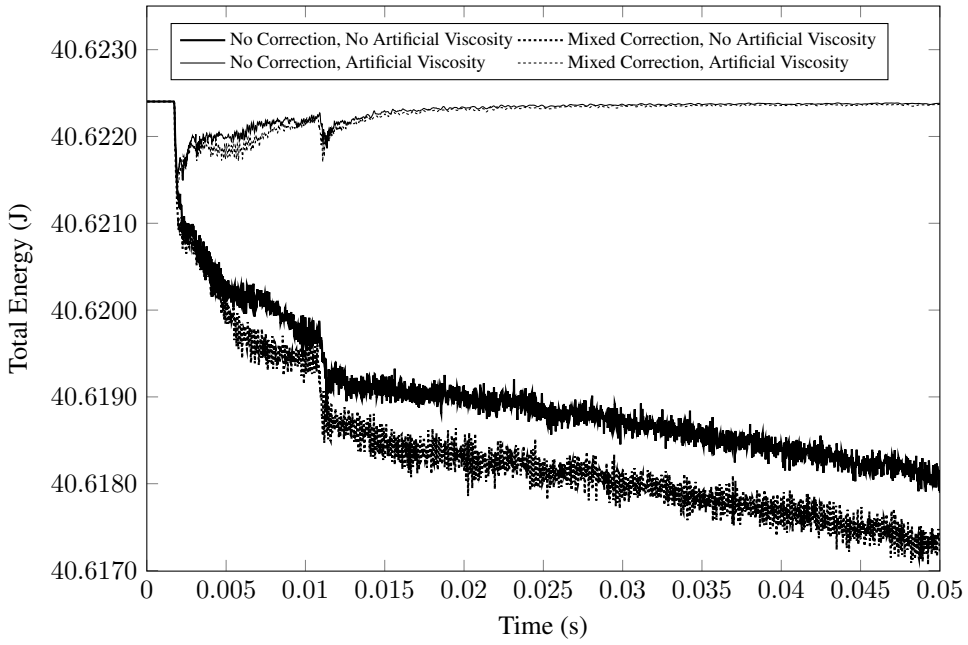

(a)

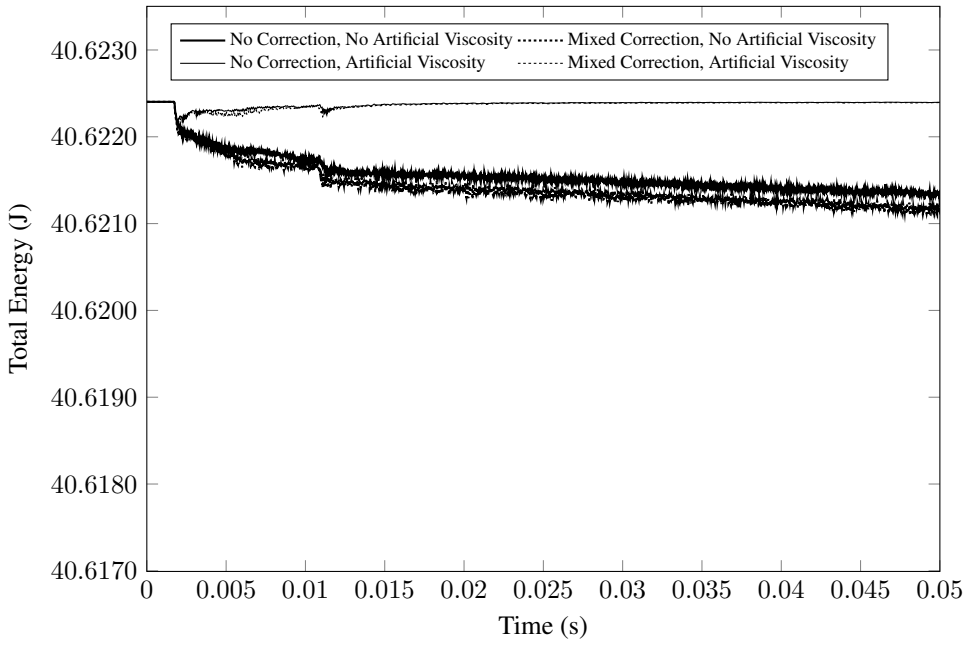

(b)

Figure 4.12: Plots of total energy vs. time for the off-centre rubber ring collision for the Total Lagrangian formulation with four different combinations of mixed correction and artificial viscosity for time steps (a) $\Delta t = 3.56\,\mu s$ and (b) $\Delta t = 1.78\,\mu s$.

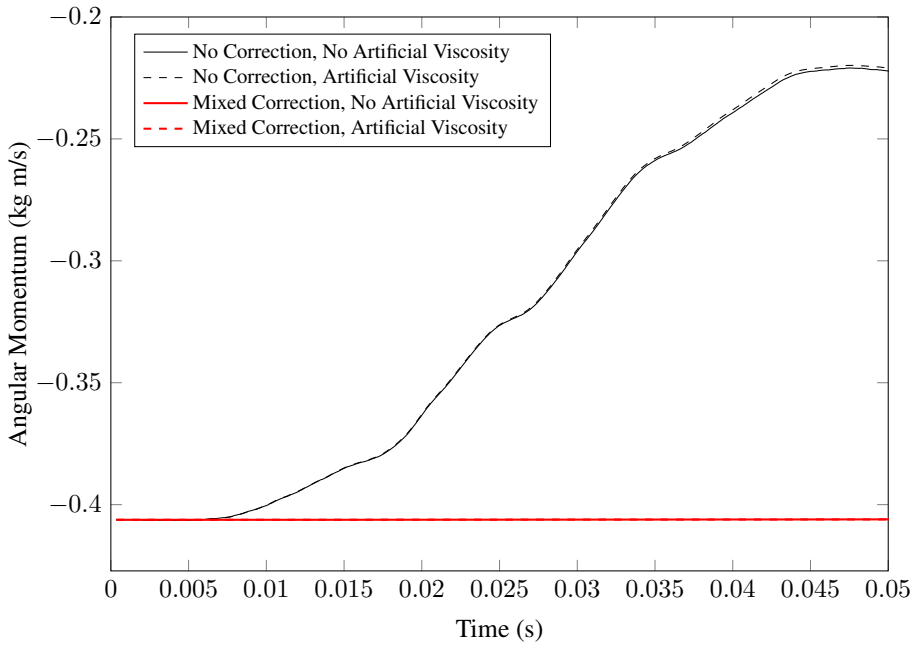

Figure 4.13: Plot of angular momentum vs. time for the off-centre rubber ring collision with and without mixed correction and with and without artificial viscosity.

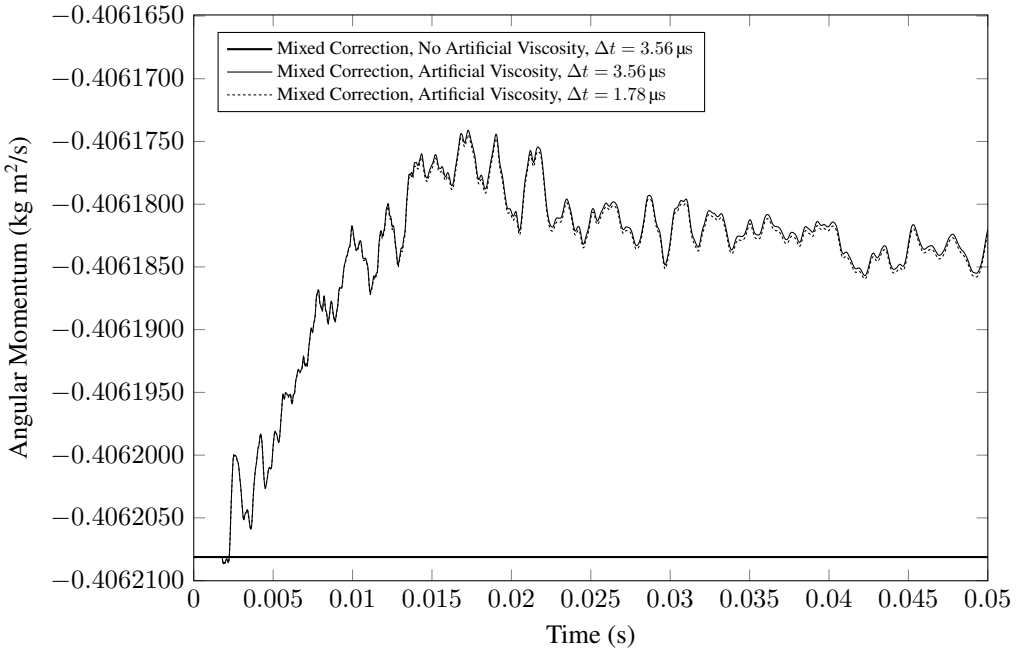

Figure 4.14: Plot of angular momentum vs. time for the off-centre rubber ring collision for the Total Lagrangian formulation with mixed correction and with and without artificial viscosity.

non-diagonal matrix. Hence, the internal forces caused by the Total Lagrangian form of artificial viscosity no longer result in moments about the origin that sum to zero. It is speculated that this could be the source of this error in the angular momentum. This theory was tested by again halving the time step to $\Delta t = 3.56\,\mu s$ and plotting the angular momentum for the mixed correction Total Lagrangian formulation with artificial viscosity. This too is visible on Figure 4.14 where it can be seen that the time step had close to no effect on the error in the angular momentum, indicating that the aforementioned theory is plausible.

From this numerical example, it is evident that the proposed form of symmetrical mixed correction conserves both linear and angular momentum exactly. Exact energy conservation was not achieved due to an error introduced by the time integration scheme. Artificial viscosity reduced this error but resulted in the approximate, rather than exact, conservation of angular momentum.

4.6 Coupled artificial stress implementation

The test presented by Swegle, Hicks and Attaway [24] was recreated in order to highlight the effectiveness of artificial stress with the Eulerian mixed correction formulation and the coupled mixed correction methods. Swegle et al. highlighted the tensile instability by applying a velocity perturbation to a single particle in a stationary two-dimensional square body of size 0.02 m by 0.02 m. They discretised the domain using a uniform particle spacing of $\delta x = 0.001$ m and applied a velocity of $v = 1\,\mu$m/s. Swegle et al. pointed out that a compressive stress does not alter the particle positions as the initial velocity perturbation is small. Additionally, they noted that a tensile stress leads to the instant clumping of particles and the creation of voids. They noted this phenomenon regardless of whether the problem was run in one, two or three dimensions. Reveles [109] presented a modified form of this test in his PhD thesis, where he replaced the velocity perturbation with a tensile pressure and applied this to all particles in the domain.

In this example, a 1 m $\times$ 1 m square body was discretised by 100×100 particles. The intial condition was a uniform pressure of 10 Pa, applied to a patch of size 0.5 m $\times$ 0.5 m in the centre of the body. The pressure was initially 0 Pa elsewhere in the domain. Unlike Swegle et al. [24] or Reveles [109] the boundary particles were not fixed and the domain was free to contract and expand periodically, much like in the patch test explored by Ganzenmüller [36]. A schematic of this test is displayed in Figure 4.15. In Chapter 2, the Cauchy stress tensor was defined as $\boldsymbol{\sigma} = \boldsymbol{\sigma}' - p\mathbf{I}$. Therefore, in this test the initial condition for both the Cauchy stress and first Piola-Kirchhoff stress was given by $\boldsymbol{\sigma} = \mathbf{P} = -p\mathbf{I}$. The material was modelled as linear elastic with density $\rho = 1$ kg/m^3, Young's modulus $E = 1$ Pa and Poisson's ratio $\nu = 0.3$. As this test was intended to be illustrative rather than physical, the material parameters were not of great importance. The cubic spline kernel was used, following Swegle et al. The smoothing length was fixed with $h = 1.2\delta x$. Artificial viscosity was implemented with the parameters set to $\alpha = 0.2$ and $\beta = 0.4$. The time step was calculated to be $\Delta t = 2.59$ ms. This test was simulated using a Total Lagrangian and an Eulerian mixed correction formulation. Figure 4.16 displays the results of both after 180 steps or 0.46 s. From this figure, it is clear that the Total Lagrangian formulation remained stable whilst the Eulerian formulation exhibited the tensile instability. This is evident due to the clear clumping of particles and the voids that formed. Following this snapshot, the Eulerian simulation became unstable due to the growth

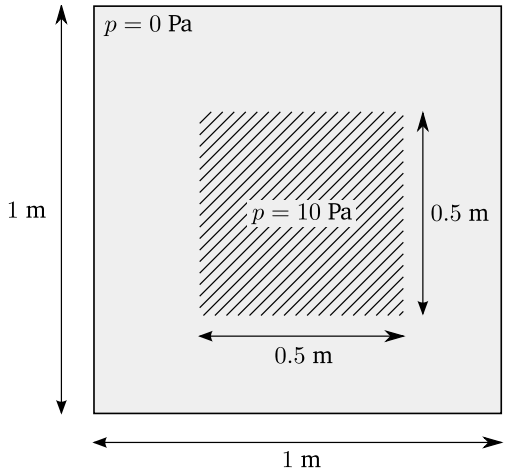

Figure 4.15: Schematic of the two-dimensional tensile instability test. An initial condition of tensile pressure of 10 Pa is applied to the central patch of size 0.5 m × 0.5 m.

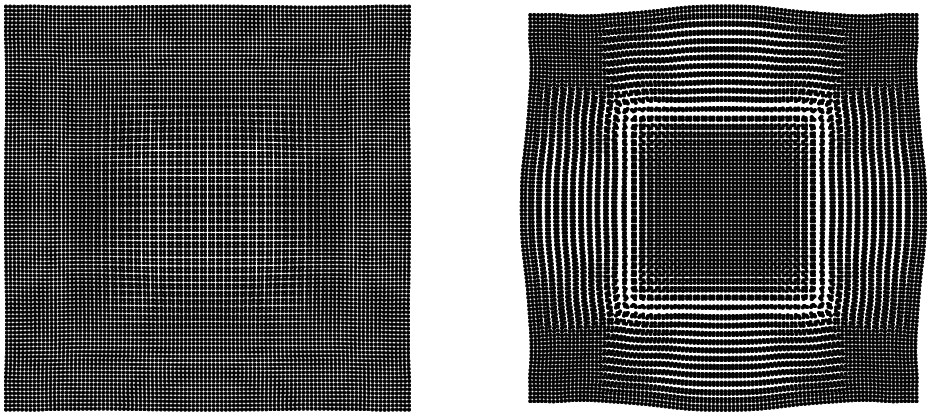

(a) Total Lagrangian formulation

(b) Eulerian formulation

Figure 4.16: Particle positions of the (a) Total Lagrangian formulation and (b) the Eulerian formulation both with mixed correction and artificial viscosity ($\alpha = 0.2$ and $\beta = 0.4$) after 0.46 s. The Eulerian formulation exhibits the tensile instability as shown by the particle clumping and voids.

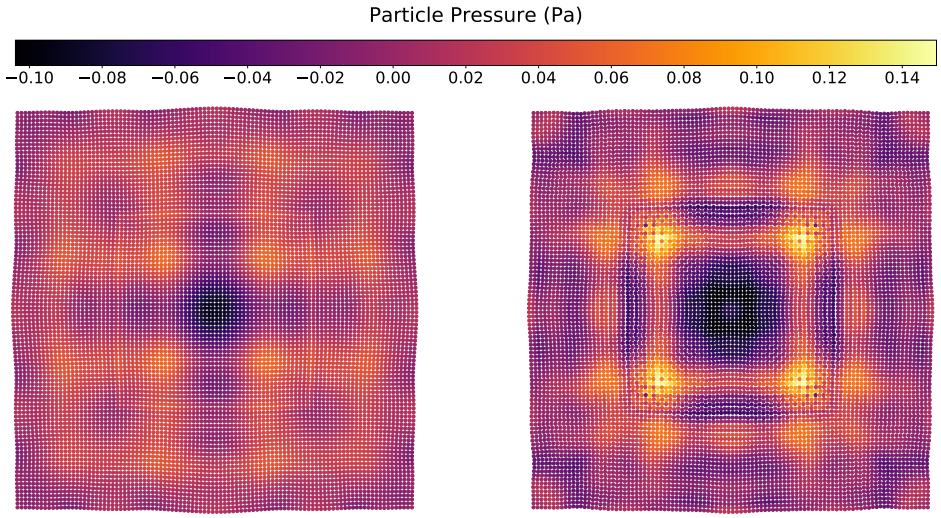

(a) Total Lagrangian formulation

(b) Eulerian formulation with artificial stress

Figure 4.17: Particle pressures calculated from the (a) Total Lagrangian formulation and (b) the Eulerian formulation with artificial stress ($n_{as} = 4$ and $\epsilon_{as} = 0.3$) after 1.29 s. Both formulations use mixed correction and artificial viscosity ($\alpha = 0.2$ and $\beta = 0.4$). The Eulerian formulation no longer exhibits the tensile instability, although some slight clumping is still visible.

of particle velocity, caused by the tensile instability. The mixed correction formulation of artificial stress, as detailed in Section 3.3, was then applied to the Eulerian particles. The artificial stress parameters were set to $n_{as} = 4$ and $\epsilon_{as} = 0.3$. These values were selected as Gray et al. [30] found that $n_{as} = 4$ was best when using the cubic spline function as it restricts the impact of artificial stress to nearest neighbours. Figure 4.17 compares the pressure found using the Total Lagrangian formulation to that found using the Eulerian formulation with artificial stress after 500 time steps or 1.29 s. Although the tensile instability was much reduced, some clumping is still visible. It is also noted that the maximum pressure was approximately 2.23 times larger in the Eulerian formulation with artificial stress than in the Total Lagrangian formulation. This was most likely due to the excessive stress that was introduced through artificial stress. The minimum pressures were similar, differing by approximately 12.05 %. In both cases, the deformed shapes were similar. The Eulerian formulation was re-tested with $n_{as} = 3$ and $n_{as} = 2$. The results were not presented here due to the similarity with $n_{as} = 4$. It was observed that for $n_{as} = 3$ and $n_{as} = 2$ the void increased in size. Considering that n_{as} controls the range over which the artificial stress operates, this would appear to be reasonable.

Having defined a benchmark using the Total Lagrangian formulation and the Eulerian formulation with artificial stress, the coupling methods were tested with artificial stress. This was done by splitting the domain horizontally into two halves. The top half was populated by particles with an Eulerian kernel and the bottom half by particles with a Total Lagrangian kernel.

The first coupling method with artificial stress was implemented using two approaches, as discussed in Section 2.6 and Section 3.3. Firstly, artificial stress was only applied to particles with an Eulerian kernel, as the Total Lagrangian formulation does not exhibit the tensile instability. Secondly, artificial stress was applied to Total Lagrangian particles in the interface zone (see Section 2.6) in addition to all the Eulerian particles. The reasoning for this approach was that the Total Lagrangian particles in the interface zone received acceleration contributions from Eulerian particles using an Eulerian kernel. Consequently, the tensile instability could manifest in Total Lagrangian particles in the interface. Figure 4.18 displays the results of both approaches after 500 time steps. It can be seen

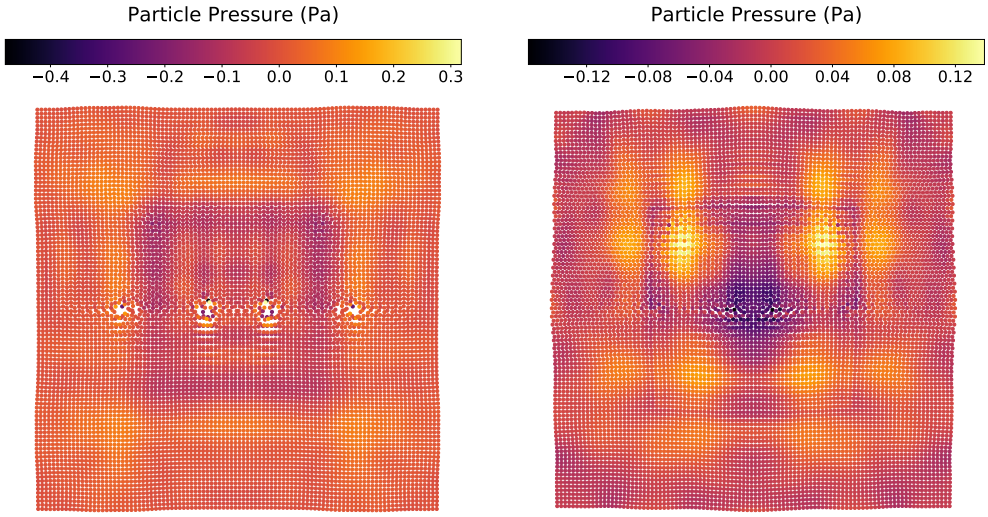

(a) No artificial stress used in the interface

(b) Artificial stress used in the interface

Figure 4.18: Scatter plot coloured by particle pressure for a domain which is top half Eulerian and bottom half Total Lagrangian with the first coupling method after 1.29 s. Mixed correction and artificial viscosity ($\alpha = 0.2$ and $\beta = 0.4$) are used. Artificial stress ($n_{as} = 4$ and $\epsilon_{as} = 0.3$) is applied (a) only to Eulerian particles (b) to Total Lagrangian particles in the interface as well as to Eulerian particles. Both cases exhibit an instability in the interface.

that neither of these two approaches worked as intended due to the instability that is present at the interface. Note that, in this case, the interface is a horizontal band of width $4\delta x$ that bisects the domain. Different colour bars were used for Figures 4.18(a) and 4.18(b) as the pressure range was significantly larger for the former. In addition to having a pressure range which far exceeded that found in the fully Total Lagrangian test (Figure 4.17(a)), or the fully Eulerian test with artificial stress (Figure 4.17(b)), the approach which did not include artificial stress in the interface was far more unstable than the approach which did. In Figure 4.18(a), four large voids are visible along the interface, which included the peak and minimum pressure. Figure 4.18(b) does not contain these large voids but it does display symmetrical particle clumping near the centre of the domain, across the interface. From Figure 4.18 it is evident that artificial stress should be applied to the Total Lagrangian particles in the interface as well as the Eulerian particles. Although this may eliminate the tensile instability, it causes a secondary instability at the interface. It is for this reason that this coupling method is not implemented in scenarios where tensile stresses may cause the tensile instability to manifest.

Artificial stress could be reasonably implemented in three different ways, considering the second coupling method, as discussed in Section 2.6. Either no artificial stress could be used between the Eulerian and Total Lagrangian interface pairs, artificial stress could be used for both the Eulerian and Total Lagrangian interface pairs, or artificial stress could be calculated using both kernel types in the interface but only be applied to the Eulerian particles. The third approach does not conserve momentum and energy as the pair-based values would not be equal and opposite. Regardless, all three approaches were tested and were found to produce highly similar results. Figure 4.19 displays the results for the second approach. No instabilities are found at the interface using this coupling method. The bottom half of the domain is similar to the Total Lagrangian simulation in Figure 4.17(a) and the top half of the domain is similar to the Eulerian simulation in Figure 4.17(b). The range of pressure values (−0.09 Pa to 0.12 Pa) is slightly lower than for the non-coupled simulations (−0.10 Pa

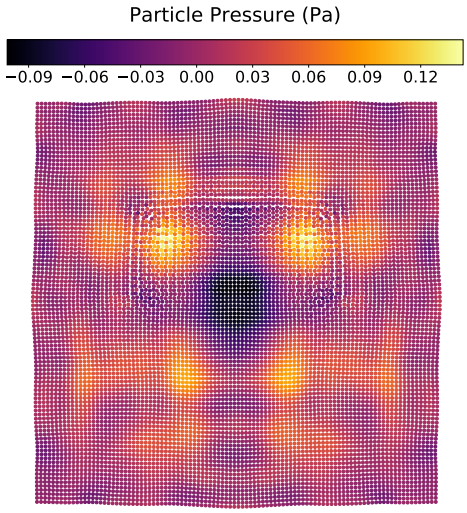

Figure 4.19: Scatter plot coloured by particle pressure for a domain which is top half Eulerian and bottom half Total Lagrangian with the second coupling method after 1.29 s. Mixed correction and artificial viscosity ($\alpha = 0.2$ and $\beta = 0.4$) are used. Artificial stress ($n_{as} = 4$ and $\epsilon_{as} = 0.3$) is applied to Total Lagrangian particles in the interface as well as to Eulerian particles.

to 0.14 Pa) but still in good agreement. Most importantly, the pressure can be seen to transition smoothly across the interface. The only notable difference between the three approaches, apart from minor differences in values of pressure (maximum difference of 3.6 % in peak pressure), was that the third approach produced particles which were slightly shifted upwards by approximately 1.2 mm, most likely due to the unequal pairwise internal forces at the interface.

4.7 Uniaxial Compression

The aim of this example was to validate the proposed coupling methods against the conventional Eulerian and Total Lagrangian formulations. Firstly, it is shown that the Eulerian formulation produces results that are consistent with the Total Lagrangian formulation, with and without mixed correction. This is also demonstrated for the modified form of artificial viscosity. Once this has been verified, the effectiveness of the coupling procedures are demonstrated. Only the first coupling method is evaluated, as both methods give the same results for small displacements. Das and Cleary [79], who evaluated the accuracy and stability of the classical SPH method under uniaxial compression, were revisited. In their work, they used no correction schemes. The same geometry, material, and loading conditions were used as given in their work and displayed in Figure 4.20. In this test, a specimen of Crossley sandstone of height 140 mm and width 82 mm was axially loaded. The sandstone had a Young's Modulus $E = 7.4654$ GPa, a Poisson's ratio $\nu = 0.3980$ and a density $\rho = 2300$ kg/m^3. Using the relationship given by Woan [100] for the longitudinal elastic wave speed in a thin plate as $c = \sqrt{E/(\rho(1-\nu^2))}$, the speed of sound was calculated as $c = 1964$ m/s. The specimen was fixed at the bottom whilst the compressive force was applied to the top by a constant velocity piston of $v = 1.5$ mm/s. The specimen was regularly discretised into 140×82 particles, each of area 1 mm^2. No virtual particles were used. Artificial viscosity as given in Equations 3.6 and 3.8

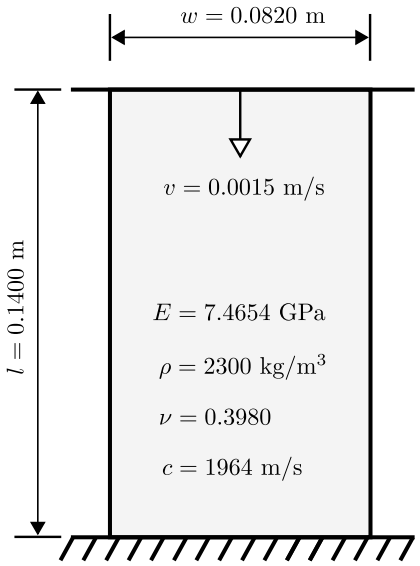

Figure 4.20: Schematic of a two-dimensional uniaxial compression test with dimensions, loading condition and material properties labelled.

was used. In keeping with Das and Cleary, the artificial viscosity parameters were set to $\alpha = 1.0$ and $\beta = 2.0$. Although used by Das and Cleary, artificial stress was not used in this example, as the tensile instability did not manifest. Four different combinations of Eulerian and Total Lagrangian particle arrangements were evaluated. These are (i) fully Eulerian (ii) fully Total Lagrangian (iii) top half Total Lagrangian, bottom half Eulerian and (iv) random distribution of Eulerian and Total Lagrangian. Each of these was evaluated with and without mixed kernel-and-gradient correction. The results were compared using the von Mises stress σ_{vm} as it gives a scalar quantity with which the stress tensor can be evaluated. The von Mises stress is given by

$$\sigma_{\text{vm}} = \sqrt{\sigma_{\text{xx}}^2 - \sigma_{\text{xx}}\sigma_{\text{yy}} + \sigma_{\text{yy}}^2 + 3\sigma_{\text{xy}}^2} \tag{4.5}$$

in terms of general stress components in two dimensions. It was evaluated at the centre of the specimen for comparative purposes. The results were compared to those predicted by a FE analysis in Abaqus FEA. This FE model comprised of quadratic quadrilateral plane stress elements with reduced integration, referred to as CPS8R in Abaqus. The number of elements equalled the number of particles.

Figures 4.21 and 4.22 display the calculated von Mises stress at the centre of the specimen over 100 µs. Figure 4.21 shows that the Eulerian and Total Lagrangian formulations gave equal results regardless of the combination of correction and symmetry terms. Figure 4.21 also confirms that this was the case when the modified form of artificial viscosity was included. Again, it can be seen that all combinations of correction and symmetry terms gave the same results. As the uncorrected Total Lagrangian and uncorrected Eulerian formulations gave the same results, it appears that the transformation from a Cauchy type artificial stress to a first Piola type artificial stress was a valid approach. Likewise, both formulations produced equal results for the mixed correction. Figure 4.22 displays the results of the simulations that combined particle types in the domain. The fully Total Lagrangian results are included as a reference. Figure 4.22 shows that the combined particle type simulations gave the same results as the fully Total Lagrangian reference, both with and without

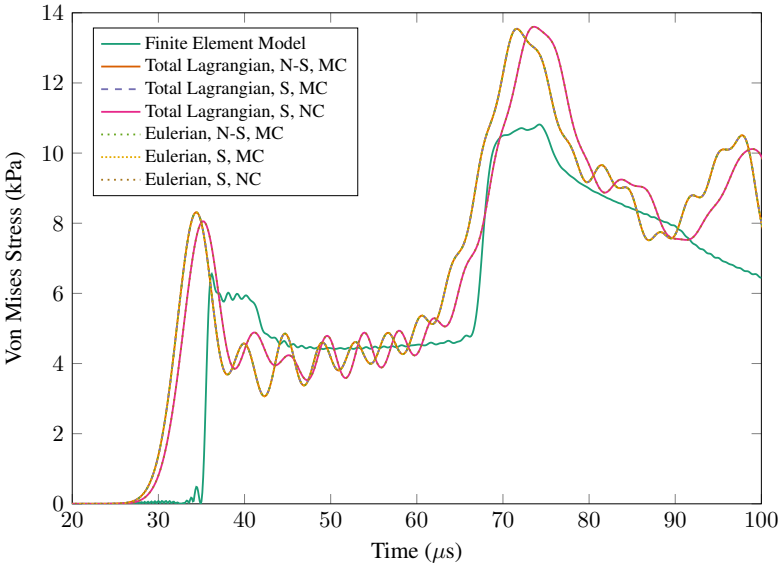

N-S : Non-symmetrical, S : Symmetrical, MC : Mixed Correction, NC : No Correction

(a)

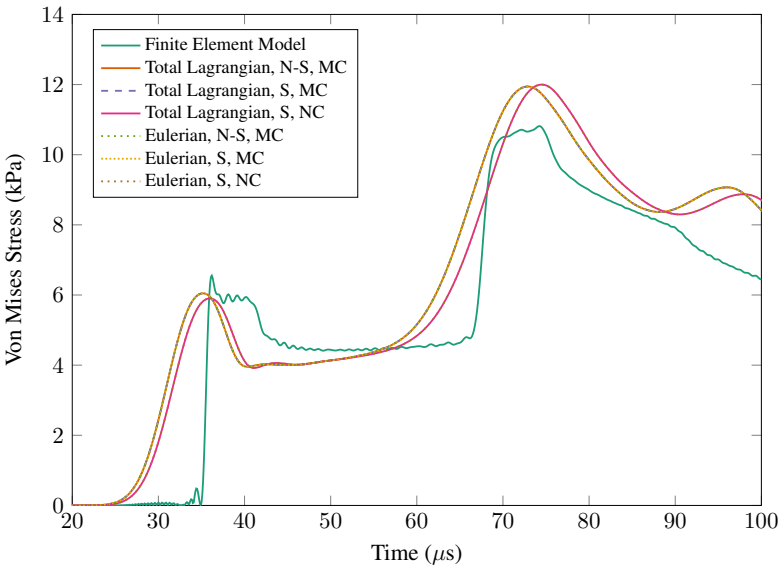

N-S : Non-symmetrical, S : Symmetrical, MC : Mixed Correction, NC : No Correction

(b)

Figure 4.21: Von Mises stress of particle located at the centre of the specimen from 20 to 100 µs for Total Lagrangian and Eulerian formulations with and without mixed correction. (a) has no artificial viscosity and (b) has $\alpha = 1.0$ and $\beta = 2.0$. FE result included for comparison. In both (a) and (b) the formulations with mixed correction are equal regardless of Eulerian and Total Lagrangian kernel type and symmetry terms. The same is true for the formulations with no correction.

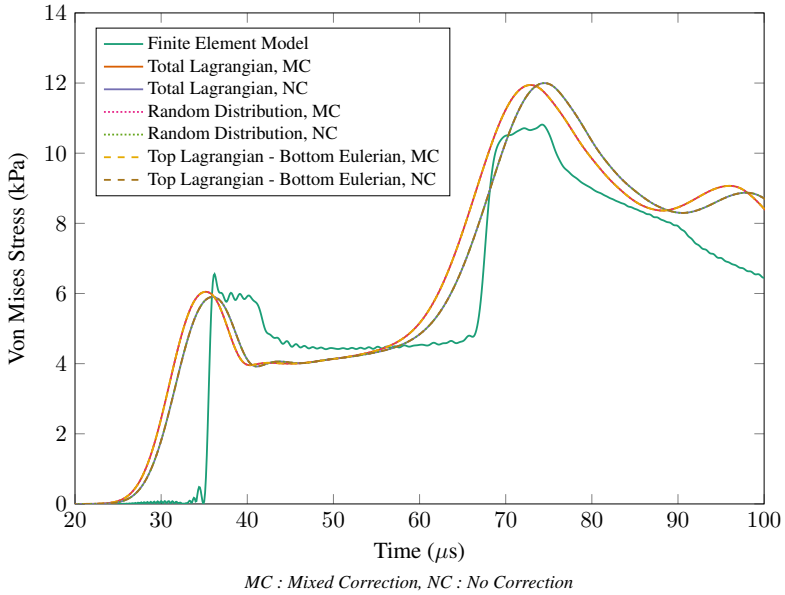

Figure 4.22: Plot of the von Mises stress of the particle located at the centre of the specimen from 20 to 100 µs for the mixed particle types with and without mixed correction. Modified form of artificial viscosity is used. FE result included for comparison. The results are independent of mixed particle type and are equal for the cases with mixed correction. The same is true for the cases with no correction.

mixed correction. Although the FE results were only included as a reference, it can be seen that the SPH results were generally in good agreement with them.

4.8 Taylor impact test

In order to validate the three-dimensional implementation of the proposed formulation, along with the Johnson-Cook plasticity model, a Taylor impact test as detailed by Johnson and Holmquist [103] was evaluated. From this reference, case E-1 (page 3901) was explored as it uses all components of the Johnson-Cook plasticity model. In this case, an OFHC copper cylinder of length 25.4 mm and diameter 7.6 mm impacted a rigid surface with velocity 190 m/s. The material specific constants were given by $A_{\mathrm{JC}} = 98$ MPa, $B_{\mathrm{JC}} = 368$ MPa, $C_{\mathrm{JC}} = 0.025$, $\dot{\epsilon}_0 = 1$ s^{-1}, $M_{\mathrm{JC}} = 1.09$ and $N_{\mathrm{JC}} = 0.70$. An OFHC copper melting temperature of $T_{\mathrm{m}} = 1083$ °C and specific heat capacity of $C_{\mathrm{v}} = 383$ J/kg°C were taken from Zhou et al. [133]. The ambient temperature was fixed at $T_{\mathrm{r}} = 20$ °C. The contact algorithm parameters were set to $K_{\mathrm{ca}} = 7.5 \times 10^{17}$ and $n_{\mathrm{ca}} = 4$ in order to model the interaction between the cylinder and the ground. The artificial viscosity parameters were set to $\alpha = 0.2$ and $\beta = 0.4$. Following Ma et al. [134], the particles were equally spaced by 0.38 mm such that the cylinder was formed by 21172 particles and the smoothing length was set to $h = 1.2\delta x$. A mixed

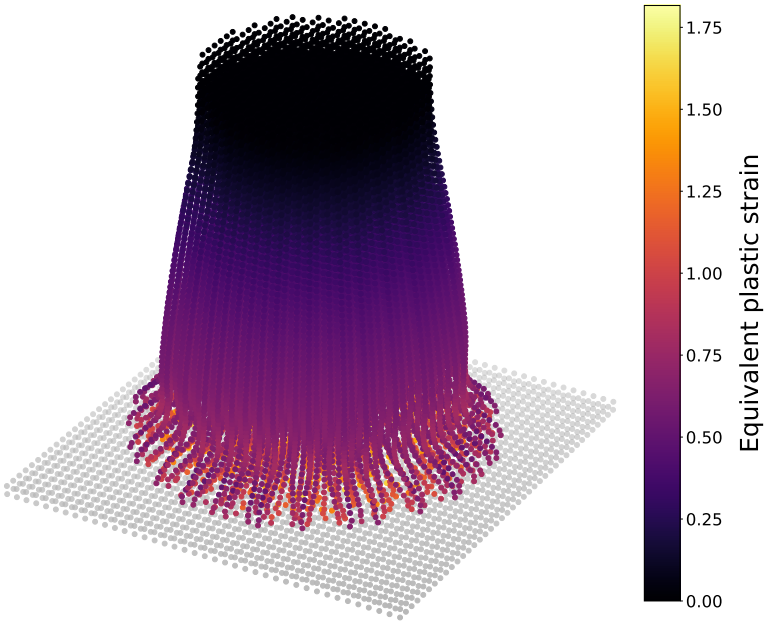

Figure 4.23: Deformed shape of a copper cylinder after impacting a rigid surface modelled using the Johnson-Cook plasticity model. The particles are coloured by equivalent plastic strain. The mixed correction Total Lagrangian formulation was used with artificial viscosity ($\alpha = 0.2$ and $\beta = 0.4$) and the contact algorithm ($K_{\text{ca}} = 7.5 \times 10^{17}$ and $n_{\text{ca}} = 4$).

correction Total Lagrangian formulation was used. Johnson and Holmquist defined an average error between simulation and experimental results as

$$\bar{\Delta} = \frac{1}{3}\left(\frac{|\Delta L|}{L} + \frac{|\Delta D|}{D} + \frac{|\Delta W|}{W}\right). \tag{4.6}$$

In this equation the denominators refer to the experimental deformed length $L = 16.2$ mm, the deformed diameter at the base $D = 13.5$ mm and the bulge width $W = 10.1$ mm, which was measured at one fifth of the original length from the base. The Δ terms refer to the differences between the experimental and numerical results. Figure 4.23 displays the deformed shape of the cylinder after impact with the particles coloured by equivalent plastic strain $\bar{\epsilon}_{\text{p}}$. The deformed length, diameter and bulge width were found to be 16.72 mm, 12.77 mm and 10.01 mm, using this deformed shape. Using these values, an average error of $\bar{\Delta} = 0.032$ was calculated. In Zhou et al.'s [133] simulation of the Taylor impact problem, with conventional Eulerian SPH, they found that increasing the artificial viscosity decreased the diameter of the deformed cylinder and increased the length. As the SPH results of this analysis under-predicted the diameter and over-predicted the length, it is speculated that fine-tuning the artificial viscosity parameters may further improve results. This average error was found to be acceptable considering that Ma et al. [134] found conventional Eulerian SPH to give an average error in the range of $0.047 - 0.075$, due to the tensile instability, and found the Material Point Method to give much improved results with an average error of 0.031. Although the results obtained are promising, it must be stated that in Johnson and Holmquist's original analysis, their FE calculations gave an average error of $\bar{\Delta} \approx 0$. Figure 4.24 displays a cross-section of the deformed cylinder both from the mixed correction Total Lagrangian simulation and from the original Finite Element analysis by Johnson and Holmquist [103] . This figure also highlights the particles' locations

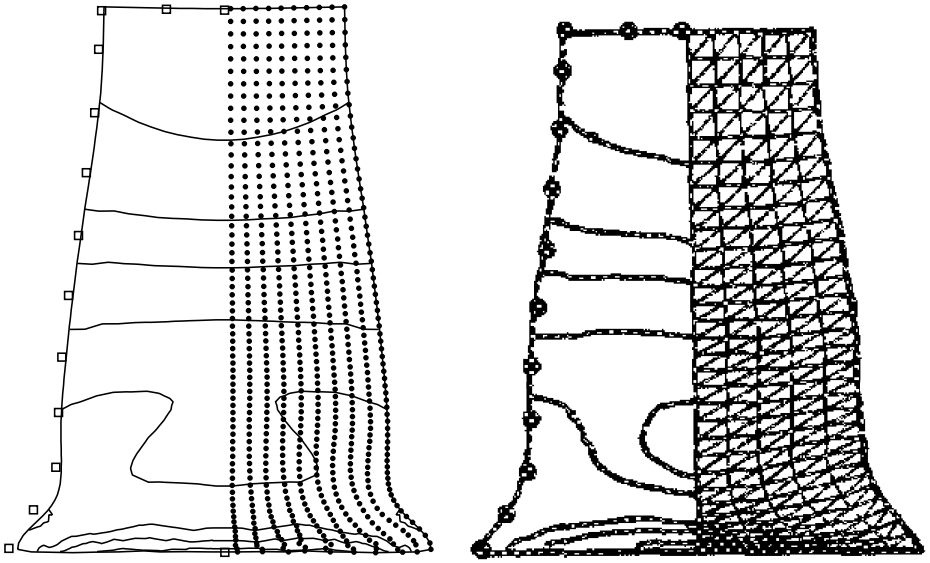

(a) (b)

Figure 4.24: Cross-section of the deformed copper cylinder post impact for (a) the mixed correction Total Lagrangian formulation and (b) the Finite Element results from Johnson and Holmquist [103]. Contours of equivalent plastic strain are shown at $0.1, 0.3, 0.4, 0.5, 0.6, 1.0, 1.2, 1.5$ following Johnson and Holmquist. The square markers represent the experimental test data, which was digitized from Johnson and Holmquist.

along with contours of effective plastic strain at $0.1, 0.3, 0.4, 0.5, 0.6, 1.0, 1.2, 1.5$ and experimental test data, which was digitised from Johnson and Holmquist [103]. It should be mentioned that the actual boundary of the domain is offset by $\delta x/2$ from the boundary displayed in this figure. This has been taken into account in the calculation of the average error. Digitising the experimental points will have introduced an error due to the resolution of the original publication and only serve as an indication of the experimental results. Regardless, it is clear that the SPH results are in good agreement with the experimental data. The contour plot is also highly similar with that given by Johnson and Holmquist. It is noted that the maximum effective plastic strain given by the SPH simulation was 1.82 whilst Johnson-Cook's FE calculations predicted a maximum effective plastic strain of 1.64. This represents a discrepancy of $\approx 10\ \%$. In simulating the Taylor impact test, Bonet and Kulasegaram [33] also noted that SPH produced a larger $\bar{\epsilon}_p$ than a FE analysis. These authors stated that the discrepancy was small but did not give quantitative results. It is feasible that this discrepancy could be minimized by manipulating the artificial viscosity parameters as the over-predicted length may have played a role in the over-predicted effective plastic strain.

It should be noted that a number of parameters used in this simulation do not have a physical basis and hence could be tuned to minimise $\bar{\Delta}$, although this was not done. The standard values of $\alpha = 0.2$ and $\beta = 0.4$ were used for the artificial viscosity, as used for the majority of numerical examples in this chapter and commonly chosen in literature. The contact algorithm parameter n_{ca} plays a similar role to n_{as} in the artificial stress. As the cubic spline smoothing function was used, this value was set to $n_{ca} = 4$ to restrict the impact of the contact algorithm to nearest neighbours, as done for the artificial stress when used. This was done for all examples in this chapter that made use of the contact algorithm. The only parameter, without a physical basis, which was specifically selected for this problem was K_{ca}, the contact algorithm stiffness penalty parameter. The value of

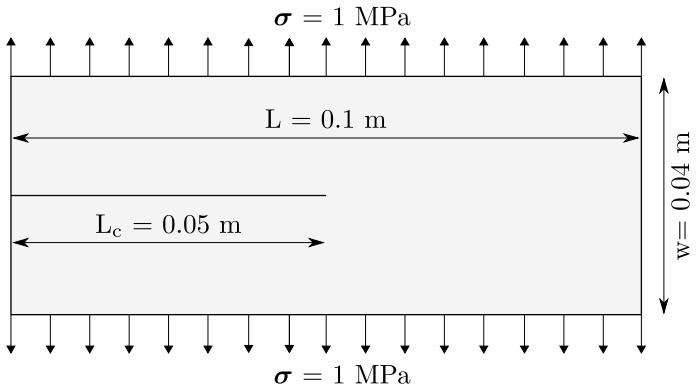

Figure 4.25: Schematic of the two-dimensional crack branching problem. Traction forces are imposed along both long edges of a pre-notched specimen resulting in crack propagation.

this parameter had to be selected so that the copper cylinder did not penetrate the rigid boundary particles but was halted just above it. As this parameter does not have a physical basis, it must be modified for every problem that makes use of the contact algorithm.

4.9 Crack branching problem

Crack formation and propogation is now investigated, having verified and validated the ability of the mixed correction formulation to accurately model elastic, hyper-elastic and plastic response. The two-dimensional crack-branching problem was explored. This has been successfully modelled previously using the Element Free Galerkin (EFG) meshless method [55, 57, 59] and the Extended Finite Element Method (XFEM) [19]. It is noted that these publications differ in values for the Young's modulus and fracture snapshot times. Experimental results are similarly available [135, 136]. In this simulation, the model set-up was taken from Belytschko et al. [19]. Figure 4.25 provides an outline of the problem. This figure displays a specimen of length 0.1 m and width 0.04 m with a notch running half of its length. The specimen experienced tensile traction forces of 1 MPa along both of its long edges. Although not stated in the references, a thickness of 1 mm was assumed, resulting in a plane stress problem. The material properties were given by a Young's Modulus $E = 32$ GPa, Poisson's ratio $\nu = 0.2$ and a density $\rho = 2450$ kg/m^3. Two damage models were explored including the Rankine damage model, as explained in Section 3.6.1, and the Lemaitre damage model, as detailed in Section 3.6.2. As the yield stress of the material was not given, a value of $\sigma_y = 5$ MPa was assumed. Batra and Lears [137], who explored the simulation of crack propagation, discussed failure criteria. In their work, they stated that brittle failure occurred when some ratio of the maximum tensile principal stress to the yield stress ($\sigma_{p,max}/\sigma_y$) was reached. They quoted values from literature, including $\sigma_{p,max}/\sigma_y = 2.0$, 2.34 and 3.0. In their work, they assumed that failure occurred when $\sigma_{p,max}/\sigma_y = 2.0$ and were followed by Raymond et al. [95] who applied this failure criterion to the Kalthoff–Winkler problem. In the problem simulated here, the Rankine damage model was activated when $\sigma_{p,max}/\sigma_y = 2.5$, which was seen to be in-line with the aforementioned values. When applying the Lemaitre damage model, the corresponding parameters were set to $A_L = 1.0$, $B_L = 7300$ and

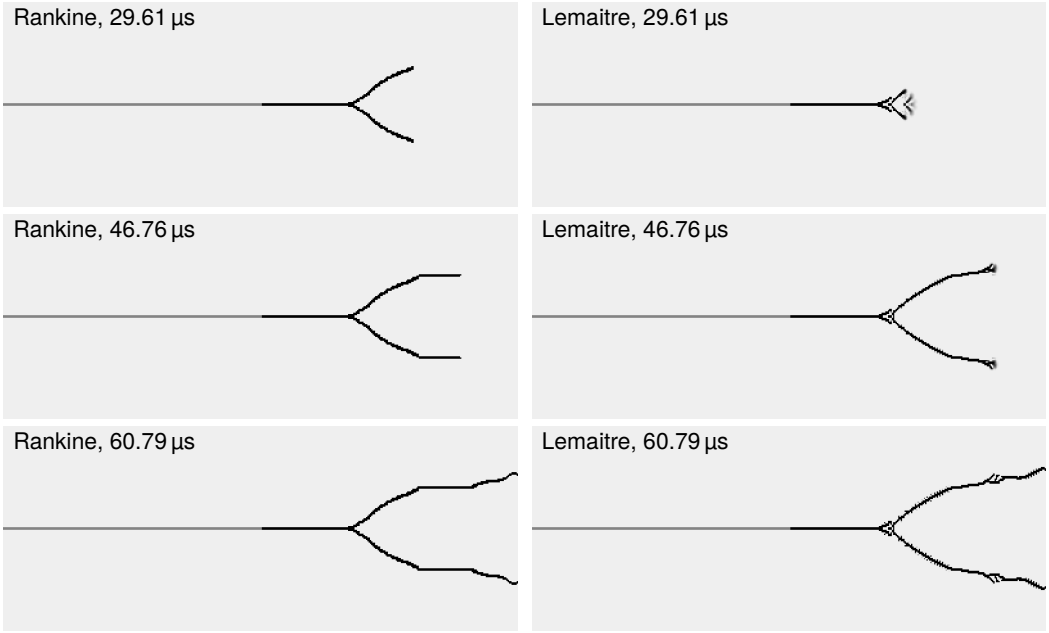

Figure 4.26: Snapshots of the crack propagation and branching for both (a) the Rankine damage model and (b) the Lemaitre damage model at times 29.61, 46.76 and 60.79 µs. Damage is denoted by the black colouring. The grey horizontal line which spans half of the specimen represents the initial notch. The mixed correction Total Lagrangian formulation was implemented with artificial viscosity ($\alpha = 0.2$ and $\beta = 0.4$).

$\epsilon_{D_0} = 8.5 \times 10^{-5}$. As the Lemaitre damage model requires the equivalent strain, the out-of-plane strain was calculated from

$$\epsilon_{zz} = -(\nu/E)(\sigma_{xx} + \sigma_{yy}) \tag{4.7}$$

for this two-dimensional plane stress problem. Consequently, the equivalent strain was calculated using the full strain tensor.

The specimen was discretised with 64,000 particles arranged on a grid of 400 by 160. Raymond et al. [95] stated that the explicit representation of notches produced more accurate results than modelling them using fully damaged particles. Although they stated this for the Kalthoff–Winkler problem, the same concept was applied here and the notch was modelled by removing two rows of particles for half the length of the specimen. The traction of 1 MPa was converted into a distributed force of 100 N and was applied instantaneously. The smoothing length was fixed at $h = 1.2\delta x$ and the artificial viscosity parameters were set to $\alpha = 0.2$ and $\beta = 0.4$. A mixed correction Total Lagrangian formulation was implemented to verify the ability of the method to correctly reproduce crack branching.

Figure 4.26 displays three snapshots in time for the Rankine and Lemaitre damage models. Note that the grey horizontal line which spans half of the specimen represents the initial notch. In these snapshots, the particle data has been interpolated back onto a uniform grid for visualisation purposes. The black colouring represents the particles' damage. In the snapshots which make use of the Lemaitre damage model, damage can be seen to appear and disappear. This is because in the Lemaitre damage model the value of damage can vary between 0 and 1, unlike the Rankine damage model which is binary. The Lemaitre damage model is dependent on the equivalent strain which varies depending on the value of particle stress.

In both cases, the crack propagated longitudinally away from the notch and then branched symmetrically until reaching the end of the specimen. It was expected that the crack branches would be symmetrical considering the geometrical symmetry and the symmetrical nature of the conservation equations. It can be seen that the Rankine model resulted in the crack branching earlier than the Lemaitre model and a less curved crack path. The snapshots presented in Figure 4.26 were taken at approximately the same times as those presented by Belytschko et al. [19] and Rabczuk et al. [55] and are in good agreement. The results are also similar to those presented by Rabczuk et al. [57]. Rajagopal and Gupta [59] also investigated the crack branching problem in their comparative study of different meshfree methods for modelling fracture. They noted two defining features of the problem, these being that the crack branches after approximately 0.3 ms and again after 0.5 ms and that the crack speed is limited by the Rayleigh wave speed. Note that these authors must have used an alternative model set-up, as their snapshot times are different, though the key features should be the same. As seen in the previous figure, the simulation that used the Lemaitre damage model fractured at approximately 30 μs yet neither damage model resulted in a second crack branching. This second crack branching was similarly not captured by Belytschko et al. [19] and Rabczuk et al. [57]. As those more complex models did not capture the secondary branching it is understandable that the simple methodology used here was similarly incapable. It should also be stated that in Belytschko et al. [19] the crack began to propagate at 11.34 μs whilst in the model presented here propagation initiated at approximately 6 μs. It is speculated that this is due to the implementation of different methods, XFEM and SPH, and different crack models: simple damage models and discontinuous enrichment.

It should be noted that in the comparative study by Rajagopal and Gupta [59], the crack branching problem was modelled using a Total Lagrangian EFG formulation. The authors used four fracture models, one of which involved the Rankine criterion. Using three discretisations of 101×41, 201×81 and 401×161, these authors found that this model produced non-symmetrical results with spurious crack patterns. The results presented here may differ from those presented by Rajagopal and Gupta due to the selection of $\sigma_{p,max}/\sigma_y$.

The Rayleigh wave speed can be calculated following Freund [138], who approximated is by $c_R/c_s = (0.862 + 1.14\nu)/(1 + \nu)$, where c_R is the Rayleigh wave speed and c_s is the shear wave speed given by $c_s = \sqrt{G/\rho}$ =2332 m/s, which gave $c_R = 2119$ m/s. In order to track the crack front a simple algorithm, which was tailored towards this problem, was implemented. At every time step each particle with a damage value 0.9999 or over was inspected. The particle which was furthest to the right and above the symmetry plane, was recorded as the crack front. The minimum distance between any of the previous particles, which represented the crack front and the new crack front particle, along with the time taken for the crack front to change position, was used to calculate the crack front velocity. This required the positional history of the crack front to be stored. The advantage of this approach was that it was conceptually simple and straightforward to implement. The disadvantage was that it required a small time step as the crack front speed was an approximate multiple of the inter-particle distance and the time step. Using this approach, the crack front speed was found not to exceed the Rayleigh wave speed with a maximum crack front speed of 2101 m/s.

The results obtained using the Rankine criterion were found to be sufficient considering that they were only required for comparative purposes in this example. However, it is noted that they could be improved by varying the failure criterion ratio along with finding a more precise value for the yield stress.

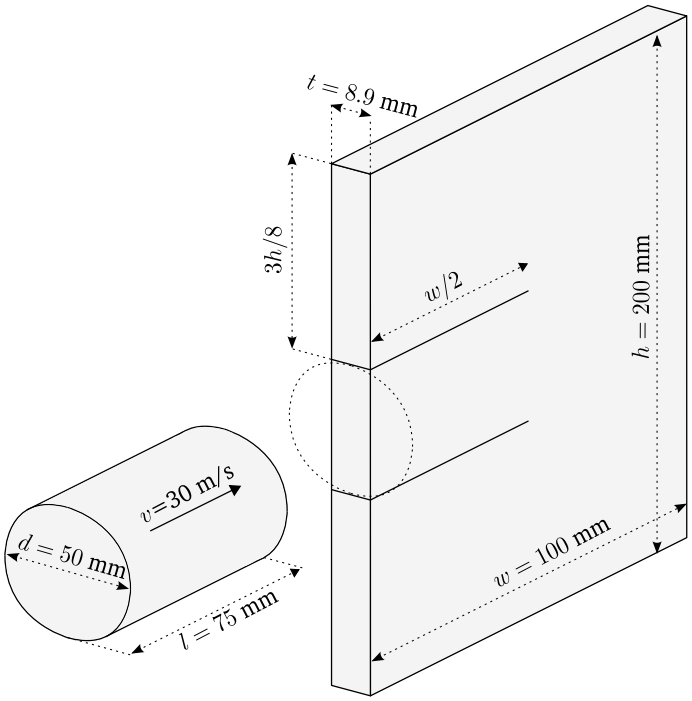

Figure 4.27: Schematic of the three-dimensional Kalthoff-Winkler problem. A cylindrical rod impacts a stationary pre-notched plate, between its two notches, resulting in either brittle or ductile fracture.

4.10 Kalthoff-Winkler problem

Kalthoff and Winkler [139] observed two distinct failure modes in their eponymous experiment, these being brittle failure and ductile failure. In their experiment, a cylindrical rod impacted a stationary double notched plate, as displayed in Figure 4.27. Depending on the impact velocity of the rod, the plate fractured either through brittle or ductile failure. For lower velocities, cracks formed through brittle failure at the end of the notches and travelled at approximately 70 ° (upper notch) and −70 ° (lower notch) to the horizontal, towards the upper and lower edges of the plate. Above some threshold velocity, the failure mode transitioned from brittle to ductile failure. In this scenario, two shear bands formed at the end of the notches and travelled at approximately -10° (upper notch) and 10° (lower notch) from the horizontal, towards the right-hand side of the plate.

As the constitutive model and damage algorithms discussed thus far are well suited to brittle fracture, this is the case investigated to further validate the proposed formulation. Raymond et al. [95] and Chakraborty and Shaw [48] previously simulated this problem using SPH. Raymond et al. used an Eulerian formulation with no correction along with both the Rankine criterion (Section 3.6.1) and Johnson-Cook plasticity model (Section 3.5.3). Chakraborty and Shaw similarly used an Eulerian formulation but with gradient correction and a pseudo-spring based fracture model, which those authors developed. The Kalthoff-Winkler experiment has also been simulated by Belytschko et al. [19] who used the XFEM and Rabczuk et al. [57] who implemented the XEFG method. Only Raymond et al. [95] modelled the problem in three dimensions.

In the example presented here, the dimensions and material properties have been taken from Raymond et al. [95] who modelled both the rod and plate as 4340 steel. It is noted that Raymond et al. took their model set-up from Batra and Lear [137] and Kalthoff and Winkler [139]. The

dimensions of the rod and plate are given in Figure 4.27. The material properties included a shear modulus $G = 73.1$ GPa, a bulk modulus $K = 158$ GPa and a density $\rho = 7830$ kg/m^3. The material specific Johnson-Cook parameters were $A_{JC} = 792$ MPa, $B_{JC} = 510$ MPa, $C_{JC} = 0.014$, $\dot{\epsilon}_0 = 1$ s^{-1}, $M_{JC} = 1.03$ and $N_{JC} = 0.26$. The reference and melting temperatures of 4340 steel were set to $T_r = 298$ K and $T_m = 1793$ K, and the specific heat capacity was given by $C_v = 477$ J/kgK. Raymond et al. [95] stated that they set the limiting principal stress, in the Rankine criterion, to twice the yield stress, following Batra and Lear [137], yet in their table of material data they stated a value of 1500 MPa, which corresponds to a factor of 1.89. This value of 1.89 was used in what follows. It is noted that Raymond et al. also arranged their particles at 45° to the horizontal as this was found to produce the most accurate results. This was not done here as it was considered to pre-empt the predicted crack path. Both Chakraborty and Shaw [48] and Raymond et al. [95] explicitly modelled the notches by removing rows of particles. An alternative approach is presented here, whereby the kernel visibility between particles on either side of a notch was restricted. According to Batra and Lear [137], the failure mode transitions from brittle to ductile at an impact speed of approximately 54 m/s. Therefore, the rod speed of 30 m/s used by Raymond et al. was found to be reasonable.

Two planes of symmetry were exploited, using the methodology explained in Section 3.7.1, allowing for only a quarter of the domain to be modelled. In order to compare the results meaningfully against those of Raymond et al., the same particle spacing of $\delta x = 1.0$ mm was used. Raymond et al. made use of the cubic spline smoothing function, although they did not state the smoothing length. For this problem $h = 1.3\delta x$ was found to produce acceptable results. Although Raymond et al. used artificial viscosity, they did not state the corresponding parameters and consequently $\alpha = 0.2$ and $\beta = 0.4$ were chosen here. It is speculated that Raymond et al. used the conventional Eulerian conservation equations to model the contact between the rod and plate. In the results presented here, the contact potential algorithm was implemented with parameters $K_{ca} = 1.0 \times 10^{16}$ and $n_{ca} = 4$. Note that ghost particles were required to contribute in this contact algorithm in order for symmetry to be satisfied. Lastly, the model was discretised using mixed correction Total Lagrangian particles.

Figure 4.28 displays a cross-section of particles located at mid thickness of the rod and plate. The brittle fracture path is shown by the damaged particles that have been coloured black. The slope was found to be approximately 68° if drawing a straight line from the initial point of fracture to the end. From this figure, it can be seen that the fracture starts close to vertical and propagates at around 62°. Following an additional vertical section the fracture path then propagates at 75°.

The sensitivity of the problem to the number of particles was tested. Interestingly, this was not done by the authors who used SPH, these being Raymond et al. [95] and Chakraborty and Shaw [48], but it was done by Belytschko et al. [19] and Rabczuk et al. [57] who used other methods. The particle spacing was halved to $\delta x = 0.5$ mm, resulting in 828,300 particles. In order to prevent inter-particle penetration, the contact potential parameters had to be modified to $K_{ca} = 2.0 \times 10^{16}$ and $n_{ca} = 4$. The crack fractured prematurely and curved to the right-hand side, rather than the upper side, when using Raymond's original value of 1.89 for the Rankine criterion. Increasing the Rankine criterion to 2.15 times the yield stress produced results similar to that achieved with the smaller number of particles. Figure 4.29 displays a cross-section of particles located at mid thickness of the rod and plate for the finer resolution. Aside from the Rankine criterion and contact potential, all other parameters remained unchanged. In this figure, a near vertical crack path is found at the edge of the notch. This is followed by a curved crack path and a vertical section. Lastly, there is a final kink prior to reaching the upper edge of the plate. As the Rankine fracture criterion is dependent on the maximum principal stress, it would appear sensible that an increase in the number of particles would require an amendment to the Rankine criterion. This is because an increase in the

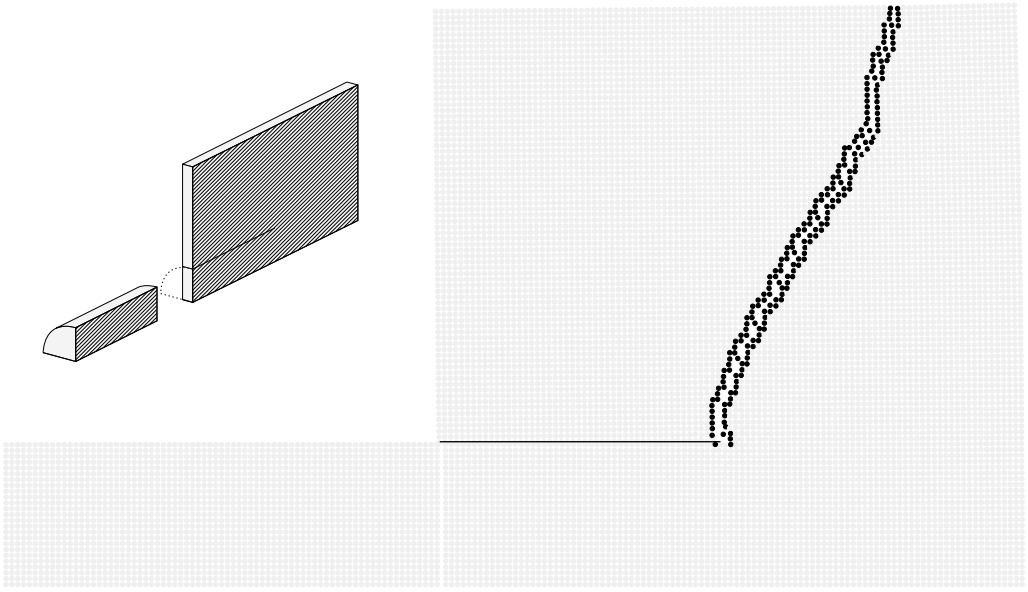

Figure 4.28: Cross-section of particles in a Kalthoff-Winkler simulation at mid thickness of the rod and plate with $\delta x = 1.0$ mm. Due to the use of symmetry planes only half of the cross-section is shown. The black coloured particles are damaged particles and represent the brittle fracture, which should

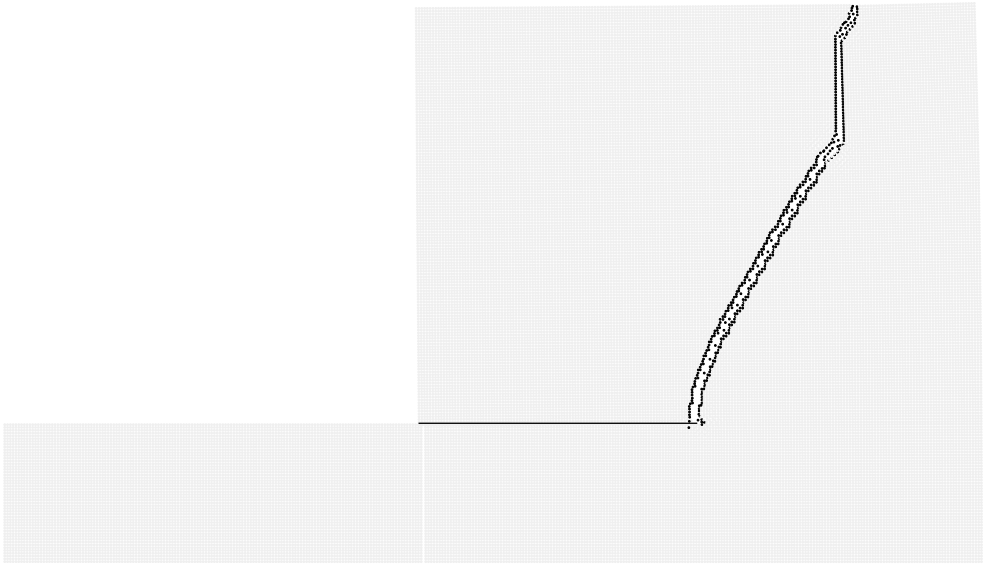

Figure 4.29: Cross-section of particles in a Kalthoff-Winkler simulation at mid thickness of the rod and plate with $\delta x = 0.5$ mm. The black coloured particles are damaged particles and represent the brittle fracture which should propagate at approximately 70° to the horizontal. The black line represents the notch from which the fracture path propagates.

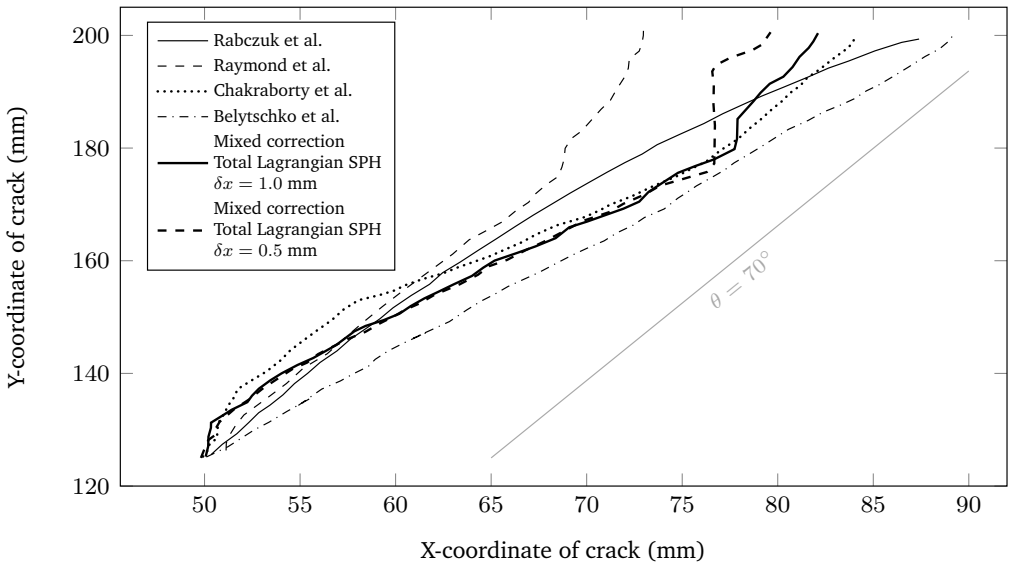

Figure 4.30: Comparison of the crack path found for the Kalthoff-Winkler problem. The mixed correction Total Lagrangian model (with δx = 1.0 mm and δx = 0.5 mm) is compared against others found in literature including Rabczuk et al. [57], Raymond et al. [95], Chakraborty and Shaw [48] and Belytschko et al. [19]. Those modelled with SPH are found to be less smooth than the other methods.

number of particles would increase the resolution of the stress at the end of the fracture path, until the solution had converged with the number of particles. Consequently, the fracture stress for the coarser resolution would not be appropriate for the fracture stress for the finer resolution.

Figure 4.30 compares the fracture path found using mixed correction Total Lagrangian SPH with δx = 1.0 mm and δx = 0.5 mm against the two-dimensional results obtained by Rabczuk et al. [57], Chakraborty and Shaw [48] and Belytschko et al. [19], and the three-dimensional results obtained by Raymond et al. [95]. It is noted that the results taken from literature have been digitised from the original publications and are therefore only representative. In comparing these results, it can be seen that Belytschko et al. obtained a near linear crack pattern using their finest XFEM mesh angled at 62°. Rabczuk et al. found the crack pattern to be quadratic in their finest XEFG results, with a crack angle of 70° at the notch. It is clear that the SPH crack patterns are the least smooth. The SPH results would appear to have a vertical or near vertical crack angle at the notch. The mixed correction Total Lagrangian results with δx = 1.0 mm show very similar features to that obtained by Raymond et al. in that, after the notch a near linear crack path is obtained followed by a vertical section and a secondary near-linear section. The results most likely differ as Raymond et al. orientated their particles at 45° to the horizontal. It is also interesting to note that the two mixed correction Total Lagrangian simulations produced very similar results up to 25 mm (horizontal distance) away from the notch. At this point, the finer discretisation displayed a larger vertical section. Regardless, both discretisations produce similar results to those given by Raymond et al. [95] and Chakraborty and Shaw [48]. That being said, the limits of this validation test should be discussed. The results were dependant on the Rankine criterion. This should be a material specific parameter but in the absence of experimental data, a Rankine criterion was estimated from literature. Additionally, the value used

for the Rankine criterion had to be adapted for the finer distribution of particles. Perhaps a more rigours validation test would make use of a fracture model that was solely dependent on material data and would not need to be modified depending on the distribution of particles.

4.11 High-velocity impact problem

The Eulerian, mixed correction, and coupled formulations were evaluated for a two-dimensional high-velocity impact problem involving a circular projectile impacting on a rectangular target. The purpose of this numerical example was to validate the Eulerian formulation with mixed correction for problems involving fracture and to highlight the effectiveness of the coupling methods. Howell and Ball [140], who used a free-Lagrange Method, originally simulated the problem. In the results presented here, the set-up was taken from Mehra and Chaturvedi [141] who applied different versions of the SPH method to this problem.

The circular projectile had a diameter of 1 cm and initial velocity of 3100 m/s. The rectangular projectile was 5 cm high and 2 cm wide. Both the projectile and the target were modelled as aluminium with a density $\rho = 2785$ kg/m^3 and a shear modulus $G = 27.60$ GPa [140]. Howell and Ball [140] gave the bulk sound speed as $c_0 = 5328$ m/s, which was converted to a bulk modulus through $K = \rho c_0^2 = 79.06$ GPa. Using these values, the Young's modulus was calculated to be $E = 74.17$ GPa and the Poisson's ratio to be $\nu = 0.344$. Mehra and Chaturvedi [141] calculated the pressure using a "stiffened gas" equation of state:

$$p = c_0^2(\rho - \rho_0) + (\gamma_0 - 1)\rho\frac{e}{m} \,. \tag{4.8}$$

In this equation c_0 is the bulk sound speed, ρ and ρ_0 have their usual meanings, γ_0 is the Gruneisen parameter, e is the internal energy, and m is the mass. As explained in Section 3.8, using an equation of state which is dependent on internal energy will result in energy not being exactly conserved. This is because it will make use of a predicted value, rather than a corrected value, of internal energy. The value of γ_0 was taken from Howell and Ball [140] as 2.00. Both the projectile and target were modelled as elastic-perfectly plastic (see Section 3.5.1) with a yield stress of $\sigma_y = 0.300$ GPa.

Mehra and Chaturvedi [141] modelled the projectile and target using 17,850 particles with a particle spacing of $\delta x = 0.01$ cm. These authors modelled the circular projectile using a rectangular grid for the majority of the body and two layers of particles arranged on the outer circumference of the projectile. This particle set-up was followed and is visible in Figure 4.31. Mehra and Chaturvedi [141] stated that they modelled the projectile using 7820 particles but this was assumed to be a typo as the projectile presented in Figure 4.31 contains 7830 particles and exactly matches the figure presented by these authors. In addition, it is noted that the particle spacing for the inner ring involves rounding down rather than rounding to the nearest integer. Subtracting the projectile leaves 10,020 particles for the rectangular target and it was therefore assumed that Mehra and Chaturvedi [141] modelled this as being 5.01 cm high. Mehra and Chaturvedi used a smoothing length of $h = 1.4\delta x$ along with the cubic kernel function. This was replicated in the present work. As these authors modelled the impact problem using conventional Eulerian SPH, it is assumed that no contact algorithm was implemented and that the momentum was transferred from the projectile to the target though the conservation equations.

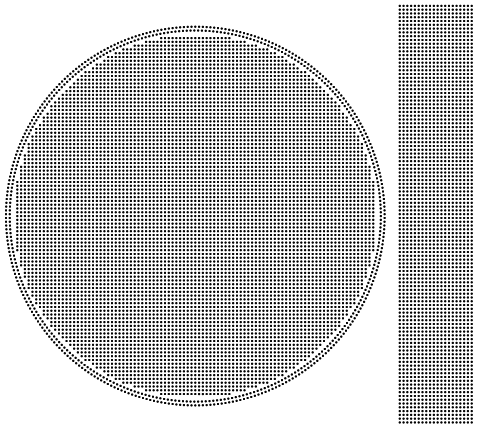

Figure 4.31: Initial particle position for the two-dimensional high-velocity impact problem. The circular projectile is populated by a rectangular distribution of particles encompassed by two rings of equally spaced particles. The circular projectile is formed by 7830 particles, which impact a rectangular target formed of 10,020 particles. The full target is not shown in this figure.

Mehra and Chaturvedi [141] modelled this problem using five types of SPH referred to as BAL, MON, CON, SAV1 and SAV2. SAV1 and SAV2 refer to conventional Eulerian SPH with artificial viscosity parameters $\alpha = 1, \beta = 2$ and $\alpha = 2.5, \beta = 2.5$. BAL referred to a scheme that made use of the Balsara switch. This switch was intended to prevent the use of excessive artificial viscosity. MON referred to a modification to artificial viscosity, as devised by Morris and Monaghan. Lastly, CON referred to an SPH formulation that solved the conservation equations by substituting a solution to the Riemann problem. Firstly, the symmetrical Eulerian formulation with no correction was applied in order to recreate SAV1. Figure 4.32 presents the particle positions of the upper half of the target and projectile 8 μs after impact. Only the upper half is required due to the problem symmetry. Impact was considered to commence in the time step when the support domains of the particles in the projectile and target overlapped. The results obtained by Mehra and Chaturvedi using BAL, MON, CON, SAV1 and SAV2 and the results found using the Eulerian formulation presented in this work are visible in this figure. It is evident that: the recreated SAV1 and the SAV1 presented by Mehra and Chaturvedi are very similar; the tensile instability spoiled both solutions due to the clumping of particles and voids in the projectile and the target; and the Riemann-based method CON produced the most plausible results with no particle clumping or voids. As an aside, it is noted that the total energy grew by 0.048 % after 8.68 μs for the recreated SAV1. This was found to be acceptable considering that Zhang and Liu [142] noted an energy decrease of 3 % after 20.00 μs in their simulation of this problem, albeit at an impact speed of 6180 m/s and with gradient correction.

A number of changes were considered in order to improve the results. These included the use of artificial stress, imposing a contact algorithm rather than using kernel contact as discussed in Section 3.7.3, and the application of mixed correction. These were evaluated in turn. Firstly, SAV1 was recreated with the inclusion of artificial stress with parameters $\epsilon_{as} = 0.3$ and $n_{as} = 4$. Secondly, SAV1 was recreated using the contact algorithm with parameters $K_{ca} = 2 \times 10^{12}$ and $n_{ca} = 4$. Thirdly,

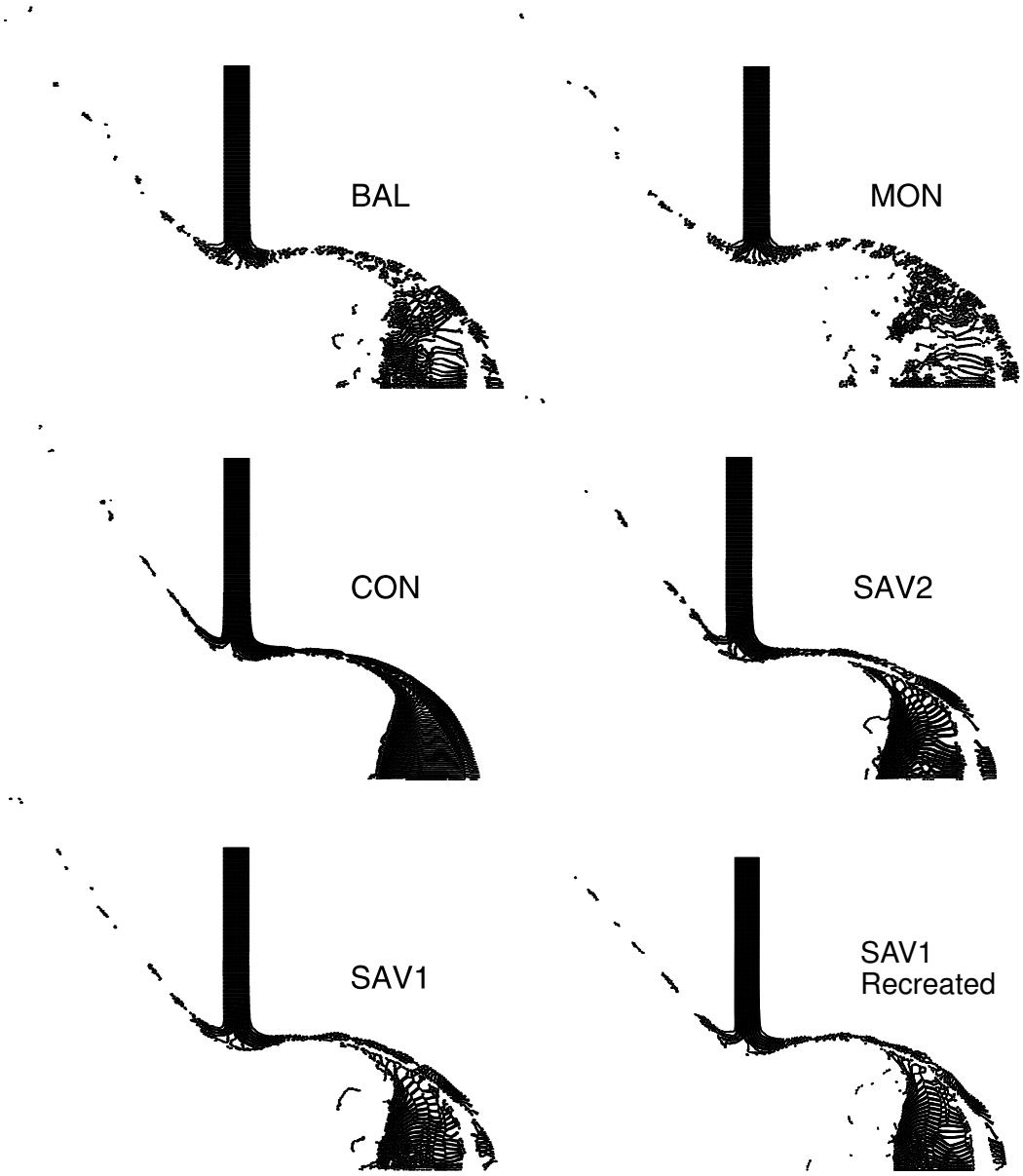

Figure 4.32: Particle positions of the high-velocity impact problem 8 μs after impact. Results for the BAL, MON, CON, SAV1 and SAV2 schemes are taken from Mehra and Chaturvedi [141]. The SAV1 scheme has been recreated to validate the Eulerian SPH formulation with no correction.

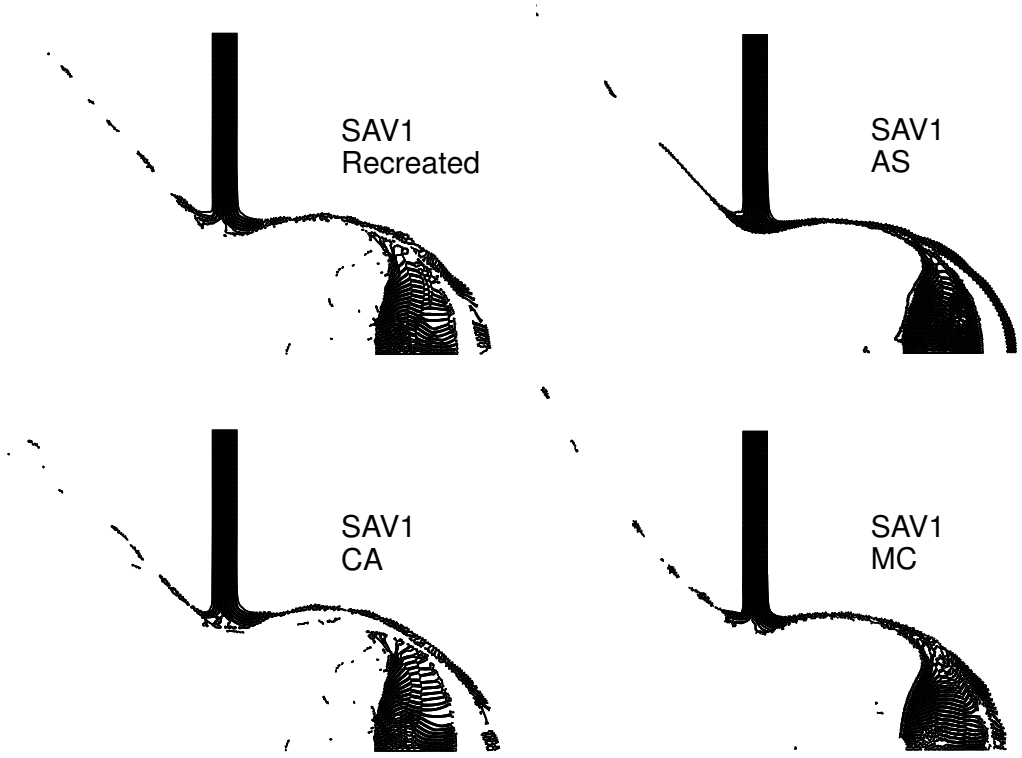

Figure 4.33: Particle positions of the high-velocity impact problem 8 µs after impact. The results are for the recreated SAV1 scheme from Mehra and Chaturvedi [141], SAV1 with artificial stress (AS), SAV1 with the contact algorithm (CA) and SAV1 with the adapted mixed correction (MC).

mixed correction was used for the SAV1 scheme. The results of each are compared against the recreated SAV1 8 µs after impact and are presented in Figure 4.33.

The implementation of mixed correction or gradient correction to simulations involving spallation is challenging. Spalled particles can have few, if any, nearest neighbours. Both the mixed correction and gradient correction scheme are dependent on the inversion of a matrix (Equations 2.117 or 2.118). This matrix is formed by the volume-weighted sum of the gradient of the corrected kernel $\nabla\widetilde{W}$ with the particle positions $\mathbf{x}$. Consequently, if a particle should only have one neighbour this matrix becomes singular, resulting in a non-invertible matrix. Some arrangement of particles with two or three neighbours can also result in a correction matrix $\mathbf{K}$, which produced large accelerations, spoiling the solution. Gradient correction, which is dependent on matrix inversion, can be applied to high-velocity impact problems as demonstrated by Zhang and Liu [142], though it is not clear how these authors dealt with the accompanying spurious accelerations. In this work, the following adaptation is proposed. All particles with only one neighbour (excluding themselves) revert to the conventional kernel gradient. For all other particles, the corrected gradient of the corrected kernel is compared against the conventional kernel gradient. If the difference between any two corresponding elements in these vectors differs by a pre-determined factor C_f then the mixed correction is neglected and the conventional kernel gradient is adopted. If the distance between particles is close to zero, in any dimension, then this rule is ignored for the corresponding element in the kernel gradient, as this will always be zero. In this case, the limiting factor was $C_\mathrm{f} = 7.5$. Ideally, this factor would be large so as to implement mixed correction wherever possible whilst preventing non-physical accelerations. It is immediately evident that this conversion from mixed correction to conventional non-corrected

Table 4.4: Pressure and geometric data for the high-velocity impact problem. P is the peak pressure at the centre of the projectile behind the leftward travelling shock wave, d_{cra} is the crater diameter, L_{extn} is the longitudinal extension (width) of the projectile and L_{proj} is the longitudinal distance travelled by the projectile measured from the leading edge. d_{cra}, L_{extn} and L_{proj} are measured 8 µs after impact.

Simulation	P (GPa)	d_{cra} (cm)	L_{extn} (cm)	L_{proj} (cm)
SAV1 [141]	18.0	2.0	0.7	1.8
B&H [140]	18.6	1.9	0.7	2.0
SAV1 Recreated	19.4	2.1	0.6	1.9
SAV1 AS[a]	19.4	2.1	0.6	1.9
SAV1 CA[b]	19.5	2.2	0.6	1.9
SAV1 MC[c]	19.5	2.1	0.7	2.0
SAV1 MC+AS[d]	19.5	2.1	0.8	2.0
SAV1 AS[a]+CA[b]+AC[e]	20.9	2.2	0.7	1.9

[a] Artificial Stress ($\epsilon_{as} = 0.3$ and $n_{as} = 4$) [b] Contact Algorithm ($K_{ca} = 2 \times 10^{12}$ and $n_{ca} = 4$)
[c] Mixed Correction ($C_f = 7.5$) [d] Mixed Correction and Artificial Stress ($\epsilon_{as} = 0.3$, $n_{as} = 4$ and $C_f = 90.0$)
[e] Kernel Adaptive Conversion

SPH will destroy the scheme's conservation properties. It was speculated that this might be confined to the regions of spallation and that overall the effect would be minor.

In Figure 4.33, it can be seen that artificial stress improved the results. There was minor spallation from the target and the implementation of artificial stress largely succeeded at removing the particle clumps and voids. The only other scheme to achieve this was the Riemann based CON scheme by Mehra and Chaturvedi [141]. The CON scheme succeeded at maintaining particle order in the projectile whilst the SAV1 scheme with artificial stress displayed a larger degree of particle disorder. Voids and particle clumping are visible in the upper portion of the projectile, indicating that the use of artificial stress did not completely suppress the tensile instability, as corroborated by a later publication by Mehra et al. [143]. The contact algorithm did not noticeably affect the results other than increasing the target crater diameter. Although the application of mixed correction reduced the void between the projectile and the target, it also caused spalled particles to clump together. Additionally, a void is visible near the centre of the projectile, which was caused by the tensile instability. In all other schemes this void was re-populated by particles but the mixed correction scheme was unable to achieve this. The application of mixed correction with a switch value of $C_f = 7.5$ resulted in an energy increase of 0.98 %. Whilst this is significantly greater than the energy increase of 0.048 % for the recreated SAV1, it was still found to be within acceptable levels considering the low threshold applied to convert from the mixed correction kernel gradient to the conventional kernel gradient.

Mehra and Chaturvedi [141] compared their results against those obtained by Howell and Ball [140] using the peak pressure in the projectile P, peak tension in the projectile, crater diameter d_{cra} , width of the projectile L_{extn} and the distance travelled by the projectile L_{proj}. The same metrics are used in Table 4.4 with the exception of the peak tension. This could not be captured due to the tensile instability that caused voids to form in the projectile prior to the reflected shock wave reaching the centre of the projectile. The original SAV1 results presented by Mehra and Chaturvedi [141] and the results obtained by Howell and Ball [140] are given in this table. The recreated SAV1 results appear to differ from the original SAV1. However, it is noted that the recreated SAV1 results are in agreement with those presented by Asadi Kalameh et al. [144], who also simulated this problem using Eulerian SPH. These authors gave no values for pressure. Additionally, Mehra and Chaturvedi [141] evaluated the peak pressure by using an SPH summation, whilst in Table 4.4 the pressure was taken

Figure 4.34: Particle positions of the high-velocity impact problem 8 µs after impact. The results are for the recreated SAV1 scheme from Mehra and Chaturvedi [141] and SAV1 combined with artificial stress (AS) and the adapted mixed correction (MC).

on a particle basis from the equation of state. Consequently, the recreated SAV1 pressure should be larger as they have not been smoothed. Lastly, Mehra and Chaturvedi [141] quote their lengths to a precision of 0.1 cm. The attempts to improve upon SAV1 did not make any noteworthy changes to the results in Table 4.4. Artificial stress did not affect the geometric or pressure values and the contact algorithm increased the crater diameter and peak pressure. The mixed correction also increased the peak pressure along with the projectile width and the distance travelled.

The mixed correction scheme was combined with artificial stress. The inclusion of artificial stress allowed the mixed correction factors to be raised to $C_f = 90$. Figure 4.34 compares the results of the recreated SAV1 against the SAV1 scheme with artificial stress ($\epsilon_{as} = 0.3$ and $n_{as} = 4$) and mixed correction ($C_f = 90.0$). From this figure, it is evident that the mixed correction has prevented the voids caused by the tensile instability from closing. These voids are significantly larger than those seen in the other trials. Table 4.4 highlights the pressure and geometric values obtained using this combination. The addition of artificial stress does not affect these results, as was the case without the mixed correction, with the exception of the longitudinal extension that has increased. In this simulation, the total energy increased by 0.136 % which was a significant reduction from the increase of 0.98 % with $C_f = 7.5$. From these trials it would appear that, although the mixed correction removes the void between the projectile and the target, the combination of artificial viscosity and artificial stress produced the results most similar to CON.

It is clear that although artificial stress aids in suppressing it, the tensile instability is still present in this problem. Therefore, the high velocity impact problem was modelled using Total Lagrangian particles that adaptively converted to Eulerian particles as discussed in Section 3.6.4. Both coupling methods were tested. The distribution of particles in the projectile had to be modified as the two outer layers of particles on the circumference penetrated the projectile upon impact. This was due to the low number of neighbours in the reference state. The particles in the projectile were therefore arranged by keeping an approximate arc and radial distance of 0.1 mm between particles, resulting in 8012 particles. SAV1 with artificial stress with parameters $\epsilon_{as} = 0.3$ and $n_{as} = 4$ was recreated. As no damage criterion was used in this problem, particles changed kernel type when the equivalent strain:

$$\bar{\epsilon} = \sqrt{\frac{2}{3}\boldsymbol{\epsilon}' : \boldsymbol{\epsilon}'}\,, \tag{4.9}$$

Figure 4.35: Particle positions of the high-velocity impact problem 2 µs, 4 µs, 6 µs and 8 µs after impact. The results are for the recreated SAV1 scheme from Mehra and Chaturvedi [141] modelled using Total Lagrangian kernel types (black) that adaptively converted to Eulerian kernel types (grey).

exceeded a value of 0.85. Note that this problem was under plane stress conditions and consequently the out-of-plane strain had to be calculated as

$$\epsilon_{33} = -\frac{\nu}{E}(\sigma_{xx} + \sigma_{yy}) \, . \tag{4.10}$$

As the domain was initially modelled with Total Lagrangian particles, the contact algorithm was used with parameters $K_{\text{ca}} = 2 \times 10^{12}$ and $n_{\text{ca}} = 4$. The first coupling method was incapable of modelling this problem, even without the inclusion of artificial stress. This was due to the distortions at the interface and large differences between the support domains in the reference configuration and the deformed configuration. The results for the second coupling method, at 2 µs, 4 µs, 6 µs, and 8 µs after impact are displayed in Figure 4.35 and are coloured by particle kernel type. The particles that changed from Total Lagrangian to Eulerian kernel type are represented by the lighter colour. A number of comments can be made if comparing these results to those obtained by Mehra and Chaturvedi [141] in Figure 4.32 and the further trials in Figure 4.34. The crater diameter is less circular. This was most likely caused by the progressive change of particles from Total Lagrangian to Eulerian in the crater, which led to a different response to the tensile stresses. There is a larger void between the projectile and the crater. This can be largely attributed to the use of the contact algorithm, as previously seen. Perhaps most interesting is the final shape of the deformed projectile. As the majority of the back of the projectile remained Total Lagrangian, the particles are still ordered, as in the CON simulation. Additionally, particles do not spall from the back of the projectile due to the Total Lagrangian formulation, in combination with the different particle arrangement. The

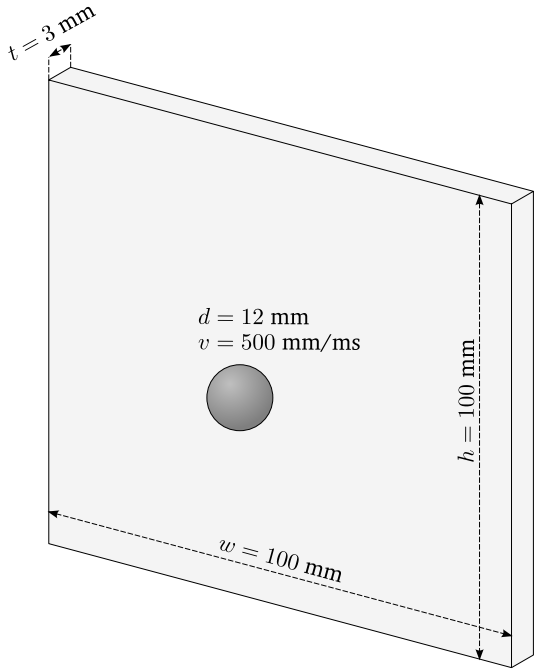

Figure 4.36: Schematic of the debris impact problem. A spherical piece of debris with diameter 12 mm travels at 500 m/s perpendicularly to a square metal plate of dimensions $100 \times 100 \times 3$ mm which is clamped along its edges.

tensile instability can be seen to manifest in the Eulerian particles as in the previous simulations. The geometric and pressure values for the adaptive simulation are listed in Table 4.4. It is not strictly correct to compare simulations with different initial particle arrangements as the adaptive simulation contained nearly 200 more particles in the projectile that the previous simulations. Using this adaptive particle conversion, it was possible to capture the pressure wave as it reflected, unlike in the previous Eulerian simulations. The peak tension in the projectile after the reflection of the initial pressure was found to be 22.5 GPa at 2.3 µs after impact. In comparison, Mehra and Chaturvedi [141] found this to be 18.5 GPa at 2.2 µs after impact. Higher pressures may be seen in the adaptive simulation due the larger mass of the projectile caused by the additional particles.

4.12 Three-dimensional debris impact

In this final problem, both coupling methods were applied to a three-dimensional debris impact simulation. This involved a spherical projectile impacting a stationary square target. The problem set-up was taken from Reveles' [109] PhD thesis with a number of amendments. The projectile was modelled as a 12 mm diameter steel sphere with an initial velocity of 500 m/s and the plate as aluminium with height 100 mm, width 100 mm and thickness 3 mm. A schematic of the configuration is presented in Figure 4.36. The outer edges of the plate were fixed.

The material properties for aluminium were given by $\rho = 2870$ kg/m^3, $E = 70$ GPa, $\nu = 0.33$ and $\sigma_y = 479$ MPa. The plastic response of the aluminium target was captured using the Johnson-Cook plasticity model. The Johnson-Cook parameters were given by $A_{\text{JC}} = 479$ MPa, $B_{\text{JC}} = 323$ MPa,

$C_{JC} = 0.101$, $\dot{\epsilon}_0 = 1.0\ s^{-1}$, $M_{JC} = 1.80$, $N_{JC} = 0.410$, $T_r = 300$ K, $T_m = 850$ K and $C_v = 875$ J/kgK. The Johnson-Cook damage model was also used with parameters $D_1 = 0.45$, $D_2 = 0$, $D_3 = 0$, $D_4 = 0.0138$ and $D_5 = 0$. The commercial software LS-DYNA provides three spall models, if using the Johnson-Cook damage model. Reveles [109] made use of the "pressure limit model", which places a restriction, p_{min}, on the minimum value of tensile pressure. Note that this presumes a convention where tensile pressure is negative. Any pressures which are more tensile that this value are reset to p_{min}. Following Reveles, the minimum tensile pressure was set to $p_{min} = -800$ MPa. The pressure in the aluminium plate was calculated using the cubic Hugoniot form of the Mie-Gruneisen equation of state (Section 3.4.2) with parameters $c = 5328$ m/s, $\gamma_0 = 2$, $a_{mg} = 0.480$, $s_1 = 1.338$, $s_2 = 0$ and $s_3 = 0$.

The material properties for steel were given by $\rho = 7870$ kg/m^3, $E = 200$ GPa, $\nu = 0.30$ and $\sigma_y = 315$ MPa. The steel debris was modelled as elastic-plastic with isotropic hardening (Section 3.5.2) using a plastic modulus of $E_p = 16.216$ GPa. Damage was not considered for the debris. The pressure was calculated using the elastic equation of state (Section 3.4.1).

Both the plate and debris were modelled using an inter-particle spacing $\delta x = 1$ mm, resulting in 912 particles in the debris and 30,000 particles in the plate. The particles in the debris only approximated the sphere as they were distributed on a cubic lattice. Artificial viscosity was used with parameters $\alpha = 1.0$ and $\beta = 2.0$. These values were chosen as they were found to be effective in the impact problem previously discussed in Section 4.11. The smoothing length was set to $h = 1.2\delta x$. Lastly, the contact algorithm was used between the debris and plate with $K_{ca} = 1 \times 10^{16}$ and $n_{ca} = 4$.

Five combinations of particle kernel types were investigated: (i) both the debris and target were modelled using Eulerian particles, (ii) both the debris and target were modelled using Total Lagrangian particles, (iii) both the debris and target were modelled using Total Lagrangian particles and a central patch of the plate of size 16 mm × 16 mm × 3 mm was modelled using Eulerian particles, (iv) both the debris and target were modelled using Total Lagrangian particles that adaptively converted kernel type to Eulerian particles once damaged with the first coupling method, and (iv) both the debris and target were modelled using Total Lagrangian particles that adaptively converted kernel type to Eulerian particles once damaged with the second coupling method. A discussion on this adaptive particle conversion is given in Section 3.6.4. Simulations (i) and (ii) were included as limiting cases considering that (i) will suffer from the tensile instability and (ii) will require that damaged particles have their field variables set to zero and are deleted from neighbour lists, in order to model fracture. This too is discussed in Section 3.6.4. The mixed correction was not applied in this example as it was found to complicate the previous high-velocity impact problem in Section 4.11. Note that if a particle converted type in the adaptive simulation with the second coupling method (v) a large number of neighbours were also required to convert type. This was because this problem was three-dimensional and if this was not done, Total Lagrangian particles had Eulerian neighbours with non-physical deformation gradients.

Figure 4.37 presents a three-dimensional view of the particles' locations and kernel types 153 μs after impact. Figure 4.38 displays cross-sections of the domains. Neither of these figures display the wholly Eulerian simulation (i) as the results were visually indistinguishable from the simulation with the Eulerian patch (iii). From these figures, it would appear that both the Eulerian simulation (i) and the Total Lagrangian simulation with the Eulerian patch (iii) were dominated by petalling with minor plugging and no spallation. It is speculated that this was driven by the tensile instability, which, upon impact, caused the particles to clump together along either side of the axis of symmetry. This may have been influenced by the regular grid arrangement of particles in the plate. The Total Lagrangian simulation (ii) produced a larger plug that the previously mentioned simulations but

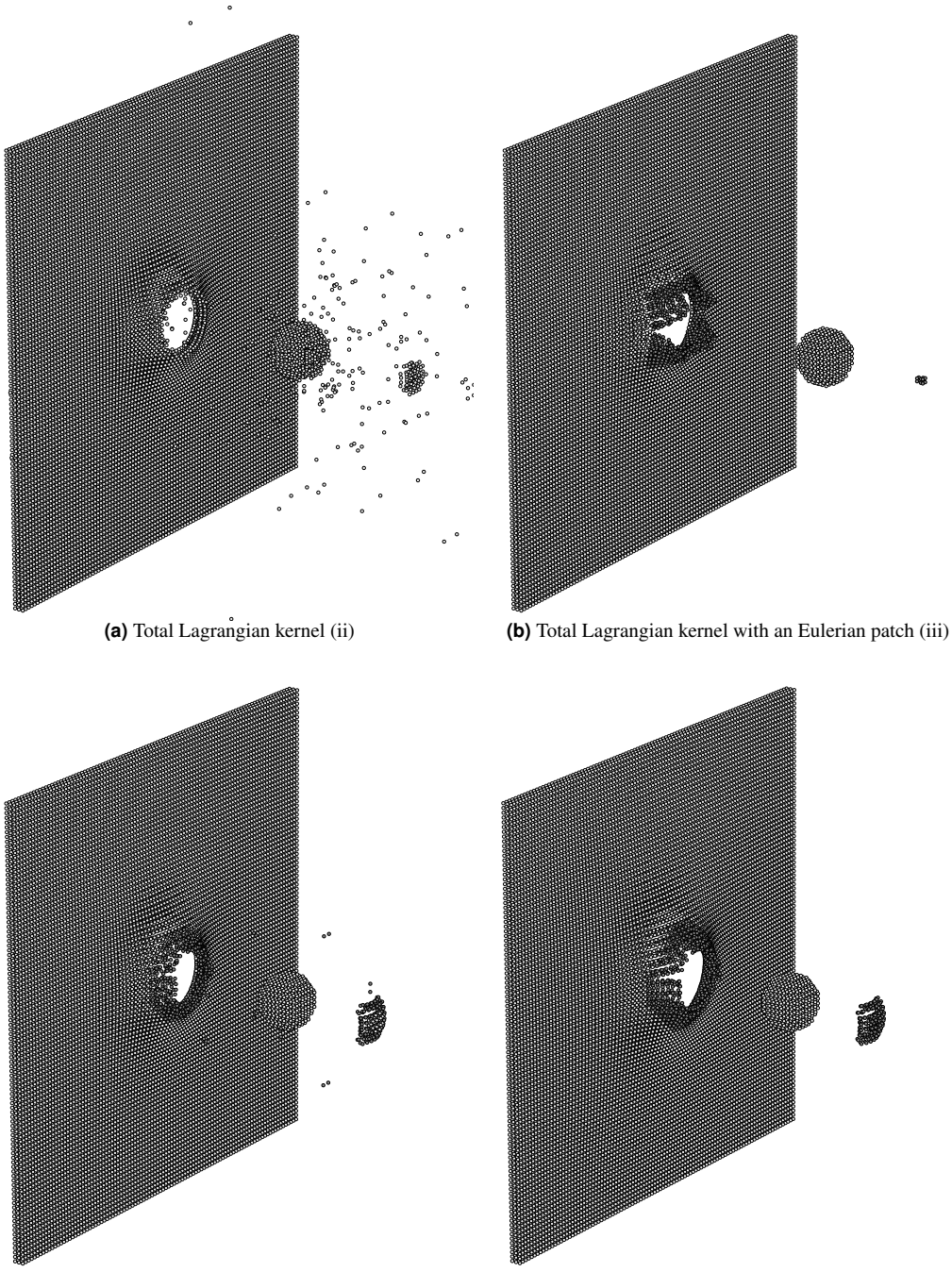

(a) Total Lagrangian kernel (ii)

(b) Total Lagrangian kernel with an Eulerian patch (iii)

(c) Adaptive kernel with first coupling method (iv)

(d) Adaptive kernel with second coupling method (v)

Figure 4.37: Three-dimensional view of the particle positions and kernel types 153 μs after impact. The darker colour represents particles with an Eulerian kernel and the lighted colour represents particles with a Total Lagrangian kernel.

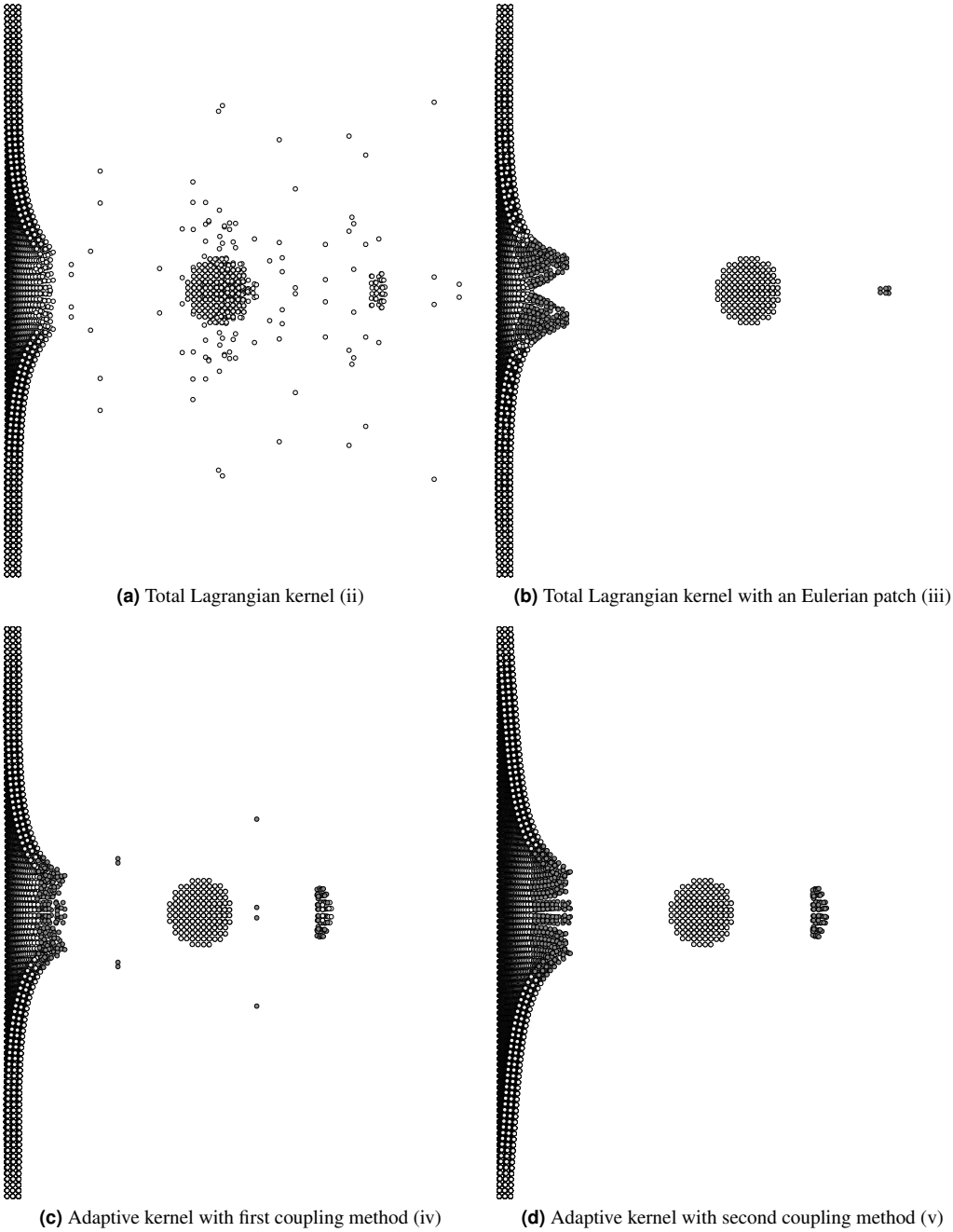

(a) Total Lagrangian kernel (ii)

(b) Total Lagrangian kernel with an Eulerian patch (iii)

(c) Adaptive kernel with first coupling method (iv)

(d) Adaptive kernel with second coupling method (v)

Figure 4.38: Cross-sections of the particle positions and kernel types 153 μs after impact. The darker colour represents particles with an Eulerian kernel and the lighted colour represents particles with a Total Lagrangian kernel.

Table 4.5: Geometric data for the three-dimensional debris impact problem using four combinations of kernel types. v_d and v_p are the post-impact velocities of the debris and plug, d_i is the impact diameter, w_p is the plug width and h_{pl} is the plate lip height. All measurements were taken 153 µs after impact.

Simulation	v_d (mm/ms)	v_p (mm/ms)	d_i (mm)	w_p (mm)	h_{pl} (mm)
Eulerian (i)	324	463	13.32	0.88	9.76
Total Lagrangian (ii)	270	443	13.92	5.88	5.69
Eulerian patch (iii)	319	449	13.44	0.88	9.79
Adaptive first method (iv)	242	368	12.95	8.30	8.08
Adaptive second method (v)	257	373	14.08	8.38	10.16

conversely produced no petalling and a very large degree of spallation. The adaptive simulation with the first coupling method (iv) produced a large plug along with minor spallation and no petalling. Lastly, the adaptive simulation with the second coupling method (v) produced the largest plug along with no spallation and minor petalling. As stated by Reveles [109], plugging and petalling are typical of low velocity impact on ductile materials, rather than spallation. For this reasons, it would appear that the adaptive conversion of particle kernel types produced the most plausible results.

An attempt was made to implement a three-dimensional form of artificial stress in the Eulerian simulations. This implementation has not been well covered in the literature. The naive approach attempted in this work was to extend the theory detailed in Section 3.3 to three dimensions by finding the eigenvalues and eigenvectors (see Section 3.6.1) of the Cauchy stress tensor. The principal components were then modified, if tensile, and then rotated back to their original directions, as in Section 3.3. This produced significantly more spalled particles with no discernible plug. Therefore, the three-dimensional implementation of artificial stress was not investigated further.

Table 4.5 compares the post-impact velocity of the debris v_d and the plug v_p, the impact diameter d_i, the plug width w_p and the plate lip height h_{pl}, 153 µs after impact. The impact diameter was measured as twice the average radius of the particles at the outermost edges of the plate lip. The plate lip height was measured as the perpendicular distance between a fixed edge particle along the outer face of the plate and a particle on the outermost edges of the lip. The simulations involving particle conversion, (iv) and (v), produced the lowest post-impact debris and plug velocities. This was expected considering that both the simulations which made use of the Eulerian kernel (i) and the Eulerian patch (iii) would be expected to manifest the tensile instability, resulting in particle clumping and less resistance to the passage of the debris. Similarly, the simulation that made use of the Total Lagrangian kernel (ii) would offer lesser resistance to the debris considering that, once damaged, the particles had their field variables set to zero. Both (i) and (iii) gave similar crater diameters as both simulations displayed the artificial petalling. The Total Lagrangian simulation (ii) produced a comparatively large crater diameter, most likely due to the excessive spallation. The adaptive simulation with the first coupling method (iv) displayed the smallest crater diameter with no artificial petalling, while the adaptive simulation with the second coupling method (v) produced the largest crater diameter. Again, (i) and (iii) gave very similar plate lip heights, whilst (ii) displayed the smallest lip height, again due to the spallation. The lip height of the adaptive simulation (iv) was close to the average of the other two. The adaptive simulation (v) produced the largest lip height, though this was similar to the Eulerian (i) and (iii) patch simulations.

This numerical example is not strictly a form of validation considering that no comparisons are made against numerical or experimental results found in literature. It serves to highlight how the adaptive conversion of kernel particle types can aid in the simulations of impact and fracture using

SPH. It would appear that both the adaptive particle conversion simulations produced superior results to the simulations that made use of one kernel type or a predetermined patch of Eulerian particles.

4.13 Concluding remarks

These numerical example have highlighted a number important features concerning the theory presented in Chapters 2 and 3. The two approximations of a velocity gradient using mixed correction with and without symmetry terms supported the claim that the mixed correction gave equal results regardless of symmetry terms. However, it is important to note that the first coupled mixed correction formulation exclusively makes use of the formulation with symmetry terms, as this results in the particle pair-based internal forces being equal and opposite. The two-dimensional oscillating bar problem demonstrated how the mixed correction reduced particle clumping and produced results consistent with the Finite Element Method. The off-centre rubber ring impact supported the claim that the formulations without correction conserve linear momentum, but not angular momentum. It further demonstrated how the proposed form of mixed correction artificial viscosity conserves linear momentum exactly, and angular momentum approximately using a Total Lagrangian formulation. The coupled artificial stress test highlighted how artificial stress reduces the impact of the tensile instability in an Eulerian formulation and could be successfully applied to the second coupling method but not the first. The uniaxial compression test demonstrated how both coupled methods produces results that are consistent with both the Eulerian and Total Lagrangian formulations, for small deformations and if the tensile instability is not activated. The Taylor impact test verified and validated the implementation of the Johnson-Cook plasticity model and highlighted the ability of the Total Lagrangian formulation to reproduce plasticity. The crack branching and Kalthoff-Winkler examples confirmed that ability of the mixed correction Total Lagrangian formulation to accurately predict fracture paths using the Rankine and Lemaitre damage models. A high velocity impact test validated the ability of the Eulerian formulation to reproduce fracture and spallation and highlighted how the second coupling method may improve these results. This example further highlighted how the mixed correction appears to degrade the results for problem involving spallation. Lastly, the debris impact problem demonstrated that the proposed coupled methods with adaptive kernel type conversion is capable of modelling high-velocity impact and fracture and can outperform the other formulations.

Conclusions

5

5.1 Overview

Having discussed the proposed formulations and demonstrated their abilities to model elastic dynamics and fracture, some concluding remarks are given. Firstly, the significance and implications of this work are discussed. Lastly, the limitations of the proposed formulation are given along with recommendations for future work.

5.2 Significance and implications

The aim of this research was to couple the Eulerian and Total Lagrangian formulations to model elastic dynamics and fracture. From the numerical examples presented, it is evident that the first coupling method failed to achieve this whilst the second coupling method succeeded. The first coupling method is not appropriate for problems where the Total Lagrangian support domain has deformed and largely differs from the Eulerian support domain, in the interface zone. It is noted that this first coupling method is more computationally efficient than the second and did produce positive results for the hard debris impact problem. The second coupling method can be seen to meet the aim of this research. Although more complex, this coupling method was able to model both the high velocity impact problem and the hard debris impact problem. More importantly, it is not reliant on particles in the interface zone having support domains that did not evolve over time.

Although similar, the second coupling method presented in this work is a significant development upon that described by Lacome et al. [61]. Although Lacome et al. write their equations of motion with gradient correction, they are not equal and opposite for particle pairs. In the formulations presented here, the conservation equations made use of mixed correction and have been derived in such a way that they are equal and opposite. Hence, both coupling methods in this work achieve 1st order consistency of gradient approximations and energy and momentum conservation, unlike Lacome et al. [61]. Furthermore, in this work, the usage of both coupling methods with artificial viscosity, artificial stress, ghost particles and a contact algorithm are discussed and explained which was not done by Lacome et al. [61]. Lastly, a time integration scheme was given along with the order of calculations required in order for both formulations, and consequently the coupling methods, to give equal results if the tensile instability did not manifest.

The SPH approximations for the conservation of mass, momentum, and energy were given using both a Total Lagrangian and an Eulerian formulation. These formulations did not make use of the symmetric kernel property, that being $\nabla_a W_{ab} = -\nabla_b W_{ba}$. The conservation of linear momentum and energy was proven for both formulations and the conditions necessary for the conservation of angular momentum was given. This made it possible to apply a mixed kernel-and-gradient correction scheme that upheld the conservation properties and ensured the conservation of angular momentum. This mixed correction also ensured 0^{th} order consistency of a function and 1^{st} order consistency of a

gradient. The given mixed correction Eulerian and Total Lagrangian formulations produced equal and opposite particle internal forces, unlike the conventional forms of the conservation equations with gradient correction. The Eulerian and Total Lagrangian formulations were then coupled using two methods. The first assumed that a particle in an Eulerian formulation should exert an equal and opposite force on a Total Lagrangian neighbour. Although this might not be strictly true due to the differences in discretisation, it was found to produce a novel method for modelling fracture. The second coupling method ensured that the Eulerian and Total Lagrangian particles only viewed each other in their respective configurations. This required the Eulerian particles to search through the Total Lagrangian particles at each time step. It similarly required that Eulerian neighbours in the interface zone had physical deformation gradients.

Artificial viscosity was extended to the proposed formulations and a novel algorithm was given for a Total Lagrangian formulation. Artificial stress was found to be incompatible with the first coupled method but suitable for the second. A number of numerical examples validated the proposed mixed correction Total Lagrangian and Eulerian formulations. These were shown to be capable of modelling elastic dynamics, plasticity, and fracture. The formulations were found to be equal for the uniaxial compression test, although in this simulation the particle displacements were small and consequently the spatial configuration did not greatly diverge from the reference configuration. The advantages of the coupled formulations were demonstrated for the high velocity impact problem and the debris impact test, where Total Lagrangian particles adaptively converted to Eulerian particles once damaged. It was found that the coupled methods produced superior results to the Eulerian formulation, which suffered the tensile instability, or the Total Lagrangian formulation, which required damaged particles to have their field properties set to zero.

5.3 Future work

Only basic fracture models were used in this work including the Rankine, Lematire and Johnson-Cook damage models. It would be an improvement to include more complex meshless fracture models, such as the “cracking particles” method by Rabczuk et al. [58].

In this work, a scalar strain or damage value was used as a switch to convert particle kernel types from Total Lagrangian to Eulerian. Perhaps a more intelligent switch could be used for problems with large distortions to convert from Total Lagrangian to Eulerian kernel types. This switch may be centred on the value of the deformation gradient and identify when this starts to become non-physical.

Updates of the reference configuration were not explored in this work. It would be an improvement to apply these updates along with the “Hessian’s Difference Stabilization” developed by Vidal et al. [35] to control the zero energy modes which these updates can excite. Comparing the results of the formulation presented in this thesis with the second coupling method against an updated Total Lagrangian formulation for problems involving fracture may prove interesting.

Lastly, two distinct Eulerian (moving support domains) and Total Lagrangian (fixed support domains) formulations were applied in this thesis. It is speculated that an improved formulation might make use of a switch to convert from one formulation to another, as recently done by Fourtakas et al. [63] for a Lagrangian (moving particles) Eulerian (fixed particles) formulation using incompressible SPH for fluid flows.

❖

Bibliography

[1] Liu, G. R. and Liu, M. B. *Smoothed Particle Hydrodynamics A Meshfree Particle Method*. World Scientific Publishing Co Pte Ltd, 2003.

[2] Violeau, D. *Fluid Mechanics and the SPH Method*. 1st ed. Oxford: Oxford University Press, 2012. Chap. 1, pp. 28–30.

[3] Monaghan, J. J. "Smoothed particle hydrodynamics". In: *Reports Prog. Phys.* 68.8 (2005), pp. 1703–1759.

[4] Vignjevic, R. and Campbell, J. C. "Review of Development of the Smooth Particle Hydrodynamics (SPH) Method". In: *Predictive Modeling of Dynamic Processes*. Ed. by S. Hiermaier. Boston, MA: Springer US, 2009, pp. 367–396.

[5] Liu, M. B. and Liu, G. R. "Smoothed Particle Hydrodynamics (SPH): an Overview and Recent Developments". In: *Arch. Comput. Methods Eng.* 17.1 (2010), pp. 25–76.

[6] Monaghan, J. J. "Smoothed Particle Hydrodynamics and Its Diverse Applications". In: *Annu. Rev. Fluid Mech.* 44.1 (2012), pp. 323–346.

[7] Rabczuk, T. "Computational Methods for Fracture in Brittle and Quasi-Brittle Solids : State-of-the-art Review and Future Perspectives". In: *Int. Sch. Res. Not. Appl. Math.* 2013.1 (2012), pp. 1–61.

[8] Sahama, T. R. and Diamond, N. T. "Computer experiment: A case study for modelling and simulation of manufacturing systems". In: *Aust. J. Mech. Eng.* 7.1 (2009), pp. 1–8.

[9] Frederich, O., Wassen, E., Thiele, F., Jensch, M., Brede, M., Hüttmann, F., and Leder, A. "Numerical Simulation of the Flow Around a Finite Cylinder with Ground Plate in Comparison to Experimental Measurements". In: *New Results in Numerical and Experimental Fluid Mechanics VI*. Ed. by C. Tropea, S. Jakirlic, H.-J. Heinemann, R. Henke, and H. Hönlinger. Berlin, Heidelberg: Springer Berlin Heidelberg, 2008, pp. 348–355.

[10] Courant, R., Friedrichs, K., and Lewy, H. "Über die partiellen Differenzengleichungen der mathematischen Physik". In: *Math. Ann.* 100.1 (1928), pp. 32–74.

[11] Courant, R., Friedrichs, K., and Lewy, H. "On the Partial Difference Equations of Mathematical Physics". In: *IBM J. Res. Dev.* 11.2 (1967), pp. 215–234.

[12] Forsythe, G. E. *Finite-difference methods for partial differential equations.* New York: Wiley, 1960.

[13] Zienkiewicz, O. C. *The finite element method in engineering science*. London: McGraw-Hill, 1971.

[14] Favorski, A. P. "Variational-discrete models of hydrodynamics equations". In: *Differ. Equations* 16.7 (1981), pp. 1308–1321.

[15] Margolin, L. G. and Adams, T. F. *Spatial differencing for finite difference codes*. Tech. rep. LA-10249. Los Alamos National Laboratory, 1985.

[16] Nguyen, V. P., Rabczuk, T., Bordas, S., and Duflot, M. "Meshless methods: A review and computer implementation aspects". In: *Math. Comput. Simul.* 79.3 (2008), pp. 763–813.

[17] Moës, N., Dolbow, J., and Belytschko, T. “A finite element method for crack growth without remeshing”. In: *Int. J. Numer. Methods Eng.* 46.1 (1999), pp. 131–150.

[18] Belytschko, T., Moës, N., Usui, S., and Parimi, C. “Arbitrary discontinuities in finite elements”. In: *Int. J. Numer. Methods Eng.* 50.4 (2001), pp. 993–1013.

[19] Belytschko, T., Chen, H., Xu, J., and Zi, G. “Dynamic crack propagation based on loss of hyperbolicity and a new discontinuous enrichment”. In: *Int. J. Numer. Methods Eng.* 58.12 (2003), pp. 1873–1905.

[20] Gingold, R. A. and Monaghan, J. J. “Smoothed particle hydrodynamics: theory and application to non-spherical stars”. In: *Mon. Not. R. Astron. Soc.* 181.3 (1977), pp. 375–389.

[21] Lucy, L. B. “A numerical approach to the testing of the fission hypothesis”. In: *Astron. J.* 82.12 (1977), p. 1013.

[22] Shadloo, M., Oger, G., and Le Touzé, D. “Smoothed particle hydrodynamics method for fluid flows, towards industrial applications: Motivations, current state, and challenges”. In: *Comput. Fluids* 136 (2016), pp. 11–34.

[23] Libersky, L. D. and Petschek, A. G. “Smooth particle hydrodynamics with strength of materials”. In: *Advances in the Free-Lagrange Method Including Contributions on Adaptive Gridding and the Smooth Particle Hydrodynamics Method*. Ed. by H. Trease, M. Fritts, and W. Crowley. Vol. 395. Lecture Notes in Physics, Berlin Springer Verlag. Berlin, Heidelberg: Springer Berlin Heidelberg, 1991, pp. 248–257.

[24] Swegle, J. W., Hicks, D. L., and Attaway, S. W. “Smoothed Particle Hydrodynamics Stability Analysis”. In: *J. Comput. Phys.* 116.1 (1995), pp. 123–134.

[25] Bonet, J. and Kulasegaram, S. “Remarks on tension instability of Eulerian and Lagrangian corrected smooth particle hydrodynamics (CSPH) methods”. In: *Int. J. Numer. Methods Eng.* 52.11 (2001), pp. 1203–1220.

[26] Dyka, C. T. and Ingel, R. P. “An approach for tension instability in smoothed particle hydrodynamics (SPH)”. In: *Comput. Struct.* 57.4 (1995), pp. 573–580.

[27] Dyka, C. T., Randles, P. W., and Ingel, R. P. “Stress Points For Tension Instability In SPH”. In: *Int. J. Numer. Methods Eng.* 40.13 (1997), pp. 2325–2341.

[28] Randles, P. W. and Libersky, L. D. “Normalized SPH with stress points”. In: *Int. J. Numer. Methods Eng.* 48.10 (2000), pp. 1445–1462.

[29] Monaghan, J. J. “SPH without a Tensile Instability”. In: *J. Comput. Phys.* 159.2 (2000), pp. 290–311.

[30] Gray, J. P., Monaghan, J. J., and Swift, R. P. “SPH elastic dynamics”. In: *Comput. Methods Appl. Mech. Eng.* 190.49-50 (2001), pp. 6641–6662.

[31] Belytschko, T., Guo, Y., Kam Liu, W., and Ping Xiao, S. “A unified stability analysis of meshless particle methods”. In: *Int. J. Numer. Methods Eng.* 48.9 (2000), pp. 1359–1400.

[32] Belytschko, T., Liu, W. K., Moran, B., and Elkhodary, K. *Nonlinear Finite Elements for Continua and Structures*. 1st. Chichester: Wiley, 2000, pp. 45–54.

[33] Bonet, J. and Kulasegaram, S. “Alternative Total Lagrangian Formulations for Corrected Smooth Particle Hydrodynamics (CSPH) Methods in Large Strain Dynamic Problems”. In: *Rev. Eur. des Éléments Finis* 11.7-8 (2002), pp. 893–912.

[34] Bonet, J., Kulasegaram, S., Rodriguez-Paz, M. X., and Profit, M. “Variational formulation for the smooth particle hydrodynamics (SPH) simulation of fluid and solid problems”. In: *Comput. Methods Appl. Mech. Eng.* 193.12-14 (2004), pp. 1245–1256.

[35] Vidal, Y., Bonet, J., and Huerta, A. “Stabilized updated Lagrangian corrected SPH for explicit dynamic problems”. In: *Int. J. Numer. Methods Eng.* 69.13 (2007), pp. 2687–2710.

[36] Ganzenmüller, G. C. “An hourglass control algorithm for Lagrangian Smooth Particle Hydrodynamics”. In: *Comput. Methods Appl. Mech. Eng.* 286 (2015), pp. 87–106.

[37] Ganzenmüller, G. C., Sauer, M., May, M., and Hiermaier, S. “Hourglass control for Smooth Particle Hydrodynamics removes tensile and rank-deficiency instabilities”. In: *Eur. Phys. J. Spec. Top.* 225.2 (2016), pp. 385–395.

[38] Monaghan, J. J. “Smoothed Particle Hydrodynamics”. In: *Annu. Rev. Astron. Astrophys.* 30.1 (1992), pp. 543–574.

[39] Monaghan, J. J. “SPH and Riemann Solvers”. In: *J. Comput. Phys.* 136.2 (1997), pp. 298–307.

[40] Johnson, G. R. and Beissel, S. R. “Normalized Smoothing Functions For Sph Impact Computations”. In: *Int. J. Numer. Methods Eng.* 39.16 (1996), pp. 2725–2741.

[41] Randles, P. W. and Libersky, L. D. “Smoothed Particle Hydrodynamics: Some recent improvements and applications”. In: *Comput. Methods Appl. Mech. Eng.* 139.1-4 (1996), pp. 375–408.

[42] Bonet, J. and Lok, T. S. L. “Variational and momentum preservation aspects of Smooth Particle Hydrodynamic formulations”. In: *Comput. Methods Appl. Mech. Eng.* 180.1-2 (1999), pp. 97–115.

[43] Li, S. and Liu, W. K. “Moving least-square reproducing kernel method Part II: Fourier analysis”. In: *Comput. Methods Appl. Mech. Eng.* 139.1-4 (1996), pp. 159–193.

[44] Chen, J. K. and Beraun, J. E. “A generalized smoothed particle hydrodynamics method for nonlinear dynamic problems”. In: *Comput. Methods Appl. Mech. Eng.* 190.1-2 (2000), pp. 225–239.

[45] Chen, J. K., Beraun, J. E., and Carney, T. C. “A corrective smoothed particle method for boundary value problems in heat conduction”. In: *Int. J. Numer. Methods Eng.* 46.2 (1999), pp. 231–252.

[46] Vignjevic, R., Campbell, J. C., and Libersky, L. D. “A treatment of zero-energy modes in the smoothed particle hydrodynamics method”. In: *Comput. Methods Appl. Mech. Eng.* 184.1 (2000), pp. 67–85.

[47] Libersky, L. D., Petschek, A. G., Carney, T. C., Hipp, J. R., and Allahdadi, F. A. “High Strain Lagrangian Hydrodynamics”. In: *J. Comput. Phys.* 109.1 (1993), pp. 67–75.

[48] Chakraborty, S. and Shaw, A. “A pseudo-spring based fracture model for SPH simulation of impact dynamics”. In: *Int. J. Impact Eng.* 58 (2013), pp. 84–95.

[49] Chakraborty, S. and Shaw, A. “Crack Propagation in Bi-Material System via Pseudo-Spring Smoothed Particle Hydrodynamics”. In: *Int. J. Comput. Methods Eng. Sci. Mech.* 15.3 (2014), pp. 294–301.

[50] Chakraborty, S. and Shaw, A. “Prognosis for ballistic sensitivity of pre-notch in metallic beam through mesh-less computation reflecting material damage”. In: *Int. J. Solids Struct.* 67-68 (2015), pp. 192–204.

[51] Benz, W. and Asphaug, E. “Simulations of brittle solids using smooth particle hydrodynamics”. In: *Comput. Phys. Commun.* 87.1-2 (1995), pp. 253–265.

[52] Weibull, W. *A statistical theory of the strength of materials*. Stockholm: Ingeniorsvetenskaps Akademiens Handlingar, 1939, pp. 5–45.

[53] Das, R. and Cleary, P. W. “Effect of rock shapes on brittle fracture using Smoothed Particle Hydrodynamics”. In: *Theor. Appl. Fract. Mech.* 53.1 (2010), pp. 47–60.

[54] De Vuyst, T. and Vignjevic, R. “Total Lagrangian SPH modelling of necking and fracture in electromagnetically driven rings”. In: *Int. J. Fract.* 180.1 (2013), pp. 53–70.

[55] Rabczuk, T. and Belytschko, T. “Cracking particles: a simplified meshfree method for arbitrary evolving cracks”. In: *Int. J. Numer. Methods Eng.* 61.13 (2004), pp. 2316–2343.

[56] Rabczuk, T. and Belytschko, T. “A three-dimensional large deformation meshfree method for arbitrary evolving cracks”. In: *Comput. Methods Appl. Mech. Eng.* 196.29-30 (2007), pp. 2777–2799.

[57] Rabczuk, T. and Zi, G. “A Meshfree Method based on the Local Partition of Unity for Cohesive Cracks”. In: *Comput. Mech.* 39.6 (2007), pp. 743–760.

[58] Rabczuk, T., Zi, G., Bordas, S., and Nguyen-Xuan, H. “A simple and robust three-dimensional cracking-particle method without enrichment”. In: *Comput. Methods Appl. Mech. Eng.* 199.37-40 (2010), pp. 2437–2455.

[59] Rajagopal, S. and Gupta, N. “Meshfree modelling of fracture—a comparative study of different methods”. In: *Meccanica* 46.5 (2011), pp. 1145–1158.

[60] Bažant, Z. P. and Oh, B. H. “Crack band theory for fracture of concrete”. In: *Matériaux Constr.* 16.3 (1983), pp. 155–177.

[61] Lacome, J.-l., Espinosa, C., and Limido, J. “SPH Formulation with Lagrangian Eulerian adaptive kernel”. In: *Proc. 4th SPHERIC Work.* Ed. by D. Le Touzé. 1. Nantes: 4th SPHERIC Workshop Local Organization Committee, 2009, pp. 294 –301.

[62] Lind, S. J. and Stansby, P. K. “High-order Eulerian incompressible smoothed particle hydrodynamics with transition to Lagrangian free-surface motion”. In: *J. Comput. Phys.* 326 (2016), pp. 290–311.

[63] Fourtakas, G., Stansby, P. K., Rogers, B. D., and Lind, S. J. “An Eulerian–Lagrangian incompressible SPH formulation (ELI-SPH) connected with a sharp interface”. In: *Comput. Methods Appl. Mech. Eng.* 329.Supplement C (2018), pp. 532–552.

[64] Scott MacDonald Coxeter, H. “Coordinates”. In: *Introduction to Geometry*. 2nd ed. Wiley, 1989. Chap. 8, pp. 107–110.

[65] Einstein, A. “Die Grundlage der allgemeinen Relativitätstheorie”. In: *Ann. Phys.* 354.7 (1916), pp. 769–822.

[66] Bonet, J. and Wood, R. D. *Nonlinear Continuum Mechanics for Finite Element Analysis*. Cambridge: Cambridge University Press, 2008.

[67] Gonzalez, O. and Stuart, A. M. *A First Course in Continuum Mechanics*. Cambridge Texts in Applied Mathematics. Cambridge: Cambridge University Press, 2008. Chap. 2, pp. 47–52.

[68] Phan-Thien, N. “Tensor Notation”. In: *Understanding Viscoelasticity: Basics of Rheology*. Berlin, Heidelberg: Springer Berlin Heidelberg, 2002. Chap. 1, p. 19.

[69] Malvern, L. E. “Vectors and Tensors”. In: *Introduction to the Mechanics of a Continuous Medium*. Englewood Cliffs: Prentice-Hall, 1969. Chap. 2, pp. 57–61.

[70] Hjelmstad, K. D. “Vectors and Tensors”. In: *Fundamentals of Structural Mechanics*. Boston, MA: Springer US, 2005. Chap. 1, pp. 44–45.

[71] Basa, M., Quinlan, N. J., and Lastiwka, M. “Robustness and accuracy of SPH formulations for viscous flow”. In: *Int. J. Numer. Methods Fluids* 60.10 (2009), pp. 1127–1148.

[72] Dirac, P. A. M. “The Delta Function”. In: *The Principles of Quantum Mechanics (International Series of Monographs on Physics)*. 4th ed. Oxford: Clarendon Press, 1988. Chap. 3, pp. 58–62.

[73] Arfken, G. B., Weber, H. J., and Harris, F. E. “Vector Analysis”. In: *Mathematical Methods for Physicists*. 7th ed. Elsevier, 2013. Chap. 3, pp. 123–203.

[74] Monaghan, J. J. “Particle methods for hydrodynamics”. In: *Comput. Phys. Reports* 3.2 (1985), pp. 71–124.

[75] Monaghan, J. J. and Lattanzio, J. C. “A refined particle method for astrophysical problems”. In: *Astron. Astrophys.* 149 (1985), pp. 135–143.

[76] Morris, J. P. “A study of the stability properties of SPH”. In: *Appl. Math. reports Prepr.* (1994).

[77] Morris, J. P. “Analysis of smoothed particle hydrodynamics with applications”. PhD thesis. Monash University, 1996.

[78] Fulk, D. A. and Quinn, D. W. “An Analysis of 1-D Smoothed Particle Hydrodynamics Kernels”. In: *J. Comput. Phys.* 126.1 (1996), pp. 165–180.

[79] Das, R. and Cleary, P. W. “Evaluation of Accuracy and Stability of the Classical SPH Method Under Uniaxial Compression”. In: *J. Sci. Comput.* 64.3 (2015), pp. 858–897.

[80] Price, D. J. “Smoothed particle hydrodynamics and magnetohydrodynamics”. In: *J. Comput. Phys.* 231.3 (2012), pp. 759–794.

[81] Quinlan, N. J., Basa, M., and Lastiwka, M. “Truncation error in mesh-free particle methods”. In: *Int. J. Numer. Methods Eng.* 66.13 (2006), pp. 2064–2085.

[82] Vignjevic, R., Campbell, J. C., Jaric, J., and Powell, S. “Derivation of SPH equations in a moving referential coordinate system”. In: *Comput. Methods Appl. Mech. Eng.* 198.30-32 (2009), pp. 2403–2411.

[83] Kundu, P. K., Cohen, I. M., and Dowling, D. R. “Cartesian Tensors”. In: *Fluid Mechanics*. 5th ed. Elsevier, 2012. Chap. 2, pp. 39–64.

[84] Monaghan, J. J. “An introduction to SPH”. In: *Comput. Phys. Commun.* 48.1 (1988), pp. 89–96.

[85] Price, D. J. “Magnetic fields in Astrophysics”. PhD thesis. University of Cambridge, 2004, pp. 46–51.

[86] Hernquist, L. and Katz, N. “TREESPH - A unification of SPH with the hierarchical tree method”. In: *Astrophys. J. Suppl. Ser.* 70 (1989), p. 419.

[87] Di G. Sigalotti, L., Klapp, J., Rendón, O., Vargas, C. A., and Peña-Polo, F. “On the kernel and particle consistency in smoothed particle hydrodynamics”. In: *Appl. Numer. Math.* 108 (2016), pp. 242–255.

[88] Young, J., Alcantara, I., Teixeira-Dias, F., Ooi, J., and Mill, F. “Regular or Random: A discussion on SPH initial particle distribution”. In: *IV Int. Conf. Part. Methods*. Ed. by E Onate, M Mischoff, D. R. J. Owen, P. Wriggers, and T. Zohdi. Barcelona: International Center for Numerical Methods in Engineering, 2015, pp. 1105–1116.

[89] Liu, M. B. and Liu, G. R. “Restoring particle consistency in smoothed particle hydrodynamics”. In: *Appl. Numer. Math.* 56.1 (2006), pp. 19–36.

[90] Liu, W. K., Li, S., and Belytschko, T. “Moving least-square reproducing kernel methods (I) Methodology and convergence”. In: *Comput. Methods Appl. Mech. Eng.* 143.1-2 (1997), pp. 113–154.

[91] Liu, W. K., Jun, S., and Zhang, Y. F. “Reproducing kernel particle methods”. In: *Int. J. Numer. Methods Fluids* 20.8-9 (1995), pp. 1081–1106.

[92] Price, D. J. “Smoothed Particle Hydrodynamics: Things I Wish My Mother Taught Me”. In: *Adv. Comput. Astrophys. Methods, Tools, Outcome*. Ed. by R Capuzzo-Dolcetta, M Limongi, and A Tornambè. Vol. 453. Astronomical Society of the Pacific Conference Series. 2012, p. 249.

[93] Monaghan, J. J. and Gingold, R. A. “Shock simulation by the particle method SPH”. In: *J. Comput. Phys.* 52.2 (1983), pp. 374–389.

[94] Lattanzio, J. C., Monaghan, J. J., Pongracic, H., and Schwarz, M. P. “Controlling Penetration”. In: *SIAM J. Sci. Stat. Comput.* 7.2 (1986), pp. 591–598.

[95] Raymond, S., Lemiale, V., Ibrahim, R., and Lau, R. “A meshfree study of the Kalthoff–Winkler experiment in 3D at room and low temperatures under dynamic loading using viscoplastic modelling”. In: *Eng. Anal. Bound. Elem.* 42 (2014), pp. 20–25.

[96] Cullen, L. and Dehnen, W. “Inviscid smoothed particle hydrodynamics”. In: *Mon. Not. R. Astron. Soc.* 408.2 (2010), pp. 669–683.

[97] Inutsuka, S.-i. “Reformulation of Smoothed Particle Hydrodynamics with Riemann Solver”. In: *J. Comput. Phys.* 179.1 (2002), pp. 238–267.

[98] Sugiura, K. and Inutsuka, S.-i. “An extension of Godunov SPH II: Application to elastic dynamics”. In: *J. Comput. Phys.* 333 (2017), pp. 78–103.

[99] Zel’dovich, Y. B. and Raizer, Y. P. “Shock waves in solids”. In: *Physics of Shock Waves and High-Temperature Hydrodynamic Phenomena*. Elsevier, 1967, pp. 685–784.

[100] Woan, G. *The Cambridge Handbook of Physics Formulas*. Cambridge University Press, 2000.

[101] Randles, P. W., Carney, T. C., Libersky, L. D., Renick, J. D., and Petschek, A. G. “Calculation of oblique impact and fracture of tungsten cubes using smoothed particle hydrodynamics”. In: *Int. J. Impact Eng.* 17.4-6 (1995), pp. 661–672.

[102] Hallquist, J. O. *LS-DYNA Theory Manual*. Livermore: Livermore Software Technology Coorporation, 2006.

[103] Johnson, G. R. and Holmquist, T. J. “Evaluation of cylinder-impact test data for constitutive model constants”. In: *J. Appl. Phys.* 64.8 (1988), pp. 3901–3910.

[104] Forsythe, G. E., Malcolm, M. A., and Moler, C. B. *Computer Methods for Mathematical Computations*. Prentice Hall Professional Technical Reference, 1977.

[105] Kopp, J. “Efficient Numerical Diagonalization Of Hermitian 3×3 Matrices”. In: *Int. J. Mod. Phys. C* 19.03 (2008), pp. 523–548.

[106] Lemaitre, J. “Evaluation of dissipation and damage in metals submitted to dynamic loading”. In: *Proc. Int. Congr. Math.* Kyoto, 1971.

[107] Johnson, G. R. and Cook, W. H. “Fracture characteristics of three metals subjected to various strains, strain rates, temperatures and pressures”. In: *Eng. Fract. Mech.* 21.1 (1985), pp. 31–48.

[108] Mirone, G. “Role of stress triaxiality in elastoplastic characterization and ductile failure prediction”. In: *Eng. Fract. Mech.* 74.8 (2007), pp. 1203–1221.

[109] Reveles, J. R. “Development of a total Lagrangian SPH code for the simulation of solids under dynamic loading”. PhD thesis. Cranfield University, 2007.

[110] Kulasegaram, S., Bonet, J., Lewis, R. W., and Profit, M. “A variational formulation based contact algorithm for rigid boundaries in two-dimensional SPH applications”. In: *Comput. Mech.* 33.4 (2004), pp. 316–325.

[111] Feldman, J. and Bonet, J. “Dynamic refinement and boundary contact forces in SPH with applications in fluid flow problems”. In: *Int. J. Numer. Methods Eng.* 72.3 (2007), pp. 295–324.

[112] Ferrand, M., Laurence, D. R., Rogers, B. D., Violeau, D., and Kassiotis, C. “Unified semi-analytical wall boundary conditions for inviscid, laminar or turbulent flows in the meshless SPH method”. In: *Int. J. Numer. Methods Fluids* 71.4 (2013), pp. 446–472.

[113] Mayrhofer, A., Rogers, B. D., Violeau, D., and Ferrand, M. “Investigation of wall bounded flows using SPH and the unified semi-analytical wall boundary conditions”. In: *Comput. Phys. Commun.* 184.11 (2013), pp. 2515–2527.

[114] Violeau, D., Leroy, A., and Mayrhofer, A. “Exact computation of SPH wall renormalising integrals in 3-D”. In: *9th Int. SPHERIC Work.* Ed. by D. Violeau, A. Hérault, and A. Joly. Paris, 2014, pp. 95–102.

[115] Leroy, A., Violeau, D., Ferrand, M., and Kassiotis, C. “Unified semi-analytical wall boundary conditions applied to 2-D incompressible SPH”. In: *J. Comput. Phys.* 261 (2014), pp. 106–129.

[116] Leroy, A., Violeau, D., Ferrand, M., Fratter, L., and Joly, A. “A new open boundary formulation for incompressible SPH”. In: *Comput. Math. with Appl.* 72.9 (2016), pp. 2417–2432.

[117] Monaghan, J. J. “Simulating Free Surface Flows with SPH”. In: *J. Comput. Phys.* 110.2 (1994), pp. 399–406.

[118] Colagrossi, A. and Landrini, M. “Numerical simulation of interfacial flows by smoothed particle hydrodynamics”. In: *J. Comput. Phys.* 191.2 (2003), pp. 448–475.

[119] Gourma, M. “Towards Better Understanding of the Smooth Particle Hydrodynamic Method”. PhD thesis. Cranfield University, 2003, pp. 84–98.

[120] Rogers, D. F. and Adams, J. A. *Transformations*. 2nd ed. New York: McGraw-Hill, Inc., 1990. Chap. 3.

[121] Lee, C. H., Gil, A. J., Greto, G., Kulasegaram, S., and Bonet, J. “A new Jameson–Schmidt–Turkel Smooth Particle Hydrodynamics algorithm for large strain explicit fast dynamics”. In: *Comput. Methods Appl. Mech. Eng.* 311 (2016), pp. 71–111.

[122] Caleyron, F, Combescure, A, Faucher, V, and Potapov, S. “Dynamic simulation of damage-fracture transition in smoothed particles hydrodynamics shells”. In: *Int. J. Numer. Methods Eng.* 90.6 (2012), pp. 707–738.

[123] Maurel, B and Combescure, A. “An SPH shell formulation for plasticity and fracture analysis in explicit dynamics”. In: *Int. J. Numer. Methods Eng.* 76.7 (2008), pp. 949–971.

[124] Krongauz, Y. and Belytschko, T. “Enforcement of essential boundary conditions in meshless approximations using finite elements”. In: *Comput. Methods Appl. Mech. Eng.* 131.1-2 (1996), pp. 133–145.

[125] Campbell, J. C., Vignjevic, R., and Libersky, L. D. “A contact algorithm for smoothed particle hydrodynamics”. In: *Comput. Methods Appl. Mech. Eng.* 184.1 (2000), pp. 49–65.

[126] Monaghan, J. J. “On the problem of penetration in particle methods”. In: *J. Comput. Phys.* 82.1 (1989), pp. 1–15.

[127] Vignjevic, R., De Vuyst, T., and Campbell, J. C. “A Frictionless Contact Algorithm for Meshless Methods”. In: *Comput. Model. Eng. Sci.* 13.1 (2006), pp. 35–48.

[128] Vignjevic, R., De Vuyst, T., and Campbell, J. C. “A Frictionless Contact Algorithm for Meshless Methods”. In: *Int. Conf. Comput. Eng. Sci.* 2007, pp. 107–112.

[129] Mesinger, F. and Arakawa, A. “Numerical methods used in atmospheric models”. In: *Glob. Atmos. Res. Progr. Publ. Ser.* 1 (1976), p. 10.

[130] Dehnen, W. and Read, J. I. “N-body simulations of gravitational dynamics”. In: *Eur. Phys. J. Plus* 126.5 (2011), p. 55.

[131] Serna, A., Alimi, J. M., and Chieze, J. P. “Adaptive Smooth Particle Hydrodynamics and Particle-Particle Coupled Codes: Energy and Entropy Conservation”. In: *Astrophys. J.* 461 (1996), p. 884.

[132] Falahaty, H., Gotoh, H., and Khayyer, A. “A Lagrangian Hamiltonian Computational Method for Hyper-Elastic Structural Dynamics”. In: *Int. J. Math. Comput. Phys. Electr. Comput. Eng.* 10.10 (2016), pp. 486–491.

[133] Zhou, C. E., Liu, G. R., and Lou, K. Y. “Three-Dimensional Penetration Simulation Using Smoothed Particle Hydrodynamics”. In: *Int. J. Comput. Methods* 04.04 (2007), pp. 671–691.

[134] Ma, S., Zhang, X., and Qiu, X. M. “Comparison study of MPM and SPH in modeling hypervelocity impact problems”. In: *Int. J. Impact Eng.* 36.2 (2009), pp. 272–282.

[135] Sharon, E. and Fineberg, J. “Microbranching instability and the dynamic fracture of brittle materials”. In: *Phys. Rev. B* 54.10 (1996), pp. 7128–7139.

[136] Ravi-Chandar, K. “Dynamic Fracture of Nominally Brittle Materials”. In: *Int. J. Fract.* 90.1 (1998), pp. 83–102.

[137] Batra, R. C. and Lear, M. H. “Simulation of brittle and ductile fracture in an impact loaded prenotched plate”. In: *Int. J. Fract.* 126.2 (2004), pp. 179–203.

[138] Freund, L. B. *Dynamic Fracture Mechanics*. Cambridge Monographs on Mechanics. Cambridge: Cambridge University Press, 1990, p. 83.

[139] Kalthoff, J. F. and Winkler, S. “Failure mode transition at high rates of shear loading”. In: *Int. Conf. Impact Load. Dyn. Behav. Mater.* 1987, pp. 185–195.

[140] Howell, B. P. and Ball, G. J. “A Free-Lagrange Augmented Godunov Method for the Simulation of Elastic–Plastic Solids”. In: *J. Comput. Phys.* 175.1 (2002), pp. 128–167.

[141] Mehra, V. and Chaturvedi, S. “High velocity impact of metal sphere on thin metallic plates: A comparative smooth particle hydrodynamics study”. In: *J. Comput. Phys.* 212.1 (2006), pp. 318–337.

[142] Zhang, Z. L. and Liu, M. B. “Smoothed particle hydrodynamics with kernel gradient correction for modeling high velocity impact in two- and three-dimensional spaces”. In: *Eng. Anal. Bound. Elem.* 83 (2017), pp. 141–157.

[143] Mehra, V., Sijoy, C. D., Mishra, V., and Chaturvedi, S. “Tensile Instability and Artificial Stresses in Impact Problems in SPH”. In: *J. Phys. Conf. Ser.* 377 (2012), p. 012102.

[144] Asadi Kalameh, H., Karamali, A., Anitescu, C., and Rabczuk, T. “High velocity impact of metal sphere on thin metallic plate using smooth particle hydrodynamics (SPH) method”. In: *Front. Struct. Civ. Eng.* 6.2 (2012), pp. 101–110.

List of Figures

List of Tables